

Halogen-Elimination Photochemistry and Oxygen-Activation Chemistry of Late Transition-Metal Complexes

by

Thomas S. Teets

B.S. Chemistry, 2007, Case Western Reserve University

Submitted to the Department of Chemistry in partial fulfillment of the degree of

DOCTOR OF PHILOSOPHY IN INORGANIC CHEMISTRY

at the

MASSACHUSETTS INSTITUTE OF TECHNOLOGY

June 2012

© 2012 Massachusetts Institute of Technology. All rights reserved.

Signature of Author: _____
Department of Chemistry
April 30, 2012

Certified by: _____
Daniel G. Nocera
The Henry Dreyfus Professor of Energy and Professor of Chemistry
Thesis Supervisor

Accepted by: _____
Robert W. Field
Haslam and Dewey Professor of Chemistry
Chairman, Departmental Committee on Graduate Studies

This Doctoral thesis has been examined by a committee of the Department of Chemistry as follows:

Richard R. Schrock
Frederick G. Keyes Professor of Chemistry
Committee Chairman

Daniel G. Nocera
The Henry Dreyfus Professor of Energy and Professor of Chemistry
Thesis Supervisor

Christopher C. Cummins
Professor of Chemistry

Dedication:
To my family for their encouragement,
and especially my parents for instilling a “no-excuses” mindset.

Halogen-Elimination Photochemistry and Oxygen-Activation Chemistry of Late Transition-Metal Complexes

by

Thomas S. Teets

Submitted to the Department of Chemistry on April 30, 2012 in partial fulfillment of the requirements for the degree of Doctor of Philosophy.

Abstract

Multi-electron reaction chemistry, from both ground- and excited-state species, is at the heart of many topics in renewable energy and catalysis. In this thesis, two classes of reactions central to the themes of energy conversion and multi-electron chemistry are studied on mono- and bimetallic late transition-metal platforms. In the early chapters, studies of photochemical halogen elimination, the key energy-storing step in photocatalytic hydrogen production from HX (X = Cl, Br), are described. In the latter sections of the thesis, the oxygen-activation and reduction chemistries of rhodium and iridium hydride complexes are highlighted.

In Chapters 1 and 2, photochemical halogen elimination from a variety of late transition-metal complexes is described. Studies of phosphine-terminated gold(III) halide complexes demonstrated that efficient halogen photoelimination can be promoted by ligand-to-metal charge-transfer (LMCT) excitation, in complexes devoid of a formal metal–metal interaction. In addition, gold was partnered with rhodium and iridium in a series of heterobimetallic complexes, and these complexes were also shown to cleanly eliminate halogen when illuminated, with additional electronic structural insights and reactivity trends emerging from this latter suite of compounds.

In Chapters 3–6, small-molecule reactivity studies of rhodium and iridium complexes, with a particular slant towards oxygen reduction, are disclosed. A new class of two-electron mixed-valent dirhodium and diiridium complexes is described. Featuring a coordinatively unsaturated M^0 center, these complexes display an expansive reactivity with numerous small-molecule substrates. A dirhodium hydride complex, prepared by HCl addition to the mixed-valent precursor, mediates the reduction of oxygen to water. Studies on iridium model complexes, coupled with detailed kinetic studies, produced a clear mechanistic understanding of this chemistry. In particular, the preparation and reactivity of a diiridium hydroperoxo complex gave many key insights into the activation of O_2 and the subsequent release of water. Analogous oxygen-reduction chemistry was also demonstrated to occur on a monorhodium platform, which will facilitate detailed mechanistic studies enabled by systematic ligand alteration.

Thesis Supervisor: Daniel G. Nocera

Title: The Henry Dreyfus Professor of Energy and Professor of Chemistry

Table of Contents

| | |
|-------------------|----|
| Title Page | 1 |
| Thesis Committee | 3 |
| Dedication | 5 |
| Abstract | 7 |
| Table of Contents | 9 |
| List of Figures | 17 |
| List of Schemes | 23 |
| List of Tables | 27 |

Chapter 1 –

| | |
|---|-----------|
| Halogen Photoreductive Elimination from Gold(III) Centers | 29 |
| 1.1 Introduction | 30 |
| 1.2 Results | 33 |
| 1.2.1 Synthesis and Characterization of Au ^I Complexes | 33 |
| 1.2.2 Thermal Reactivity of Au ^{III} Bromide Complexes | 39 |
| 1.2.3 Solution Photochemistry of Au ^{III} Complexes | 42 |
| 1.2.4 Solid-State Photochemistry of Au ^{III} Complexes | 47 |
| 1.3 Discussion | 49 |
| 1.4 Conclusions | 53 |
| 1.5 Experimental Methods | 54 |
| 1.5.1 General Considerations | 54 |
| 1.5.2 Physical Methods | 55 |
| 1.5.3 Preparation of Au ₂ ^{I,I} (tfepma)Cl ₂ (1) | 56 |
| 1.5.4 Preparation of Au ₂ ^{I,I} (dppip)Cl ₂ (2) | 56 |
| 1.5.5 Preparation of Au ₂ ^{I,I} (tfepma)Br ₂ (7) | 57 |
| 1.5.6 Preparation of Au ₂ ^{I,I} (dppip)Br ₂ (8) | 57 |
| 1.5.7 Oxidation of 2 with PhICl ₂ to form Au ₂ ^{II,II} (dppip)Cl ₄ (13) and Au ₂ ^{I,III} (dppip)Cl ₄ (14) | 58 |
| 1.5.8 Preparation of Au ₂ ^{I,III} (dppm)Cl ₄ (15) | 58 |
| 1.5.9 Preparation of Au ₂ ^{III,III} (dppm)Cl ₆ (16) | 58 |

| | |
|---|-----------|
| 1.5.10 Preparation of Au ₂ ^{I,III} (dcpm)Cl ₄ (17) | 59 |
| 1.5.11 Preparation of Au ₂ ^{III,III} (dcpm)Cl ₆ (18) | 59 |
| 1.5.12 Preparation of Au ^{III} (PPh ₃)Cl ₃ (19) | 60 |
| 1.5.13 Preparation of Au ^{III} (PCy ₃)Cl ₃ (20) | 60 |
| 1.5.14 Preparation of Au ₂ ^{III,III} (dppm)Br ₆ (22) | 60 |
| 1.5.15 Preparation of Au ₂ ^{I,III} (dcpm)Br ₄ (23) | 61 |
| 1.5.16 Preparation of Au ₂ ^{III,III} (dcpm)Br ₆ (24) | 61 |
| 1.5.17 Preparation of Au ^{III} (PCy ₃)Br ₃ (26) | 61 |
| 1.5.18 X-Ray Crystallographic Details | 62 |
| 1.6 References | 67 |
| Chapter 2 – | |
| Halogen Photoreductive Elimination from Metal–Metal-Bonded M^{II}–Au^{II} (M = Rh, Ir) Heterobimetallic Complexes | 71 |
| 2.1 Introduction | 72 |
| 2.2 Results | 74 |
| 2.2.1 Synthesis and Characterization of M ^I Au ^I (M = Rh, Ir) Complexes | 74 |
| 2.2.2 Halogen Oxidation of M ^I Au ^I (M = Rh, Ir) Complexes to Prepare M ^{II} Au ^{II} (M = Rh, Ir) Complexes | 78 |
| 2.2.3 Photophysical Properties and Electronic Structure of M ^I Au ^I (M = Rh, Ir) Complexes | 81 |
| 2.2.4 Photophysical Properties and Electronic Structure of M ^{II} Au ^{II} (M = Rh, Ir) Complexes | 84 |
| 2.2.5 Photochemical Halogen Elimination from M ^{II} Au ^{II} (M = Rh, Ir) Complexes | 87 |
| 2.2.6 Synthesis and Reactivity of a Rh ^I Au ^I Hydride Complex | 91 |
| 2.3 Discussion | 94 |
| 2.4 Conclusions | 97 |
| 2.5 Experimental Methods | 98 |
| 2.5.1 General Considerations | 98 |
| 2.5.2 Physical Methods | 99 |
| 2.5.3 Photochemistry | 100 |
| 2.5.4 GC Measurements | 100 |

| | |
|---|------------|
| 2.5.5 Computational Methods | 100 |
| 2.5.6 Preparation of $[\text{Rh}^{\text{I}}\text{Au}^{\text{I}}(\text{dcpm})_2(\text{CO})\text{Cl}](\text{PF}_6)$ [1 -(PF ₆)] | 101 |
| 2.5.7 Preparation of $[\text{Rh}^{\text{I}}\text{Au}^{\text{I}}(\text{dcpm})_2(\text{CO})\text{Br}](\text{PF}_6)$ [2 -(PF ₆)] | 101 |
| 2.5.8 Preparation of $[\text{Rh}^{\text{I}}\text{Au}^{\text{I}}(\text{dppm})_2(\text{CO})\text{Cl}](\text{PF}_6)$ [3 -(PF ₆)] | 102 |
| 2.5.9 Preparation of $[\text{Rh}^{\text{I}}\text{Au}^{\text{I}}(\text{dppm})_2(\text{CO})\text{Br}](\text{CF}_3\text{SO}_3)$ [4 -(OTf)] | 102 |
| 2.5.10 Preparation of $[\text{Ir}^{\text{I}}\text{Au}^{\text{I}}(\text{dcpm})_2(\text{CO})\text{Cl}](\text{PF}_6)$ (5) | 103 |
| 2.5.11 Preparation of $[\text{Ir}^{\text{I}}\text{Au}^{\text{I}}(\text{dcpm})_2(\text{CO})\text{Br}](\text{PF}_6)$ (6) | 103 |
| 2.5.12 Preparation of $[\text{Ir}^{\text{I}}\text{Au}^{\text{I}}(\text{dppm})_2(\text{CN}^t\text{Bu})_2](\text{PF}_6)_2$ (7) | 104 |
| 2.5.13 Preparation of $[\text{Rh}^{\text{II}}\text{Au}^{\text{II}}(\text{dcpm})_2(\text{CO})\text{Cl}_3](\text{PF}_6)$ [8 -(PF ₆)] | 104 |
| 2.5.14 Preparation of $[\text{Rh}^{\text{II}}\text{Au}^{\text{II}}(\text{dcpm})_2(\text{CO})\text{Br}_3](\text{PF}_6)$ [9 -(PF ₆)] | 105 |
| 2.5.15 Preparation of $[\text{Rh}^{\text{II}}\text{Au}^{\text{II}}(\text{dppm})_2(\text{CO})\text{Cl}_3](\text{PF}_6)$ [10 -(PF ₆)] | 105 |
| 2.5.16 Preparation of $[\text{Rh}^{\text{II}}\text{Au}^{\text{II}}(\text{dppm})_2(\text{CO})\text{Br}_3](\text{CF}_3\text{SO}_3)$ [11 -(OTf)] | 106 |
| 2.5.17 Preparation of $[\text{Ir}^{\text{II}}\text{Au}^{\text{II}}(\text{dcpm})_2(\text{CO})\text{Cl}_3](\text{PF}_6)$ (12) | 106 |
| 2.5.18 Preparation of $[\text{Ir}^{\text{II}}\text{Au}^{\text{II}}(\text{dcpm})_2(\text{CO})\text{Br}_3](\text{PF}_6)$ (13) | 106 |
| 2.5.19 Preparation of $[\text{Ir}^{\text{II}}\text{Au}^{\text{II}}(\text{dppm})_2(\text{CN}^t\text{Bu})_2\text{Cl}_2](\text{PF}_6)_2$ (14) | 107 |
| 2.5.20 Preparation of $[\text{Ir}^{\text{II}}\text{Au}^{\text{II}}(\text{dppm})_2(\text{CN}^t\text{Bu})_2\text{Br}_2](\text{PF}_6)_2$ (15) | 107 |
| 2.5.21 Preparation of $[\text{Rh}^{\text{I}}\text{Au}^{\text{I}}(\text{dcpm})_2(\text{CO})\text{H}](\text{PF}_6)$ (16) | 108 |
| 2.5.22 Reactions of 16 with LutH^+Cl^- and PhICl_2 | 108 |
| 2.5.23 X-Ray Crystallographic Details | 108 |
| 2.6 References | 115 |
| Chapter 3 – | |
| Redox Chemistry, Acid Reactivity, and Hydrogenation Reactions of Two-Electron Mixed-Valent Dirhodium and Diiridium Complexes | 117 |
| 3.1 Introduction | 118 |
| 3.2 Results | 120 |
| 3.2.1 Synthesis and Characterization of $\text{M}_2^{0,\text{II}}(\text{tfepma})_2(\text{CN}^t\text{Bu})_2\text{Cl}_2$ (M = Rh, Ir) | 120 |
| 3.2.2 Addition of CN^tBu to 1 and 2 | 121 |
| 3.2.3 Chemical Reduction of 1 and 2 | 123 |
| 3.2.4 Chlorine Oxidation of 1 and 2 | 125 |
| 3.2.5 Protonation of 1 and 2 with HX (X = Cl^- , OTs^-) | 128 |
| 3.2.6 Protonation of 5 with HOTs | 132 |

| | |
|---|------------|
| 3.2.7 Hydrogenation of 2 | 134 |
| 3.2.8 Formation of a Bimetallic Iridium Hydride Complex by Cyclometallation | 136 |
| 3.2.9 Electronic Absorption and Emission Spectra | 138 |
| 3.3 Discussion | 139 |
| 3.4 Conclusions | 142 |
| 3.5 Experimental Details | 143 |
| 3.5.1 General Considerations | 143 |
| 3.5.2 Physical Methods | 144 |
| 3.5.3 Preparation of Rh ₂ ^{0,II} (tfepma) ₂ (CN ^t Bu) ₂ Cl ₂ (1) | 144 |
| 3.5.4 Preparation of Ir ₂ ^{0,II} (tfepma) ₂ (CN ^t Bu) ₂ Cl ₂ (2) | 145 |
| 3.5.5 Preparation of [Rh ₂ ^{0,II} (tfepma) ₂ (CN ^t Bu) ₃ Cl]Cl (3) | 146 |
| 3.5.6 Preparation of Ir ₂ ^{0,II} (tfepma) ₂ (CN ^t Bu) ₃ Cl ₂ (4) | 146 |
| 3.5.7 Preparation of Rh ₂ ^{0,0} (tfepma) ₂ (CN ^t Bu) ₃ (5) | 146 |
| 3.5.8 Preparation of Ir ₂ ^{0,0} (tfepma) ₂ (CN ^t Bu) ₃ (6) | 147 |
| 3.5.9 Preparation of Rh ₂ ^{II,II} (tfepma) ₂ (CN ^t Bu) ₂ Cl ₄ (7a) | 147 |
| 3.5.10 Preparation of Ir ₂ ^{II,II} (tfepma) ₂ (CN ^t Bu) ₂ Cl ₄ (8) | 148 |
| 3.5.11 Preparation and NMR Characterization of Rh ₂ ^{II,II} (tfepma) ₂ (CN ^t Bu) ₂ Cl ₃ H (9a and 9b) | 148 |
| 3.5.12 Crystallization and IR Characterization of Rh ₂ ^{II,II} (tfepma) ₂ (CN ^t Bu) ₂ Cl ₃ H (9a) | 149 |
| 3.5.13 Preparation of Ir ₂ ^{II,II} (tfepma) ₂ (CN ^t Bu) ₂ Cl ₃ H (10) | 149 |
| 3.5.14 Preparation of Ir ₂ ^{II,II} (tfepma) ₂ (CN ^t Bu) ₂ Cl ₂ H(OTs) (11) | 150 |
| 3.5.15 Preparation of [Rh ₂ ^{I,I} (tfepma) ₂ (CN ^t Bu) ₃ (μ-H)](OTs) (12) | 150 |
| 3.5.16 Preparation of Ir ₂ ^{II,II} (tfepma) ₂ (CN ^t Bu) ₂ Cl ₂ (H) ₂ (13) | 151 |
| 3.5.17 Preparation of Ir ₂ ^{II,II} (dppm)(PPh(<i>o</i> -C ₆ H ₄)CH ₂ PPh ₂)(CN ^t Bu) ₂ Cl ₂ H (14) | 152 |
| 3.5.18 X-Ray Crystallographic Details | 152 |
| 3.6 References | 159 |
| Chapter 4 – | |
| Oxygen Reduction Effected by Group 9 Bimetallic Hydride Complexes | 161 |
| 4.1 Introduction | 162 |
| 4.2 Results | 164 |

| | |
|--|------------|
| 4.2.1 Oxygen Reduction by Dirhodium Hydride Complex 2 | 164 |
| 4.2.2 HCl Addition to Ir ₂ ^{0,II} Complex 5 | 167 |
| 4.2.3 Reaction of 6 with O ₂ to Form Ir ₂ ^{II,II} (tfepma) ₂ (CN ^t Bu) ₂ Cl ₃ (OOH) (7) | 168 |
| 4.2.4 Reaction of 5 with O ₂ to form Ir ₂ ^{II,II} (tfepma) ₂ (CN ^t Bu) ₂ Cl ₂ (η ² -O ₂) (8) | 170 |
| 4.2.5 Rate Law for the Reaction of Rh ₂ ^{II,II} Cl ₃ H (2) with HCl and O ₂ to Form Rh ₂ ^{II,II} Cl ₄ (3) | 172 |
| 4.2.6 Rate Law for the Reaction of Ir ₂ ^{II,II} Cl ₃ H (6) with O ₂ to form Ir ₂ ^{II,II} Cl ₃ (OOH) (7) | 175 |
| 4.3 Discussion | 177 |
| 4.3.1 Reactivity of Diiridium Complexes with O ₂ | 177 |
| 4.3.2 Mechanism of Formation of Iridium Hydroperoxo 7 | 178 |
| 4.3.3 Mechanism of O ₂ Reduction by Dirhodium Complex 2 | 180 |
| 4.4 Conclusions | 184 |
| 4.5 Experimental Details | 185 |
| 4.5.1 General Considerations | 185 |
| 4.5.2 Physical Methods | 185 |
| 4.5.3 Preparation and NMR Characterization of Rh ₂ ^{II,II} (tfepma) ₂ (CN ^t Bu) ₂ Cl ₃ D (4a and 4b) | 186 |
| 4.5.4 O ₂ -Reduction Reaction of 2a and 2b | 186 |
| 4.5.5 O ₂ -Reduction Reaction of 4a and 4b and Detection of D ₂ O | 186 |
| 4.5.6 Kinetic Measurements | 187 |
| 4.5.7 Preparation of Ir ₂ ^{II,II} (tfepma) ₂ (CN ^t Bu) ₂ Cl ₃ (OOH) (7) | 187 |
| 4.5.8 Preparation of Ir ₂ ^{II,II} (tfepma) ₂ (CN ^t Bu) ₂ Cl ₂ (η ² -O ₂) (8) | 188 |
| 4.5.9 X-Ray Crystallographic Details | 188 |
| 4.6 References | 191 |
| Chapter 5 – | |
| Reactivity of a Diiridium Hydroperoxo Complex: Acidolysis and Oxygen-Atom Transfer | 195 |
| 5.1 Introduction | 196 |
| 5.2 Results | 198 |
| 5.2.1 Synthesis of Iridium Hydroperoxo Complexes | 198 |
| 5.2.2 Oxygen-Atom-Transfer Reactivity of 3 | 201 |

| | |
|---|------------|
| 5.2.3 Acidolysis Reactions of 3 | 203 |
| 5.3 Discussion | 206 |
| 5.4 Conclusions | 208 |
| 5.5 Experimental Details | 208 |
| 5.5.1 General Considerations | 208 |
| 5.5.2 Physical Methods | 209 |
| 5.5.3 Preparation of Ir ₂ ^{0,II} (tfepma) ₂ (CNAd) ₂ Cl ₂ (4) | 209 |
| 5.5.4 Preparation of Ir ₂ ^{II,II} (tfepma) ₂ (CNAd) ₂ Cl ₃ H (5) | 210 |
| 5.5.5 Preparation of Ir ₂ ^{II,II} (tfepma) ₂ (CNAd) ₂ Cl ₃ (OOH) (6) | 210 |
| 5.5.6 Preparation of Ir ₂ ^{0,II} (tfepma) ₂ (CNXy) ₂ Cl ₂ (7) | 210 |
| 5.5.7 Preparation of Ir ₂ ^{II,II} (tfepma) ₂ (CNXy) ₂ Cl ₃ H (8) | 211 |
| 5.5.8 Preparation of Ir ₂ ^{II,II} (tfepma) ₂ (CN ^t Bu) ₂ Cl ₂ H(OSO ₂ Me) (11) | 211 |
| 5.5.9 Preparation of Ir ₂ ^{II,II} (tfepma) ₂ (CN ^t Bu) ₂ Cl ₃ (OH) (12) by Reaction of Ir ₂ ^{II,II} (tfepma) ₂ (CN ^t Bu) ₂ Cl ₃ (OOH) (3) with PPh ₃ | 212 |
| 5.5.10 Preparation and Isolation of Ir ₂ ^{II,II} (tfepma) ₂ (CN ^t Bu) ₂ Cl ₃ (OH) (12) | 212 |
| 5.5.11 Reaction of Ir ₂ ^{II,II} (tfepma) ₂ (CN ^t Bu) ₂ Cl ₃ (OOH) (3) with HCl | 213 |
| 5.5.12 Preparation and Isolation of Ir ₂ ^{II,II} (tfepma) ₂ (CN ^t Bu) ₂ Cl ₄ (14) (pseudo-C _{2h} isomer) | 213 |
| 5.5.13 Reaction of Ir ₂ ^{II,II} (tfepma) ₂ (CN ^t Bu) ₂ Cl ₃ (OOH) (3) with 2,6-Lutidinium Chloride | 214 |
| 5.5.14 X-Ray Crystallographic Details | 214 |
| 5.6 References | 217 |
| Chapter 6 – | |
| Oxygen-Reduction Reactions of Monometallic Rhodium Hydride Complexes | 219 |
| 6.1 Introduction | 220 |
| 6.2 Results | 222 |
| 6.2.1 HCl Addition to Rh ^I Complexes to Furnish Rh ^{III} Hydride Complexes | 222 |
| 6.2.2 Oxygen-Reduction Chemistry of 2a–c . | 225 |
| 6.2.3 Generation and Reactivity of Rh ^{III} -peroxo Complexes | 228 |
| 6.3 Discussion | 232 |

| | |
|---|-----|
| 6.4 Conclusion | 234 |
| 6.5 Experimental Details | 235 |
| 6.5.1 General Considerations | 235 |
| 6.5.2 Physical Methods | 235 |
| 6.5.3 Preparation of <i>trans</i> -Rh ^I Cl(CNXy)(PEt ₃) ₂ (1b) | 235 |
| 6.5.4 Preparation of <i>trans</i> -Rh ^I (CNAd)Cl(PEt ₃) ₂ (1c) | 236 |
| 6.5.5 Preparation and NMR Characterization of <i>cis-trans</i> -Rh ^{III} (CO)Cl ₂ H(PEt ₃) ₂ (2a) | 236 |
| 6.5.6 Preparation of <i>cis-trans</i> -Rh ^{III} Cl ₂ (CNXy)H(PEt ₃) ₂ (2b) | 237 |
| 6.5.7 Preparation of <i>cis-trans</i> -Rh ^{III} (CNAd)Cl ₂ H(PEt ₃) ₂ (2c) | 237 |
| 6.5.8 Preparation of <i>trans</i> -Rh ^{III} (CO)Cl ₃ (PEt ₃) ₂ (3a) | 238 |
| 6.5.9 Preparation of <i>trans</i> -Rh ^{III} Cl ₃ (CNXy)(PEt ₃) ₂ (3b) | 238 |
| 6.5.10 Preparation of <i>trans</i> -Rh ^{III} (CNAd)Cl ₃ (PEt ₃) ₂ (3c) | 239 |
| 6.5.11 Preparation of <i>trans</i> -Rh ^{III} Cl(CNXy)(η ² -O ₂)(PEt ₃) ₂ (4b) | 240 |
| 6.5.12 Preparation of <i>trans</i> -Rh ^{III} (CNAd)Cl(η ² -O ₂)(PEt ₃) ₂ (4c) | 240 |
| 6.5.13 O ₂ -Reduction Reactions of 2a–2c . | 240 |
| 6.5.14 Addition of HCl to 4b to Generate 3b/5b | 241 |
| 6.5.15 Addition of HCl to 4c to Generate 3c/5c | 241 |
| 6.5.16 X-Ray Crystallographic Details | 242 |
| 6.6 References | 245 |
| Acknowledgements | 249 |
| Biographical Note | 251 |
| Curriculum Vitae | 253 |

List of Figures

Chapter 1 –

- Figure 1.1.** X-ray crystal structures of **1**, **2**, **4**, and **7**. Ellipsoids are shown at the 50% probability level with solvent molecules and hydrogen atoms omitted for clarity. 35
- Figure 1.2.** X-ray crystal structure of **13**, with ellipsoids shown at the 50% probability level and hydrogen atoms omitted for clarity. 36
- Figure 1.3.** Crystal structures of **15**, **16**, **20**, **22**, **23**, **24**, and **26**. Ellipsoids are shown at the 50% probability level with solvent molecules and hydrogen atoms omitted. 38
- Figure 1.4.** Evolution of the $^{31}\text{P}\{^1\text{H}\}$ NMR spectra for the reactions of (a) **22** and (b) **24** with 1.2 M 1-hexene in CH_2Cl_2 at 293 K. A minor side product is marked with an asterisk (*) in (a). 39
- Figure 1.5.** Time-dependent $^{31}\text{P}\{^1\text{H}\}$ NMR spectra for a 30 mM solution of $\text{Au}^{\text{III}}(\text{PPh}_3)\text{Br}_3$ (**25**) in the presence of 1.2 M 1-hexene in CH_2Cl_2 at 293 ± 1 . Spectra are referenced to an external standard of 85% D_3PO_4 . 42
- Figure 1.6.** Overlaid electronic absorption spectra, measured in CH_2Cl_2 at room temperature. The spectra of **16** (—, red) and **22** (—, green) are shown in (a), **18** (—, blue) and **24** (—, pink) in (b). 43
- Figure 1.7.** $^{31}\text{P}\{^1\text{H}\}$ NMR spectra of (top) the initial solution of **18** in 1 M 1-hexene, and under photolysis using light with $\lambda > 300$ nm at ~ 10 °C (middle) at an arbitrary midpoint during the photolytic reaction and (bottom) at the conclusion of the photolysis. Resonances for **4**, **17** and **18** are indicated. 45
- Figure 1.8.** $^{31}\text{P}\{^1\text{H}\}$ NMR spectrum of the product following photolysis of a solid-state sample of **22** for 2 h, using light with $\lambda > 300$ nm at 10 °C for 2.5 h. Resonances for **21** and **9** are observed, in addition to an unidentified side product (*). The spectrum was recorded in CH_2Cl_2 at 202.5 MHz and is referenced to an external standard of 85% D_3PO_4 . 47
- Figure 1.9.** UV/Vis absorption spectrum, in H_2O , showing formation of $[\text{DPD}]^{++}$ when the trapped Br_2 from solid-state photolysis of **22** is treated with DPD. The spectrum was recorded at room temperature. 48
- Figure 1.10.** Real-time mass spectrometry trace for liberated Cl_2 following photolysis of a solid sample of **18**. Depicted are total ion counts for ^{35}Cl (—, red) and ^{37}Cl (—, green), which form upon fragmenting Cl_2 in the ionization chamber. The inset shows the ratios of the two isotopes during the time range when the ion counts are greater than $\frac{1}{2} \times \text{max}$. 49
- ### Chapter 2 –
- Figure 2.1.** X-ray crystal structures of **1–4**. Ellipsoids are depicted at the 50% probability level with counterions, solvent molecules and hydrogen atoms omitted for clarity. 75

- Figure 2.2.** X-ray crystal structure of complexes **5** and **6**. Ellipsoids are shown at the 50% probability level with counterions, solvent molecules and hydrogen atoms omitted for clarity. 78
- Figure 2.3.** X-ray crystal structures of **8** and **9**. Ellipsoids are shown at the 50% probability level with counterions, solvent molecules and hydrogen atoms omitted for clarity. 79
- Figure 2.4.** X-ray crystal structures of **12–15**. Ellipsoids are shown at the 50% probability level with counterions, solvent molecules, CN^tBu methyl groups, and hydrogen atoms omitted. 81
- Figure 2.5.** (a) Electronic absorption (—, red) and emission (■, blue) spectra of **1**. (b) Electronic absorption spectrum of **3**. Absorption spectra were recorded at 293 K in CH₂Cl₂, the emission spectrum at 77 K in a frozen glass of 1:1 CH₂Cl₂/toluene. 82
- Figure 2.6.** Overlaid absorption (—, red), glass emission (■, green), and solid-state emission (●, blue) spectra. The spectra of **5** are shown in (a) and **7** in (b). The absorption spectra were recorded at 293 K in CH₂Cl₂ solution. Emission spectra ($\lambda_{\text{ex}} = 431$ nm (**5**); 490 nm (**7**)) were recorded at 77 K; the frozen glass was of a 1:1 CH₂Cl₂/toluene solvent mixture. 83
- Figure 2.7.** Room-temperature UV-vis absorption spectra of **8**-(PF₆) (—, red) and **9**-(PF₆) (■, green) recorded in CH₂Cl₂ solution. 84
- Figure 2.8.** Overlaid electronic absorption spectra, measured in CH₂Cl₂ at 293 K. The spectra of **12** (—, red) and **13** (■, green) are shown in (a), **14** (—, red) and **15** (■, green) in (b). 85
- Figure 2.9.** Partial orbital energy diagrams for model complexes **12'**, **13'**, **14'**, and **15'**. 86
- Figure 2.10.** Plots for the predominant orbitals involved in the most intense electronic transitions of **13'** and **15'**, with contour levels of 0.04 a.u. Geometry optimizations were initiated from coordinates obtained from the crystal structures of **13** and **15**. Excitation energies ($E = 3.69$ eV for **13'** and $E = 3.53$ for **15'**) and oscillator strengths ($f_{336 \text{ nm}} = 0.38$ for **13'** and $f_{351 \text{ nm}} = 0.53$ for **15'**) were determined from time-dependent DFT calculations. 87
- Figure 2.11.** Spectral evolution for the photolysis of **8** (a) and **9** (b) with monochromatic 320 nm light in acetonitrile with 2.2 M DMBD at 283 K. In (a) traces shown from 0 to 39 min in 3 min intervals, in (b) spectra are shown from 0 to 8 min; 2 min interval for the first spectrum and 1 min intervals afterward. The inset in (b) shows the dependence of the photochemical quantum yield on the concentration of [DMBD], with 320 nm excitation. 88
- Figure 2.12.** (a) Spectral evolution during the photolysis of (a) **12** with monochromatic 320 nm and (b) **13** with monochromatic 370 nm light, in CH₂Cl₂ with 2.2 M DMBD at 283 K. The open circles depict the values for the product appearance quantum yields, Φ_p , measured in 2.2 M DMBD as a function of excitation wavelength. The inset in (b) shows the dependence of the quantum yield on [DMBD], with $\lambda_{\text{ex}} = 370$ nm. 89

| | |
|--|-----|
| Figure 2.13. Spectral evolution during the photolysis of (a) 14 and (b) 15 with 320 nm light in CH ₂ Cl ₂ with 2.2 M DMBD at 283 K. | 91 |
| Figure 2.14. Low-frequency region of the ¹ H NMR spectrum of 16 . The fully coupled spectrum is shown in (a), (b) shows the fully decoupled ¹ H{ ³¹ P} spectrum, and (c) shows the partially ³¹ P decoupled spectrum. | 92 |
| Figure 2.15. Electronic absorption spectrum of 16 , recorded at 293 K in benzene. | 92 |
| Figure 2.16. X-ray crystal structure of 16 . Ellipsoids are shown at the 50% probability level with counterions, solvent molecules and carbon-bound hydrogen atoms omitted. | 93 |
| Chapter 3 – | |
| Figure 3.1. X-ray crystal structures of 1 and 2 . Ellipsoids are shown at the 50% probability level with –CH ₂ CF ₃ groups and hydrogen atoms omitted for clarity. | 121 |
| Figure 3.2. X-ray crystal structures of 3 and 4a . Ellipsoids are shown at the 50% probability level with –CH ₂ CF ₃ groups, CN ^t Bu methyl groups, outer-sphere anions and hydrogen atoms omitted for clarity. | 122 |
| Figure 3.3. X-ray crystal structures of 5 and 6 . Ellipsoids are shown at the 50% probability level with –CH ₂ CF ₃ groups and hydrogen atoms omitted for clarity. | 124 |
| Figure 3.4. Variable-temperature ¹ H NMR spectra for complex 5 (a) and 6 (b), showing the <i>tert</i> -butyl resonances. Spectra were recorded in toluene- <i>d</i> ₈ at 500 MHz. | 125 |
| Figure 3.5. X-ray crystal structures of 7a and 7b . Ellipsoids are shown at the 50% probability level with –CH ₂ CF ₃ groups and hydrogen atoms omitted for clarity. The atoms in 7b are represented as isotropic spheres. | 126 |
| Figure 3.6. X-ray crystal structure of 8 . Ellipsoids are shown at the 50% probability level with –CH ₂ CF ₃ groups and hydrogen atoms omitted for clarity. | 127 |
| Figure 3.7. (a) ³¹ P{ ¹ H} and (b) low-frequency ¹ H NMR spectra of 9a and 9b , prepared by treating 1 with 25 eq. of HCl gas in THF- <i>d</i> ₈ . The inset in (b) is an expansion of the Rh–H resonance of 9a . Spectra were recorded at 20 °C at 202.5 MHz (³¹ P) and 500 MHz (¹ H). | 128 |
| Figure 3.8. X-ray crystal structures of 9a and 10 . Ellipsoids are drawn at the 50% probability level. Solvent molecules, carbon-bound hydrogen atoms and –CH ₂ CF ₃ groups are omitted for clarity. | 129 |
| Figure 3.9. X-ray crystal structure of 11a . Ellipsoids are shown at the 50% probability level with solvent molecules, –CH ₂ CF ₃ groups and carbon-bound hydrogen atoms are omitted. | 131 |
| Figure 3.10. X-ray crystal structure of the cation of 12 . Ellipsoids are shown at the 50% probability level with –CH ₂ CF ₃ groups, the outer-sphere tosylate anion and carbon-bound hydrogen atoms omitted for clarity. | 132 |
| Figure 3.11. Variable-temperature ¹ H NMR spectra for complex 12 , showing the <i>tert</i> -butyl resonances. Spectra were recorded in THF- <i>d</i> ₈ at 500 MHz. | 133 |

- Figure 3.12.** ^1H (a) and $^1\text{H}\{^{31}\text{P}\}$ (b) NMR spectra of **12**, showing the Rh–H resonance. Spectra were recorded in CD_3CN at 500 MHz and 293 K. 134
- Figure 3.13.** Low-frequency region of the ^1H NMR spectrum of **13**, showing the Ir–H resonances for the major and minor isomers. The structure of the major isomer and a likely structure of the minor isomer are shown near the peaks they are assigned to. 135
- Figure 3.14.** X-ray crystal structure of **13a**. Ellipsoids are shown at the 50% probability level with $-\text{CH}_2\text{CF}_3$ groups and carbon-bound hydrogen atoms omitted for clarity. 136
- Figure 3.15.** X-ray crystal structure of **14**. Ellipsoids are shown at the 50% probability level with the solvent molecule, $-\text{CH}_2\text{CF}_3$ groups and carbon-bound hydrogen atoms omitted for clarity. 137
- Figure 3.16.** Electronic absorption (—, blue) and emission (---, red) spectra of **2** (a) and **8** (b). The absorption spectra were recorded at 295 K in CH_3CN , the emission spectra were recorded at 77 K in 2-MeTHF with $\lambda_{\text{ex}} = 325$ nm (a) and 280 nm (b). 138

Chapter 4 –

- Figure 4.1.** ^2H NMR spectrum of the reaction of **1** with 10 eq. of DCl and 2.3 eq. of O_2 , after consumption of excess DCl by treatment with 2,6-lutidine. The spectrum shows the presence of 1 eq. of D_2O , as judged by integration against the internal C_6D_6 standard. Peaks marked with an asterisk (*) are minor impurities resulting from solvent decomposition caused by DCl; these peaks are also present in the control sample (no **1** present). The spectrum was recorded at 77.8 MHz in THF at 293 K. 165
- Figure 4.2.** (a) Overlaid electronic absorption spectra of **2** (—, red) and **3** (---, blue), recorded at 295 K in THF. (b) Spectral evolution during the reaction of **2** (40 μM) with O_2 (0.80 atm) in the presence of HCl (55 mM). The reaction was carried out in THF at 293 K, and spectra were recorded every 5 min. 166
- Figure 4.3.** (a) Electronic absorption spectra of **1** (—, red) and **3** (---, blue) recorded in THF at 295 K. (b) Spectral evolution for the photolysis of **3** (56 μM) in THF, using broadband light with $\lambda > 313$ nm. Spectra were recorded every 2 min for a total of 40 min. 166
- Figure 4.4.** X-ray crystal structure of **7**. Ellipsoids are shown at the 50% probability level with $-\text{CH}_2\text{CF}_3$ groups and carbon-bound hydrogen atoms omitted for clarity. 169
- Figure 4.5.** (a) Overlaid electronic absorption spectra of **6** (—, red) and **7** (---, blue), recorded at 295 K in THF. (b) Spectral evolution during the reaction of **6** (67 μM) with O_2 (0.40 atm). The reaction was carried out in THF at 293 K, and spectra were recorded every 5 min. 170
- Figure 4.6.** X-ray crystal structure of **8**. Ellipsoids are shown at the 50% probability level with $-\text{CH}_2\text{CF}_3$ groups and hydrogen atoms omitted for clarity. 171
- Figure 4.7.** Representative kinetic trace for the reaction of **2** with O_2 (1.6 atm) and HCl (5.5 mM), showing the change in the absorbance at 350 nm ($A_{350\text{ nm}}$) vs. time. The solid line shows the best-fit monoexponential curve. The reaction was executed at

20 °C in THF, and was preceded by ~ 2 min of manual shaking to ensure equilibration of dissolved O₂.

173

Figure 4.8. (a) Dependence of k_{obs} on $p(\text{O}_2)$ for the reaction of **2** with O₂ and HCl, with the [HCl] at 5.5 mM (▼), 11 mM (▲), 27 mM (●) and 55 mM (■). The solid lines show the best-fit lines for each dataset. (b) The slopes of the best-fit lines of k_{obs} vs. $p(\text{O}_2)$ from (a) are plotted against $[\text{HCl}]^{-1}$. The best-fit line is shown.

173

Figure 4.9. (a) Dependence of k_{obs} on $[\text{HCl}]^{-1}$ for the reaction of **2** with O₂ and HCl, with $p(\text{O}_2)$ at 0.4 atm (■), 0.8 atm (●), 1.6 atm (▲) and 3.2 atm (▼). Data are the same as those depicted in Figure 4.8. The solid red lines show the best-fit lines for each dataset. (b) The slopes of the best-fit lines of k_{obs} vs. $[\text{HCl}]^{-1}$ from (a) are plotted against $p(\text{O}_2)$. The best-fit line is shown. (c) The y -intercepts of the best-fit lines of k_{obs} vs. $[\text{HCl}]^{-1}$ from (a) are plotted against $p(\text{O}_2)$. The best-fit line is shown.

174

Figure 4.10. Representative kinetic trace for the reaction of **6** with O₂ (3.2 atm) at 20 °C, showing the change in the absorbance at 277 nm ($A_{277 \text{ nm}}$) vs. time. The solid line shows the best-fit monoexponential curve.

175

Figure 4.11. Dependence of k_{obs} on $p(\text{O}_2)$ for the reaction of **6** with O₂. The horizontal line is drawn at the average of value of $k_{\text{obs}} = 0.072 \text{ min}^{-1}$.

176

Figure 4.12. (a) Plot of k_{obs} vs. $[\text{HCl}]^{-1}$ for the reaction of **6** with O₂ (0.80 atm). Rate constants were calculated from initial rate data. A best-fit line to the three highest [HCl] values is shown. (b) Plot of initial rate vs. $p(\text{O}_2)$ for the reaction of **6** with O₂ in the presence of HCl (1.4 μM). The $[\mathbf{6}]_0$ is 9.7 μM.

177

Chapter 5 –

Figure 5.1. X-ray crystal structure of **6**. Ellipsoids are shown at the 50% probability level, with solvent molecules, –CH₂CF₃ groups and carbon-bound hydrogen atoms omitted for clarity.

199

Figure 5.2. ³¹P{¹H} NMR spectrum recorded of the product mixture isolated from the reaction of **3** with 2 eq. of PPh₃ for 12 h. The spectrum was recorded at 121.5 MHz in THF-d₈. Peaks corresponding to O=PPh₃, unreacted PPh₃, and **12** are marked accordingly.

201

Figure 5.3. X-ray crystal structure of **12**, with ellipsoids shown at the 50% probability level. In (a) all non-carbon atoms are labeled, whereas in (b) a view down the metal–metal axis with an analogous color scheme is shown. Solvent molecules, carbon-bound hydrogen atoms, and –CH₂CF₃ groups are omitted for clarity. Only one of the two disordered orientations is shown.

202

Figure 5.4. Evolution of the ³¹P{¹H} NMR spectrum upon treatment of **3** with HCl (1.1 eq) at room temperature. The time is indicated at the right, and the resonances attributed to **13** and **14** are denoted. The spectra were recorded at 121.5 MHz in THF-d₈.

204

Figure 5.5. X-ray crystal structure of **14**, with ellipsoids shown at the 50% probability level. In (a) all non-carbon atoms are labeled, whereas in (b) a view down the

metal–metal axis with an analogous color scheme is shown. Carbon-bound hydrogen atoms and $-\text{CH}_2\text{CF}_3$ groups are omitted for clarity. 205

Chapter 6 –

Figure 6.1. X-ray crystal structure of **2b**. Ellipsoids are shown at the 50% probability level with all carbon-bound hydrogen atoms omitted for clarity. 224

Figure 6.2. X-ray crystal structure of **3b**. Ellipsoids are shown at the 50% probability level, with hydrogen atoms are omitted for clarity. 225

Figure 6.3. Temporal evolution of the $^{31}\text{P}\{^1\text{H}\}$ NMR spectra when **2a**, in the presence of 2.1 M HCl, is treated with ca. 0.2 atm of O_2 at room temperature. Spectra were collected at the time intervals depicted on the right of the plot. The resonances attributed to **2a** and **3a** are labeled. 226

Figure 6.4. Time-resolved $^{31}\text{P}\{^1\text{H}\}$ NMR spectra when **2b**, in the presence of (a) 77 mM HCl or (b) 250 mM HCl, is treated with 1 atm of O_2 at room temperature. Spectra were collected at the time intervals depicted on the right of the plot. The resonances attributed to **2b** and **3b** are labeled. 227

Figure 6.5. Time-resolved $^{31}\text{P}\{^1\text{H}\}$ NMR spectra when **2c**, in the presence of (a) 77 mM HCl or (b) 250 mM HCl, is treated with 1 atm of O_2 at room temperature. Spectra were collected at the time intervals depicted on the right of the plot. The resonances attributed to **2c** and **3c** are labeled. 228

Figure 6.6. X-ray crystal structure of **4b**. Ellipsoids are shown at the 50% probability level with hydrogen atoms omitted for clarity. 229

Figure 6.7. X-ray crystal structure **5c**, with ellipsoids shown at the 50% probability level. All carbon-bound hydrogen atoms and solvent molecules are omitted for clarity. In (a), the cation is shown, with the outer-sphere Cl^- omitted. In (b), the counterion is included, as well as a second molecule of **5c** generated by a crystallographic inversion center. Dashed lines indicate located hydrogen bonds, and atoms labeled with an asterisk (*) are symmetry equivalents of those with conventional labels. 232

List of Schemes

Chapter 1 –

- Scheme 1.1.** Half-reactions and energetics for water splitting and HX (X = Cl, Br) splitting. 30
- Scheme 1.2.** General photocatalytic cycle for HX splitting. 31
- Scheme 1.3.** Synthesis of Au^I complexes. Isolated yields are listed in parentheses. 34
- Scheme 1.4.** Oxidation of **2** with PhICl₂. Approximate NMR yields are listed in parentheses. 35
- Scheme 1.5.** Halogen oxidation of Au^I and Au₂^{I,I} complexes to prepare a series of Au^{III}-containing complexes. Isolated yields are listed in parentheses. 37
- Scheme 1.6.** Thermal bromine elimination from Au₂^{III,III}-bromide complexes. 40
- Scheme 1.7.** Comproportionation of Au₂^{III,III} and Au₂^{I,I} complexes. 40
- Scheme 1.8.** Solution photochemistry of Au₂^{III,III} complexes. 44
- Scheme 1.9.** Electrophilic mechanism for thermal reaction of Au^{III} bromide complexes with alkenes. 50
- Scheme 1.10.** Proposed intramolecular trapping/photoisomerization mechanism for Au₂^{I,III} complexes. 52

Chapter 2 –

- Scheme 2.1.** Previous examples of iridium–gold heterobimetallic complexes. 73
- Scheme 2.2.** Previous examples of rhodium–gold heterobimetallic complexes. 74
- Scheme 2.3.** Synthesis of Rh^IAu^I complexes **1–4**. Isolated yields are listed in parentheses. 74
- Scheme 2.4.** Synthesis of Ir^IAu^I complexes **5** and **6**. Isolated yields are listed in parentheses. 76
- Scheme 2.5.** Synthesis of Ir^IAu^I complex **7**. Isolated yield is listed in parentheses. 77
- Scheme 2.6.** Halogen oxidation of Rh^IAu^I complexes to furnish Rh^{II}Au^{II} complexes. Isolated yields are listed in parentheses. 78
- Scheme 2.7.** Halogen oxidation of Ir^IAu^I complexes to prepare Ir^{II}Au^{II} complexes. Isolated yields are listed in parentheses. 80
- Scheme 2.8.** Photochemistry of M^{II}Au^{II} complexes. 88
- Scheme 2.9.** Synthesis of Rh^IAu^I hydride complex **16**. Isolated yield is listed in parentheses. 91
- Scheme 2.10.** Reactivity of Rh^IAu^I hydride complex **16**. 94

Chapter 3 –

- Scheme 3.1.** Previous examples of dirhodium and diiridium hydride model complexes. 119

| | |
|--|-----|
| Scheme 3.2. Synthesis of $M_2^{0,II}$ complexes 1 and 2 . Isolated yields are listed in parentheses. | 120 |
| Scheme 3.3. Addition of CN^tBu to 1 and 2 . Isolated yields are listed in parentheses. | 121 |
| Scheme 3.4. Synthesis of $M_2^{0,0}$ complexes 5 and 6 . Isolated yields are listed in parentheses. | 123 |
| Scheme 3.5. Oxidation of 1 and 2 with $PhICl_2$. Isolated yields are listed in parentheses. | 125 |
| Scheme 3.6. HCl addition to 1 and 2 . Yields are listed in parentheses; those for 9a/9b are from a reaction with 25 eq of HCl. | 128 |
| Scheme 3.7. Addition of HOTs to 2 . | 130 |
| Scheme 3.8. Synthesis of 12 by HOTs addition to 5 . Isolated yield is listed in parentheses. | 132 |
| Scheme 3.9. Hydrogenation of 2 . NMR yields are listed in parentheses. | 134 |
| Scheme 3.10. Synthesis of cyclometallated complex 14 . | 136 |
| Scheme 3.11. Proposed cyclometallation mechanism for 14 . | 142 |
| Chapter 4 – | |
| Scheme 4.1. Established mechanisms for aerobic oxidation of metal hydrides. | 163 |
| Scheme 4.2. Oxygen reduction to water mediated by complex 2a/b . | 165 |
| Scheme 4.3. Synthetic cycle for O_2 reduction mediated by 2 . | 167 |
| Scheme 4.4. Thermodynamic cycle for the determination of K_{HCl} for the addition of HCl to 5 . | 168 |
| Scheme 4.5. Aerobic oxidation chemistry of 5 and 6 . Isolated yields are listed in parentheses. | 169 |
| Scheme 4.6. Proposed mechanisms for O_2 reduction mediated by hydride complex 2 . | 182 |
| Chapter 5 – | |
| Scheme 5.1. Synthetic routes to late-metal hydroperoxo complexes. | 196 |
| Scheme 5.2. Previously characterized reactions of late-metal hydroperoxo and alkylperoxo complexes. | 197 |
| Scheme 5.3. Synthesis of diiridium hydroperoxo complexes 3 and 6 . Isolated yields are listed in parentheses. | 198 |
| Scheme 5.4. Synthesis of thermally unstable hydroperoxo complex 9 . | 199 |
| Scheme 5.5. O_2 reactivity of hydrido-sulfonate complexes 10 and 11 . Isolated yields are listed in parentheses. | 200 |
| Scheme 5.6. Oxygen-atom-transfer reactivity of 3 , generating 12 . Isolated yield is listed in parentheses. | 201 |
| Scheme 5.7. Reaction of 3 with HCl. Isolated yield is listed in parentheses. | 203 |

| | |
|--|-----|
| Scheme 5.8. Reaction of complex 3 with 2,6-lutidinium chloride. | 206 |
| Chapter 6 – | |
| Scheme 6.1. Synthesis of Rh ^I precursors 1a–c . Isolated yields are listed in parentheses. | 222 |
| Scheme 6.2. HCl addition to form hydride complexes 2a–c . Isolated yields are listed in parentheses. | 223 |
| Scheme 6.3. Oxygen-reduction chemistry of 2a–c . | 225 |
| Scheme 6.4. Synthesis of Rh ^{III} -peroxo complexes 4b/c . Isolated yields are listed in parentheses. | 229 |
| Scheme 6.5. HCl reactivity of Rh ^{III} -peroxo complexes 4b/c . | 230 |

List of Tables

Chapter 1 –

| | |
|---|----|
| Table 1.1. Rate constants for the thermal reduction of 22 and 24 . ^a | 41 |
| Table 1.2. Quantum yields (Φ_p) for photochemical reduction of 15–26 . ^a | 46 |
| Table 1.3. Crystallographic summary for complexes 1 , 2 , and 4 . | 63 |
| Table 1.4. Crystallographic summary for complexes 7 , 13 , and 15 . | 64 |
| Table 1.5. Crystallographic summary for complexes 16 , 20 , and 22 . | 65 |
| Table 1.6. Crystallographic summary for complexes 23 , 24 , and 26 . | 66 |

Chapter 2 –

| | |
|---|-----|
| Table 2.1. Summary of 77 K emission data for complexes 5–7 . Parenthetical numbers represent the relative contributions of the two biexponential fitting parameters. | 83 |
| Table 2.2. Crystallographic summary for complexes 1 and 2 . | 110 |
| Table 2.3. Crystallographic summary for complexes 3 and 4 . | 111 |
| Table 2.4. Crystallographic summary for complexes 5 , 6 , and 8 . | 112 |
| Table 2.5. Crystallographic summary for complexes 9 , 12 , and 13 . | 113 |
| Table 2.6. Crystallographic summary for complexes 14–16 . | 114 |

Chapter 3 –

| | |
|--|-----|
| Table 3.1. Crystallographic summary for 1–3 . | 154 |
| Table 3.2. Crystallographic summary for 4a , 5 , and 6 . | 155 |
| Table 3.3. Crystallographic summary for 7a , 8 , and 9a . | 156 |
| Table 3.4. Crystallographic summary for 10 and 11a . | 157 |
| Table 3.5. Crystallographic summary for 12 , 13a , and 14 . | 158 |

Chapter 4 –

| | |
|---|-----|
| Table 4.1. Crystallographic summary for 7 and 8 . | 190 |
|---|-----|

Chapter 5 –

| | |
|--|-----|
| Table 5.1. Crystallographic summary for 6 , 12 , and 14 . | 216 |
|--|-----|

Chapter 6 –

| | |
|---|-----|
| Table 6.1. Crystallographic summary for 2b and 3b . | 243 |
| Table 6.2. Crystallographic summary for 4b and 5c . | 244 |

Chapter 1 – Halogen Photoreductive Elimination from Gold(III) Centers

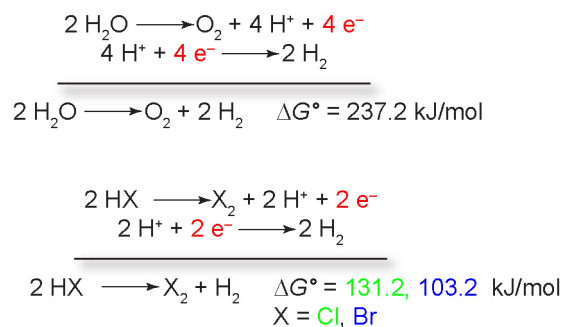
Portions of this work have been previously published:

Reproduced in part with permission from Teets, T. S.; Nocera, D. G. *J. Am. Chem. Soc.* **2009**, *131*, 7411–7420. Copyright 2009 American Chemical Society.

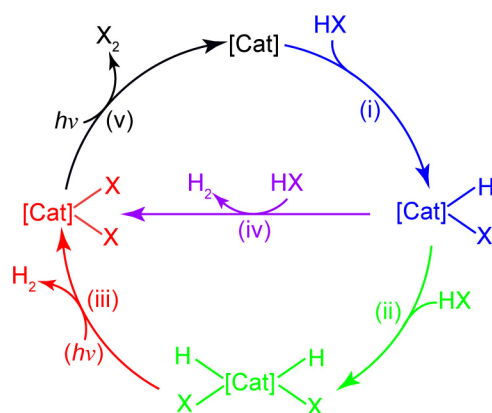
Teets, T. S.; Nocera, D. G.; *Chem. Commun.* **2011**, *47*, 9268–9274. Reproduced by permission of the Royal Society of Chemistry.

1.1 Introduction

The first two chapters of this thesis concern photochemical halogen elimination, an important topic in the context of solar energy utilization. Solar energy will not be used as a large-scale energy supply for society unless it can be stored.^{1,2} Although numerous storage technologies are available, and many are used commercially for storage of conventional power, the highest energy density for the storage of solar energy is in chemical bonds, thus defining the imperative for developing catalysts that promote fuel-forming reactions.³ A preeminent energy-storing reaction is water splitting,^{4,5} though the transformation of this small molecule presents formidable challenges. This water-to-hydrogen fuel conversion is accompanied by the removal of four protons and four electrons from water to produce oxygen.^{6,7} Hydrogen can be produced in simpler two-electron, two-proton reactions⁸ of which HX-splitting (X = Cl or Br) possesses nearly equivalent energy storage to that of H₂O splitting. Scheme 1.1 summarizes the half-reactions and energetics of water splitting and HX splitting. The thermodynamics of HX splitting depend on the identity of the halide, and although the absolute energy storage is less than that of water splitting, the energy stored per electron, i.e. the formal potential, is nearly identical. The stored energy of water or HX splitting can be recovered in a fuel cell, and though not as extensively studied as H₂/O₂ fuel cells, the efficiencies of H₂/X₂ fuel cells reign supreme.⁹ Whereas H₂/O₂ fuel cells have maximal efficiencies of ~ 50%,¹⁰ efficiencies for H₂/Cl₂ fuel cells can be ~ 70%,¹¹ with efficiencies as high as 90% for H₂/Br₂ cells.¹² For all of these preceding reasons, HX splitting is certainly an attractive alternative to the water-splitting reaction, and our group has focused much effort on the development of molecular photocatalysts for this transformation.



Scheme 1.1. Half-reactions and energetics for water splitting and HX (X = Cl, Br) splitting.



Scheme 1.2. General photocatalytic cycle for HX splitting.

In Scheme 1.2, a generalized catalytic cycle for HX splitting, mediated by a molecular photocatalyst, is presented. The individual steps in Scheme 1.2 are color-coded and numbered for clarity. (i) HX oxidatively adds to the photocatalyst ([Cat]), producing a hydrido-halide intermediate; from here two pathways are possible. (ii) A second HX addition gives a dihydrido-dihalide species, which in (iii) reductively eliminates H₂ in a process that may be photochemical. Alternatively, if the [Cat](H)(X) intermediate formed in (i) possesses a M–H bond that is sufficiently hydridic, direct protonation by HX (iv) produces H₂ and generates the final [Cat](X)₂ intermediate. The sequential HX oxidative-addition steps in (i) and (ii) are likely only operative in very reducing bimetallic catalysts, where a +4 change in formal oxidation state is feasible because the oxidative equivalents can be shared between two metals. In monometallic catalysts or complexes with a less reducing resting state, the acid-base pathway in (iv) is most probable. Whatever the mechanism of H₂ production, the final step (v) involves the thermodynamically demanding photoelimination of X₂ to close the cycle. The efficiency of HX splitting is typically not limited by the reductive H₂ half-reaction but rather by this oxidative X₂ half-reaction. Hence, the success of HX-splitting energy storage depends crucially on using light to drive the unfavorable energetics associated with X₂ production. Most examples of X₂ photoelimination occur from organic substrates and by using high-energy light.^{13–16} The photoelimination of halogen from metal centers is rare and typically driven by the presence of a trap,^{17–19} only with trap can appreciable quantities of H₂ be photoproduced from HX.^{20,21} An obvious strategy for improving the H₂ production from HX is to increase the quantum yield of M–X bond activation and ultimately effect X₂ photoproduction without the need for trap so that maximal energy may be stored.

The quantum efficiency of X₂ elimination may be enhanced by using late transition-metal complexes in high oxidation states to drive M–X photoactivation. Whereas the Rh^{II}–Au^{II} complex, [Rh^{II}Au^{II}(tfepma)₂(CN^tBu)₂Cl₃]AuCl₂ (tfepma = CH₃N(P[OCH₂CF₃]₂)₂), is thermally unstable,²² a stable d⁷–d⁹ complex may be realized by replacing Rh(II) with Pt(III). The [Pt^{III}Au^{II}(dppm)₂PhCl₃]PF₆ (dppm = bis(diphenylphosphino)methane) complex is photoreduced to its Pt^{II}Au^I congener upon irradiation in the presence of 2,3-dimethyl-1,3-butadiene.¹⁷ The quantum yield of halogen elimination achieves a maximum of 5.7% at 5 M trap concentration, nearly a tenfold increase over halogen elimination from a d⁷–d⁹ Rh^{II}–Rh⁰ bimetallic core.^{19,23} Even higher quantum yields are obtained from more highly oxidizing Pt^{III}–Pt^{III} cores. Pt₂^{III,III}(tfepma)₂Cl₆ undergoes efficient two-electron photoreduction ($\Phi_p = 38\%$) at high trap concentrations, and is able to eliminate Cl₂ when irradiated in the solid state, providing what is the first example of authentic, trap-free X₂ reductive photoelimination from a transition-metal center.¹⁸

In this chapter, X₂ photoelimination is generalized by showing that the reaction may proceed efficiently from Au^{III} centers of mono- and bimetallic cores without the need for a halogen trap. Despite thorough characterization of the photophysical properties of Au^I compounds,^{24–29} photochemical transformations involving molecular gold compounds are limited, particularly for Au^{III}.^{30,31} Reductive elimination from Au^{III} centers has been demonstrated extensively in carbon-carbon bond-forming reactions,^{32–34} frequently from Au^{III} species of the type LAuR₂X (L = phosphine, R = alkyl or aryl, X = halide). Though the light sensitivity of some Au₂^{II,II} and Au^{III} halide species has been noted,³⁵ a well-defined halogen-elimination photochemistry from gold has eluded characterization.³⁶ The two-electron Au^{III/I} redox couple is well matched to the two-electron equivalency of halogen photoreductive elimination. Hence an attractive possibility was effecting two- and four-electron halogen-photoelimination reactions from mono- and bimetallic complexes, respectively. The unique observation is made that M–X bond activation and authentic X₂ elimination can be achieved by LMCT excitation of complexes lacking a metal–metal bond. Though LMCT photochemistry has been conventionally confined to one-electron redox transformations,³⁷ the LMCT excitation of the Au^{III} centers described in this chapter allows for (i) the facile four-electron reduction of Au₂^{III,III} complexes to give the corresponding Au₂^{I,I} species, and (ii) the unprecedented photoelimination of X₂ from a monometallic center. This photochemistry is paralleled by a

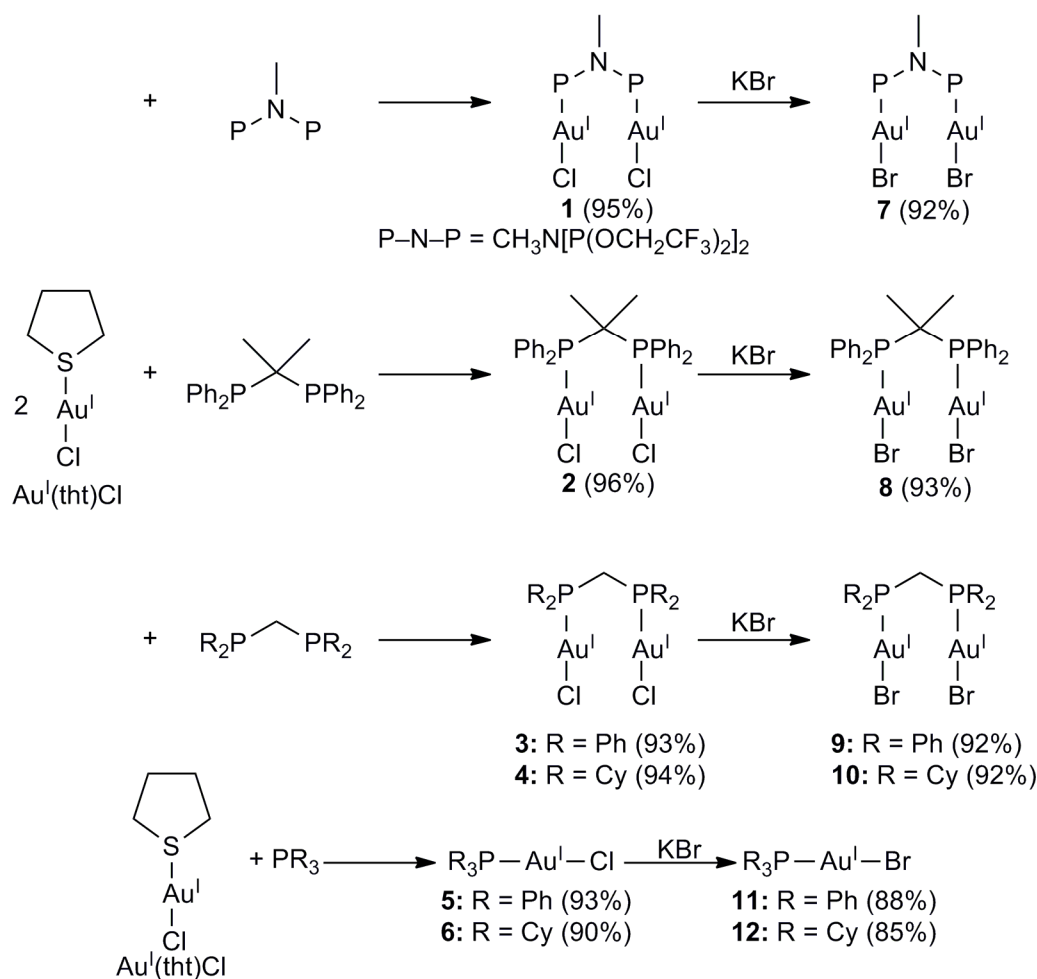
thermal reaction chemistry on a timescale amenable to kinetic interrogation. Bimetallic Au₂^{III,III} species are observed to reductively eliminate much more rapidly than their monometallic Au^{III} counterparts. Characterization of the haloalkane product resulting from thermal and photochemical reactions in the presence of alkene indicates that the thermal and photochemical reactions proceed by disparate mechanisms. Whereas photoreductive elimination from complexes in solution requires the use of halogen traps, the reaction proceeds smoothly in the solid state in the absence of trap. The X₂ back-reaction is prevented by virtue of the production of a volatile X₂ photoproduct. Because X₂ will react thermally with any of the Au^I centers studied here to produce the corresponding Au^{III} analogue, the solid-state photoinduced elimination of halogen is an energy-storing photoreaction.

1.2 Results

1.2.1 Synthesis and Characterization of Au^I Complexes

Mono- and bimetallic Au^I chloride precursors were synthesized by stoichiometric reaction of the appropriate phosphine with the versatile Au^I starting material Au^I(tbt)Cl.³⁸ Scheme 1.3 summarizes the syntheses, as well as the numerical designations that are used for all phosphine-ligated Au^I compounds that will be considered here. Conversion of chloride complexes **1–6** to the bromide complexes **7–12** was accomplished by treating a CH₂Cl₂ solution of the chloride precursor with a fivefold excess of aqueous KBr. This metathesis method has proven to be a general for halide exchange of phosphine-ligated Au^I species.³⁹

All complexes in Scheme 1.3 were fully characterized by ¹H NMR, ³¹P{¹H} NMR and elemental analysis (see section 1.5). Several of the complexes were obtained as single crystals, and their structures were validated by X-ray diffraction. Figure 1.1 collects the structures of Au₂^{I,I} complexes **1**, **2**, **4**, and **7**. All of these structures show approximately linear coordination about the two Au^I atoms, with an aurophilic interaction⁴⁰ also apparent in all cases, as judged by the close contacts of the two gold atoms. In tfepma-bridged **1** and **7** the Au···Au distances are 3.0678(4) (average of two crystallographically independent molecules) and 3.0803(7) Å, respectively. For complex **2**, spanned by bis(diphenylphosphino)isopropane (dppip), the Au···Au separation lengthens to 3.1616(2) Å and in **4**, spanned by bis(dicyclohexylphosphino)methane (dcpm) the longest intermetallic distance is observed, at 3.262(9) Å. Analogous structures for



Scheme 1.3. Synthesis of Au^I complexes. Isolated yields are listed in parentheses.

Au₂^{I,I}(dppm)X₂ (X = Cl (**3**), Br (**9**); dppm = bis(diphenylphosphino)methane) have been reported elsewhere by other groups.^{39,41,42}

Complexes **1** and **7**, bridged by tfepma (CH₃[P(OCH₂CF₃)₂]₂), were chosen on the basis of our group's previous success using this ligand to bridge metal–metal-bonded complexes of late transition metals.^{18,21,43} However, treatment of **1** and **7** with the halogen oxidants PhICl₂ and Br₂, respectively, led to incomplete oxidations with mixtures of unstable oxidized products. In both cases, products of the type Au₂^{I,III}(tfepma)X₄ were identified in crude reaction mixtures, but in neither case were these products isolated and structurally characterized.

Complexes **2** and **8**, bridged by the ligand dppip, were targeted because of earlier reports that halogen oxidation affords valence-symmetric metal–metal-bonded complexes of the type

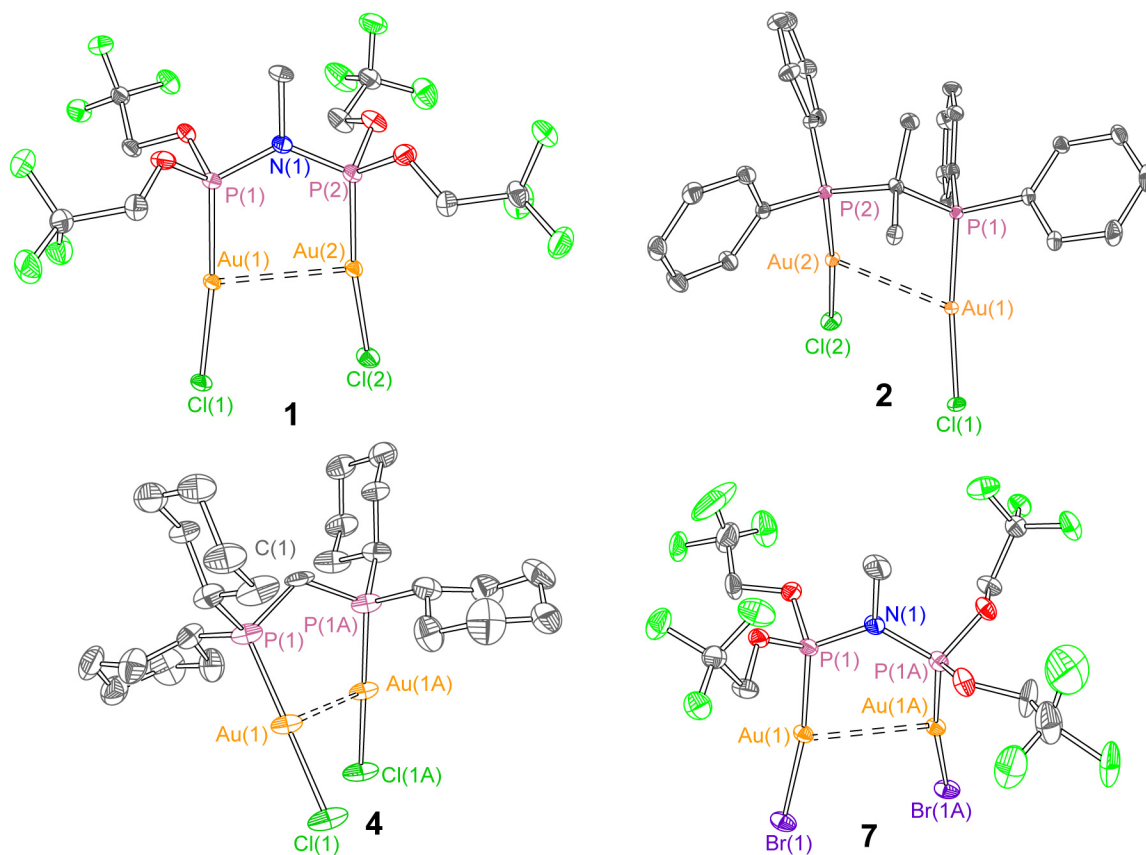
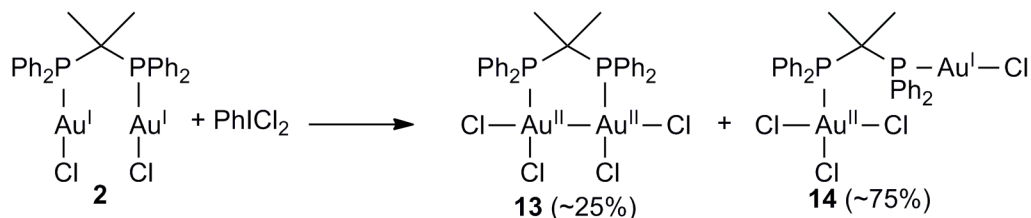


Figure 1.1. X-ray crystal structures of **1**, **2**, **4**, and **7**. Ellipsoids are shown at the 50% probability level with solvent molecules and hydrogen atoms omitted for clarity.

$\text{Au}_2^{\text{II,II}}(\text{dppip})\text{X}_4$, assigned as such from ^{197}Au -Mössbauer spectroscopy.⁴⁴ A study of the photochemistry of this class of complexes would provide an interesting parallel to our earlier work on halogen elimination from metal–metal-bonded complexes.^{17–19} As shown in Scheme 1.4, treatment of $\text{Au}_2^{\text{I,I}}(\text{dppip})\text{Cl}_2$ (**2**) with PhICl_2 gave a mixture of two isomeric products, $\text{Au}_2^{\text{II,II}}(\text{dppip})\text{Cl}_4$ (**13**), and $\text{Au}_2^{\text{I,III}}(\text{dppip})\text{Cl}_4$ (**14**), the latter characterized by two doublets in the $^{31}\text{P}\{\text{^1H}\}$ NMR spectrum of the crude reaction mixture. Yellow-orange crystals of the valence-symmetric product **13** were preferentially obtained, and this complex was structurally



Scheme 1.4. Oxidation of **2** with PhICl_2 . Approximate NMR yields are listed in parentheses.

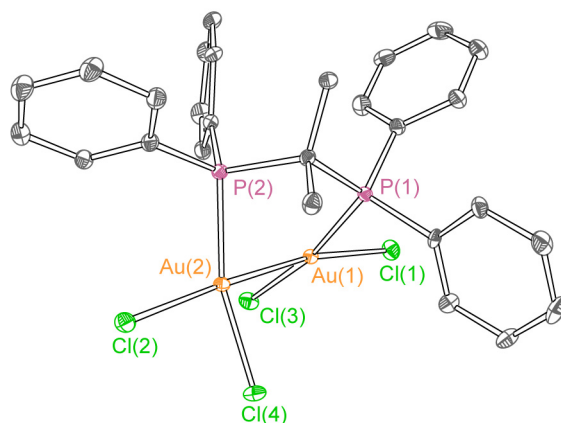
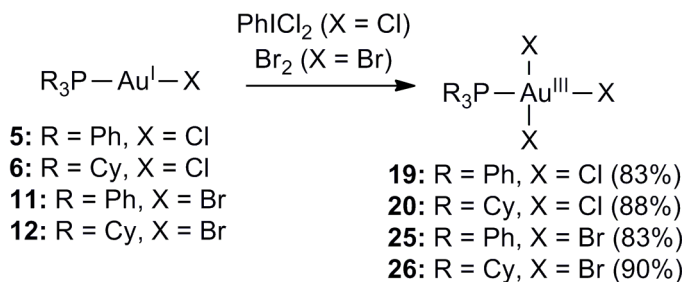
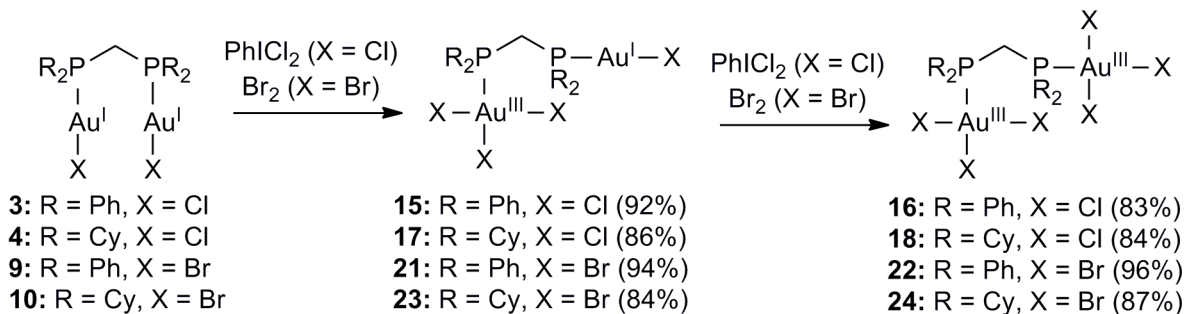


Figure 1.2. X-ray crystal structure of **13**, with ellipsoids shown at the 50% probability level and hydrogen atoms omitted for clarity.

characterized for the first time, as shown in Figure 1.2. Both Au^{II} centers feature approximately square-planar coordination environments, and the Au(1)–Au(2) distance of 2.5592(3) Å is among the shortest ever (per a search of the CSD) and clearly indicative of a formal gold–gold bond. Dissolution of crystals of **13** produces a mixture of isomeric **13** (25%) and **14** (75%), and as such further interrogation of the optical and photochemical properties of **13** were not pursued.

Halogen oxidation of complexes bridged by methylene-spaced diphosphines, **3**, **4**, **9**, and **10**, as well as monometallic complexes **5**, **6**, **11**, and **12**, gave a suite of Au^{III}-containing complexes which were suitable for further photochemical interrogation, as described in sections 1.2.3 and 1.2.4. Scheme 1.5 summarizes the synthetic routes to prepare the oxidized gold complexes. In a slight variation of precedent, oxidation of chloride complexes **3–6** to prepare bimetallic Au₂^{I,III} or Au₂^{III,III} (**15–18**) and monometallic Au^{III} complexes (**19**, **20**) was performed in CH₂Cl₂ using PhICl₂ to deliver chlorine. Though the reactions are slower than direct Cl₂ oxidation, in some cases requiring more than 12 hours to complete, the stoichiometry is very easy to control using solid PhICl₂ as the source of chlorine. All reactions proceeded cleanly and quantitatively as judged by ³¹P NMR spectra of reaction mixtures. Oxidation of **9–12** with Br₂ in CH₂Cl₂ gave gold(III)-containing **21–26**; complexes **21** and **25** have been previously reported by the same procedure. All Au^{III} complexes were obtained in isolated yields of more than 80% and gave satisfactory microanalyses.

Oxidation of bimetallic Au₂^{I,I} species with a single equivalent of halogen can potentially produce either Au₂^{II,II} or Au₂^{I,III} complexes. For the bimetallic compounds shown in Scheme 1.5,



Scheme 1.5. Halogen oxidation of Au^{I} and $\text{Au}_2^{\text{I,I}}$ complexes to prepare a series of Au^{III} -containing complexes. Isolated yields are listed in parentheses.

room-temperature $^{31}\text{P}\{^1\text{H}\}$ and ^1H NMR spectroscopic analyses unambiguously demonstrate that oxidation of $\text{Au}_2^{\text{I,I}}$ chloride complexes **3** and **4** with one equivalent of PhICl_2 and oxidation of $\text{Au}_2^{\text{I,I}}$ bromide complexes **9** and **10** with one equivalent of Br_2 exclusively produce mixed-valent $\text{Au}_2^{\text{I,III}}$ compounds in solution. Two distinct peaks are apparent in the 121.5 MHz $^{31}\text{P}\{^1\text{H}\}$ NMR spectra of the $\text{Au}_2^{\text{I,III}}$ oxidation products **15**, **17**, **21** and **23**. For dppm complexes **15** (X = Cl) and **21** (X = Br), $^2J_{\text{P-P}}$ coupling constants of 17 Hz and 21 Hz are observed, whereas dcpm-bridged **17** (X = Cl) shows a much smaller coupling constant of 9 Hz. The coupling in $\text{Au}_2^{\text{I,III}}(\text{dcpm})\text{Br}_4$ (**23**) is too weak to be observed and two singlets are present in the $^{31}\text{P}\{^1\text{H}\}$ NMR spectrum. In the ^1H NMR spectra, the CH_2 resonances for the mixed-valent species **15**, **17**, **21** and **23** appear as doublets of doublets, due to coupling to two inequivalent phosphorus nuclei. In contrast, this same resonance in the valence-symmetric bimetallic compounds **3**, **4**, **9**, **10**, **16**, **18**, **22** and **24** is manifested as a triplet, as expected for coupling to two equivalent phosphorus nuclei. $\text{Au}_2^{\text{I,III}}(\text{dppm})\text{Cl}_4$ (**15**) was previously used as a starting material to prepare Au^{II} -aryl complexes and was reported to exist as a valence-symmetric, metal–metal-bonded $\text{Au}_2^{\text{II,II}}$ complex,⁴⁵ though no details of the synthesis or characterization were given. However, all of the spectroscopic and structural evidence given here clearly identifies **15** as a mixed-valent compound.

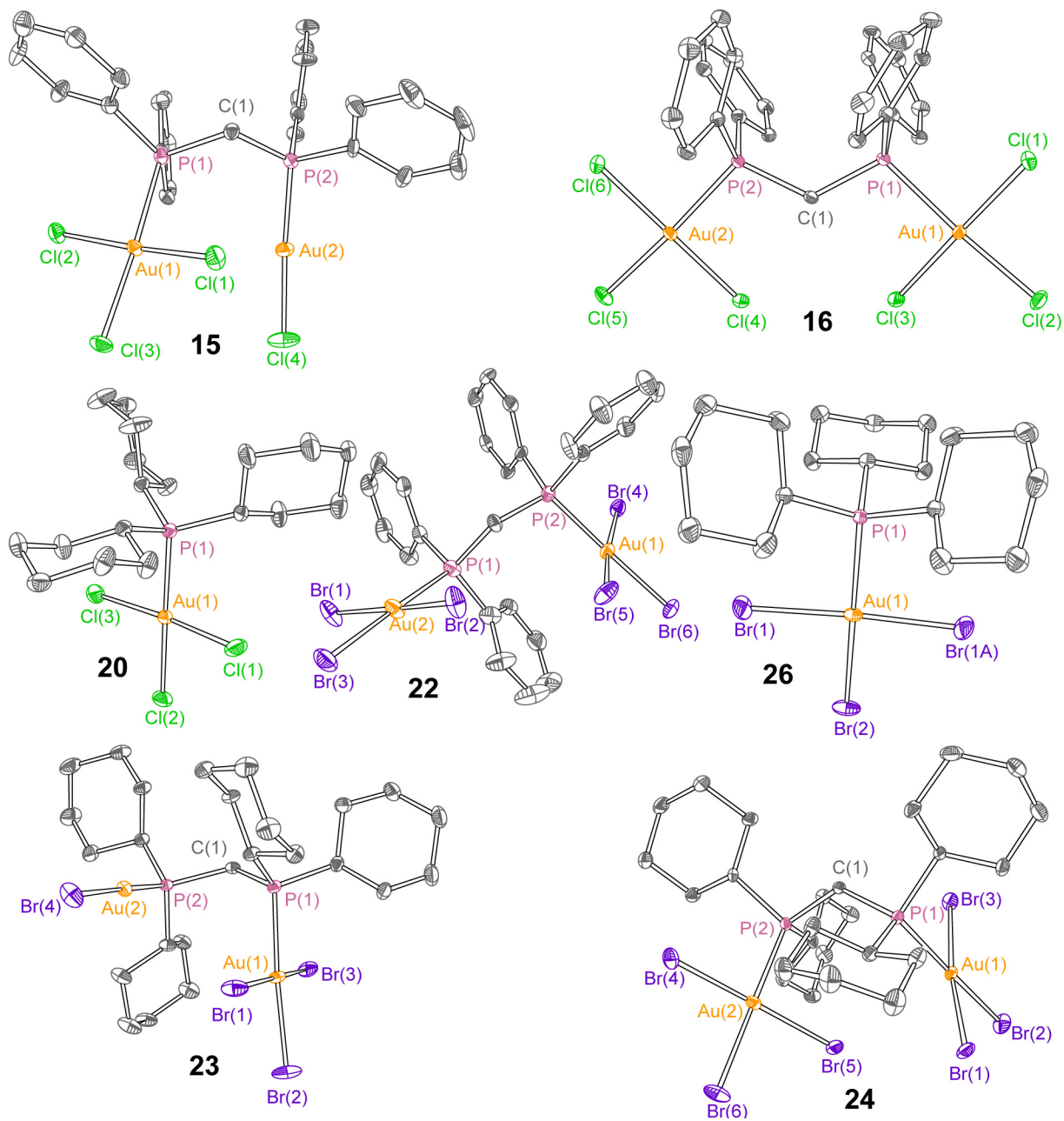


Figure 1.3. Crystal structures of **15**, **16**, **20**, **22**, **23**, **24**, and **26**. Ellipsoids are shown at the 50% probability level with solvent molecules and hydrogen atoms omitted.

X-ray crystal structures for **15**, **16**, **20**, **22**, **23**, **24** and **26** are depicted in Figure 1.3. In all cases, typical Au–P and Au–X bond distances are observed. All Au^{III} centers possess a nearly square-planar coordination geometry, as expected for a d⁸ metal, whereas the Au^I atoms in mixed-valent Au₂^{I,III}(dppm)Cl₄ (**15**) and Au₂^{I,III}(dcpm)Br₄ (**23**) show the expected linear two-coordinate environment for d¹⁰ Au^I. The singly bridged framework with a methylene-spaced

diphosphine ligand affords a very flexible geometry as is evident from the multitude of solid-state conformations shown in Figure 1.1 and 1.3, together with previously reported structures of $\text{Au}_2^{\text{I,I}}(\text{dppm})\text{Cl}_2$ (**1**),^{41,42} $\text{Au}_2^{\text{I,I}}(\text{dppm})\text{Br}_2$ (**9**),³⁹ and $\text{Au}_2^{\text{I,III}}(\text{dppm})\text{Br}_4$ (**21**).³⁹ Intramolecular π -stacking interactions contribute to the observed conformation of $\text{Au}_2^{\text{III,III}}(\text{dppm})\text{Br}_6$ (**22**); an obvious intra- or intermolecular ligand- or metal-based interaction is not apparent in X-ray crystal structures for any other Au^{III} -containing complex. The solution NMR spectra of all $\text{Au}_2^{\text{III,III}}$ complexes are consistent with an average C_2 symmetry, indicating that the solid-state structures do not persist in solution. Notably, the structures of all bimetallic Au^{III} complexes are devoid of any metal–metal interactions in the solid state.

1.2.2 Thermal Reactivity of Au^{III} Bromide Complexes

The Au^{III} bromide complexes are cleanly reduced to their respective Au^{I} precursors in the presence of an alkene, with the complete exclusion of light. Digold compounds **22** and **24** and monogold compounds **25** and **26** react with *cis*-2-hexene, *trans*-2-hexene, 3,3-dimethyl-1-butene, 3-methyl-1-pentene and *trans*-4-methyl-2-pentene to furnish the dibromoalkane product; where possible, only the diastereomer resulting from *anti* addition across the carbon–carbon double bond is observed. Figure 1.4 shows the time-dependent $^{31}\text{P}\{^1\text{H}\}$ NMR spectra for the thermal decay of **22** (R = Ph) and **24** (R = Cy) in 1.2 M 1-hexene/ CH_2Cl_2 . The spectra indicate that the elimination of halogen is stepwise from these bimetallic complexes, allowing $\text{Au}_2^{\text{I,III}}$ complexes

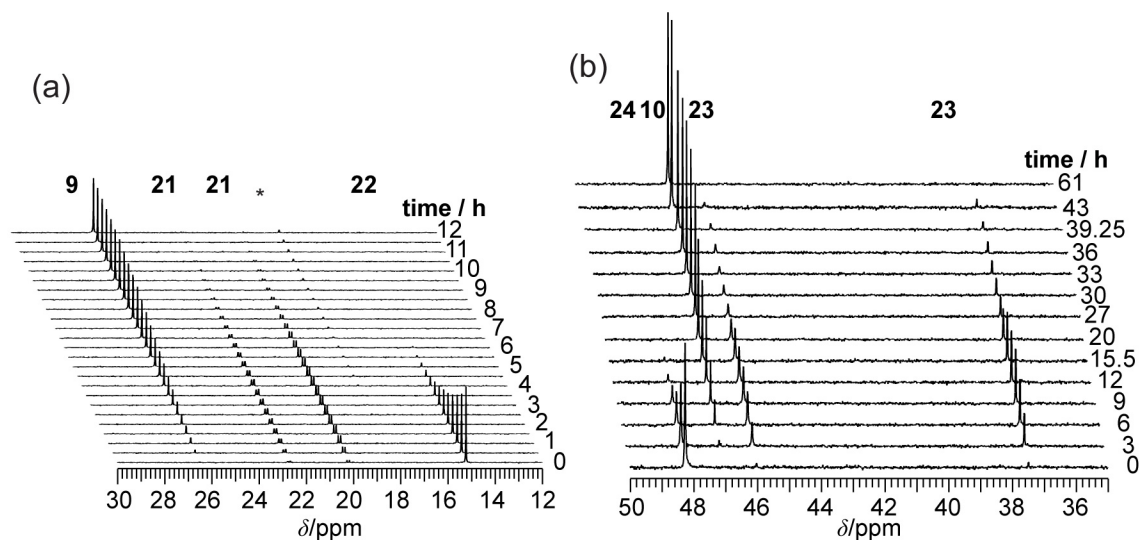
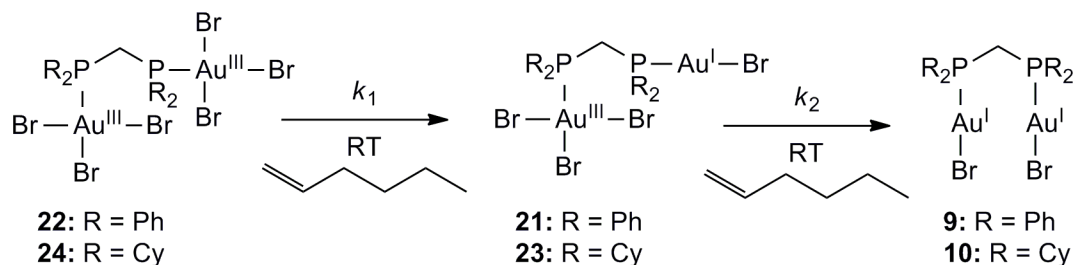
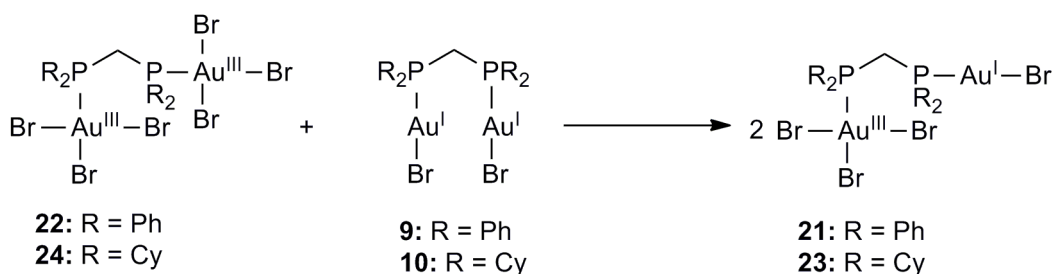


Figure 1.4. Evolution of the $^{31}\text{P}\{^1\text{H}\}$ NMR spectra for the reactions of (a) **22** and (b) **24** with 1.2 M 1-hexene in CH_2Cl_2 at 293 K. A minor side product is marked with an asterisk (*) in (a).



Scheme 1.6. Thermal bromine elimination from $\text{Au}_2^{\text{III,III}}$ -bromide complexes.

21 and **23** to be observed as intermediates, as depicted in Scheme 1.6. A minor and undetermined side product, estimated to be < 5% in quantity, grows in at later time points of the decay of **22**. The very small amount of $\text{Au}_2^{\text{I,III}}$ present in the $t = 0$ spectrum of **24** appeared during the lag time between mixing the sample and acquisition of the first spectrum. Under the same conditions, solutions of the Au^{III} chloride complexes **15–20** do not smoothly undergo two-electron reductive elimination. Although the two-electron reduced species are observed in the ^{31}P NMR spectra, several intractable side products also appear, and we observe visual evidence of the formation of Au^0 in some cases. As the thermal reduction of the $\text{Au}_2^{\text{III,III}}$ bromide complexes proceeds and appreciable $\text{Au}_2^{\text{I,I}}$ complex is accrued, a competing comproportionation reaction between $\text{Au}_2^{\text{III,III}}$ reactant and $\text{Au}_2^{\text{I,I}}$ product is established. This halogen-exchange reaction is summarized in Scheme 1.7. Equimolar mixtures of dppm-bound **22** and **9** react quite rapidly; within 90 minutes, quantitative formation of **21** is observed for a starting reactant concentration of ~ 3 mM. The reaction between dcpm complexes **24** and **10** is much slower, but within 19 h a solution containing 6 mM each of **10** and **24** shows near complete formation of **23**. The transfer of halogen between Au^{I} and Au^{III} centers is not unprecedented, and has been implicated as one of several steps involved in the halide redistribution that occurs when phosphine-gold(I) chloride complexes are oxidized with Br_2 .⁴⁶



Scheme 1.7. Comproportionation of $\text{Au}_2^{\text{III,III}}$ and $\text{Au}_2^{\text{I,I}}$ complexes.

Table 1.1. Rate constants for the thermal reduction of **22** and **24**.^a

| | k_1/min^{-1} | k_2/min^{-1} |
|-----------|--------------------------------|----------------------------------|
| 22 | $(6.5 \pm 0.6) \times 10^{-3}$ | $(6.1 \pm 0.5) \times 10^{-3}$ |
| 24 | $(3.7 \pm 0.1) \times 10^{-3}$ | $(1.66 \pm 0.03) \times 10^{-3}$ |

^a Recorded in 1.2 M 1-hexene in CH₂Cl₂ at 20 ± 1 °C. Values are an average of 2 or more trials with standard errors.

The rate constants k_1 and k_2 (Scheme 1.6), listed in Table 1.1, were determined for the reactions of **22** and **24** with 1-hexene under pseudo-first-order conditions ([1-hexene] = 1.2 M, [Au] = 3–6 mM). The kinetics were ascertained by monitoring the disappearance of the single ³¹P{¹H} NMR resonance of Au₂^{III,III} complexes (for k_1) and the two ³¹P{¹H} NMR resonances of the Au₂^{I,III} complexes (for k_2). The pseudo-first-order rate constant was determined from plots of ln([A]/[A]₀) vs. time; ln([A]/[A]₀) was obtained from the relative integration of the ³¹P{¹H} NMR signals of **22** and **24** and the sum of the integrations for the two signals of **21** and **23**. Linear plots were obtained, from which the values for the rate constants were extracted. In the case of **22**, k_1 was determined by only considering early time points, for which the concentration of **9** was low (< 0.05[**22**]), and the comproportionation step shown in Scheme 1.7 could be ignored. For complex **24**, comproportionation with **10** occurs at an appreciably small rate such that deviations from linearity in the ln([A]/[A]₀) vs. time plot are not observed over all time points. The rate constant for comproportionation was not determined for either bimetallic system owing to large associated errors with absolute concentration measurements from ³¹P{¹H} NMR spectra.

The monometallic Au^{III} complexes likewise convert to the Au^I congeners in the presence of olefin. The reduction of Au^{III}(PCy₃)Br₃ (**26**) to Au^I(PCy₃)Br (**12**) is very sluggish, requiring about a month to complete in 1 M olefin, and for this reason detailed kinetic studies of **26** were not pursued. After 12 h, only ~ 10% of Au^{III}(PPh₃)Br₃ (**25**) converts to Au^I(PPh₃)Br (**11**) in 1.2 M 1-hexene; in comparison a solution of bimetallic **22** completely converts to fully reduced **9** in the same timeframe. Stacked ³¹P{¹H} NMR spectra for the reduction of **25** are shown in Figure 1.5 below, which show clean conversion of **25** to **11** without the buildup of any intermediate species. The slope of a plot of ln([A]/[A]₀) vs. time gradually increases in magnitude as the reduction of **25** proceeds to completion, indicating that the product **11** accelerates the reaction

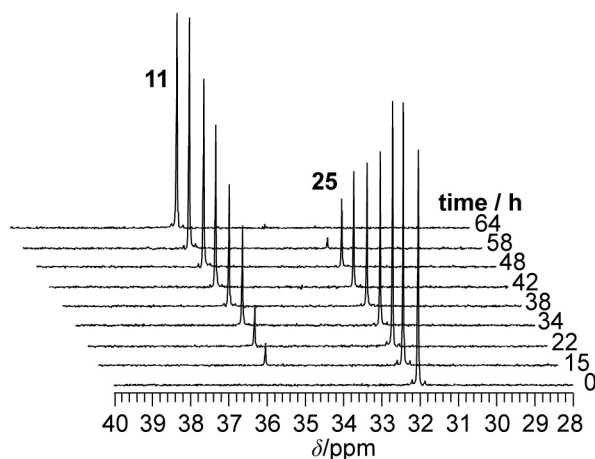


Figure 1.5. Time-dependent $^{31}\text{P}\{^1\text{H}\}$ NMR spectra for a 30 mM solution of $\text{Au}^{\text{III}}(\text{PPh}_3)\text{Br}_3$ (**25**) in the presence of 1.2 M 1-hexene in CH_2Cl_2 at 293 ± 1 . Spectra are referenced to an external standard of 85% D_3PO_4 .

and a description of this system with pseudo-first-order kinetics is not valid. In a separate experiment, reduction of **25** in the presence of two equivalents of **11**, under otherwise identical conditions, resulted in much more rapid consumption of **25**; $\sim 60\%$ conversion to **11** was observed in the first 12 h. The reduction of **25** (with no **11** initially) approximates pseudo-first-order behavior at early time points ($t < 24$ h), when the concentration of **11** is comparatively low. The apparent rate constant during this early time period is $\sim 2 \times 10^{-4} \text{ min}^{-1}$, an order-of-magnitude smaller than the rate constants for the bimetallic systems listed in Table 1.1.

1.2.3 Solution Photochemistry of Au^{III} Complexes

The electronic absorption spectra ($\lambda > 300 \text{ nm}$) of the gold halide compounds reported here are largely determined by $\text{X} \rightarrow \text{Au}^{\text{III}}$ charge transfer as shown by a comparison of the spectra of (i) chloride and bromide congeners and (ii) Au^{III} and Au^{I} analogs. Figure 1.6 displays the electronic spectra for the halide complexes of $\text{Au}_2^{\text{III,III}}$ cores, which are representative of a complex containing at least one Au^{III} center; spectra for all other complexes show very similar features and trends. The Au^{III} complexes exhibit a distinct and intense low-energy absorption band that tails into the visible spectral region and is responsible for the red ($\text{X} = \text{Br}$) and yellow ($\text{X} = \text{Cl}$) colors observed for concentrated solutions of the complexes. As seen in Figure 1.6, the position of the low-energy absorption band is influenced primarily by the nature of the halide. Mono- and bimetallic species with the same halide and similar phosphine substitution essentially absorb at the same energy for this low-energy maximum, though the extinction coefficient is

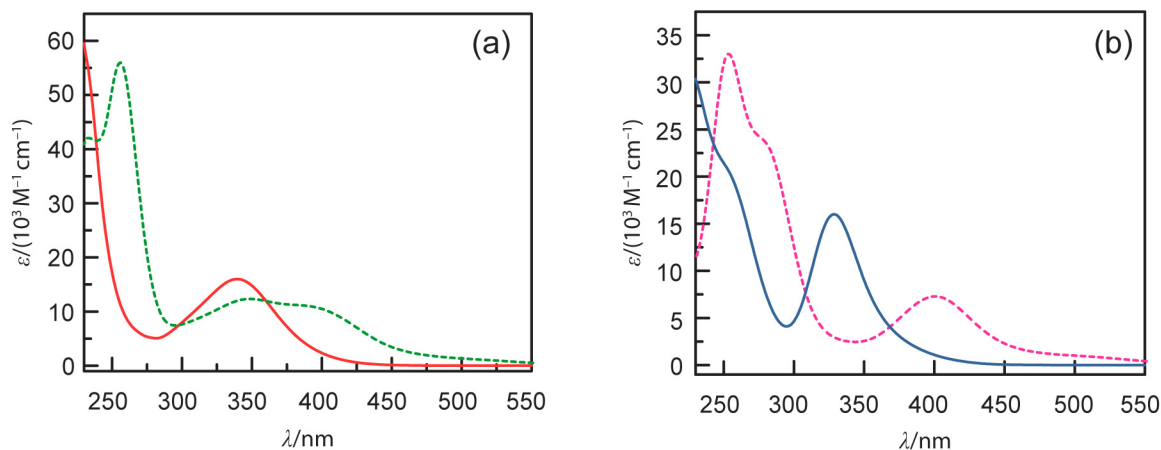
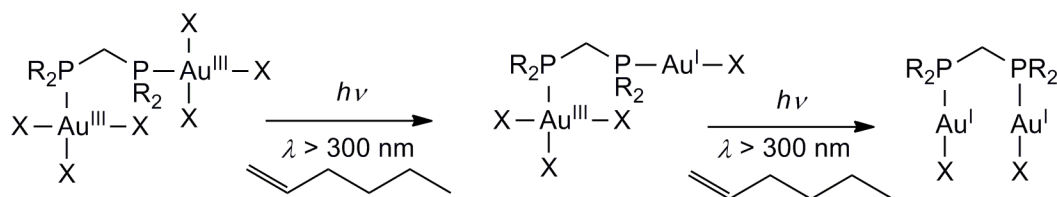


Figure 1.6. Overlaid electronic absorption spectra, measured in CH_2Cl_2 at room temperature. The spectra of **16** (—, red) and **22** (---, green) are shown in (a), **18** (—, blue) and **24** (---, pink) in (b).

augmented in the bimetallic $\text{Au}_2^{\text{III,III}}$ complexes relative to their analogous $\text{Au}_2^{\text{I,III}}$ and Au^{III} complexes. As an example, the lowest-energy absorption maximum for $\text{Au}^{\text{III}}(\text{PPh}_3)\text{Br}_3$ (**25**) appears at 346 nm, shifting only minimally to the 349 nm low-energy maximum of $\text{Au}_2^{\text{III,III}}(\text{dppm})\text{Br}_6$ (**22**). The bromide complexes possess overlapping low-energy absorption bands, which are most apparent in the spectra of $\text{Au}_2^{\text{I,III}}$ and $\text{Au}_2^{\text{III,III}}$ dppm complexes **21** and **22**, respectively. In other bromide complexes, a second band can be seen as a weak shoulder whereas the chloride complexes appear to show a single, generally sharper absorption band. The most distinguishing feature between the chloride and bromide series is the pronounced bathochromic shift of the low-energy band of the latter series. The magnitude of this energy difference for the lowest energy transition is between $4000\text{--}5000\text{ cm}^{-1}$, which is in accordance with the bathochromic shift of a halide-based LMCT transition between halide and Au^{III} .⁴⁷ Of course, in the case of a d^{10} metal center, the LMCT transition is obviated. Au^{I} mono- and bimetallic halide complexes **3–6** and **9–12** are colorless, exhibiting absorption from the solvent cut-off wavelength to $\leq 270\text{ nm}$.

When solution samples of Au^{III} complexes **15–26** are irradiated within their low-energy absorption manifold in the presence of alkene, clean conversion to the corresponding reduced species is observed. Unlike the thermal reaction chemistry, the photochemical reduction proceeds for both chloride and bromide metal complexes. Because the spectra of $\text{Au}_2^{\text{III,III}}$ and



Scheme 1.8. Solution photochemistry of $\text{Au}_2^{\text{III,III}}$ complexes.

$\text{Au}_2^{\text{I,III}}$ complexes exhibit energetically similar maxima and lack an isosbestic point in the visible spectral region, $^{31}\text{P}\{^1\text{H}\}$ NMR was a more informative method for monitoring photochemical reactions. The overall photochemical transformation is generalized in Scheme 1.8. The $^{31}\text{P}\{^1\text{H}\}$ NMR spectra of Figure 1.7 show the spectral changes that accompany the irradiation of **18** and 1 M 1-hexene in CH_2Cl_2 with light coincident with the lowest-energy absorption band; these changes are representative of all $\text{Au}_2^{\text{III,III}}$ complexes photolyzed under analogous conditions. When the photolysis of **18** is halted at an arbitrary and intermediate time point, all three $\text{Au}_2^{\text{III,III}}$, $\text{Au}_2^{\text{I,III}}$, and $\text{Au}_2^{\text{I,I}}$ complexes are present. Continued photolysis of the solution results in complete conversion to **4**. Photolysis of Au^{III} parent complexes proceeds directly to their Au^{I} relatives without the detection of an intermediate. For mono- and bimetallic rhodium chloride complexes **15–20**, minor side products were frequently observed in the $^{31}\text{P}\{^1\text{H}\}$ NMR spectra immediately after photolysis. In all cases we estimate these impurities to comprise $< 10\%$ of the product. We suspect that the phosphine is labilized and subsequently oxidized by the liberated Cl_2 or $\text{Cl}\cdot$, though attempts to positively identify the minor side products were unsuccessful. The dihaloalkane is obtained as the predominant trap product for photochemical reduction using a variety of mono-olefins. As with the thermal reduction experiments, a variety of asymmetrically substituted olefins was employed, allowing us to gain insight into the photochemical transformation. The product of direct, *anti* addition of X_2 across the double bond is obtained as the major organic product in all cases. However, unlike the thermal reaction chemistry, the *syn*-addition diastereomer is observed as a minor product for internal alkenes. Bromide complexes **21–26** all lead to the formation of $\sim 30\%$ *syn*-addition product as judged by integration of ^1H NMR spectra, whereas for chloride complexes, cyclohexyl-substituted complexes **18** and **20** give a smaller percentage of the *syn* product, generally 10–20%, as compared to $\sim 30\%$ for phenyl-substituted **16** and **19**. The amount of *syn*-addition product is independent of the alkene's stereochemistry; *cis* and *trans* alkene isomers result in nearly identical ratios of the *syn* and *anti*-addition diastereomers for a given complex. The ^1H NMR spectra of photochemical reaction

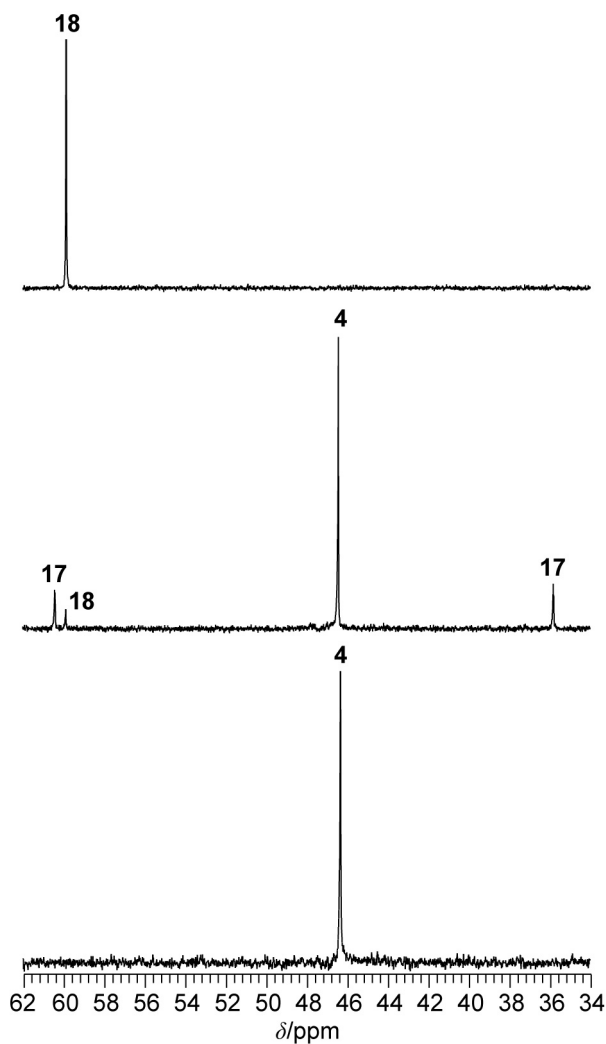


Figure 1.7. $^{31}\text{P}\{^1\text{H}\}$ NMR spectra of (top) the initial solution of **18** in 1 M 1-hexene, and under photolysis using light with $\lambda > 300$ nm at ~ 10 °C (middle) at an arbitrary midpoint during the photolytic reaction and (bottom) at the conclusion of the photolysis. Resonances for **4**, **17** and **18** are indicated.

solutions reveal that the gold complexes described here catalytically isomerize alkenes when irradiated, likely contributing to the observed mixture of dihaloalkane diastereomers. A 0.5 M *cis*-2-hexene solution in the presence of 33 mM **25** is stable in the dark; but as shown by ^1H NMR, photolysis of the solution at $\lambda > 300$ nm for about 5 min showed 60% conversion to *trans*-2-hexene with concomitant formation of **11**. This chemistry is quite general and is replicated using different Au^{III} complexes and alkenes. Photolysis of Au^{I} complexes **9–12** also proceeds to give the thermodynamic *cis/trans* ratio of the alkene.

Table 1.2. Quantum yields (Φ_p) for photochemical reduction of **15–26**.^a

| Cmpd. | 0.125 M | 0.25 M | 0.5 M | 1 M |
|-----------|----------|----------|----------|----------|
| 15 | 0.09(1) | 0.089(1) | 0.09(1) | 0.14(2) |
| 16 | 0.13(2) | 0.16(3) | 0.21(3) | 0.14(4) |
| 17 | 0.15(1) | 0.16(1) | 0.14(2) | 0.17(3) |
| 18 | 0.23(3) | 0.24(2) | 0.25(2) | 0.26(4) |
| 19 | 0.11(1) | 0.12(1) | 0.13(1) | 0.13(1) |
| 20 | 0.14(3) | 0.15(2) | 0.16(3) | 0.16(1) |
| 21 | 0.024(3) | 0.018(1) | 0.020(2) | 0.018(4) |
| 22 | 0.10(3) | 0.12(5) | 0.15(3) | 0.14(2) |
| 23 | 0.08(2) | 0.10(1) | 0.11(1) | 0.11(2) |
| 24 | 0.18(1) | 0.17(2) | 0.20(3) | 0.20(2) |
| 25 | 0.15(1) | 0.15(1) | 0.17(2) | 0.20(3) |
| 26 | 0.16(3) | 0.15(1) | 0.14(1) | 0.15(2) |

^a Measured in CH₂Cl₂ with 1-hexene trap in the stated concentrations. All values are the average of three independent trials.

Quantum yields listed in Table 1.2 for the reduction of mono- and bimetallic Au^{III} halide compounds **15–26** in varying concentrations of 1-hexene were measured using potassium ferrioxalate actinometry. Chloride complexes **15–20** were excited with monochromatic 320 nm light, while bromide complexes **21–26** were excited at 370 nm. For a given compound, the quantum yield is similar within experimental error for all trap concentrations. Au₂^{III,III} complexes consistently exhibit higher quantum yields than their Au₂^{I,III} congeners. This effect is most dramatic for **21**, for which $\Phi_p \approx 2\%$, compared to the fully oxidized **22**, which has quantum yields ranging from 10–15% over the range of trap concentrations. The data in Table 1.2 also show that, in most case, complexes with cyclohexyl-substituted phosphines demonstrate higher solution quantum yields than their phenyl-substituted analogues. The lone exception to this trend is complex **25**, which has a minimally higher quantum yield than **26**. Finally, in comparing chloride complexes to their bromide analogues, the chloride complexes generally have slightly higher quantum yields.

1.2.4 Solid-State Photochemistry of Au^{III} Complexes

Irradiation of solids of bimetallic Au₂^{III,III} bromide complexes **22** and **24** and monometallic bromide complexes **25** and **26** with light enveloping the low-energy absorption band gives the corresponding reduced species as major products. Solid-state photolysis experiments were conducted in an evacuated H-shaped cell. The gold complex was housed in one compartment, and the other compartment was frozen in liquid N₂ to trap and isolate volatile photoproducts. Upon completion of the photolysis, the solid was taken up in CH₂Cl₂ and analyzed by ³¹P{¹H} NMR. Figure 1.8 shows the ³¹P{¹H} NMR spectrum that results when a thin layer of solid **22** was photolyzed at 10 °C for 2.5 h. The spectrum shows a mixture of **21** and **9** in yields of approximately 60% and 30% relative to starting **22**, with a minor side product also evident. No detectable amount of **22** is observed in the ³¹P{¹H} NMR. This observation is consistent with either the complete photochemical conversion of the reactant or the comproportionation of **22** with **9** upon taking up the solid photoproducts in CH₂Cl₂ for NMR analysis. The ³¹P{¹H} NMR spectra for all other solid-state photolysis experiments likewise display productive photoconversion, with some side products typically evident. In all cases with Au^{III} bromide complexes a volatile photoproduct was isolated from vacuum transfer within the H-shaped cell onto frozen H₂O. Visual inspection of the frozen compartment reveals some red-brown condensate, consistent with the isolation of elemental bromine. Upon thawing, treatment with *N,N*-diethyl-1,4-phenylenediamine sulfate (DPD) gave additional evidence that the

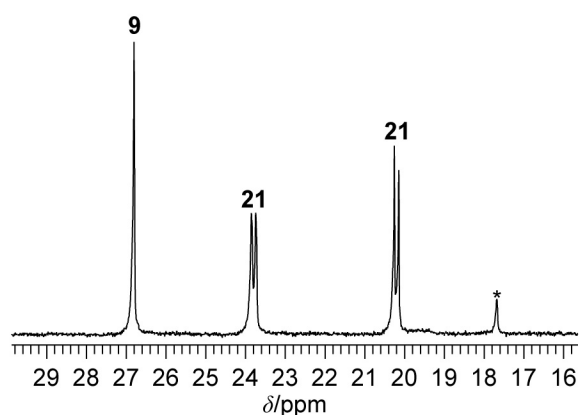


Figure 1.8. ³¹P{¹H} NMR spectrum of the product following photolysis of a solid-state sample of **22** for 2 h, using light with $\lambda > 300$ nm at 10 °C for 2.5 h. Resonances for **21** and **9** are observed, in addition to an unidentified side product (*). The spectrum was recorded in CH₂Cl₂ at 202.5 MHz and is referenced to an external standard of 85% D₃PO₄.

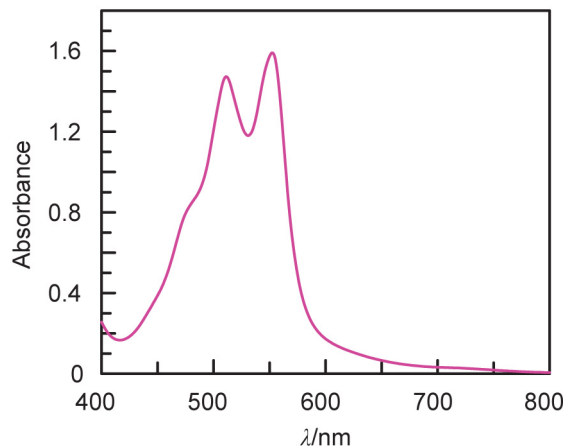


Figure 1.9. UV/Vis absorption spectrum, in H₂O, showing formation of [DPD]^{•+} when the trapped Br₂ from solid-state photolysis of **22** is treated with DPD. The spectrum was recorded at room temperature.

photoproduct is bromine, which oxidizes the colorless DPD to produce the intensely pink [DPD]^{•+}. The absorption spectrum of the resulting solution, shown in Figure 1.9, is a perfect match for that of [DPD]^{•+}.^{48,49} DPD is certainly not selective for Br₂, and will be oxidized by a number of species, but bromine is likely the only volatile photoproduct in these reactions which could oxidize DPD.

Solid-state irradiation of chloride complexes also results in photoreduction. Photolyses of Au₂^{III,III}(dcpm)Cl₆ (**18**) and Au(PCy₃)Cl₃ (**20**) form Au₂^{I,I}(dcpm)Cl₂ (**4**) and Au^I(PCy₃)Cl (**6**), respectively, as the major species. For these reactions, many of the minor side products exhibit ³¹P NMR chemical shifts very similar to **4** and **6**, possibly indicating chlorination of C–H bonds on the phosphine. Compounds **16** and **19**, with phenyl-substituted phosphines, produce **3** and **5** respectively in lower yields. Several decomposition products are evident in the NMR spectra, and phosphine oxidation of the aryl-substituted phosphine by liberated chlorine is suspected to be a major culprit. An attempt was made to isolate the chlorine the same way as with bromine, by trapping in frozen water, but in all cases the DPD test showed no evidence for successful isolation of Cl₂. The inability to isolate Cl₂ in this manner most likely is a result of the high reactivity and volatility of chlorine, which leads to a very low trapping efficiency in the photolysis setup. To demonstrate formation of Cl₂, the condensed gases following photolysis of **18** in the solid state were thawed and flowed into a mass spectrometer. Figure 1.10 shows the MS trace for ³⁵Cl and ³⁷Cl, which form upon fragmentation of Cl₂ in the ionization chamber.

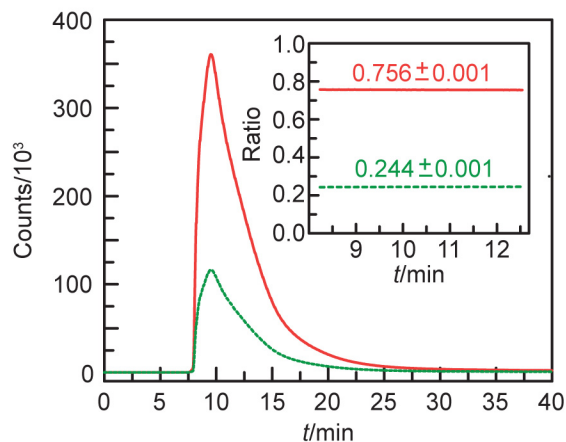


Figure 1.10. Real-time mass spectrometry trace for liberated Cl_2 following photolysis of a solid sample of **18**. Depicted are total ion counts for ^{35}Cl (—, red) and ^{37}Cl (---, green), which form upon fragmenting Cl_2 in the ionization chamber. The inset shows the ratios of the two isotopes during the time range when the ion counts are greater than $\frac{1}{2} \times \text{max}$.

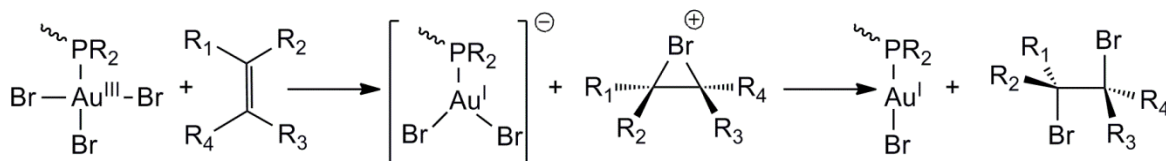
Upon thawing, a sharp increase in signal from baseline values is observed. Also, the isotopic ratio of 0.756 ± 0.001 for ^{35}Cl is consistent with the literature value of 0.758 for the natural abundance of ^{35}Cl .⁵⁰

The reverse reaction in solid-state photolysis experiments, that is, the reaction of Au^{I} centers with elemental X_2 to reform Au^{III} , is spontaneous and rapid. When solid samples of bimetallic $\text{Au}_2^{\text{I,I}}(\text{dcpm})\text{Br}_2$ (**10**) or monometallic $\text{Au}^{\text{I}}(\text{PPh}_3)\text{Br}$ (**11**) are exposed to excess Br_2 , an immediate color change from white to dark orange is observed as the Br_2 vapors come into contact with the solid. After brief (< 10 min) exposure, solution $^{31}\text{P}\{^1\text{H}\}$ and ^1H NMR spectra of the product shows clean conversion to the corresponding oxidized species $\text{Au}_2^{\text{III,III}}(\text{dcpm})\text{Br}_6$ (**24**) or $\text{Au}^{\text{III}}(\text{PPh}_3)\text{Br}_3$ (**25**). Brief exposure of colorless $\text{Au}_2^{\text{I,I}}(\text{dcpm})\text{Cl}_2$ (**4**) to Cl_2 gas leads to an immediate color change to yellow, and $^{31}\text{P}\{^1\text{H}\}$ NMR of the dissolved product shows a mixture of $\text{Au}_2^{\text{I,III}}$ (**17**) and $\text{Au}_2^{\text{III,III}}$ (**18**), in addition to starting material. Prolonged exposure to an excess of Cl_2 gas leads to an intractable mixture of decomposition products.

1.3 Discussion

The efficient reductive elimination of halogen may be thermally and photochemically driven from $\text{Au}(\text{III})$ centers of mono- and bimetallic centers. In solution, halogen must be chemically trapped. Solutions of mono- and bimetallic compounds **21–26**, in the presence of an

olefin and in the absence of light, are cleanly reduced to their respective Au^I complexes at room temperature, over the course of hours to days. Analysis of the regio- and stereochemistry of the dihaloalkane product of a variety of monoalkene traps provides insight into the mechanism of thermal reductive elimination. For alkenes with two prochiral centers (e.g., *cis*-2-hexene, *trans*-2-hexene, and *trans*-4-methyl-2-pentene), a single diastereomer is obtained that is consistent with an electrophilic mechanism proceeding through a bromonium intermediate to furnish the *anti*-addition product.⁵¹ Such a mechanism involving a Au^{III} bromide complex is depicted in Scheme 1.9, and though the precise nature of the Au^I intermediate is unknown, the presence of the bromonium intermediate is implied by the stereochemical outcome. These results contrast with the products anticipated from a radical mechanism, which is expected to involve a planar sp² radical that can undergo either *syn* or *anti* addition to give a 50:50 mixture of both diastereomers, with possible rearrangement and oligomerization of radical intermediates. For 3-methyl-1-pentene and 3,3-dimethyl-1-butene, it is not possible to distinguish *syn*- and *anti*-addition products, but a radical intermediate would presumably rearrange to a stable tertiary radical, leading to products of altered connectivity. Such rearranged products are not observed. Comparison of the thermal elimination kinetics of Au₂^{III,III} complexes with Au^{III} monometallic complexes is revealing. The rate constant for early time points in the reduction of monogold complex **25** is an order of magnitude lower than the rate constants for the bimetallic complexes **22** and **24**. These data suggest that the two gold atoms in the tethered bimetallic complexes interact to facilitate the reductive elimination of halogen from both the Au₂^{III,III} and Au₂^{I,III} complexes. In line with this observation, the reduction of **25** is promoted by **11**, which results in deviations from pseudo-first-order behavior when the concentration of **11** is appreciable. Halide-bridged intermediates have been postulated in ligand-redistribution reactions,⁴⁶ so it is possible that such an intermediate, albeit short-lived and not spectroscopically identifiable, could form when **25** is in the presence of **11**. As we have shown,^{52,53} bridged intermediates are crucial to

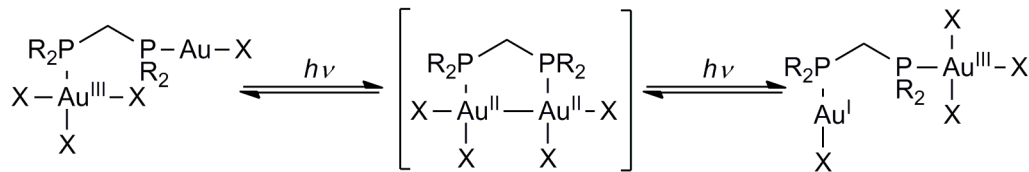


Scheme 1.9. Electrophilic mechanism for thermal reaction of Au^{III} bromide complexes with alkenes.

facilitating reductive elimination from bimetallic cores.

Product analysis reveals that the photochemical reaction mechanism deviates from that of the thermal reaction. Excitation of the low-energy absorption bands of Au^{III} complexes yields significant amounts of the *syn*-addition haloalkane product, in addition to the major *anti*-addition diastereomer that is exclusively observed in the thermal reaction. The presence of the *syn*-addition diastereomer is partly accounted for by the observation deduced from ¹H NMR spectra of the final product mixtures, showing that phosphine-gold compounds photocatalyze the *cis/trans* isomerization of alkenes. Nonetheless, the observed ratio of *syn* to *anti*-addition products is higher than the ratio of photoisomerized alkene, particularly for photoreactions involving *trans* alkenes. These results suggest that a radical-based mechanism is operative in addition to an electrophilic mechanism, which should exclusively lead to *anti* addition across the carbon-carbon double bond of the trap.

The quantum yields for these photochemical transformations were measured for 12 Au^{III} halide complexes in the presence of varying concentrations of 1-hexene (Table 1.2). In general, very good quantum efficiencies are observed, with most values in the vicinity of 15%. The quantum yield for the complex Au₂^{III,III}(dcpm)Cl₆ (**18**) was found to be as high as 26%, among the highest ever for photochemical halogen elimination.^{17–19,23} In discerning trends associated with ligand substitution, either with respect to halides or phosphines, some modest, albeit noticeable, patterns emerge. In general, compounds with cyclohexyl-substituted phosphines gave higher quantum yields than otherwise analogous complexes with phenyl-substituted phosphine ligands. This may be a result of subtle differences in electronic structure—as gleaned from Figure 1.6, the bathochromic shift accompanying substitution of bromide for chloride is more pronounced in cyclohexyl-substituted complexes. This is suggestive that more substantial halide LMCT character gives rise to more efficient photochemistry. Another noticeable trend from the data in Table 1.2 is that Au₂^{I,III} complexes have substantially lower quantum yields than their Au₂^{III,III} counterparts. This effect is especially pronounced when comparing Au₂^{I,III}(dppm)Br₄ (**21**), to its Au₂^{III,III} relative **22**. For **21**, the lowest quantum yield in the series, ~ 2%, is observed, compared to values of ~ 10–15% for **22**. This effect may be due to an internal halogen-transfer pathway, whereby photoexcitation of the Au^{III} center leads to halogen transfer to Au^I; i.e. the Au^I and the alkene compete as halogen traps. This hypothesis, which has no strong experimental



Scheme 1.10. Proposed intramolecular trapping/photoisomerization mechanism for $\text{Au}_2^{1,\text{III}}$ complexes.

backing at this point, is summarized in Scheme 1.10. One final trend that emerges from the extensive list of quantum yields is that, in general, the values show minimal sensitivity to the concentration of alkene trap, suggesting very efficient trapping of photoliberated halogen even at the lowest extremes of concentration that were studied.

The photochemical reaction occurs upon excitation of absorption bands with significant ligand-to-metal charge transfer (LMCT) character. The significant shift of the low-energy absorption band upon substituting chlorides for bromides in otherwise identical complexes is a qualitative indicator of significant LMCT character.⁴⁷ LMCT excitation of late-metal halide complexes typically results in liberation of halogen radicals and a formal one-electron reduction of the metal.⁵⁴ This behavior has been extensively studied for the $[\text{Pt}^{\text{IV}}\text{Cl}_6]^{2-}$ anion, which photochemically reduces to the $[\text{Pt}^{\text{II}}\text{Cl}_4]^{2-}$ anion, in a process involving a $[\text{Pt}^{\text{III}}\text{Cl}_5]^{2-}$ intermediate.⁵⁵ Similar behavior is postulated for $\text{Au}^{\text{III}}\text{Cl}_4^-$ ion.³⁶ For either Pt or Au systems, extensive thermal chemistry follows the initial one-electron photoreduction. To this end, the Au^{III} photochemistry reported here is exceptional as the inorganic and organic photoproducts are consistent with X_2 elimination. If $\text{X}\cdot$ is liberated upon LMCT excitation, then (i) cage escape of $\text{X}\cdot$ is minimal based on the haloalkane product analysis and (ii) the subsequent elimination of a second $\text{X}\cdot$ must be sufficiently rapid to overwhelm recombination of $\text{X}\cdot$ and the Au^{II} primary photoproduct, since haloalkane products characteristic of radical-based chemistry are produced in minor quantities. Solid-state photolysis reactions provide further evidence for X_2 elimination. Au^{I} complexes and X_2 are produced under conditions where radical trapping or stabilization is not feasible. Thus a stepwise elimination of $\text{X}\cdot$ to furnish X_2 must be extremely rapid. Alternatively, $\text{X}\cdot$ is not the predominant photoproduct species. Terminal ligands in the equatorial waist of the two-electron mixed-valent cores exhibit a propensity to migrate to and from bridging positions, owing to low reorganization energies arising from the ability of the bimetallic core to preserve the electronic and coordination asymmetry accompanying

rearrangement.^{52,53,56} Such a migration permits X₂ elimination and averts X• formation. The photochemistry of complexes involving two-electron mixed-valent metal complexes was previously confined to those compounds containing a metal–metal bond. In these cases, the metal–metal bond provides a visible chromophore from which to drive the photoreductive elimination. As was shown here, when no metal–metal bond exists, the LMCT transition of high-oxidation-state metals may be exploited as a visible chromophore and a productive two-electron photochemistry may be achieved.

Finally, the observation that X₂ thermally adds to the Au^I compounds in the solid state to give the Au^{III} photoreactants is noteworthy. Under the same physical conditions, the reaction may be reversed using light, establishing that the photoreaction is energy-storing. The ability to effect trap-free halogen photoelimination greatly eases the complexity of the criteria for the design of a solar-energy-storing HX-splitting cycle.

1.4 Conclusions

In this chapter, studies on thermal and photochemical halogen elimination from Au^{III} halide complexes were described. Phosphine-terminated Au^{III} bromide complexes react thermally with alkenes, delivering a Br₂ equivalent via an exclusively electrophilic mechanism. Bimetallic complexes react much more rapidly than their monometallic congeners, suggesting some form of bimetallic cooperativity in this thermal reaction chemistry. Photochemical irradiation of these complexes also results in clean halogen elimination, at greatly accelerated rates compared to the thermal reactions. These photochemical reactions occur with generally very good quantum yields, as high as 26%, and close inspection of the stereochemical outcome of alkene trapping reveals some mechanistic differences from the thermal reactions, namely some participation of radical chemistry. In addition, the photochemistry is operative in the solid state, providing rare examples of trap-free, authentic X₂ elimination from transition-metal complexes.

Taken together, these preceding results present several advances and new insights in halogen-elimination photochemistry. Our group had begun to recognize the importance of LMCT excited-state character in photochemical halogen elimination, but had confined our studies to metal–metal-bonded bimetallic complexes. However, the results here demonstrate that

complexes with purely LMCT excited states can mediate efficient halogen photoelimination, generalizing halogen-elimination photochemistry to a whole new class of complexes. Included in these findings are the first demonstrations of authentic X₂ elimination from such complexes, in a trap-free setup where the volatile halogen photoproducts were collected and identified. Our ability to drive the thermodynamically uphill X₂-elimination reaction overcame one of the greatest challenges in photocatalytic HX splitting, and could lead to photocatalysts with much improved efficiencies and the ability to store solar energy. The fact that X₂ elimination can occur with LMCT excitation in complexes devoid of metal–metal bonds opens up numerous additional possibilities for the design of multimetallic catalysts or catalyst systems that can achieve HX splitting to generate H₂ and X₂.

1.5 Experimental Methods

1.5.1 General Considerations

All solvents were obtained commercially and used as received except for CH₂Cl₂ and THF, which were dried by passage through an alumina column. Air-sensitive phosphines were handled in a nitrogen-filled glovebox. All gold compounds reported here are air-stable and were routinely handled in an ambient atmosphere. The phosphines PPh₃, PCy₃, dppm, and dcpm were obtained from Strem Chemicals, bromine was obtained from Sigma-Aldrich (reagent grade) and chlorine was delivered as the iodobenzene adduct, PhICl₂.⁵⁷ The ligands CH₃N[P(OCH₂CF₃)₂]₂ (tfepma)^{58,59} and bis(diphenylphosphino)isopropane (dppip)⁶⁰ were prepared by published procedures. The starting materials Au₂^{I,I}(dppm)Cl₂ (**3**),⁴¹ Au₂^{I,I}(dcpm)Cl₂ (**4**),⁶¹ Au^I(PPh₃)Cl (**5**),²⁶ and Au^I(PCy₃)Cl (**6**)⁶² were prepared by reacting stoichiometric amounts of the appropriate phosphine with chloro(tetrahydrothiophene)gold(I) [Au^I(tht)Cl]³⁸ in THF, followed by precipitation with pentane and isolation by vacuum filtration. Halide exchange to prepare Au₂^{I,I}(dppm)Br₂ (**9**), Au₂^{I,I}(dcpm)Br₂ (**10**), Au^I(PPh₃)Br (**11**), and Au^I(PCy₃)Br (**12**) was carried out by reaction with excess aqueous KBr, and Au₂^{I,III}(dppm)Br₄ (**21**) and Au^{III}(PPh₃)Br₃ (**25**) were prepared following known methods.³⁹ All thermal reductions of Au^{III} were carried out at room temperature in 1 M olefin solutions; light was rigorously excluded by thoroughly wrapping all reaction vessels in aluminum foil.

1.5.2 Physical Methods

NMR spectra were recorded at the MIT Department of Chemistry Instrumentation Facility on a Varian Mercury-300 NMR Spectrometer, operating at 300 MHz (^1H) or 121.5 MHz (^{31}P), or a Varian Inova-500 NMR Spectrometer operating at 500 MHz (^1H) or 202.5 MHz (^{31}P). $^{31}\text{P}\{^1\text{H}\}$ NMR spectra were referenced to an external standard of 85% D_3PO_4 and ^1H spectra were referenced to the residual proteo solvent resonances. $^{31}\text{P}\{^1\text{H}\}$ NMR kinetics experiments were performed at 20 °C using triphenylphosphate as an internal integration standard. $^{31}\text{P}\{^1\text{H}\}$ spectra of solid-state photolysis samples were quantified with a known concentration of triphenylphosphate as an internal standard; a spectrometer delay time of 30 s was employed. UV-vis spectra were recorded at room temperature in quartz cuvettes on a Varian Cary 5000 UV-vis-NIR spectrophotometer. Extinction coefficients were determined over a concentration range of ~ 5–100 μM , for which all compounds obeyed Beer's Law.

Photochemical reactions were performed using a 1000 W high-pressure Hg/Xe arc lamp (Oriel). The beam was passed through a water-jacketed filter holder containing appropriate long-pass filters, an iris and collimating lens. Dichloromethane solutions of samples prepared for large-scale photolysis experiments were contained in standard borosilicate NMR tubes or glass Schlenk tubes. Solid-state photolysis experiments were conducted in a custom-built H-shaped cell with the two compartments separated by a Teflon valve; one of the two compartments was equipped with an inlet and outlet port for gas measurements. To obtain a uniform coating of solid for photolysis experiments, a 10–15 mg sample was dissolved in a minimum amount of CH_2Cl_2 , which was deposited in the cell and evaporated under reduced pressure. The entire apparatus was evacuated to < 200 mTorr prior to photolysis. The photolysis cell was periodically rotated during irradiation to ensure maximum exposure to the beam. The surface of the sample photolyzed rapidly, though in many cases starting material was observed in the product mixture after > 3 h irradiation times. Longer photolysis times did lead to further conversion, at the expense of an increased buildup of side products in the sample. Evolved Cl_2 was collected by opening the valve dividing the two cell compartments and immersing the sample-free compartment in liquid nitrogen. Chlorine was analyzed by mass spectrometry using an Agilent Technologies 5975C Mass Selective Detector operating in electron impact ionization mode. The liquid nitrogen cooled side of the sample cell that contained evolved gases was purged with He carrier gas for

two hours until a stable baseline was obtained. The frozen compartment was rapidly warmed by immersion in water and the evolved gases were fed into the mass spectrometer for real-time analysis. Data were collected until all gas levels returned to near baseline values. The mass spectrometer was operated in selective ion mode that monitored for 35 (Cl_2 fragment), 37 (Cl_2 fragment), 70 (Cl_2), 72 (Cl_2) and 74 (Cl_2) amu ions. The three Cl_2 ions gave very weak signals and were not considered in the data analysis. Evolved Br_2 was collected in a similar fashion to the methods employed for Cl_2 , except that the frozen cell compartment was pre-charged with 5 mL of distilled water. The resulting aqueous Br_2 solution was analyzed by DPD titrimetry.⁶³

For solution quantum yield experiments, samples were contained in a quartz cuvette equipped with a Teflon-coated magnetic stir bar. Monochromatic light was generated by combining the output from a long-pass filter with a Hg line filter of 320 nm for Au^{III} chlorides and 370 nm for Au^{III} bromides. Potassium ferrioxalate was synthesized via a published procedure and used as a chemical actinometer.⁶⁴ The photon flux was determined from the average of the actinometric measurements collected before and after irradiation of a set of three samples. UV-vis spectra for quantum yield measurements were recorded on a Spectral Instruments 400 diode array spectrophotometer and were blanked to the appropriate solvent.

1.5.3 Preparation of $\text{Au}_2^{\text{I}}(\text{tfepma})\text{Cl}_2$ (1)

A solution of tfepma (175 mg, 0.359 mmol, 1.00 eq) was prepared in 2 mL of CH_2Cl_2 . A sample of $\text{Au}^{\text{I}}(\text{tht})\text{Cl}$ (230 mg, 0.719 mmol, 2.00 eq) was added as a solid. The solution was shielded from light and stirred at room temperature of 1 h. The solvent was removed in vacuo, and the resulting white powder washed with 3×3 mL of pentane and dried in vacuo. Yield: 324 mg (95%). ^1H NMR (300 MHz, CD_3CN) δ/ppm : 4.69 (m, 8H), 2.95 (t, $^3J_{\text{H-P}} = 7.5$ Hz, 3H). $^{31}\text{P}\{^1\text{H}\}$ NMR (121.5 MHz, CD_3CN) δ/ppm : 126.0 (s). Anal. Calcd. for $\text{C}_9\text{H}_{11}\text{Au}_2\text{Cl}_2\text{F}_{12}\text{NO}_4\text{P}_2$: C, 11.36; H, 1.16; N, 1.47. Found: C, 11.66; H, 1.49; N, 1.38.

1.5.4 Preparation of $\text{Au}_2^{\text{I}}(\text{dppip})\text{Cl}_2$ (2)

Solid $\text{Au}^{\text{I}}(\text{tht})\text{Cl}$ (1.462 g, 4.560 mmol, 2.00 eq) was suspended in 8 mL of THF. A solution of dppip (940 mg, 2.28 mmol, 1.00 eq) in 8 mL of THF was added dropwise with stirring, initially giving a colorless solution. Within a few minutes, a voluminous white precipitate had formed, and the mixture was stirred for 2 h. The suspension was poured into 50

mL of pentane, and the product removed by vacuum filtration. The white solid was washed with 100 mL of pentane and dried in vacuo. The solid was redissolved in CH₂Cl₂ and precipitated by adding pentane. The solid was recollected, and dried in vacuo. Yield: 2.02 g of **2**·0.5CH₂Cl₂ (96.3%). ¹H NMR (500 MHz, CDCl₃) δ/ppm: 7.90 (m, 8H), 7.52 (m, 4H), 7.39 (m, 8H), 1.69 (t, ³J_{P-H} = 15.3 Hz, 6H). ³¹P{¹H} NMR (121.5 MHz, CDCl₃) δ/ppm: 53.7 (s). Anal. Calcd. for C₂₇H₂₆Au₂Cl₂P₂·0.5CH₂Cl₂: C, 35.91; H, 2.96. Found: C, 35.30; H, 3.00.

1.5.5 Preparation of Au₂^I(tfepma)Br₂ (**7**)

A sample of **1** (498 mg, 0.523 mmol, 1.00 eq) was dissolved in 20 mL of CH₂Cl₂. To the resulting solution was added a solution of KBr (656 mg, 5.51 mmol, 10.5 eq) in 15 mL of water. The biphasic mixture was stirred vigorously for 3 h at room temperature. The organic layer was separated, and the remaining aqueous layer was extracted with 3 × 5 mL of CH₂Cl₂. The combined organic layer was dried over MgSO₄ and filtered. The solution was concentrated to < 5 mL, at which time a white solid began to precipitate. Addition of 50 mL of pentane induced further separation of white solid, which was collected by filtration and dried in vacuo. Yield: 502 mg (92.2%). ¹H NMR (300 MHz, CD₃CN) δ/ppm: 4.69 (m, 8H), 2.96 (t, ³J_{P-H} = 7.5 Hz, 3H). ³¹P{¹H} NMR (121.5 MHz, CD₃CN) δ/ppm: 127.5 (s). Anal. Calcd. for C₉H₁₁Au₂Br₂F₁₂NO₄P₂: C, 10.39; H, 1.07; N, 1.35. Found: C, 10.44; H, 1.15; N, 1.22.

1.5.6 Preparation of Au₂^I(dppip)Br₂ (**8**)

A solution of **2**·0.5CH₂Cl₂ (1.00 g, 1.08 mmol, 1.00 eq) was prepared in 70 mL of CH₂Cl₂. The solution was treated with 40 mL an aqueous solution of KBr (1.36 g, 11.4 mmol, 10.0 eq). The biphasic mixture was covered with aluminum foil and stirred at room temperature for 4.5 h. The aqueous layer was separated and washed with 3 × 15 mL of CH₂Cl₂. The combined organic extracts were washed with 3 × 10 mL of water, dried over MgSO₄ and filtered. The solution was concentrated to < 20 mL, and addition of 150 mL of pentane liberated a white solid, which was collected by filtration. The residue that was left behind was redissolved in a small amount of CH₂Cl₂, precipitated with pentane, and collected and combined with the first batch of solid. Yield: 1.02 g of **8**·0.5CH₂Cl₂ (93.2%). ¹H NMR (500 MHz, CDCl₃) δ/ppm: 7.90 (m, 8H), 7.51 (m, 4H), 7.38 (m, 8H), 1.69

(t, $^3J_{\text{P-H}} = 15.3$ Hz, 6H). $^{31}\text{P}\{^1\text{H}\}$ NMR (121.5 MHz, CDCl_3) δ/ppm : 54.1 (s). Anal. Calcd. for $\text{C}_{27}\text{H}_{26}\text{Au}_2\text{Br}_2\text{P}_2 \cdot 0.5\text{CH}_2\text{Cl}_2$: C, 32.75; H, 2.70. Found: C, 32.85; H, 2.78.

1.5.7 Oxidation of **2** with PhICl_2 to form $\text{Au}_2^{\text{II,II}}(\text{dppip})\text{Cl}_4$ (**13**) and $\text{Au}_2^{\text{I,III}}(\text{dppip})\text{Cl}_4$ (**14**)

A scintillation vial was charged with a solution of **2** ($0.5\text{CH}_2\text{Cl}_2$ (100 mg, 0.109 mmol, 1.00 eq) dissolved in 9 mL of CH_2Cl_2 . A solution of PhICl_2 (31.4 mg, 0.114 mmol, 1.05 eq) in 1.5 mL of CH_2Cl_2 was added dropwise, giving a yellow-orange solution that was stirred at room temperature for 2.5 h. At this time, $^{31}\text{P}\{^1\text{H}\}$ NMR showed a mixture of **13** (25%) and **14** (75%). The aliquot that was removed for NMR analysis was layered with pentane, producing yellow-orange crystals of **13**, which were characterized by X-ray diffraction. $^{31}\text{P}\{^1\text{H}\}$ NMR data for **13** (121.5 MHz, CH_2Cl_2) δ/ppm : 37.8 (s). $^{31}\text{P}\{^1\text{H}\}$ NMR data for **14** (121.5 MHz, CH_2Cl_2) δ/ppm : 58.0 (d, $^2J_{\text{P-P}} = 16$ Hz, 1P), 53.7 (d, $^2J_{\text{P-P}} = 16$ Hz, 1P).

1.5.8 Preparation of $\text{Au}_2^{\text{I,III}}(\text{dppm})\text{Cl}_4$ (**15**)

To a solution of **3** (100 mg, 0.118 mmol, 1.00 eq) in 5 mL of CH_2Cl_2 , was added dropwise a solution of PhICl_2 (34 mg, 0.12 mmol, 1.0 eq) in 1 mL of CH_2Cl_2 . The resulting solution was stirred for 12 h in the dark during which time some product precipitated. The mixture was layered with ~ 15 mL of pentane and stored at -20°C for 1 day. Product **15** formed as a microcrystalline pale yellow solid. The supernatant was decanted, and the remaining solid product washed with 2×15 mL pentane and dried in vacuo. Yield: 100 mg (92.3%). ^1H NMR (500 MHz, CD_2Cl_2) δ/ppm : 7.81–7.87 (m, 4H), 7.56–7.62 (m, 2H), 7.47–7.55 (m, 6H), 7.36–7.46 (m, 8H) 4.27 (dd, $^2J_{\text{P-H}} = 11.0$ Hz, 13.2 Hz, 2H). $^{31}\text{P}\{^1\text{H}\}$ NMR (121.5 MHz, CD_2Cl_2) δ/ppm : 36.2 (d, $^2J_{\text{P-P}} = 17$ Hz, 1P), 18.5 (d, $^2J_{\text{P-P}} = 16$ Hz, 1P). UV-vis (CH_2Cl_2): λ/nm ($\epsilon/(\text{M}^{-1}\text{cm}^{-1})$) 341 (9400). Anal. Calcd. for $\text{C}_{25}\text{H}_{22}\text{Au}_2\text{Cl}_4\text{P}_2$: C, 32.63; H, 2.41. Found: C, 32.82; H, 2.51.

1.5.9 Preparation of $\text{Au}_2^{\text{III,III}}(\text{dppm})\text{Cl}_6$ (**16**)

A sample of PhICl_2 (68 mg, 0.25 mmol, 2.1 eq) in 2 mL of CH_2Cl_2 was added to a stirred solution of **3** (100 mg, 0.118 mmol, 1.00 eq) in 8 mL of CH_2Cl_2 . The yellow solution was stirred in the dark for 17 h and then was concentrated to ~ 4 mL, at which time a yellow solid began to precipitate. Addition of 15 mL pentane gave the product as a yellow solid, which was separated

from the supernatant by decantation, washed with 2×15 mL pentane and dried in vacuo. Yield: 101 mg of $\mathbf{16} \cdot 0.5\text{CH}_2\text{Cl}_2$ (83.0%). ^1H NMR (500 MHz, CDCl_3) δ/ppm : 7.75–7.82 (m, 12H), 7.61–7.66 (m, 8H), 5.12 (t, $^2J_{\text{P-H}} = 14.8$ Hz, 2H). $^{31}\text{P}\{^1\text{H}\}$ NMR (121.5 MHz, CDCl_3) δ/ppm : 29.2 (s). UV-vis (CH_2Cl_2): λ/nm ($\epsilon/(\text{M}^{-1} \text{cm}^{-1})$) 339 (16000). Anal. Calcd. for $\text{C}_{25}\text{H}_{22}\text{Au}_2\text{Cl}_6\text{P}_2 \cdot 0.5\text{CH}_2\text{Cl}_2$: C, 29.63; H, 2.24. Found: C, 29.43; H, 2.37.

1.5.10 Preparation of $\text{Au}_2^{\text{I,III}}(\text{dcpm})\text{Cl}_4$ (17)

A sample of **4** (100 mg, 0.114 mmol, 1.00 eq) was dissolved in 10 mL of CH_2Cl_2 . A solution of PhICl_2 (32 mg, 0.12 mmol, 1.1 eq) in 1 mL of CH_2Cl_2 was added dropwise to give a yellow solution, which was stirred at room temperature for 3 h. The volatiles were removed to give a yellow residue, which was redissolved in 2 mL of CH_2Cl_2 and slowly added to 15 mL of pentane to furnish a yellow solid. The supernatant was decanted and the resulting solid material was washed with pentane and dried in vacuo. Yield: 93 mg (86%). ^1H NMR (500 MHz, CDCl_3) δ/ppm : 3.39–3.51 (br, m, 2H), 2.93 (dd, $^2J_{\text{P-H}} = 10.6$ Hz, 13.8 Hz, 2H), 2.30–2.41 (br, m, 2H), 1.68–2.24 (br, m, 24H), 1.19–1.62 (br, m, 16H). $^{31}\text{P}\{^1\text{H}\}$ NMR (121.5 MHz, CDCl_3) δ/ppm : 60.0 (d, $^2J_{\text{P-P}} = 9$ Hz, 1P), 35.9 (d, $^2J_{\text{P-P}} = 9$ Hz, 1P). UV-vis (CH_2Cl_2): λ/nm ($\epsilon/(\text{M}^{-1} \text{cm}^{-1})$) 327 (8500). Anal. Calcd. for $\text{C}_{25}\text{H}_{46}\text{Au}_2\text{Cl}_4\text{P}_2$: C, 31.80; H, 4.91. Found: C, 32.31; H, 4.96.

1.5.11 Preparation of $\text{Au}_2^{\text{III,III}}(\text{dcpm})\text{Cl}_6$ (18)

A solution of PhICl_2 (66 mg, 0.24 mmol, 2.1 eq) in 1.5 mL of CH_2Cl_2 was added to **4** (100 mg, 0.114 mmol, 1.00 eq) in 10 mL of CH_2Cl_2 . The yellow solution was stirred in the dark for 16 h, at which time the volatiles were removed via rotary evaporation to leave a yellow residue. The residue was taken up in ~ 2 mL of CH_2Cl_2 and added dropwise to 15 mL of pentane, prompting a pale yellow solid to separate. The supernatant was decanted and the solid was washed with pentane and dried in vacuo. Yield: 98 mg (84%). ^1H NMR (500 MHz, CDCl_3) δ/ppm : 3.64(t, $^2J_{\text{P-H}} = 13.8$ Hz, 2H), 3.14–3.24 (br, m, 4H), 2.19–2.31 (br, m, 8H), 1.79–2.02 (br, m, 20H), 1.33–1.50 (br, m, 12H). $^{31}\text{P}\{^1\text{H}\}$ NMR (121.5 MHz, CDCl_3) δ/ppm : 60.3 (s). UV-vis (CH_2Cl_2): λ/nm ($\epsilon/(\text{M}^{-1} \text{cm}^{-1})$) 328 (16000). Anal. Calcd. for $\text{C}_{25}\text{H}_{46}\text{Au}_2\text{Cl}_6\text{P}_2$: C, 29.58; H, 4.57. Found: C, 29.96; H, 4.60.

1.5.12 Preparation of Au^{III}(PPh₃)Cl₃ (19)

This compound has been reported previously by oxidation with Cl₂ gas.^{31,46} Here the synthesis is reported using PhICl₂. To a solution of **5** (100 mg, 0.202 mmol, 1.00 eq) in 2 mL of CH₂Cl₂ was added a solution of PhICl₂ (58 mg, 0.21 mmol, 1.0 eq) in 2 mL of CH₂Cl₂. After stirring for 8 h at room temperature in the dark, the solution was concentrated to < 1 mL, and ~ 15 mL of pentane was added to afford the product as a yellow powder. The solvent mixture was decanted and the solid was washed with pentane dried in vacuo. Yield: 95 mg (83%). ¹H NMR (500 MHz, CDCl₃) δ/ppm: 7.66–7.75 (m, 9H), 7.54–7.60 (m, 6H). ³¹P{¹H} NMR (121.5 MHz, CDCl₃) δ/ppm: 44.3 (s). UV-vis (CH₂Cl₂): λ/nm (ε/(M⁻¹ cm⁻¹)) 336 (13000). Anal. Calcd. for C₁₈H₁₅AuCl₃P: C, 38.22; H, 2.67. Found: C, 38.23; H, 2.66.

1.5.13 Preparation of Au^{III}(PCy₃)Cl₃ (20)

A sample of **6** (100 mg, 0.195 mmol, 1.00 eq) was dissolved in 1.5 mL of CH₂Cl₂. To this solution was added PhICl₂ (56 mg, 0.20 mmol, 1.03 eq) in 1.5 mL of CH₂Cl₂. The resulting yellow solution was stirred in the dark at room temperature for 8 h. After concentrating to < 1 mL, 15 mL of pentane was added to separate **20** as a pale yellow solid. The supernatant was decanted and the product was washed with pentane and dried in vacuo. Yield: 100 mg (87.8%). ¹H NMR (500 MHz, CDCl₃) δ/ppm: 2.95–3.06 (br, m, 3H), 2.00–2.08 (br, m, 6H), 1.86–1.96 (br, m, 6H), 1.68–1.84 (br, m, 9H) 1.27–1.40 (br, m, 9H). ³¹P{¹H} NMR (121.5 MHz, CDCl₃) δ/ppm: 74.8 (s). UV-vis (CH₂Cl₂): λ/nm (ε/(M⁻¹ cm⁻¹)) 253 (12000), 328 (8700). Anal. Calcd. for C₁₈H₃₃AuCl₃P: C, 37.03; H, 5.70. Found: C, 37.25; H, 5.63.

1.5.14 Preparation of Au₂^{III,III}(dppm)Br₆ (22)

To a solution of **9** (86 mg, 0.091 mmol, 1.0 eq) in 4 mL of CH₂Cl₂ was added a solution of Br₂ (36 mg, 0.228 mmol, 2.5 eq) in 2 mL of CH₂Cl₂. The solution turned red immediately and was stirred in the dark for 90 min. The reaction mixture was layered with pentane and stored at –20 °C to give red crystals of **22**. The supernatant was decanted and the product was washed with pentane and dried in vacuo. Yield: 111 mg (96.3%). ¹H NMR (500 MHz, CDCl₃) δ/ppm: 7.69–7.80 (m, 12H), 7.57–7.62 (m, 8H), 5.42 (t, ²J_{P-H} = 14.6 Hz, 2H). ³¹P{¹H} NMR (121.5 MHz, CDCl₃) δ/ppm: 14.6 (s). UV-vis (CH₂Cl₂): λ/nm (ε/(M⁻¹ cm⁻¹)) 256 (56000), 349 (12000). Anal. Calcd. for C₂₅H₂₂Au₂Br₆P₂: C, 23.87; H, 1.76. Found: C, 24.12; H, 2.04.

1.5.15 Preparation of Au₂^{I,III}(dcpm)Br₄ (23)

To a solution of **10** (100 mg, 0.104 mmol, 1.00 eq) in 6 mL of CH₂Cl₂ was added dropwise a solution of Br₂ (17 mg, 0.11 mmol, 1.05 eq) in 1 mL of CH₂Cl₂. The solution turned red immediately and was stirred at room temperature for 3.5 h in exclusion of light. The solution was concentrated to ~ 2 mL, and addition of 15 mL pentane gave the product as a salmon-colored powder. The solvents were decanted and the material was washed with pentane and dried in vacuo. Yield: 98 mg (84%). ¹H NMR (500 MHz, CDCl₃) δ/ppm: 3.63–3.73 (br, m, 2H), 2.92 (dd, ²J_{P-H} = 10.5 Hz, 13.6 Hz, 2H), 2.40–2.50 (br, m, 2H), 2.21–2.30 (br, m, 2H), 1.20–2.19 (br, m, 38H). ³¹P{¹H} NMR (121.5 MHz, CDCl₃) δ/ppm: 45.0 (s, 1P), 37.6 (s, 1P). UV-vis (CH₂Cl₂): λ/nm (ε/(M⁻¹ cm⁻¹)) 253 (19000), 397 (3900). Anal. Calcd. for C₂₅H₄₆Au₂Br₄P₂: C, 26.76; H, 4.13. Found: C, 27.12; H, 4.12.

1.5.16 Preparation of Au₂^{III,III}(dcpm)Br₆ (24)

A sample of **10** (100 mg, 0.104 mmol, 1.00 eq) was dissolved in 6 mL of CH₂Cl₂. A solution of Br₂ (62 mg, 0.38 mmol, 3.7 eq) in 1 mL of CH₂Cl₂ was added. The resulting red solution was stirred in exclusion of light for 6 h. After concentrating to ~ 1 mL, 15 mL of pentane was added to give a dark red solid, which was separated by decantation, washed with 2 × 15 mL of pentane and dried in vacuo. Yield: 116 mg (87.1%). ¹H NMR (500 MHz, CDCl₃) δ/ppm: 3.89 (t, ²J_{P-H} = 13.9 Hz, 2H), 3.24–3.34 (br, m, 4H), 2.23–2.31 (br, m, 8H), 1.76–2.00 (br, m, 20H), 1.35–1.50 (br, m, 12H). ³¹P{¹H} NMR (121.5 MHz, CDCl₃) δ/ppm: 48.4 (s). UV-vis (CH₂Cl₂): λ/nm (ε/(M⁻¹ cm⁻¹)) 254 (33000), 401 (7300). Anal. Calcd. for C₂₅H₄₆Au₂Br₆P₂: C, 23.42; H, 3.62. Found: C, 23.42; H, 3.56.

1.5.17 Preparation of Au^{III}(PCy₃)Br₃ (26)

To a solution of **12** (100 mg, 0.179 mmol, 1.00 eq) in 1.5 mL of CH₂Cl₂ was added a solution of Br₂ (62 mg, 0.39 mmol, 2.2 eq) in 1 mL of CH₂Cl₂. The dark red solution was shielded from light and stirred for 2 h, at which time it was concentrated to ~ 1 mL. Addition of 15 mL of pentane gave an orange solid, which was washed with pentane and dried in vacuo. Yield: 116 mg (90.4%). ¹H NMR (500 MHz, CDCl₃) δ/ppm: 3.08–3.21 (br, m, 3H), 2.01–2.12 (br, m, 6H), 1.65–1.95 (br, m, 15H), 1.29–1.42 (br, m, 9H). ³¹P{¹H} NMR (121.5 MHz, CDCl₃)

δ /ppm: 65.0 (s). UV-vis (CH₂Cl₂): λ /nm (ϵ /(M⁻¹ cm⁻¹)) 250 (23000), 279 (18000), 400 (5700).
Anal. Calcd. for C₁₈H₃₃AuBr₃P: C, 30.15; H, 4.64. Found: C, 30.16; H, 4.65.

1.5.18 X-Ray Crystallographic Details

Single crystals of **1**, **7**, and **13** were obtained from CH₂Cl₂ layered with pentane, whereas crystals of **2** were obtained in a similar fashion from CHCl₃/pentane. Single crystals of **4** were obtained from a 1,1,2,2-tetrachloroethane solution layered with heptane, **15**, **16**, **20**, **22**, and **26** were crystallized from CH₂Cl₂ solutions layered with pentane, crystals of **23** were grown from a chlorobenzene solution layered with heptane, and crystals of **24** were obtained from a 1,2-dichloroethane solution layered with heptane. The crystals were mounted on a Bruker three-circle goniometer platform equipped with an APEX detector. A graphite monochromator was employed for wavelength selection of the Mo K α radiation ($\lambda = 0.71073$ Å). The data were processed and refined using the program SAINT supplied by Siemens Industrial Automation. Structures were solved by direct methods in SHELXS and refined by standard difference Fourier techniques in the SHELXTL program suite (6.10 v., Sheldrick G. M., and Siemens Industrial Automation, 2000). Hydrogen atoms were placed in calculated positions using the standard riding model and refined isotropically; all other atoms were refined anisotropically. The crystal of **13** was a nonmerohedral twin; the final model was refined against two unit-cell domains. In the structure of **7**, one of the -CF₃ groups was modeled as a two-part disorder. A positional disorder of the three bromine atoms bonded to Au(2) in the structure of **22** was modeled. In the same structure, the CH₂Cl₂ solvate was modeled as a two-part disorder. In the structure of **24**, one of the two independent dichloroethane solvates was modeled as a two-part disorder. In the structure of **2**, the C-C distances of the solvent molecule were restrained to a reasonable value (1.54 Å) using a DFIX command. The 1-2 and 1-3 distances of all disordered parts were restrained to be similar using the SADI command; the rigid-bond restraints SIMU and DELU were also used on disordered parts. Crystallographic details for **1**, **2**, **4** (CCDC 737767), **7**, **13**, **15** (CCDC 737768), **16** (CCDC 737769), **20** (CCDC 737770), **22** (CCDC 737771), **23** (CCDC 737772), **24** (CCDC 737773) and **26** (CCDC 737774) are summarized in Tables 1.3–1.6 below.

Table 1.3. Crystallographic summary for complexes **1**, **2**, and **4**.

| | 1 | 2·CHCl₃ | 4·2.5C₂H₂Cl₄ |
|--|---|--|---|
| Formula | C ₉ H ₁₁ Au ₂ Cl ₂ F ₁₂ NO ₄ P ₂ | C ₂₈ H ₂₆ Au ₂ Cl ₅ P ₂ | C ₃₀ H ₅₁ Au ₂ Cl ₁₂ P ₂ |
| fw, g/mol | 951.96 | 995.61 | 1292.98 |
| Temperature/K | 100(2) | 100(2) | 100(2) |
| cryst. syst. | Monoclinic | Monoclinic | Trigonal |
| space group | <i>P2</i> ₁ | <i>Pn</i> | <i>P3</i> ₂ 21 |
| color | Colorless | Colorless | Colorless |
| <i>a</i> /Å | 8.8755(10) | 9.4607(6) | 15.787(2) |
| <i>b</i> /Å | 25.219(3) | 9.5806(7) | 15.787(2) |
| <i>c</i> /Å | 9.8748(11) | 17.2293(12) | 30.811(4) |
| α /° | 90 | 90 | 90 |
| β /° | 99.111(2) | 102.6190(10) | 90 |
| γ /° | 90 | 90 | 120 |
| <i>V</i> /Å ³ | 2182.4(4) | 1523.93(18) | 6650.5(16) |
| ρ (calc.)/(g cm ⁻³) | 2.897 | 2.170 | 1.937 |
| <i>Z</i> | 4 | 2 | 6 |
| no. refl. | 50656 | 34361 | 88178 |
| no. unique refl. | 13127 | 9180 | 7559 |
| <i>R</i> _{int} | 0.0402 | 0.0370 | 0.0746 |
| <i>R</i> ₁ ^a (all data) | 0.0257 | 0.0216 | 0.0471 |
| <i>wR</i> ₂ ^b (all data) | 0.0559 | 0.0420 | 0.1080 |
| <i>R</i> ₁ [(<i>I</i> > 2σ)] | 0.0241 | 0.0205 | 0.0406 |
| <i>wR</i> ₂ [(<i>I</i> > 2σ)] | 0.0551 | 0.0417 | 0.1026 |
| <i>GOF</i> ^c | 1.017 | 0.924 | 1.079 |

^a $R_1 = \frac{\sum |F_o - |F_c||}{\sum |F_o|}$. ^b $wR_2 = \frac{(\sum (w(F_o^2 - F_c^2)^2)/\sum (w(F_o^2)^2))^{1/2}}$. ^c $GOF = \frac{(\sum w(F_o^2 - F_c^2)^2/(n - p))^{1/2}}$ where *n* is the number of data and *p* is the number of parameters refined.

Table 1.4. Crystallographic summary for complexes **7**, **13**, and **15**.

| | 7 | 13 ·CH ₂ Cl ₂ | 15 |
|--|---|--|--|
| Formula | C ₉ H ₁₁ Au ₂ Br ₂ F ₁₂ NO ₄ P ₂ | C ₂₈ H ₂₈ Au ₂ Cl ₆ P ₂ | C ₂₅ H ₂₂ Au ₂ Cl ₄ P ₂ |
| fw, g/mol | 1040.88 | 1033.08 | 920.1 |
| Temperature/K | 100(2) | 100(2) | 100(2) |
| cryst. syst. | Monoclinic | Monoclinic | Orthorhombic |
| space group | <i>C2/c</i> | <i>P2₁/c</i> | <i>P2₁2₁2₁</i> |
| color | Colorless | Orange | Yellow |
| <i>a</i> /Å | 11.1212(17) | 15.9344(12) | 12.570(3) |
| <i>b</i> /Å | 25.976(4) | 10.7593(8) | 13.011(3) |
| <i>c</i> /Å | 8.7499(13) | 18.5207(14) | 16.508(3) |
| <i>α</i> /° | 90 | 90 | 90 |
| <i>β</i> /° | 94.191(2) | 97.851(2) | 90 |
| <i>γ</i> /° | 90 | 90 | 90 |
| <i>V</i> /Å ³ | 2520.9(7) | 3145.5(4) | 2700.0(9) |
| <i>Z</i> | 4 | 4 | 4 |
| <i>ρ</i> (calc.)/(g cm ⁻³) | 2.743 | 2.181 | 2.264 |
| no. refl. | 28351 | 108083 | 60788 |
| no. unique refl. | 3847 | 9654 | 7914 |
| <i>R</i> _{int} | 0.0437 | 0.0731 | 0.0744 |
| <i>R</i> ₁ ^a (all data) | 0.0428 | 0.0382 | 0.0315 |
| <i>wR</i> ₂ ^b (all data) | 0.1004 | 0.0678 | 0.0678 |
| <i>R</i> ₁ [(<i>I</i> > 2σ)] | 0.0374 | 0.0643 | 0.0293 |
| <i>wR</i> ₂ [(<i>I</i> > 2σ)] | 0.0980 | 0.0306 | 0.0671 |
| <i>GOF</i> ^c | 1.322 | 1.020 | 1.052 |

^a $R_1 = \frac{\sum ||F_o| - |F_c||}{\sum |F_o|}$. ^b $wR_2 = \frac{(\sum (w(F_o^2 - F_c^2)^2) / \sum (w(F_o^2)^2))^{1/2}}$. ^c $GOF = \frac{(\sum w(F_o^2 - F_c^2)^2 / (n - p))^{1/2}}$ where *n* is the number of data and *p* is the number of parameters refined.

Table 1.5. Crystallographic summary for complexes **16**, **20**, and **22**.

| | 16 ·CH ₂ Cl ₂ | 20 | 22 ·CH ₂ Cl ₂ |
|--|--|---|--|
| Formula | C ₂₆ H ₂₄ Au ₂ Cl ₈ P ₂ | C ₁₈ H ₃₃ AuCl ₃ P | C ₂₆ H ₂₄ Au ₂ Br ₆ Cl ₂ P ₂ |
| fw, g/mol | 1075.83 | 583.73 | 1342.69 |
| Temperature/K | 100(2) | 100(2) | 100(2) |
| cryst. syst. | Monoclinic | Monoclinic | Triclinic |
| space group | <i>P2₁/n</i> | <i>C2/c</i> | <i>PT</i> |
| color | Yellow | Yellow | Red |
| <i>a</i> /Å | 9.9293(6) | 17.2194(14) | 11.2927(12) |
| <i>b</i> /Å | 14.9256(9) | 13.7859(14) | 12.2466(13) |
| <i>c</i> /Å | 21.1774(13) | 18.2238(16) | 15.2241(15) |
| <i>α</i> /° | 90 | 90 | 73.373(2) |
| <i>β</i> /° | 93.0540(10) | 99.905(2) | 79.170(2) |
| <i>γ</i> /° | 90 | 90 | 68.124(2) |
| <i>V</i> /Å ³ | 3134.0(3) | 4261.6(7) | 1864.3(3) |
| <i>ρ</i> (calc.)/(g cm ⁻³) | 2.280 | 1.820 | 2.245 |
| <i>Z</i> | 4 | 8 | 2 |
| no. refl. | 73318 | 43886 | 42049 |
| no. unique refl. | 10118 | 6266 | 11157 |
| <i>R</i> _{int} | 0.0501 | 0.0675 | 0.0493 |
| <i>R</i> ₁ ^a (all data) | 0.0301 | 0.0437 | 0.0658 |
| <i>wR</i> ₂ ^b (all data) | 0.0507 | 0.0681 | 0.1189 |
| <i>R</i> ₁ [(<i>I</i> > 2σ)] | 0.0234 | 0.0341 | 0.0408 |
| <i>wR</i> ₂ [(<i>I</i> > 2σ)] | 0.0481 | 0.0650 | 0.1042 |
| <i>GOF</i> ^c | 1.032 | 1.122 | 1.021 |

^a $R_1 = \sum ||F_o - |F_c|| / \sum |F_o|$. ^b $wR_2 = (\sum (w(F_o^2 - F_c^2)^2) / \sum (w(F_o^2)^2))^{1/2}$. ^c $GOF = (\sum w(F_o^2 - F_c^2)^2 / (n - p))^{1/2}$ where *n* is the number of data and *p* is the number of parameters refined.

Table 1.6. Crystallographic summary for complexes **23**, **24**, and **26**.

| | 23 | 24 ·C ₂ H ₄ Cl ₂ | 26 |
|--|--|--|---|
| Formula | C ₂₅ H ₄₆ Au ₂ Br ₄ P ₂ | C ₂₇ H ₅₀ Au ₂ Br ₆ Cl ₂ P ₂ | C ₁₈ H ₃₃ AuBr ₃ P |
| fw, g/mol | 1122.13 | 1380.90 | 717.11 |
| Temperature/K | 100(2) | 100(2) | 100(2) |
| cryst. syst. | Monoclinic | Monoclinic | Orthorhombic |
| space group | <i>P2₁/n</i> | <i>P2₁/n</i> | <i>Pnma</i> |
| color | Red | Red | Orange |
| <i>a</i> /Å | 11.7519(9) | 9.5914(8) | 14.7919(9) |
| <i>b</i> /Å | 14.3982(10) | 15.0383(13) | 16.4575(10) |
| <i>c</i> /Å | 19.2592(14) | 26.602(2) | 9.0123(5) |
| α /° | 90 | 90 | 90 |
| β /° | 95.4610(10) | 96.941(2) | 90 |
| γ /° | 90 | 90 | 90 |
| <i>V</i> /Å ³ | 3244.0(4) | 3808.9(6) | 2193.9(2) |
| ρ (calc.)/(g cm ⁻³) | 2.298 | 2.408 | 2.171 |
| <i>Z</i> | 4 | 4 | 4 |
| no. refl. | 73851 | 75308 | 48982 |
| no. unique refl. | 9877 | 9102 | 3467 |
| <i>R</i> _{int} | 0.0602 | 0.0572 | 0.0568 |
| <i>R</i> ₁ ^a (all data) | 0.0444 | 0.0407 | 0.0295 |
| <i>wR</i> ₂ ^b (all data) | 0.0805 | 0.0749 | 0.0501 |
| <i>R</i> ₁ [(<i>I</i> > 2σ)] | 0.0319 | 0.0344 | 0.0224 |
| <i>wR</i> ₂ [(<i>I</i> > 2σ)] | 0.0748 | 0.0730 | 0.0474 |
| <i>GOF</i> ^c | 1.048 | 1.173 | 1.050 |

^a $R_1 = \frac{\sum |F_o - |F_c||}{\sum |F_o|}$. ^b $wR_2 = \frac{(\sum (w(F_o^2 - F_c^2)^2)/\sum (w(F_o^2)^2))^{1/2}}$. ^c $GOF = \frac{(\sum w(F_o^2 - F_c^2)^2/(n - p))^{1/2}}$ where *n* is the number of data and *p* is the number of parameters refined.

1.6 References

- (1) Lewis, N. S.; Nocera, D. G. *Proc. Natl. Acad. Sci. U.S.A.* **2006**, *103*, 15729–15735.
- (2) Kanan, M. W.; Surendranath, Y.; Nocera, D. G. *Chem. Soc. Rev.* **2009**, *38*, 109–114.
- (3) Cook, T. R.; Dogutan, D. K.; Reece, S. Y.; Surendranath, Y.; Teets, T. S.; Nocera, D. G. *Chem. Rev.* **2010**, *110*, 6474–6502.
- (4) Kanan, M. W.; Nocera, D. G. *Science* **2008**, *321*, 1072–1075.
- (5) Surendranath, Y.; Dincă, M.; Nocera, D. G. *J. Am. Chem. Soc.* **2009**, *131*, 2615–2620.
- (6) Eisenberg, R.; Gray, H. B. *Inorg. Chem.* **2008**, *47*, 1697–1699.
- (7) Betley, T. A.; Wu, Q.; Van Voorhis, T.; Nocera, D. G. *Inorg. Chem.* **2008**, *47*, 1849–1861.
- (8) Esswein, A. J.; Nocera, D. G. *Chem. Rev.* **2007**, *107*, 4022–4047.
- (9) Thomassen, M.; Sandnes, E.; Børresen, B.; Tunold, R. *J. Appl. Electrochem.* **2006**, *36*, 813–819.
- (10) Ledjeff, K. *Electrochim. Acta* **1995**, *40*, 315–319.
- (11) Yeo, R. S.; McBreen, J.; Tseung, A. C. C.; Srinivasan, S.; McElroy, J. *J. Appl. Electrochem.* **1980**, *10*, 393–404.
- (12) Livshits, V.; Ulus, A.; Peled, E. *Electrochem. Commun.* **2006**, *8*, 1358–1362.
- (13) Miranda, M. A.; Pérez-Prieto, J.; Font-Sanchis, E.; Scaiano, J. C. *Acc. Chem. Res.* **2001**, *34*, 717–726.
- (14) Marvet, U.; Brown, E. J.; Dantus, M. *Phys. Chem. Chem. Phys.* **2000**, *2*, 885–891.
- (15) Rozgonyi, T.; González, L. *J. Phys. Chem. A* **2002**, *106*, 11150–11161.
- (16) Görner, H. *J. Photochem. Photobiol. A* **1995**, *90*, 57–63.
- (17) Cook, T. R.; Esswein, A. J.; Nocera, D. G. *J. Am. Chem. Soc.* **2007**, *129*, 10094–10095.
- (18) Cook, T. R.; Surendranath, Y.; Nocera, D. G. *J. Am. Chem. Soc.* **2009**, *131*, 28–29.
- (19) Heyduk, A. F.; Macintosh, A. M.; Nocera, D. G. *J. Am. Chem. Soc.* **1999**, *121*, 5023–5032.
- (20) Heyduk, A. F.; Nocera, D. G. *Science* **2001**, *293*, 1639–1641.
- (21) Esswein, A. J.; Veige, A. S.; Nocera, D. G. *J. Am. Chem. Soc.* **2005**, *127*, 16641–16651.
- (22) Esswein, A. J.; Dempsey, J. L.; Nocera, D. G. *Inorg. Chem.* **2007**, *46*, 2362–2364.
- (23) Odom, A. L.; Heyduk, A. F.; Nocera, D. G. *Inorg. Chim. Acta* **2000**, *297*, 330–337.
- (24) Partyka, D. V.; Esswein, A. J.; Zeller, M.; Hunter, A. D.; Gray, T. G. *Organometallics* **2007**, *26*, 3279–3282.

- (25) Teets, T. S.; Partyka, D. V.; Esswein, A. J.; Updegraff, J. B.; Zeller, M.; Hunter, A. D.; Gray, T. G. *Inorg. Chem.* **2007**, *46*, 6218–6220.
- (26) Sinha, P.; Wilson, A. K.; Omary, M. A. *J. Am. Chem. Soc.* **2005**, *127*, 12488–12489.
- (27) Forward, J. M.; Bohmann, D.; Fackler, J. P.; Staples, R. J. *Inorg. Chem.* **1995**, *34*, 6330–6336.
- (28) Fernández, E. J.; Laguna, A.; López-de-Luzuriaga, J. M.; Monge, M.; Montiel, M.; Olmos, M. E.; Rodríguez-Castillo, M. *Dalton Trans.* **2006**, 3672–3677.
- (29) Wing-Wah Yam, V.; Chung-Chin Cheng, E. In *Photochemistry and Photophysics of Coordination Compounds II*; Balzani, V.; Campagna, S., Eds.; Springer Berlin Heidelberg: Berlin, Heidelberg; Vol. 281, pp. 269–309.
- (30) Bachman, R. E.; Bodolosky-Bettis, S. A.; Pyle, C. J.; Gray, M. A. *J. Am. Chem. Soc.* **2008**, *130*, 14303–14310.
- (31) Serafimova, I. M.; Hoggard, P. E. *Inorg. Chim. Acta* **2002**, *338*, 105–110.
- (32) Bennett, M. A.; Bhargava, S. K.; Hockless, D. C. R.; Welling, L. L.; Willis, A. C. *J. Am. Chem. Soc.* **1996**, *118*, 10469–10478.
- (33) Komiya, S.; Kochi, J. K. *J. Am. Chem. Soc.* **1976**, *98*, 7599–7607.
- (34) Komine, N.; Ichikawa, K.; Mori, A.; Hirano, M.; Komiya, S. *Chem. Lett.* **2005**, *34*, 1704–1705.
- (35) Fackler, J. P. *Inorg. Chem.* **2002**, *41*, 6959–6972.
- (36) Vogler, A. *Coord. Chem. Rev.* **2001**, *219-221*, 489–507.
- (37) Ronco, S.; Ferraudi, G. In *Handbook of Photochemistry and Photobiology*; Nalwa, H. S., Ed.; American Scientific Publishers: Stevenson Ranch, CA, 2003; pp. 283–343.
- (38) Uson, R.; Laguna, A.; Laguna, M.; *Inorg. Synth.* **1989**, *26*, 85–91.
- (39) Schneider, D.; Schier, A.; Schmidbaur, H. *Dalton Trans.* **2004**, 1995–2005.
- (40) Schmidbaur, H.; Schier, A. *Chem. Soc. Rev.* **2008**, *37*, 1931–1951.
- (41) Schmidbaur, H.; Wohlleben, A.; Wagner, F.; Orama, O.; Huttner, G. *Chem. Ber.* **1977**, *110*, 1748–1754.
- (42) Healy, P. C. *Acta Crystallogr. Sect. E* **2003**, *59*, m1112–m1114.
- (43) Heyduk, A. F.; Nocera, D. G. *J. Am. Chem. Soc.* **2000**, *122*, 9415–9426.
- (44) Schmidbaur, H.; Wohlleben, A.; Wagner, F. E.; Van de Vondel, D. F.; Van der Kelen, G. *P. Chem. Ber.* **1977**, *110*, 2758–2764.
- (45) Usón, R.; Laguna, A.; Fernández, E. J.; Mendia, A.; Jones, P. G. *J. Organomet. Chem.* **1988**, *350*, 129–138.

- (46) Attar, S.; Nelson, J. H.; Bearden, W. H.; Alcock, N. W.; Solujic', L.; Milosavljevic', E. B. *Polyhedron* **1991**, *10*, 1939–1949.
- (47) Lever, A. B. P. In *Inorganic electronic spectroscopy*; Elsevier: Amsterdam, 1986; p. Chapter 5.
- (48) Nickel, U.; Chen, Y.-H.; Schneider, S.; Silva, M. I.; Burrows, H. D.; Formosinho, S. J. *J. Phys. Chem.* **1994**, *98*, 2883–2888.
- (49) Bader, H.; Sturzenegger, V.; Hoigné, J. *Water Res.* **1988**, *22*, 1109–1115.
- (50) Lide, D. R. *CRC handbook of chemistry and physics : a ready-reference book of chemical and physical data : 2003-2004.*; CRC Press: Boca Raton, 2003.
- (51) Bruice, P. Y. *Organic chemistry*; Pearson/Prentice Hall: Upper Saddle River, NJ, 2004.
- (52) Gray, T. G.; Veige, A. S.; Nocera, D. G. *J. Am. Chem. Soc.* **2004**, *126*, 9760–9768.
- (53) Esswein, A. J.; Veige, A. S.; Piccoli, P. M. B.; Schultz, A. J.; Nocera, D. G. *Organometallics* **2008**, *27*, 1073–1083.
- (54) Balzani, V.; Carassiti, V. *Photochemistry of coordination compounds.*; Academic Press: London; New York, 1970.
- (55) Goursot, A.; Kirk, A. D.; Waltz, W. L.; Porter, G. B.; Sharma, D. K. *Inorg. Chem.* **1987**, *26*, 14–18.
- (56) Veige, A. S.; Gray, T. G.; Nocera, D. G. *Inorg. Chem.* **2005**, *44*, 17–26.
- (57) Zielinska, A.; Skulski, L. *Tetrahedron Lett.* **2004**, *45*, 1087–1089.
- (58) Balakrishna, M. S.; Prakasha, T. K.; Krishnamurthy, S. S.; Siriwardane, U.; Hosmane, N. S. *J. Organomet. Chem.* **1990**, *390*, 203–216.
- (59) Ganesan, M.; Krishnamurthy, S. S.; Nethaji, M. *J. Organomet. Chem.* **1998**, *570*, 247–254.
- (60) Pons, A.; Rossell, O.; Seco, M.; Solans, X.; Font-Bardía, M. *J. Organomet. Chem.* **1996**, *514*, 177–182.
- (61) Yam, V. W.-W.; Cheung, K.-L.; Yip, S.-K.; Cheung, K.-K. *J. Organomet. Chem.* **2003**, *681*, 196–209.
- (62) Isab, A. A.; Fettouhi, M.; Ahmad, S.; Ouahab, L. *Polyhedron* **2003**, *22*, 1349–1354.
- (63) Eaton, A. D.; Clesceri, L. S.; Rice, W. E.; Greenberg, A. E. In *Standard Methods for the Examination of Water and Wastewater*; American Public Health Association, American Water Works Association, Water Pollution Control Federation: Washington, D. C., 2005; p. Chapter 4.
- (64) Montalti, M.; Murov, S. L. *Handbook of photochemistry.*; CRC/Taylor & Francis: Boca Raton, 2006.

**Chapter 2 –
Halogen Photoreductive Elimination from Metal–Metal-Bonded
M^{II}–Au^{II} (M = Rh, Ir) Heterobimetallic Complexes**

Portions of this work have been previously published:

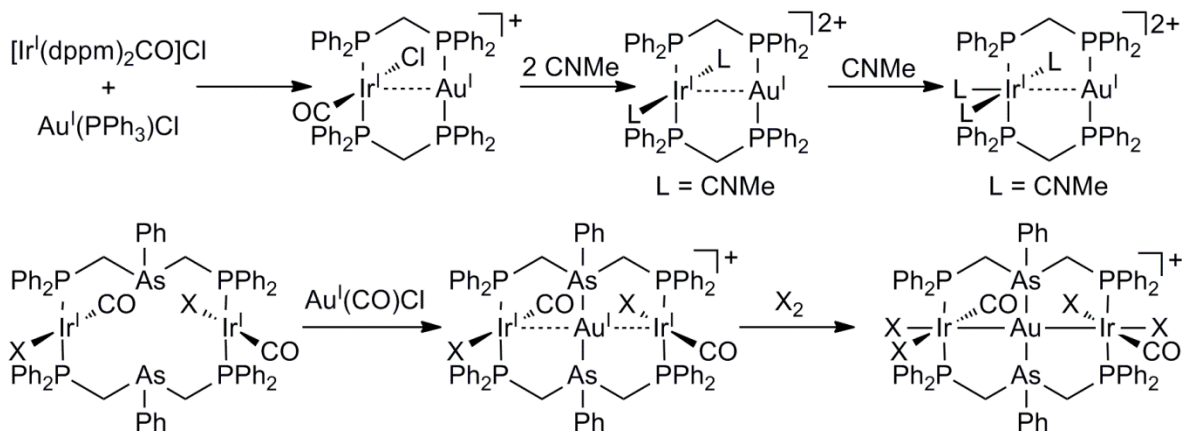
Reproduced in part with permission from Teets, T. S.; Lutterman, D. A.; Nocera, D. G. *Inorg. Chem.* **2010**, *49*, 3035–3043. Copyright 2010 American Chemical Society.

Teets, T. S.; Neumann, M. P.; Nocera, D. G. *Chem. Commun.* **2011**, *47*, 1485–1487. Reproduced by permission of the Royal Society of Chemistry.

2.1 Introduction

In this chapter, the theme of developing more efficient HX-splitting (X = Cl, Br) photocatalysts continues, again with much focus on the more thermodynamically challenging X₂ photoelimination. Our group's first foray into HX splitting centered around dirhodium complexes, which were catalytic for hydrogen evolution^{1,2} but exceedingly sluggish at eliminating X₂,^{3,4} which only occurred in the presence of a chemical trap. In the preceding chapter, it was demonstrated that photolysis of Au^{III} halide complexes elicits efficient X₂ elimination, and that this photoreaction can be executed in the absence of a halogen trap. This knowledge, coupled with our group's other findings that more oxidizing late transition-metal complexes containing platinum and/or gold also show high quantum yields for halogen photoelimination,^{5,6} has led us to consider designs of next-generation HX-splitting catalysts incorporating these later metals. Our interest in heterobimetallic complexes stems from a desire to strike a balance in designing molecular photocatalysts that can manage the formal reduction of protons to hydrogen but at the same time are oxidizing enough to efficiently eliminate halogen to complete HX-splitting cycles. Armed with the knowledge (i) that metal–metal-bonded dirhodium and diiridium complexes display a rich reaction chemistry with hydrohalic acids and reversibly add hydrogen^{2,7} and (ii) that complexes containing more oxidizing transition metals efficiently eliminate halogen (vide supra), we turned our attention to rhodium–gold and iridium–gold heterobimetallic complexes as promising candidates as next-generation HX-splitting catalysts.

Iridium(I)–gold(I) heterobimetallic complexes were first reported by Shaw and coworkers, who detailed the synthesis of [Ir^IAu^I(dppm)₂(CO)Cl]Cl (dppm = bis(diphenylphosphino)methane),⁸ and later described synthetic methods for substituting methyl isocyanide (MeNC) onto the iridium center.⁹ Since these initial reports, efforts led by the Balch and Crosby groups have elucidated many of the key photophysical^{10–13} aspects of these complexes; the ubiquitous dσ* → pσ transition dominates the low-energy electronic spectra of these complexes, which will be considered in more detail later in this chapter. Computational studies of Ir^IAu^I complexes have also emerged, providing additional insights on the electronic structure.¹⁴ However, the reactivity of these complexes had remained underexplored. Reactions with select Lewis acids such as HgCl₂ and BF₃ have been characterized for [Ir^IAu^I(dppm)₂(CO)Cl](PF₆)¹⁵ and a trimetallic Ir^IAu^IIr^I complex has been oxidized.¹⁶ Scheme

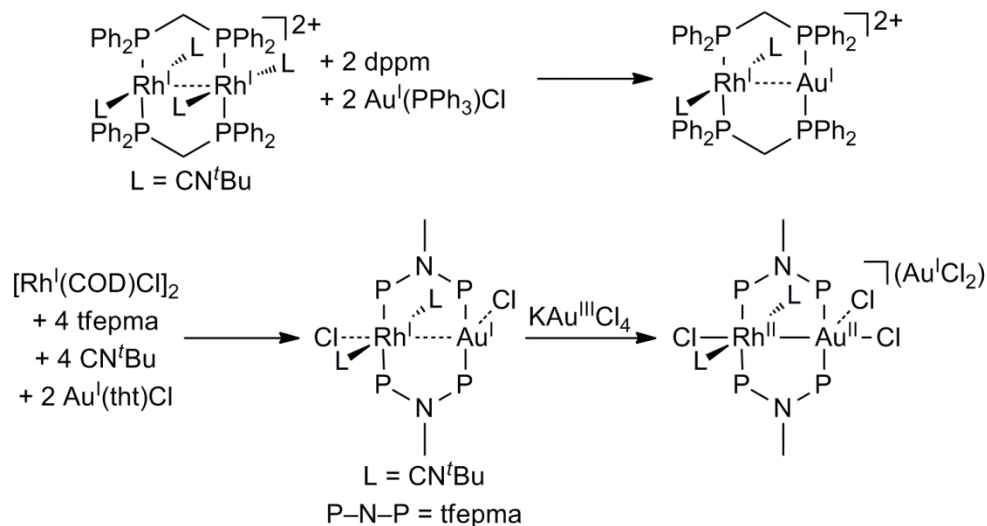


Scheme 2.1. Previous examples of iridium–gold heterobimetallic complexes.

2.1 summarizes the assembly and key transformations of iridium–gold complexes which have been reported primarily by the groups of Shaw and Balch. Of note is that two general classes of bimetallic $\text{Ir}^{\text{I}}\cdots\text{Au}^{\text{I}}$ complexes emerge from these previous studies—monocationic complexes featuring a “Vaska-type” iridium(I) center, and dicationic complexes where a full complement of neutral ligands is bound to iridium(I). These previous studies did not include oxidative-addition reactions of bimetallic iridium–gold species, and photochemical transformations involving iridium–gold heterobimetallics are likewise unknown.

Rhodium–gold heterobimetallic complexes have been described to even less of an extent, with one such complex, $[\text{Rh}^{\text{I}}\text{Au}^{\text{I}}(\text{dppm})_2(\text{CN}^t\text{Bu})_2]^{2+}$ as a lone example outside of our group. This complex was first prepared by Shaw and coworkers,⁹ and was also subjected to rigorous photophysical studies by two different groups.^{17,18} Our group later described the first d^7 – d^9 metal–metal-bonded rhodium–gold complex, which could only be synthesized when the dppm bridging ligand was replaced with $\text{CH}_3\text{N}[\text{P}(\text{OCH}_2\text{CF}_3)_2]_2$ (tfepma). Oxidation of $\text{Rh}^{\text{I}}\text{Au}^{\text{I}}(\text{tfepma})_2(\text{CN}^t\text{Bu})_2\text{Cl}_2$ with $\text{KAu}^{\text{III}}\text{Cl}_4$ produced the metal–metal-bonded complex $[\text{Rh}^{\text{II}}\text{Au}^{\text{II}}(\text{tfepma})_2(\text{CN}^t\text{Bu})_2\text{Cl}_3][\text{Au}^{\text{I}}\text{Cl}_2]$, but ultimately this product was too thermally unstable to allow for detailed photochemical characterization.¹⁹ These previous examples of rhodium–gold heterobimetallic complexes are summarized in Scheme 2.2.

In this chapter, syntheses of new $d^8\cdots d^{10}$ $\text{M}^{\text{I}}\text{Au}^{\text{I}}$ ($\text{M} = \text{Rh}, \text{Ir}$) complexes spanned by two bridging diphosphines are described. Halogen oxidation furnishes d^7 – d^9 $\text{M}^{\text{II}}\text{Au}^{\text{II}}$ bimetallic complexes; this electron count has heretofore not been observed for Ir bonded to Au. Included in this suite of complexes are the first examples of thermally robust $\text{Rh}^{\text{II}}\text{Au}^{\text{II}}$ complexes. The



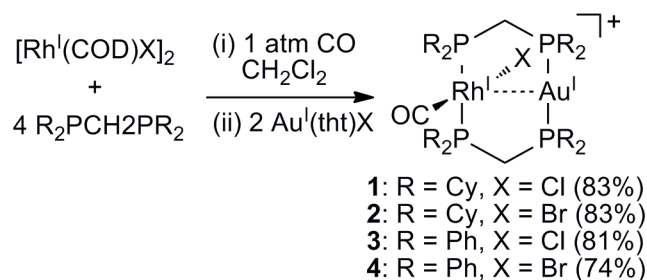
Scheme 2.2. Previous examples of rhodium–gold heterobimetallic complexes.

complexes possess a formal metal–metal σ bond, which is validated by structural metrics from X-ray crystallography. Experimental and computational studies establish an electronic structure that is dominated by $d\sigma \rightarrow d\sigma^*$ character with significant halide LMCT admixture. Consistent with this bonding formulation, irradiation of the $M^{\text{II}}\text{Au}^{\text{II}}$ complexes activates M–X bonds and halogen photoreductive elimination is achieved. The enhanced thermal stability of the new class of rhodium–gold complexes permits the first photochemical study of this type of complex.

2.2 Results

2.2.1 Synthesis and Characterization of $M^{\text{I}}\text{Au}^{\text{I}}$ ($M = \text{Rh}, \text{Ir}$) Complexes

$\text{Rh}^{\text{I}}\text{Au}^{\text{I}}$ halide complexes are prepared in the stepwise procedure outlined in Scheme 2.3, generating heterobimetallic complexes **1–4**, which are isolated as either PF_6^- (**1–3**) or trifluoromethanesulfonate (OTf^-) (**4**) salts. The common Rh^{I} starting material $[\text{Rh}^{\text{I}}(\text{COD})\text{Cl}]_2$ (COD = 1,5-cyclooctadiene) is treated with 4 eq of the bridging phosphine, $\text{CH}_2(\text{PR}_2)_2$ [$R = \text{Cy}$



Scheme 2.3. Synthesis of $\text{Rh}^{\text{I}}\text{Au}^{\text{I}}$ complexes **1–4**. Isolated yields are listed in parentheses.

(dcpm), Ph (dppm)]. This generates the bischelate complex $[\text{Rh}^{\text{I}}(\kappa^2\text{-CH}_2(\text{PR}_2)_2)_2]\text{Cl}$, which may be isolated and used as the starting material, though equally satisfying results are obtained if this complex is generated in situ. Whether isolated or generated in situ, this Rh^{I} intermediate is treated with excess CO, at which time the labile Au^{I} starting material $\text{Au}^{\text{I}}(\text{tht})\text{Cl}$ (tht = tetrahydrothiophene) is introduced, assembling the heterobimetallic complexes. Crude NMR spectra suggest near quantitative formation of the $\text{Rh}^{\text{I}}\text{Au}^{\text{I}}$ complexes, which can be purified and isolated in yields of 74–83%. The $\text{Rh}^{\text{I}}\text{Au}^{\text{I}}$ complexes are readily identified by their $^{31}\text{P}\{^1\text{H}\}$ NMR spectra, which show two AA'XX' multiplets largely

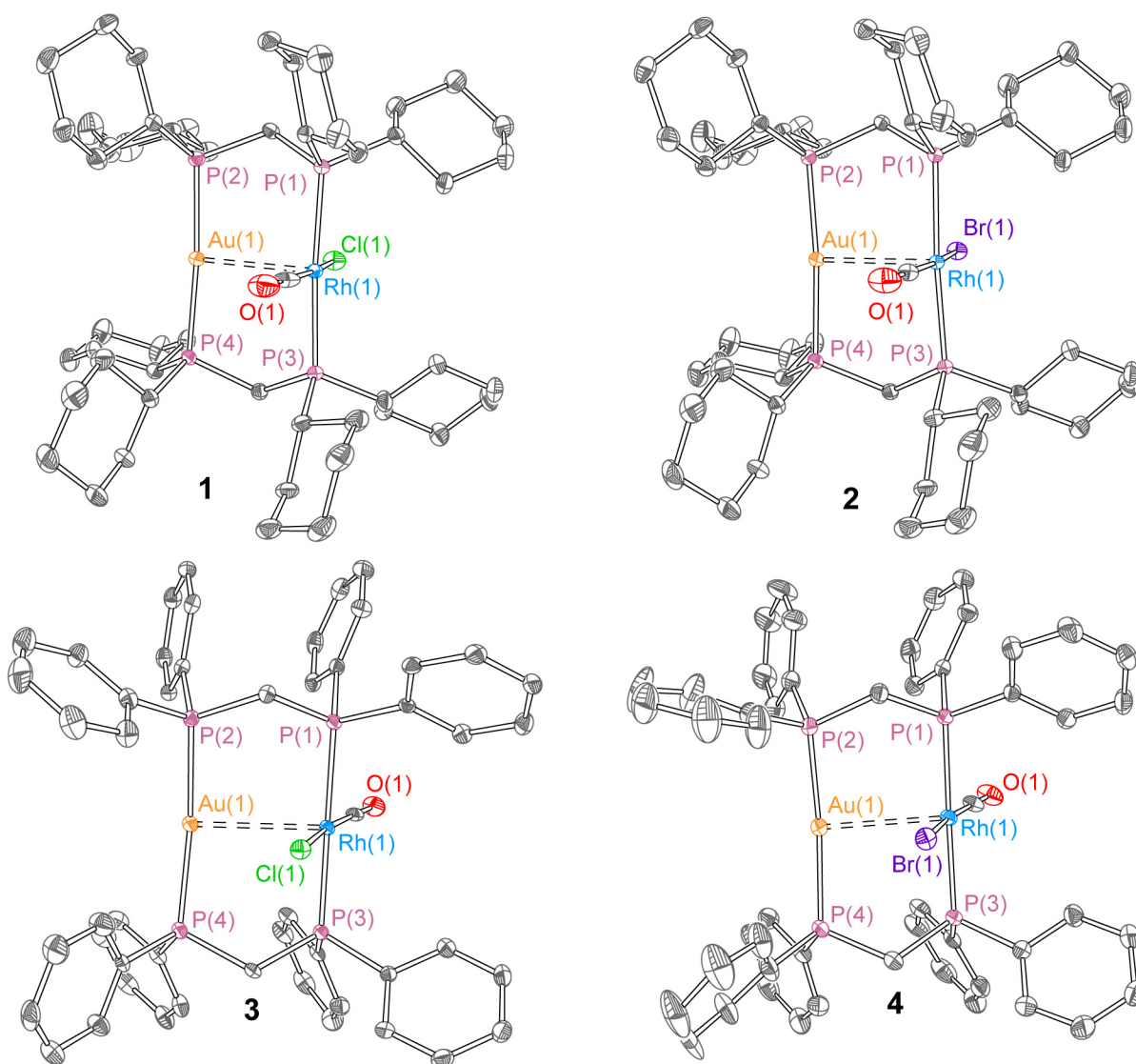
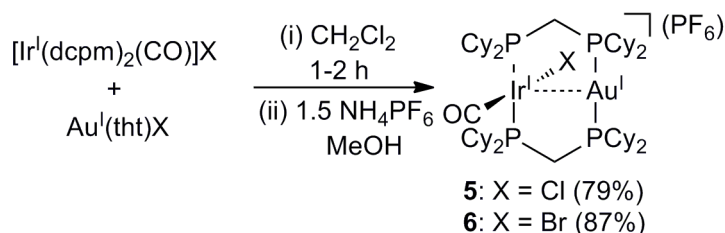


Figure 2.1. X-ray crystal structures of 1–4. Ellipsoids are depicted at the 50% probability level with counterions, solvent molecules and hydrogen atoms omitted for clarity.

reminiscent of the splitting observed for isostructural $\text{Ir}^{\text{I}}\text{Au}^{\text{I}}$ complexes (vide infra). One of the two multiplets is additionally coupled to ^{103}Rh , allowing for unambiguous assignment of the $^{31}\text{P}\{^1\text{H}\}$ resonances. The observed $^1J_{\text{Rh-P}}$ values are 113–120 Hz.

All four $\text{Rh}^{\text{I}}\text{Au}^{\text{I}}$ complexes were characterized by X-ray diffraction, and their structures are collected in Figure 2.1. Complexes **1–4** are structurally similar to one another, with approximately square-planar Rh^{I} centers and approximately linear Au^{I} centers. In all cases, the anion (PF_6^- or OTf^-) is outer-sphere, and no interaction with either metal center is apparent. The $\text{Rh}\cdots\text{Au}$ internuclear distances are quite similar across the series. The $\text{Rh}(1)\cdots\text{Au}(1)$ distances of 2.9250(4) Å and 2.9187(2) Å in dcpm-bridged **1** and **2** elongate slightly to 2.9551(3) Å and 2.9537(5) Å in dppm-bridged **3** and **4**. These values are indicative of a weak metal–metal interaction, but the absence of a formal bond, as expected for the $d^8\cdots d^{10}$ electron count.

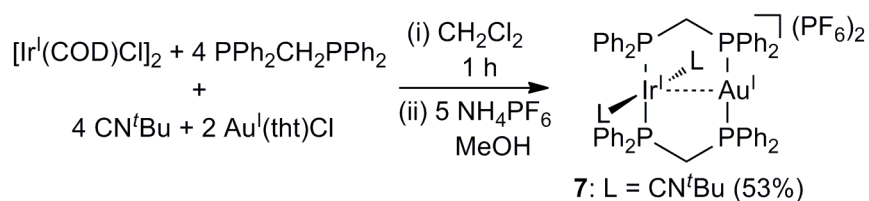
Monocationic $\text{Ir}^{\text{I}}\text{Au}^{\text{I}}$ compounds, with “Vaska-type” Ir^{I} centers, were synthesized by following the route depicted in Scheme 2.4. This method furnishes the complexes $[\text{Ir}^{\text{I}}\text{Au}^{\text{I}}(\text{dcpm})_2(\text{CO})\text{X}](\text{PF}_6)$ [$\text{X} = \text{Cl}$ (**5**), Br (**6**)] in a manner similar to that used for the synthesis of the dppm-bridged complex.⁸ $[\text{Ir}^{\text{I}}(\text{dcpm})_2\text{CO}]\text{X}$ is prepared by treatment of Vaska’s complex, *trans*- $\text{Ir}^{\text{I}}(\text{PPh}_3)_2(\text{CO})\text{X}$, with two equivalents of dcpm. This precursor is combined with $\text{Au}^{\text{I}}(\text{tht})\text{X}$ in CH_2Cl_2 to assemble the heterobimetallic complex. Anion exchange with methanolic NH_4PF_6 affords **5** and **6** as bright orange solids. This reaction is similar to the aforementioned $\text{Rh}^{\text{I}}\text{Au}^{\text{I}}$ synthesis, with the exception that the CO-bound Ir^{I} starting material is isolable and is used as the starting point. The ^1H NMR spectra of **5** and **6** are not particularly informative, consisting mainly of broad, overlapping cyclohexyl resonances. The compounds are most readily identified by ^{31}P NMR. In the $^{31}\text{P}\{^1\text{H}\}$ spectrum of both **5** and **6**, 14 of the 20 possible lines resulting from the $\text{AA}'\text{XX}'$ spin system can be resolved, and the position of the two frequencies is responsive to halide substitution. The two peaks in the spectrum of **5**, centered at 51.0 and 25.3 ppm, shift to



Scheme 2.4. Synthesis of $\text{Ir}^{\text{I}}\text{Au}^{\text{I}}$ complexes **5** and **6**. Isolated yields are listed in parentheses.

50.4 and 23.2 ppm in **6**. The larger shift of the upfield resonance suggests that it originates from the phosphorus atoms bound to iridium, which is the site of the halide substitution. Complexes **5** and **6** also possess distinctive C≡O IR stretching frequencies at 1944 cm⁻¹ (**5**) and 1945 cm⁻¹ (**6**), which are invariant to halide substitution. A dicationic Ir^IAu^I complex, with isocyanide ligands on the iridium, was also prepared. Though the methyl isocyanide complex [Ir^IAu^I(dppm)₂(CNMe)₂](PF₆)₂ was reported by Shaw and co-workers,⁹ we opted to prepare the *tert*-butyl isocyanide (CN^tBu) complex owing to the commercial availability of this isocyanide. As shown in Scheme 2.5, the desired [Ir^IAu^I(dppm)₂(CN^tBu)₂]²⁺ product, which can be isolated as its green PF₆⁻ salt (**7**), is obtained in moderate yields in a stepwise fashion starting with [Ir(COD)Cl]₂, which reacts sequentially with stoichiometric amounts of dppm, CN^tBu, and Au^I(tbt)Cl, in a manner similar to the synthesis of some Rh^IAu^I complexes.¹⁹ The ³¹P{¹H} NMR spectrum of **7** shows a complex splitting pattern similar to that of **5** and **6**, with two multiplets centered at 30.0 and 10.4 ppm. As with **5** and **6**, 14 of the 20 lines can be discerned. The splitting pattern is distinct from that of **5** and **6**, however, because the two outermost lines of each 7-line multiplet are the most intense. Complex **7** shows a characteristic C≡N stretch in the IR spectrum at 2138 cm⁻¹.

Compounds **5** and **6** were structurally characterized by X-ray crystallography. The thermal ellipsoid plots of the structures of **5** and **6**, shown in Figure 2.2, exhibit the expected square-planar coordination environment for d⁸ Ir^I and linear geometry for d¹⁰ Au^I. The Ir...Au distance of 2.9411(3) Å in **5** changes minimally with halide substitution, contracting by < 0.03 Å to 2.9174(2) Å in bromide-substituted **6**. The Ir...Au distances in **5** and **6** are nearly identical to the isostructural Rh^IAu^I complexes discussed above and slightly shorter than the distance of 2.986(1) Å reported for the dppm-bridged analogue [Ir^IAu^I(dppm)₂(CO)Cl](PF₆).¹⁰ Complex **7** eluded structural characterization, but the related complex [Ir^IAu^I(dppm)₂(CNMe)₂](PF₆)₂ has a



Scheme 2.5. Synthesis of Ir^IAu^I complex **7**. Isolated yield is listed in parentheses.

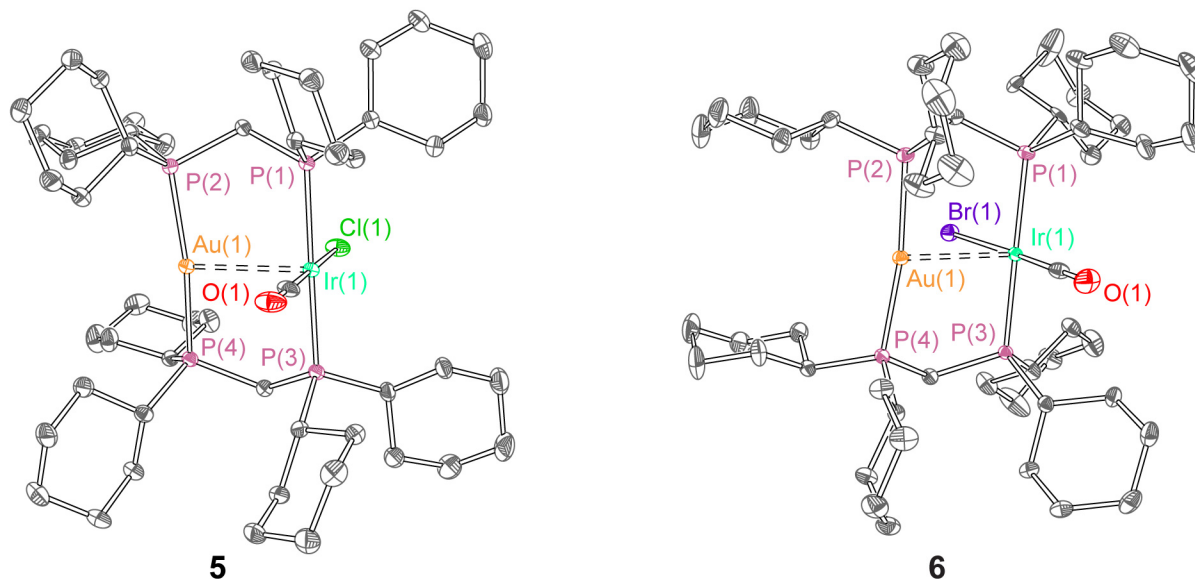
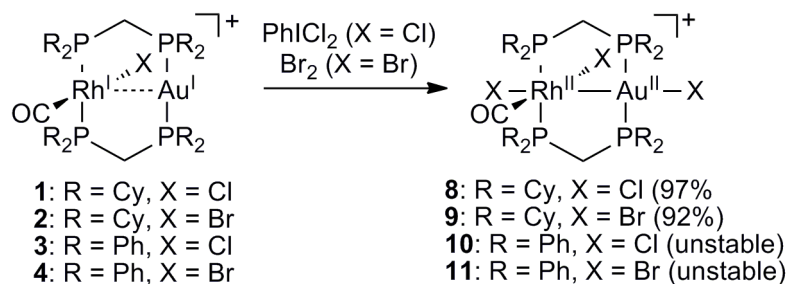


Figure 2.2. X-ray crystal structure of complexes **5** and **6**. Ellipsoids are shown at the 50% probability level with counterions, solvent molecules and hydrogen atoms omitted for clarity.

reported Ir...Au distance of 2.944(1) Å.¹¹

2.2.2 Halogen Oxidation of $M^I Au^I$ ($M = Rh, Ir$) Complexes to Prepare $M^{II} Au^{II}$ ($M = Rh, Ir$) Complexes

Halogen oxidation of $Rh^I Au^I$ complexes **1–4** affords $Rh^{II} Au^{II}$ complexes **8–11** quantitatively, as shown in Scheme 2.6. A substantial upfield shift of the ^{31}P resonances of the $Rh^I Au^I$ precursor occurs upon its treatment with $PhICl_2$ or Br_2 . A deceptively simple triplet splitting pattern is observed for the $AA'XX'$ spin system, and additional coupling is observed for one of the resonances, with $^1J_{Rh-P}$ values slightly smaller than those of the $Rh^I Au^I$ precursors, at 74–79 Hz. Whereas dppm-bridged **10** and **11** decompose above -20 °C to an intractable mixture of products, dcpm-bridged **8** and **9** are stable in solution at room temperature for at least 8 h with



Scheme 2.6. Halogen oxidation of $Rh^I Au^I$ complexes to furnish $Rh^{II} Au^{II}$ complexes. Isolated yields are listed in parentheses.

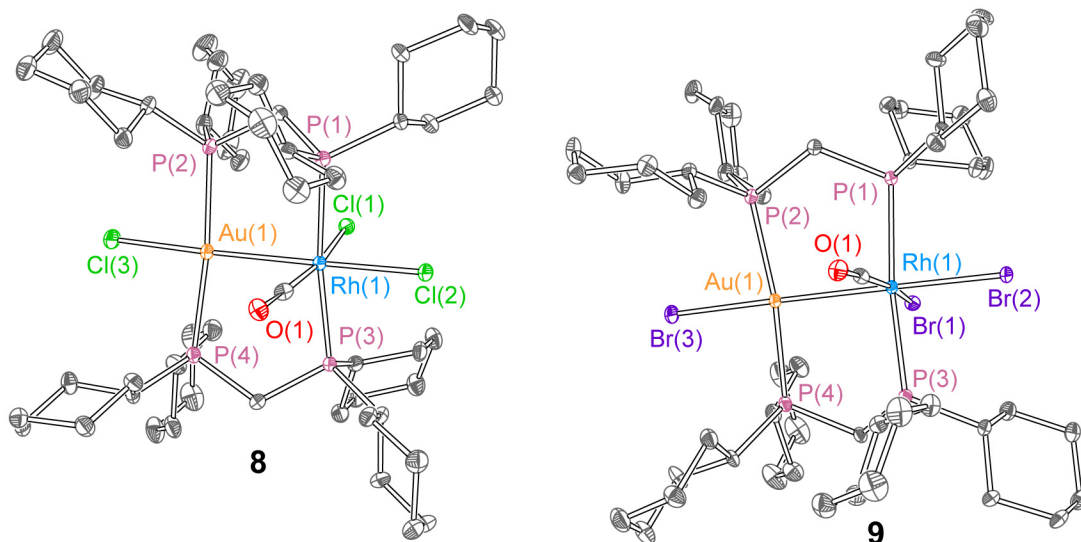
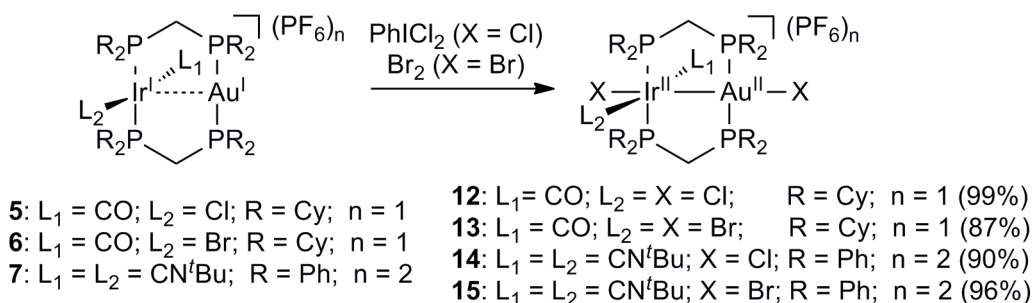


Figure 2.3. X-ray crystal structures of **8** and **9**. Ellipsoids are shown at the 50% probability level with counterions, solvent molecules and hydrogen atoms omitted for clarity.

no observable change in the ^{31}P spectrum.

The X-ray crystal structures of **8** and **9** are shown in Figure 2.3. Crystallographic characterization of the complexes reveals the presence of a metal–metal bond. The $\text{Rh}^{\text{I}}\cdots\text{Au}^{\text{I}}$ intermetallic distances of 2.9250(4) Å in **1** and 2.9187(2) Å in **2** contract to 2.6812(4) Å in **8** and 2.6960(3) Å in **9**, consistent with formation of a metal–metal bond. These values are slightly longer than the 2.6549(4) Å Rh–Au distance in $[\text{Rh}^{\text{II}}\text{Au}^{\text{II}}(\text{tfepma})_2(\text{CN}^t\text{Bu})_2\text{Cl}_3](\text{Au}^{\text{I}}\text{Cl}_2)$, the only other example of a σ -bonded rhodium–gold complex.¹⁹ This slight difference may reflect the differences in bite angles between methylene spaced dcpm and methylamine-spaced tfepma, the latter of which incurs substantial sp^2 character at the bridgehead nitrogen.² The typical octahedral coordination environment of metal–metal-bonded d^7 Rh^{II} and the square-planar environment of d^9 Au^{II} centers are readily apparent in the crystal structures of **8** and **9**.

Whereas treatment of the known complex $[\text{Ir}^{\text{I}}\text{Au}^{\text{I}}(\text{dppm})_2(\text{CO})\text{Cl}](\text{PF}_6)^8$ with PhICl_2 leads to a mixture of two products that decompose in a matter of hours to an intractable white solid, treatment of complexes **5–7** with PhICl_2 or Br_2 leads to a clean two-electron oxidation that quantitatively furnishes d^7 – d^9 $\text{Ir}^{\text{II}}\text{Au}^{\text{II}}$ complexes. The complexes $[\text{Ir}^{\text{II}}\text{Au}^{\text{II}}(\text{dcpm})_2(\text{CO})\text{X}_3](\text{PF}_6)$ ($\text{X} = \text{Cl}$ (**12**); Br (**13**)) and $[\text{Ir}^{\text{II}}\text{Au}^{\text{II}}(\text{dppm})_2(\text{CN}^t\text{Bu})_2\text{X}_2](\text{PF}_6)_2$ ($\text{X} = \text{Cl}$ (**14**); Br (**15**)) were prepared in good isolated yields by halogen oxidation of the appropriate $\text{Ir}^{\text{I}}\text{Au}^{\text{I}}$ starting material.



Scheme 2.7. Halogen oxidation of $\text{Ir}^{\text{I}}\text{Au}^{\text{I}}$ complexes to prepare $\text{Ir}^{\text{II}}\text{Au}^{\text{II}}$ complexes. Isolated yields are listed in parentheses.

Scheme 2.7 summarizes the syntheses of these complexes, where either PhICl_2 or Br_2 are used as halogen oxidants. Oxidation of the $\text{Ir}^{\text{I}}\text{Au}^{\text{I}}$ complexes results in a sizable upfield shift of the $^{31}\text{P}\{\text{H}\}$ spectrum, which for the $\text{Ir}^{\text{II}}\text{Au}^{\text{II}}$ complexes consists of two deceptively simple AA'XX' 1:2:1 triplets where only 6 of the 20 lines of the AA'XX' splitting pattern are resolved. The AA'XX' triplets undergo a significant upfield shift upon substituting chloride for bromide in otherwise identical complexes. Resonances at 31.6 and -11.0 ppm in the $^{31}\text{P}\{\text{H}\}$ NMR spectrum of **12** shift to 25.7 and -18.6 ppm in bromide-substituted **13**. Similarly, peaks at 7.7 and -17.6 ppm in the spectrum of **14** shift upfield to 3.1 and -22.2 ppm for bromide complex **15**. This substantial perturbation of both ^{31}P resonances is consistent with halogen ligation of both metal centers. Complexes **12–15** also possess distinct $\text{C}\equiv\text{O}$ or $\text{C}\equiv\text{N}$ stretching frequencies, which appear at 2009 (**12**), 2007 (**13**), 2192 (**14**) and 2189 cm^{-1} (**15**). These IR stretches show minimal dependence on the identity of the halogen ligands.

Structural characterization of **12–15** confirms the assignment of these products as metal–metal-bonded $\text{Ir}^{\text{II}}\text{Au}^{\text{II}}$ complexes. Thermal ellipsoid plots for **12–15** are depicted in Figure 2.4. Clearly evident are the octahedral and square-planar coordination environments of the d^7 Ir^{II} and the d^9 Au^{II} centers, respectively. Furthermore, a significant contraction in the Ir–Au bond distance is observed upon oxidation. For the $[\text{Ir}^{\text{II}}\text{Au}^{\text{II}}(\text{dcpm})_2(\text{CO})\text{X}_3](\text{PF}_6)$ series, the Ir–Au bond lengths of $2.6954(3)\text{ \AA}$ (**12**) and $2.7096(4)\text{ \AA}$ (**13**) are $> 0.2\text{ \AA}$ shorter than those of their precursors **5** and **6**, and are again very similar to the isostructural $\text{Rh}^{\text{II}}\text{Au}^{\text{II}}$ complexes described in the previous section. The metal–metal bond lengths in isocyanide complexes **14** and **15** at $2.6729(4)\text{ \AA}$ and $2.6840(4)\text{ \AA}$, respectively, are slightly shorter than their CO analogs **12** and **13**, but are still consistent with a metal–metal single bond. As with other complexes in this series, all

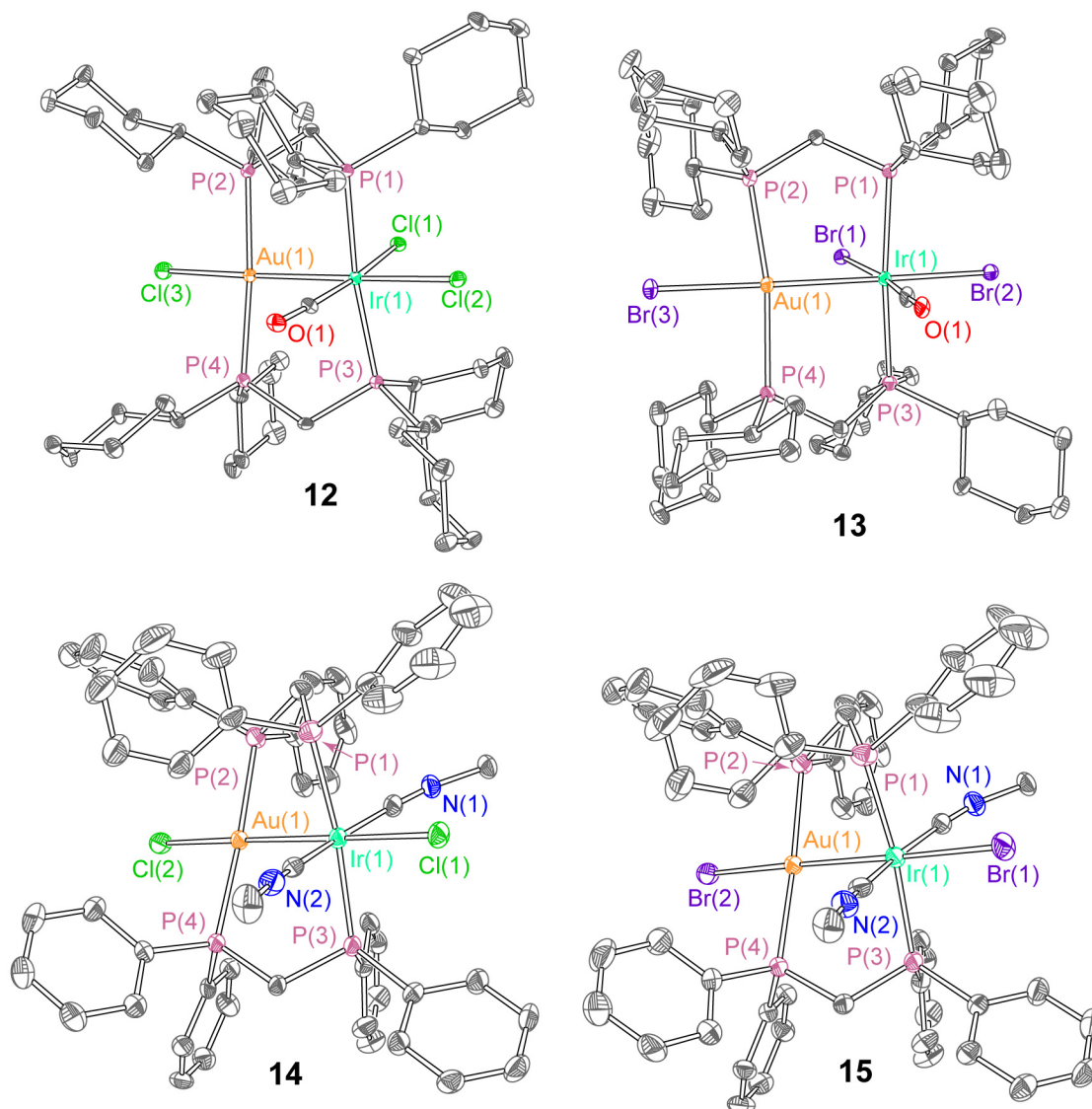


Figure 2.4. X-ray crystal structures of **12–15**. Ellipsoids are shown at the 50% probability level with counterions, solvent molecules, CN^tBu methyl groups, and hydrogen atoms omitted.

counterions, in this case PF₆⁻, are strictly outer-sphere and have no impact on the observed solid-state structures.

2.2.3 Photophysical Properties and Electronic Structure of M^IAu^I (M = Rh, Ir) Complexes

The photophysical properties of d⁸...d¹⁰ complexes,¹⁷ including those of rhodium and iridium with gold,^{12,13,18} have been studied extensively, and will be considered here briefly. The Rh^IAu^I halide complexes **1–4** all show a single, strong absorption feature in the visible region, attributed to a dσ* → pσ transition characteristic of d⁸...d¹⁰ complexes.¹⁷ This absorption

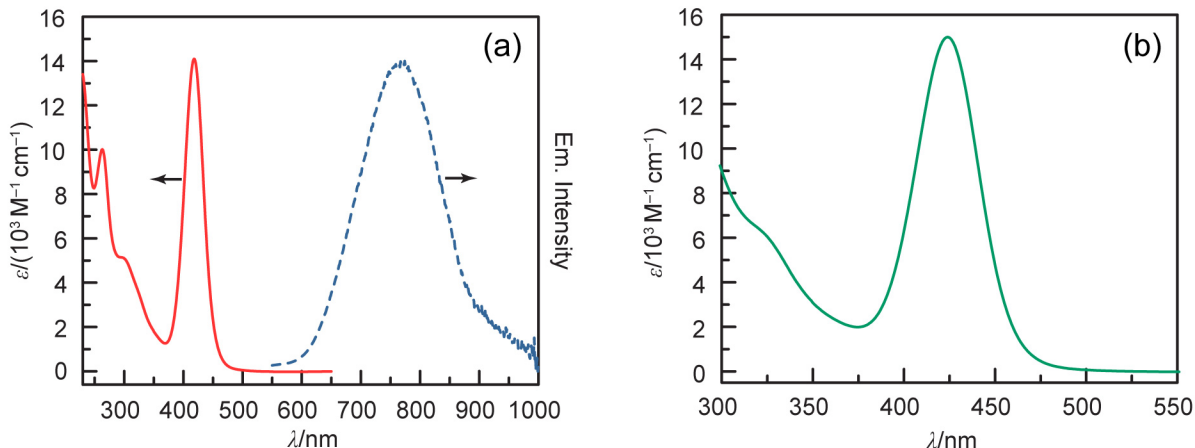


Figure 2.5. (a) Electronic absorption (—, red) and emission (---, blue) spectra of **1**. (b) Electronic absorption spectrum of **3**. Absorption spectra were recorded at 293 K in CH_2Cl_2 , the emission spectrum at 77 K in a frozen glass of 1:1 CH_2Cl_2 /toluene.

maximum is minimally sensitive to substitution of either the bridging diphosphine or the halide, occurring at 418 nm (**1**), 423 nm (**2**), 424 nm (**3**) and 430 nm (**4**). In the case of complexes **1** and **2**, bridged by dcpm, luminescence is observed at 77 K, when the low-energy absorption peak is excited. The emission maxima occur at ~ 770 nm for both **1** and **2**, and the large Stokes shift is suggestive of emission from a triplet excited state. As representative examples, the electronic spectra of **1** and **3** are depicted in Figure 2.5.

Figure 2.6 displays electronic spectra for $\text{Ir}^{\text{I}}\text{Au}^{\text{I}}$ complexes **5** and **7**; which are qualitatively similar to those of **1–4**. The spectra of **6** are nearly identical to **5** and are not shown here. The absorption profiles are again dominated by the intense $d\sigma^* \rightarrow p\sigma$ transition, as has been assigned for other complexes of this type.^{10,11} The transition is fairly metal localized as indicated by a minimal shift in the band maximum from 431 nm ($\epsilon = 17000 \text{ M}^{-1} \text{ cm}^{-1}$) for **5** to 437 nm ($\epsilon = 18000 \text{ M}^{-1} \text{ cm}^{-1}$) for **6**. These maxima are slightly red-shifted compared to those of the isostructural $\text{Rh}^{\text{I}}\text{Au}^{\text{I}}$ congeners **1** and **2**. Complex **7**, $[\text{Ir}^{\text{I}}\text{Au}^{\text{I}}(\text{dppm})_2(\text{CN}^t\text{Bu})_2](\text{PF}_6)_2$, shows an intense low-energy maximum that is even further red-shifted, at 490 nm ($\epsilon = 26000 \text{ M}^{-1} \text{ cm}^{-1}$). Time-dependent DFT calculations on the truncated phosphine model complexes $[\text{Ir}^{\text{I}}\text{Au}^{\text{I}}(\text{dmpm})_2(\text{CO})\text{X}]^+$ ($\text{X} = \text{Cl}$ (**5'**); $\text{X} = \text{Br}$ (**6'**)) and $[\text{Ir}^{\text{I}}\text{Au}^{\text{I}}(\text{dmpm})_2(\text{CNMe})_2]^{2+}$ (**7'**), where dmpm = bis(dimethylphosphino)methane, confirm the $d\sigma^* \rightarrow p\sigma$ nature of the intense low-energy transitions in **5–7**. Moreover, minimal halide contributions to the computed

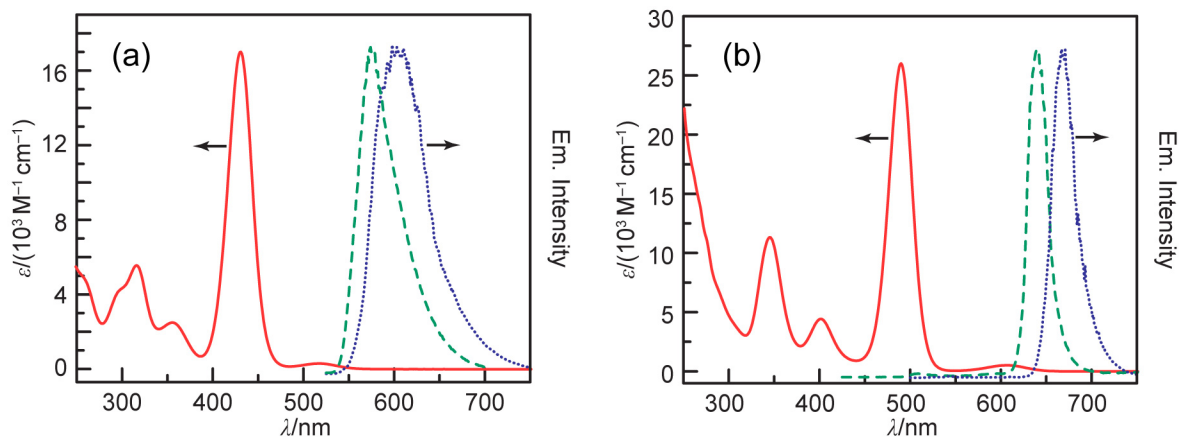


Figure 2.6. Overlaid absorption (—, red), glass emission (---, green), and solid-state emission (···, blue) spectra. The spectra of **5** are shown in (a) and **7** in (b). The absorption spectra were recorded at 293 K in CH₂Cl₂ solution. Emission spectra ($\lambda_{\text{ex}} = 431$ nm (**5**); 490 nm (**7**)) were recorded at 77 K; the frozen glass was of a 1:1 CH₂Cl₂/toluene solvent mixture.

frontier orbitals of **5'** and **6'** are observed. Our results are consistent with recent computational findings on a series of Ir^IAu^I complexes.¹⁴

The $d\sigma^*p\sigma$ excited states of these complexes are emissive at 77 K, both in rigid solvent glass (1:1 CH₂Cl₂/toluene) and in the solid state (Figure 2.6). Emission data for **5–7** are summarized in Table 2.1. The 77 K emission spectra in 1:1 CH₂Cl₂/toluene display maxima of 575 nm (**5**), 582 nm (**6**), and 640 nm (**7**), corresponding to Stokes shifts of 5800 cm⁻¹ (**5**), 5700 cm⁻¹ (**6**), and 4800 cm⁻¹ (**7**), respectively. These emission maxima for **5** and **6** represent substantial hypsochromic shifts relative to the Rh^IAu^I analogs **1** and **2**, in spite of the similar

Table 2.1. Summary of 77 K emission data for complexes **5–7**. Parenthetical numbers represent the relative contributions of the two biexponential fitting parameters.

| Cmpd. | Solution ^a | | Solid State | | |
|----------|---------------------------------|--------------------|---------------------------------|----------------------|----------------------|
| | $\lambda_{\text{em}}/\text{nm}$ | $\tau/\mu\text{s}$ | $\lambda_{\text{em}}/\text{nm}$ | $\tau_1/\mu\text{s}$ | $\tau_2/\mu\text{s}$ |
| 5 | 575 | 9.8 | 605 | 0.81 (0.49) | 6.7 (0.51) |
| 6 | 582 | 9.8 | 620 | 0.55 (0.55) | 4.0 (0.45) |
| 7 | 640 | 6.8 | 670 | 0.67 (0.42) | 3.6 (0.68) |

^a 4×10^{-5} M in 1:1 CH₂Cl₂/toluene

energies of the absorption features. The emission in **5–7** is further red-shifted by ca. 1000 cm^{-1} in the solid state. Emission of samples in solvent glass decay monoexponentially ($\tau = 9.8\ \mu\text{s}$ (**5**), $9.8\ \mu\text{s}$ (**6**), and $6.8\ \mu\text{s}$ (**7**)) whereas the emission decays of solid-state samples are better approximated by a biexponential fit. The lifetimes and excited-state characteristics of **5–7** are in line with previous studies on triplet-state emission of $\text{Ir}^{\text{I}}\text{Au}^{\text{I}}$ heterobimetallic complexes.^{10–13}

2.2.4 Photophysical Properties and Electronic Structure of $\text{M}^{\text{II}}\text{Au}^{\text{II}}$ ($\text{M} = \text{Rh}, \text{Ir}$) Complexes

The electronic spectra of the $\text{M}^{\text{II}}\text{Au}^{\text{II}}$ complexes are markedly different than their $\text{M}^{\text{I}}\text{Au}^{\text{I}}$ precursors, reflecting the change in electronic structure upon oxidizing the $d^8\cdots d^{10}$ core to d^7-d^9 . The spectra of $\text{Rh}^{\text{II}}\text{Au}^{\text{II}}$ complexes **8** and **9** are collected in Figure 2.7. Substitution of the chlorides in **8** with bromides in **9** causes a noticeable bathochromic shift in the three distinct absorption features, indicative of LMCT character in the excited states.

The spectral properties of the $\text{Ir}^{\text{I}}\text{Au}^{\text{I}}$ likewise core change markedly upon oxidation to $\text{Ir}^{\text{II}}\text{Au}^{\text{II}}$. Figure 2.8 displays overlaid absorption spectra for complexes **12–15**, measured at 293 K in CH_2Cl_2 solution. The most intense absorption features occur at significantly higher energies for the $\text{Ir}^{\text{II}}\text{Au}^{\text{II}}$ complexes, as compared to both their $\text{Ir}^{\text{I}}\text{Au}^{\text{I}}$ precursors, and in the case of **12** and **13**, to their $\text{Rh}^{\text{II}}\text{Au}^{\text{II}}$ structural analogs. Nonetheless, the absorption features for **8/9**, with three distinct maxima, are markedly similar to those of **12/13**, notwithstanding the sizeable shift in absorption energies. In contrast, the spectra of dicationic isocyanide-bound complexes **14** and **15**, while demonstrating a similar bathochromic shift upon halide substitution, are dominated by a

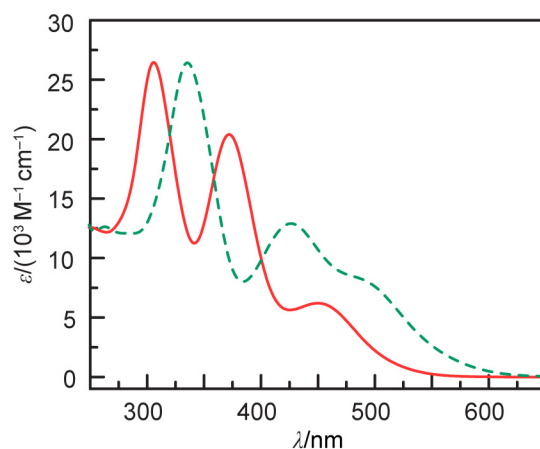


Figure 2.7. Room-temperature UV-vis absorption spectra of **8**-(PF₆) (—, red) and **9**-(PF₆) (---, green) recorded in CH_2Cl_2 solution.

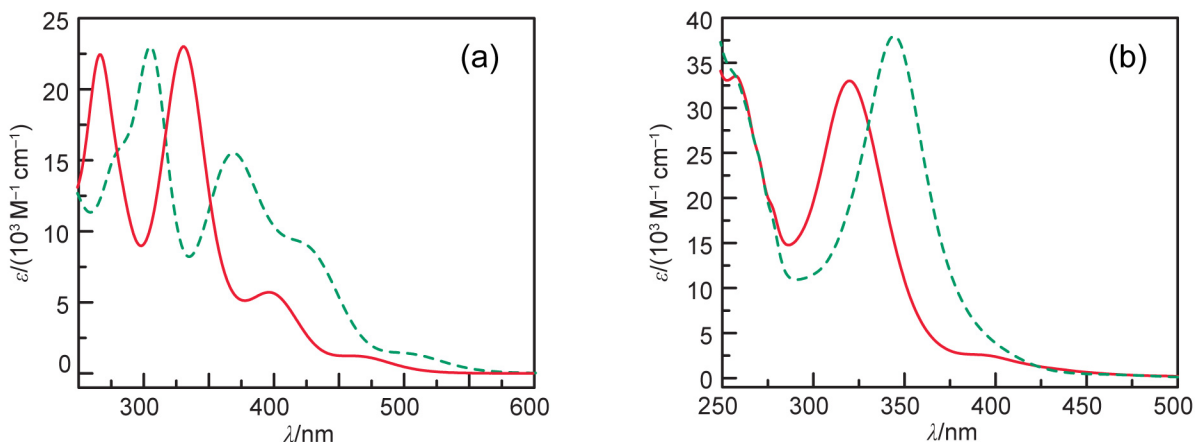


Figure 2.8. Overlaid electronic absorption spectra, measured in CH_2Cl_2 at 293 K. The spectra of **12** (—, red) and **13** (---, green) are shown in (a), **14** (—, red) and **15** (---, green) in (b).

single intense feature. For these $\text{Ir}^{\text{II}}\text{Au}^{\text{II}}$ complexes, the absorption maxima shift bathochromically upon substitution of bromide for chloride in otherwise isostructural complexes. The $\text{M}^{\text{II}}\text{Au}^{\text{II}}$ complexes are non-emissive at room temperature and 77 K, both in solution and in the solid state.

To better understand the electronic structure that gives rise to the aforementioned optical spectra, the $\text{Ir}^{\text{II}}\text{Au}^{\text{II}}$ complexes were examined by DFT calculations. Model complexes were truncated by replacing all phenyl, cyclohexyl, and *tert*-butyl groups with methyl groups, and counterions were omitted ($[\text{Ir}^{\text{II}}\text{Au}^{\text{II}}(\text{dmpm})_2(\text{CO})\text{X}_3]^+$, X = Cl (**12'**); Br (**13'**) and $[\text{Ir}^{\text{II}}\text{Au}^{\text{II}}(\text{dmpm})_2(\text{CNMe})_2\text{X}_2]^{2+}$, X = Cl (**14'**); Br (**15'**)). Frequency calculations ensured that all optimized geometries represent minima on the potential-energy surface. Metal–metal distances in the geometry-optimized models are consistently 0.06–0.10 Å longer than the observed distances from X-ray crystallography, but in general there is good agreement between calculated and observed structures. The orbital manifolds of **12'** and **13'** each contain two distorted σ -bonding orbitals responsible for the net metal–metal bond. The HOMO is primarily derived from d orbitals with nearly equal contribution from the two metal atoms. The HOMO–7 also shows σ -orbital density between the metal atoms; this orbital is polarized towards the iridium and is of mixed d and p parentage, with considerable Au s contribution as well. In **14'** and **15'**, a single cylindrically symmetric σ -bonding orbital of mixed d and p parentage at the HOMO–2 level is responsible for the metal–metal bond. The HOMO in these complexes is a primarily iridium-centered $d\pi^*$ orbital. The LUMO in **12'**–**15'** is the $d\sigma^*$ orbital, which is also σ -antibonding with

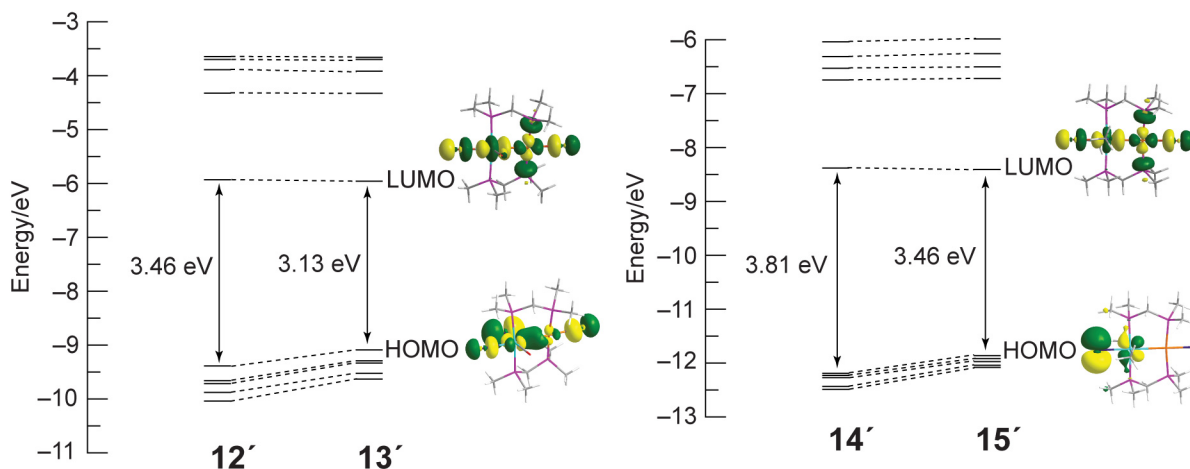


Figure 2.9. Partial orbital energy diagrams for model complexes **12'**, **13'**, **14'**, and **15'**.

respect to the axial halide ligands. Consistent with the sizable bathochromic shift that was observed in the absorption spectrum of the Ir^{II}Au^{II} complexes upon substitution of chloride, the HOMO and other nearby filled orbitals for bromide-substituted **13'** and **15'** are destabilized by ~ 0.3 eV, as shown in the partial energy level diagrams of Figure 2.9. These higher-lying occupied orbitals involve M–X σ^* or π^* interactions, which are responsible for the destabilization that occurs when chloride is replaced with bromide. In contrast, the LUMOs and other nearby virtual orbitals, which feature comparatively small halide contributions, are very minimally perturbed upon halide substitution.

Time-dependent DFT calculations on the geometry optimized models provide insight into the nature of Ir^{II}Au^{II} excited states. Calculations show that the most intense electronic transitions are primarily metal–metal $\sigma \rightarrow \sigma^*$ in character. Figure 2.10 shows the orbitals that are involved in this transition for bromide complexes **13'** and **15'**. The transitions involved in the analogous chloride complexes are essentially identical. The most intense electronic transition in **12'** and **13'** is between the HOMO–7, a distorted σ -bonding orbital of mixed d and p parentage, and the $d\sigma^*$ LUMO. This one-electron promotion comprises 74% (**12'**) and 81% (**13'**) of the excited state of the highest oscillator strength. The calculated transitions at 314 nm for **12'** and 336 nm for **13'** are reasonably close to the observed wavelengths of 331 and 369 nm for **12** and **13**. The transitions in **14'** and **15'** are also best described as $(d,p)\sigma \rightarrow d\sigma^*$ and are reminiscent of the electronic transition calculated for an isostructural Rh^{II}Au^{II} complex.¹⁹ The most intense excitation in **14'** is calculated to occur at 328 nm, whereas that for **15'** at 351 nm. Again, these

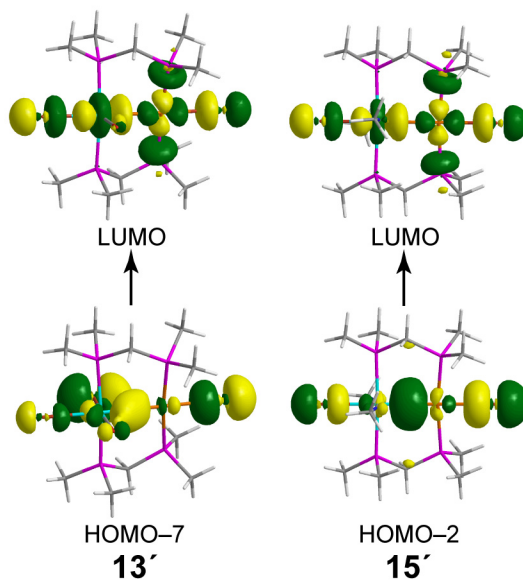
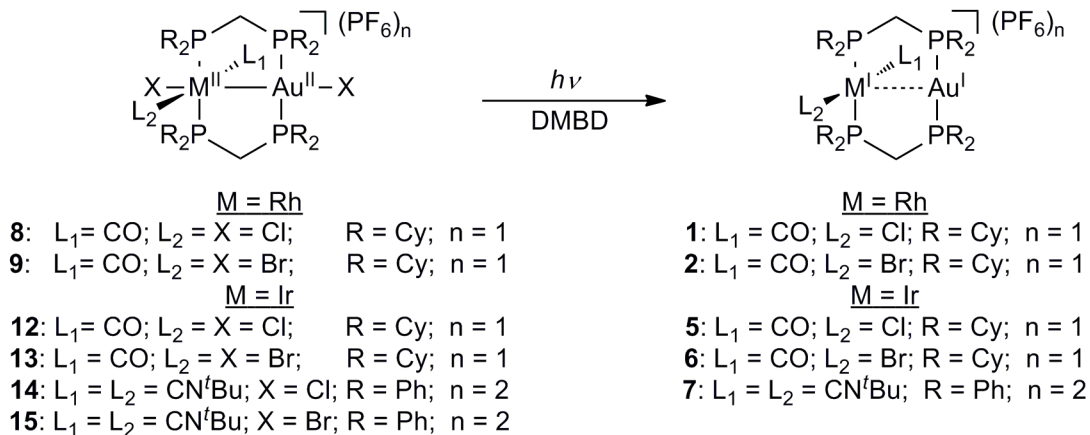


Figure 2.10. Plots for the predominant orbitals involved in the most intense electronic transitions of **13'** and **15'**, with contour levels of 0.04 a.u. Geometry optimizations were initiated from coordinates obtained from the crystal structures of **13** and **15**. Excitation energies ($E = 3.69$ eV for **13'** and $E = 3.53$ eV for **15'**) and oscillator strengths ($f_{336\text{ nm}} = 0.38$ for **13'** and $f_{351\text{ nm}} = 0.53$ for **15'**) were determined from time-dependent DFT calculations.

are reasonably close to the observed transitions of 320 and 344 nm for **14** and **15**. The calculations also demonstrate that there is significant LMCT character in the low-energy transitions of **12'**–**15'**. In all cases, the Ir–Au σ -bonding orbital possesses substantial halide character, whereas the $d\sigma^*$ LUMO has greater metal character as a percentage of the total orbital composition. As a representative example, the HOMO–7 (d,p) σ orbital for **13'** has a 66.8% contribution from bromine atomic orbitals, but the $d\sigma^*$ LUMO is only 18.1% derived from bromine atomic orbitals.

2.2.5 Photochemical Halogen Elimination from $M^{\text{II}}\text{Au}^{\text{II}}$ ($M = \text{Rh}, \text{Ir}$) Complexes

The LMCT character of the excited states of the $M^{\text{II}}\text{Au}^{\text{II}}$ complexes suggests that a halogen-elimination photochemistry may be accessible. Indeed, irradiation of solutions of thermally stable complexes **8**, **9**, and **12**–**15**, in the presence of a suitable halogen trap, leads to photoelimination of halogen and regeneration of the reduced $M^{\text{I}}\text{Au}^{\text{I}}$ complex. This transformation is generalized in Scheme 2.8, with details for each subset of complexes considered below.



Scheme 2.8. Photochemistry of $M^{\text{II}}\text{Au}^{\text{II}}$ complexes.

Photolysis of acetonitrile solutions of complexes **8**-(PF_6) or **9**-(PF_6) with UV light in the presence of 2,3-dimethyl-1,3-butadiene (DMBD) as a halogen trap results in smooth conversion to the corresponding $\text{Rh}^{\text{I}}\text{Au}^{\text{I}}$ complexes **1**-(PF_6) and **2**-(PF_6). Figure 2.11 shows the evolution of the UV-vis spectra during the photoconversion of the $\text{Rh}^{\text{II}}\text{Au}^{\text{II}}$ complexes **8** and **9**. Figure 2.11a depicts the spectral change associated with the conversion of chloride complex **8** ($40 \mu\text{M}$) to **1** when irradiated at 320 nm in the presence of 2.2 M DMBD. Well-anchored isosbestic points are maintained at 400 and 440 nm, suggesting a clean conversion with no steady-state intermediates, and the final spectrum matches an authentic spectrum of **1**. The product-forming quantum yield (Φ_p) for this transformation was found to be 9.4(8)% in 2.2 M DMBD. The quantum efficiency

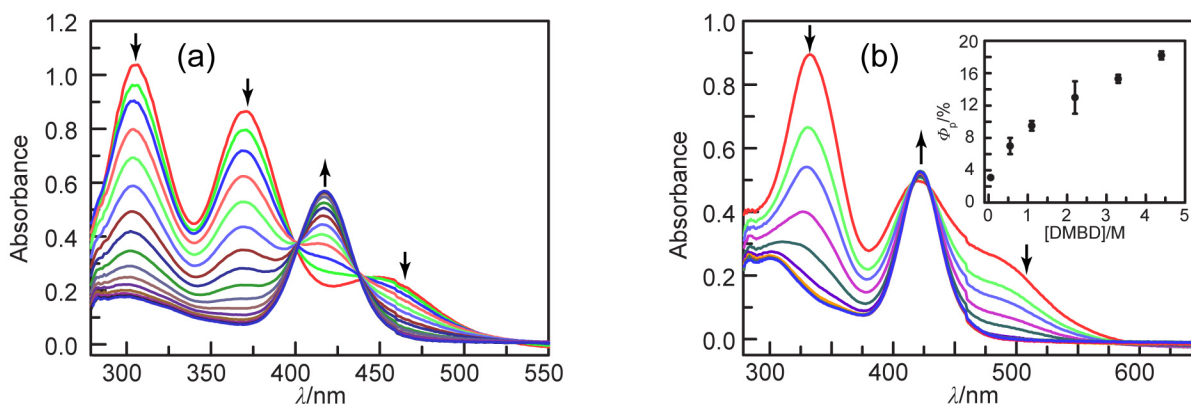


Figure 2.11. Spectral evolution for the photolysis of **8** (a) and **9** (b) with monochromatic 320 nm light in acetonitrile with 2.2 M DMBD at 283 K. In (a) traces shown from 0 to 39 min in 3 min intervals, in (b) spectra are shown from 0 to 8 min; 2 min interval for the first spectrum and 1 min intervals afterward. The inset in (b) shows the dependence of the photochemical quantum yield on the concentration of $[\text{DMBD}]$, with 320 nm excitation.

is minimally responsive to the DMBD concentration in the range of 0.55 to 4.4 M.

Photoconversion of bromide-substituted **9** to its $\text{Rh}^{\text{I}}\text{Au}^{\text{I}}$ precursor **2** is likewise facile with 320 nm excitation, as gleaned from the UV-vis traces in Figure 2.11b. Isosbestic points are maintained at 416 and 429 nm, and again quantitative photoreduction is apparent. For this conversion, the quantum yield, Φ_p , increases significantly as the [DMBD] is increased, as shown in the inset of Figure 2.11b. The photochemical quantum yield, Φ_p , at 0.055 M DMBD is 3.1(2)%, and a value of 18.2(5)% is attained when the DMBD concentration is 4.4 M.

In a similar fashion, irradiation of the $\text{Ir}^{\text{II}}\text{Au}^{\text{II}}$ complexes **12–15** in the presence of the halogen trap, 2,3-dimethyl-1,3-butadiene (DMBD), and with the exclusion of O_2 , results in the prompt conversion of the photoreactants to the corresponding $\text{Ir}^{\text{I}}\text{Au}^{\text{I}}$ complexes. In the cases of monocationic CO complexes **12** and **13**, the photoconversion is once again quantitative, as was observed for the $\text{Rh}^{\text{II}}\text{Au}^{\text{II}}$ complexes discussed just prior. Figure 2.12a depicts the evolution of the absorption spectrum when a CH_2Cl_2 solution of $[\text{Ir}^{\text{II}}\text{Au}^{\text{II}}(\text{dcpm})_2(\text{CO})\text{Cl}_3](\text{PF}_6)$, **12**, at 45 μM , is irradiated with monochromatic 320 nm light in the presence of 2.2 M DMBD. Pristine isosbestic points are maintained at 408, 462 and 506 nm, indicating the absence of photochemical intermediates on a steady-state time scale. The final spectrum indicates quantitative production of the $\text{Ir}^{\text{I}}\text{Au}^{\text{I}}$ complex **5**. Clean formation of **5** is also observed when **12** is irradiated at other wavelengths within the photoreactant's absorption manifold. The dependence of the product-

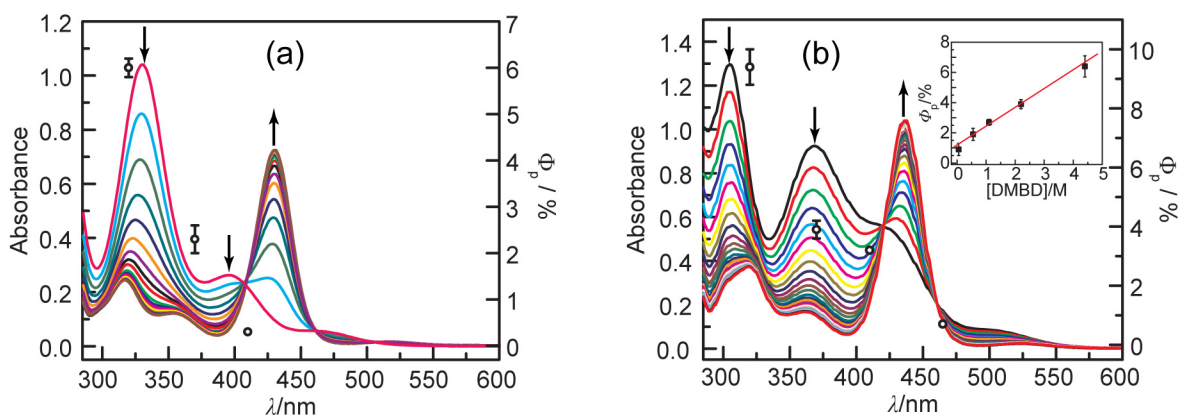


Figure 2.12. (a) Spectral evolution during the photolysis of (a) **12** with monochromatic 320 nm and (b) **13** with monochromatic 370 nm light, in CH_2Cl_2 with 2.2 M DMBD at 283 K. The open circles depict the values for the product appearance quantum yields, Φ_p , measured in 2.2 M DMBD as a function of excitation wavelength. The inset in (b) shows the dependence of the quantum yield on [DMBD], with $\lambda_{\text{ex}} = 370$ nm.

formation quantum yield, Φ_p , on the wavelength of excitation, with 2.2 M DMBD present, is also presented in Figure 2.12a. The observed photochemical quantum yield decreases dramatically as the excitation energy is lowered. At 320 nm excitation, the observed quantum yield is 6.0(2)%, which decreases to 2.3(3)% at 370 nm and 0.30(3)% at 410 nm. At 465 nm excitation, negligible photoconversion is observed. The dependence of the quantum yield on DMBD concentration was investigated for $\lambda_{\text{ex}} = 320$ nm and 370 nm. In both cases, the quantum yields were found to be independent of trap concentration, over the range of 0.055 M to 2.2 M for $\lambda_{\text{ex}} = 320$ nm and 0.055 M to 4.4 M for $\lambda_{\text{ex}} = 370$ nm.

The photochemistry of bromide-substituted **13** largely parallels that observed for **12**. Figure 2.12b shows the changes in the absorption spectrum during the photolysis ($\lambda_{\text{ex}} = 370$ nm) of a CH_2Cl_2 solution containing $[\text{Ir}^{\text{II}}\text{Au}^{\text{II}}(\text{dcpm})_2(\text{CO})\text{Br}_3](\text{PF}_6)$, **13**, at 60 μM and 2.2 M DMBD. Well-anchored isosbestic points are maintained at 421 and 461 nm, and the final absorption spectrum reveals the quantitative formation of $\text{Ir}^{\text{I}}\text{Au}^{\text{I}}$ complex **8**. Clean photochemistry is reproduced at other excitation wavelengths that fall within absorption manifold of **13** (Figure 2.8a). The photochemical quantum yield of **13** decreases substantially as the excitation wavelength is increased, with values of 9.4(6)% at 320 nm, 3.9(3)% at 370 nm, 3.2(1)% at 410 nm, and 0.7(1)% at 465 nm, when the DMBD concentration is held at 2.2 M. In contrast to **12**, however, the photochemical quantum yield of **13** is sensitive to the DMBD concentration. As shown in the inset of Figure 2.12b, the photochemical quantum yield increases linearly over the range of 0.055 to 4.4 M-DMBD.

UV irradiation of $[\text{Ir}^{\text{II}}\text{Au}^{\text{II}}(\text{dppm})_2(\text{CN}^t\text{Bu})_2\text{X}_2](\text{PF}_6)_2$, **14** and **15**, results in the formation of **7**, as judged by the changes to the UV-vis absorption spectra. Figure 2.13 depicts the evolution of the absorption spectra when **14** and **15** are photolyzed at 320 nm in the presence of 2.2 M DMBD. Photoproduct **7** is unstable to photolytic reaction conditions; the absorption bands of **7** bleach over extended irradiation times, and a colorless UV-absorbing species forms. Consistent with these observations, isosbestic points are not maintained over the course of photolysis of either **14** or **15**, and the final absorption spectra indicate low yields of the $\text{Ir}^{\text{I}}\text{Au}^{\text{I}}$ product **7**.

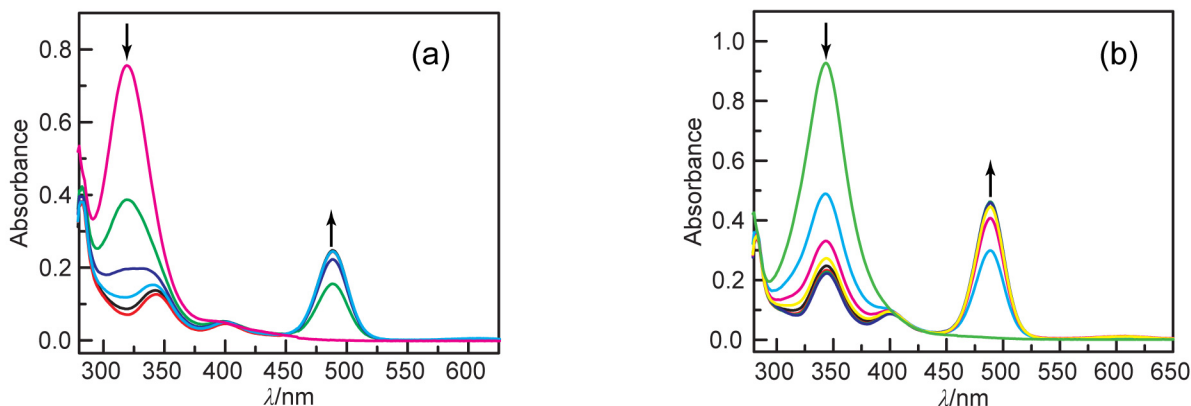
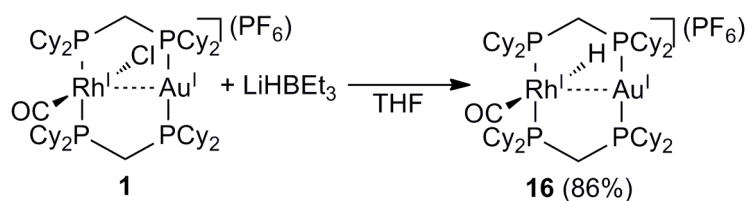


Figure 2.13. Spectral evolution during the photolysis of (a) **14** and (b) **15** with 320 nm light in CH_2Cl_2 with 2.2 M DMBD at 283 K.

2.2.6 Synthesis and Reactivity of a $\text{Rh}^{\text{I}}\text{Au}^{\text{I}}$ Hydride Complex

Having established the halogen-elimination photochemistry of rhodium–gold and iridium–gold complexes, their reactivity with HX (X = Cl, Br) was assessed. It was found that heterobimetallic halide-bound complexes **1**, **2**, **5**, and **6** were all unreactive towards HX, both in their ground and excited states. Undeterred, hydride-bound analogues, which would be likely intermediates in a HX-splitting scheme, were sought. Such complexes would allow further interrogation of chemistry relevant to HX splitting, and ascertain which step(s) in the cycle prove to be problematic. In one instance, conditions were established to synthetically install a hydride on a $\text{M}^{\text{I}}\text{Au}^{\text{I}}$ heterobimetallic complex, and the results of studies on this complex are described in this section.

As depicted in Scheme 2.9, treatment of chloride-bound $\text{Rh}^{\text{I}}\text{Au}^{\text{I}}$ complex **1**-(PF_6) with a stoichiometric amount of $\text{Li}(\text{HBEt}_3)$ (Super-Hydride[®]) yields the hydride complex $[\text{Rh}^{\text{I}}\text{Au}^{\text{I}}(\text{dcpm})_2(\text{CO})\text{H}](\text{PF}_6)$ (**16**), which was isolated in 86% yield. An analogous strategy has been used to prepare a gold(I) hydride,²⁰ though in our case the hydride is bound to rhodium, owing to the strong tendency of gold(I) to remain in a linear, two-coordinate geometry. The most



Scheme 2.9. Synthesis of $\text{Rh}^{\text{I}}\text{Au}^{\text{I}}$ hydride complex **16**. Isolated yield is listed in parentheses.

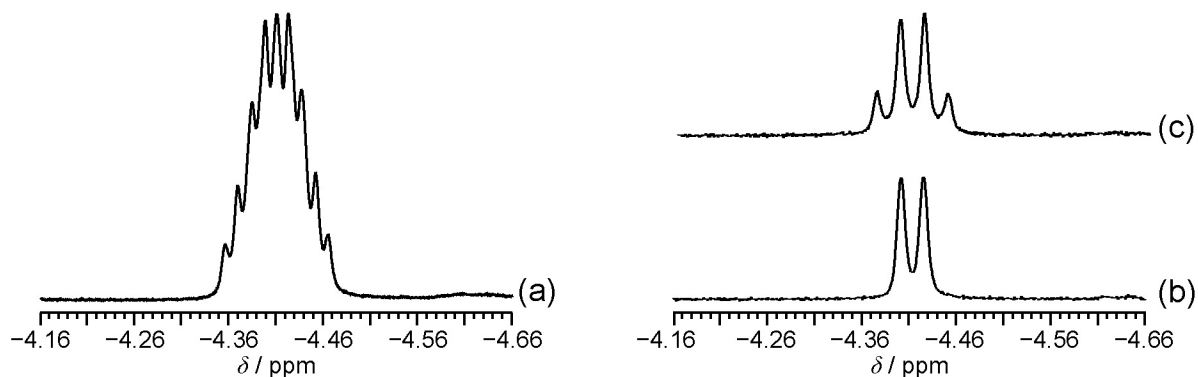


Figure 2.14. Low-frequency region of the ^1H NMR spectrum of **16**. The fully coupled spectrum is shown in (a), (b) shows the fully decoupled $^1\text{H}\{^{31}\text{P}\}$ spectrum, and (c) shows the partially ^{31}P decoupled spectrum.

definitive evidence for the presence of a hydride ligand comes from the ^1H NMR spectrum. Figure 2.14 shows the hydride region of the ^1H NMR spectrum, with different levels of ^{31}P decoupling. The fully coupled spectrum of Figure 2.14a shows a symmetric nine-line multiplet centered at -4.41 ppm for the hydride bound to rhodium. $^1\text{H}\{^{31}\text{P}\}$ NMR spectra provided additional insight into the splitting pattern. A fully decoupled $^1\text{H}\{^{31}\text{P}\}$ spectrum shows a doublet splitting pattern, with $^1J_{\text{Rh-H}} = 12$ Hz (Figure 2.14b). With a lower decoupling power, only short-range ^{31}P coupling is observed, resulting in an apparent quartet splitting pattern indicative of a $^2J_{\text{P-H}}$ coupling constant that is also 12 Hz (Figure 2.14c). The remainder of the nine-line splitting pattern is generated by considering long-range $^3J_{\text{P-H}}$ coupling with a value of 6 Hz. This collection of coupling constants predicts a 1:2:4:6:6:6:4:2:1 nonet, which is precisely what is observed. The optical spectrum of **16** (Figure 2.15) is consistent with the formulation of a $\text{d}^8\cdots\text{d}^{10}$

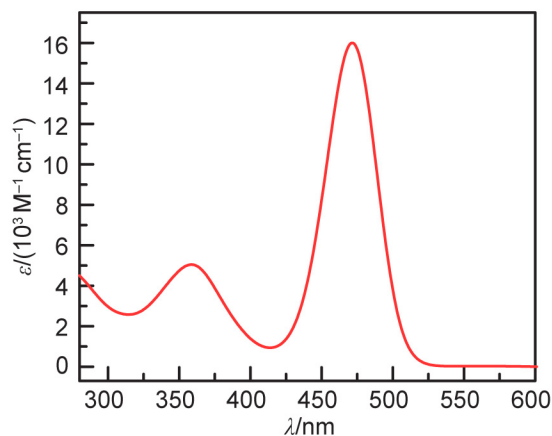


Figure 2.15. Electronic absorption spectrum of **16**, recorded at 293 K in benzene.

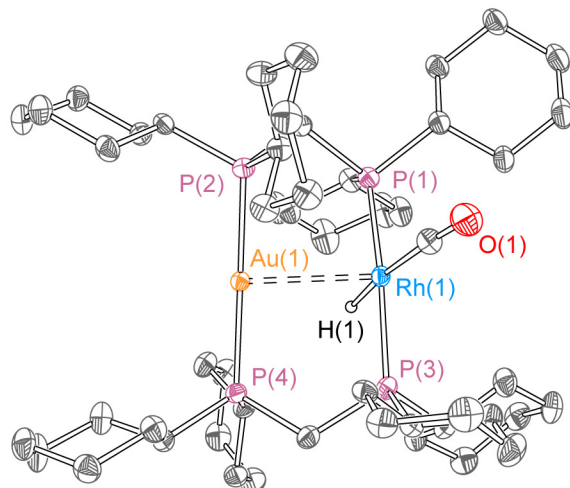
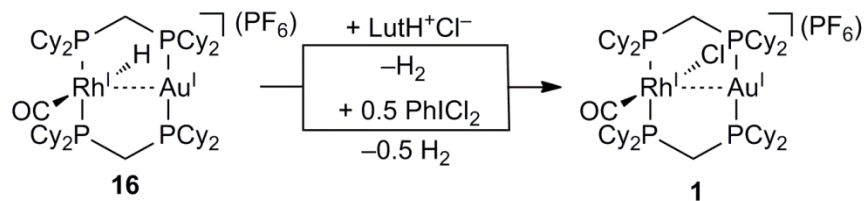


Figure 2.16. X-ray crystal structure of **16**. Ellipsoids are shown at the 50% probability level with counterions, solvent molecules and carbon-bound hydrogen atoms omitted.

electronic structure. The intense $d\sigma^* \rightarrow p\sigma$ transition is clearly evident, and red-shifted relative to that of chloride complex **1**.

Crystallographic characterization verifies the identity of **16**, as shown in the thermal ellipsoid plot in Figure 2.16. The intermetallic distance of 2.8556(5) Å in **16** is only slightly shorter than the one found in **1** and is consistent with a weak metal–metal interaction, as observed in other $d^8 \cdots d^{10}$ complexes.^{5,10,19} The coordination geometries around the metal centers are also reminiscent of these previous examples. Additionally, the *trans* influence of the hydride ligand, which was located in the difference map, is evident when comparing the structure of hydride complex **16** to those of halide complexes **1** and **2**. The Rh–C internuclear distance, which is 1.828(4) Å in **1** and 1.807(3) Å in **2**, lengthens to 1.885(4) Å in **16**.

With the goal of accessing a mixed hydrido-halide $Rh^{II}Au^{II}$ complex, **16** was treated with one equivalent of $PhICl_2$. $^3P\{^1H\}$ NMR of the reaction mixture showed a ca. 1:1 mixture of Rh^IAu^I chloride complex **1** and the $Rh^{II}Au^{II}$ complex **8**, suggesting that hydride **16** is completely consumed with a substoichiometric amount of $PhICl_2$. Indeed, treatment of hydride-bound **16** with 0.5 equivalents of $PhICl_2$ furnishes **1** cleanly. The same reaction, carried out in benzene in the presence of 2,6-lutidine, leads to precipitation of 2,6-lutidinium hydrochloride ($LutH^+Cl^-$) and incomplete consumption of **16**, demonstrating that HCl is produced during the reaction. Hydride complex **16** reacts rapidly with $LutH^+Cl^-$ in solvents such as acetonitrile, where both are



Scheme 2.10. Reactivity of Rh^IAu^I hydride complex **16**.

substantially soluble. The overall reactivity of complex **16** is summarized in Scheme 2.10. Such reactivity is well-documented for late-transition-metal hydride complexes,²¹ and precludes the isolation of mixed hydrido-halide Rh^{II}Au^{II} complexes.

Further support of the reaction pathways depicted in Scheme 2.10 is provided by GC analysis of the headspace gases evolved from each of the reactions. For both reactions, GC measurements demonstrated that H₂ was the exclusive gaseous product. Reaction of **16** with one equivalent of LutH⁺Cl⁻ yielded 0.84 ± 0.08 equivalents of H₂, in good agreement with the expected stoichiometry. The reaction of **16** with 0.5 equivalents of PhICl₂ produced 0.38 ± 0.03 equivalents of H₂ (relative to **16**), again reasonably close to the expected 0.5 equivalents.

2.3 Discussion

In this chapter, the preparation and photochemical reactivity of a series of rhodium–gold and iridium–gold heterobimetallics were the focus. As a first objective, the synthesis of thermally stable M^{II}Au^{II} (M = Rh, Ir) complexes was sought. Our group had previously shown that halogen oxidation of the known complex [Rh^IAu^I(dppm)₂(CN^tBu)₂]²⁺ produced an intractable mixture of products, and only very limited thermal stability of a Rh^{II}Au^{II} core was obtained by oxidation of the modified complex Rh^IAu^I(tfepma)₂(CN^tBu)₂Cl₂. Similarly, halogen oxidation of the known complex [Ir^IAu^I(dppm)₂(CO)Cl]⁺ gave a mixture of products, which rapidly and nonspecifically decomposed.

With these limitations in mind, modifications to these known complexes were sought, in hopes of discovering new classes of complexes with enhanced stabilities. The first success came with the compounds [Ir^IAu^I(dcpm)₂(CO)X](PF₆) (X = Cl (**5**), Br (**6**)), where the more electron-donating dcpm bridging ligand replaces dppm. The compounds are furnished by following methods similar to that employed by Shaw and co-workers. In their preparation of [Ir^IAu^I(dppm)₂(CO)Cl]Cl, they treated [Ir^I(dppm)₂(CO)]Cl with Au^I(PPh₃)Cl in boiling acetone.⁸

In combination with the starting material $[\text{Ir}^{\text{I}}(\text{dcpm})_2(\text{CO})]\text{X}$, we elected to use the Au^{I} starting material $\text{Au}^{\text{I}}(\text{tht})\text{X}$, which is more labile and thus allows for milder reaction conditions to assemble heterobimetallic complexes **5** and **6** in high yields. Considerable π back-donation from the Ir^{I} center is evident from the low energy of the $\text{C}\equiv\text{O}$ stretching vibrations ($\tilde{\nu}_{\text{C}=\text{O}} = 1944$ and 1945 cm^{-1} for **5** and **6** vs. 2143 cm^{-1} for $^{12}\text{C}^{16}\text{O}$).²² A second type of $\text{Ir}^{\text{I}}\text{Au}^{\text{I}}$ complex, $[\text{Ir}^{\text{I}}\text{Au}^{\text{I}}(\text{dppm})_2(\text{CN}^t\text{Bu})_2](\text{PF}_6)_2$ (**7**), was prepared as previously described for isostructural $\text{Rh}^{\text{I}}\text{Au}^{\text{I}}$ complexes.¹⁹ Initial attempts to prepare **3** by treatment of $[\text{Ir}^{\text{I}}\text{Au}^{\text{I}}(\text{dppm})_2(\text{CO})\text{Cl}](\text{PF}_6)$ with two equivalents of CN^tBu resulted in a mixture of starting material, bis- CN^tBu and tris- CN^tBu complexes, but the stepwise route described in Scheme 2.5 gave exclusively the desired product. The $\text{C}\equiv\text{N}$ IR stretch for **3** is observed at 2138 cm^{-1} , which is nearly identical to the value of 2136 cm^{-1} for free CN^tBu .

Halogen oxidation of **5–7** gives complexes **12–15**, the first examples of d^7 – d^9 iridium–gold metal–metal-bonded complexes, which show prolonged thermal stability both in solution and solid-state, particularly for monocationic CO-bound complexes **12** and **13**. Encouraged by these findings, rhodium–gold complexes isostructural to **12** and **13** were sought. The $\text{Rh}^{\text{I}}\text{Au}^{\text{I}}$ precursors **1** and **2** were heretofore unknown, but were conveniently accessed by sequential addition of dcpm , CO gas, and $\text{Au}^{\text{I}}(\text{tht})\text{Cl}$ to a solution of $[\text{Rh}^{\text{I}}(\text{COD})\text{Cl}]_2$. The analogous dppm -bridged complexes **3** and **4** were obtained in the same fashion. Whereas halogen oxidation of these latter complexes gave $\text{Rh}^{\text{II}}\text{Au}^{\text{II}}$ complexes with only minimal stability at low temperatures, oxidation of **1** and **2** with PhICl_2 and Br_2 , respectively, produced thermally robust $\text{Rh}^{\text{II}}\text{Au}^{\text{II}}$ complexes **8** and **9** quantitatively. Thus, simple ligand substitutions in otherwise structurally analogous complexes greatly enhanced the stability of the $\text{Rh}^{\text{II}}\text{Au}^{\text{II}}$ complexes, enabling the in-depth spectroscopic and photochemical studies that were described in this chapter.

Metal–metal bonding in the $\text{M}^{\text{II}}\text{Au}^{\text{II}}$ species is supported by all physical and spectroscopic characterization methods employed in this study. The $\text{C}\equiv\text{O}$ and $\text{C}\equiv\text{N}$ IR stretches shift by ~ 50 – 75 cm^{-1} to higher energy, consistent with diminished π back-donation resulting from oxidation of the bimetallic core. The crystal structures of these complexes show a contraction of the M – Au bond length that is indicative of direct metal–metal σ bonding. The metal–metal bond lengths of **8**, **9**, and **12–15** compare favorably with those of other d^7 – d^9 bimetallic complexes; they are slightly longer than the bond lengths of structurally characterized

Pt^{III}Au^{II} **5** and Pt^{III}Pt^I **6** complexes, and slightly shorter than found in isoelectronic Ir^{II}Ir⁰ complexes.⁷ The electronic structure of the M^{II}Au^{II} core is also dominated by the metal–metal bonding interaction. The most intense absorptions in **8**, **9**, and **12–15** arise from metal–metal $\sigma \rightarrow \sigma^*$ transitions; the transition is Laporte allowed and gives rise to intense UV absorption features. Moreover, the metal–metal bond shows characteristic mixing with the terminal halide ligands, especially from the halide axially coordinated along the metal–metal bond. The pronounced bathochromic shift in the absorption features upon substitution of chloride for bromide is indicative of substantial LMCT character in the excited state. In contrast, the M^IAu^I complexes show intense HOMO \rightarrow LUMO absorptions that are primarily metal-centered. In the reduced bimetallic core, the $d\sigma^*$ orbital is filled and the metal-based transition is of $d\sigma^* \rightarrow p\sigma$ character. As is typical of this type of excited state,^{23–25} a pronounced emission is observed for both solution and solid-state samples of the Ir^IAu^I complexes, and for solutions of Rh^IAu^I complexes **1** and **2**. With axial ligands removed from the metal–metal axis together with a reduced metal core, halide mixing into the metal-based transitions of the M^IAu^I complexes is greatly diminished. As an example, the absorption maximum of chloride-substituted **5** shifts by only $\sim 300\text{ cm}^{-1}$ in bromide-substituted **6**, consistent with a primarily metal-based transition devoid of significant halide character, an observation which is corroborated by time-dependent DFT calculations.

The presence of LMCT character in the lowest energy excited state of the M^{II}Au^{II} complexes gives rise to a significant photochemistry. We have previously noted^{3,5,6} that $d\sigma^*$ excited states with heavily admixed LMCT character can promote the photoreductive elimination of halogen with the concomitant two-electron reduction of the metal core. The photochemistry of the complexes described in this chapter establishes that the same excited-state reactivity is retained for M^{II}Au^{II} cores. Complexes of the type [M^{II}Au^{II}(dcpm)₂(CO)X₃](PF₆) cleanly reduce to [M^IAu^I(dcpm)₂(CO)X](PF₆), when illuminated in the presence of a halogen trap. For the iridium–gold complexes, it was shown that the quantum yields for this photoreaction decrease substantially as the excitation wavelength is increased, as has been observed previously for d⁷–d⁹ bimetallic cores ligated by halide.³ However, the dependence of quantum yields on the trap concentration for chloride-bound **8** and **12** and bromide-bound **9** and **13** is different. The photochemical quantum yields of **8** and **12** are invariant with respect to trap concentration over the range of 55 mM to 4.4 M DMBD, whereas the observed quantum yields for **9** and **13** increase

linearly over the same range of concentrations. This divergent behavior suggests possible mechanistic differences in the photochemical transformations of the two complexes. Also of note are comparisons of the quantum yields for structurally homologous rhodium–gold and iridium–gold complexes. At parity of excitation wavelength and [DMBD], the rhodium–gold complexes **8** and **9** have higher quantum yields than iridium–gold complexes **12** and **13**. For example, with [DMBD] = 2.2 M, and $\lambda_{\text{ex}} = 320$ nm, the photochemical quantum yield for **8** is 9.4(8)%, and is only 6.0(2)% for **12**. For the bromide complexes under these same conditions, the quantum yield for **9** is 13(2)%, and is 9.4(6)% for **13**.

The primary motivation for pursuing heterobimetallic complexes is the desire to strike a balance between efficient halogen elimination, rendered possible by the presence of more oxidizing centers, and hydrogen production, enabled by the group 9 metal. Having established the halogen-elimination photochemistry of rhodium–gold and iridium–gold complexes, forays into HX splitting with these complexes was undertaken. None of the rhodium–gold or iridium–gold halide complexes are reactive towards HCl or HBr, indicating that the presence of the Au^I center substantially attenuates the reactivity of the M^I (M = Rh, Ir) center. A rhodium–gold hydride complex **16** was synthetically prepared, and its reactivity relevant to HX splitting was deciphered. The rhodium–hydrogen bond is hydridic enough to be protonated by the acid 2,6-lutidinium chloride, liberating one equivalent of H₂. In addition, treatment with the chlorine oxidant PhICl₂ results in generation of HCl, which reacts further with remaining hydride. This latter reaction suggests that Rh^{II}Au^{II} hydrido-chloride complex may form but is unstable with respect to HCl loss, confirming the earlier observation that HCl does not oxidatively add to the Rh^IAu^I core.

2.4 Conclusions

In this chapter, it was demonstrated that d⁷–d⁹ metal–metal-bonded M^{II}Au^{II} (M = Rh, Ir) complexes are prepared by halogen oxidation of d⁸–d¹⁰ M^IAu^I complexes. In contrast to thermally unstable tfepma-bridged Rh^{II}Au^{II} complexes, which are prepared by halogen transfer from a tetrachloroaurate, the M^{II}Au^{II} complexes described here are robust and their synthesis is general and straightforward. This suite of metal–metal-bonded complexes includes the first examples of iridium–gold bimetallic complexes with a formal σ bond, as well as the first examples of thermally stable rhodium–gold bonds. The M^{II}Au^{II} complexes add to a growing

library of d^7-d^9 species that photoeliminate X_2 by reductive elimination. Previous to the d^7-d^9 class of compounds, X_2 reductive elimination had not been observed from coordination or organometallic compounds. As demonstrated here for the $M^{II}Au^{II}$ complexes, the electronic structure of d^7-d^9 compounds late in the transition-metal series features significant mixing of halide-centered orbitals into the metal–metal-bonding manifold, particularly for the highest occupied orbitals. As such, the low-energy excited states of these complexes possess substantial halide LMCT character, which is an important determinant for efficient halogen-elimination photochemistry, a key step in photocatalytic HX splitting.

However, what the results here also showed is that this class of group 9/gold heterobimetallic complexes is unable to oxidatively add HX, the first step in a HX-splitting cycle. The reactivity of an isolable $Rh^I Au^I$ hydride complex, described in this chapter, confirms this contention. Although the hydride does react with HX to liberate H_2 , the putative $M^{II}Au^{II}$ hydrido-dihalide species, which would form from HCl addition, was found to be thermodynamically inaccessible. As such, the production of H_2 from HCl, using these complexes as catalysts, is thermodynamically prohibited in the ground state. These results highlight the continuing challenge in developing efficient HX-splitting catalysts, where a delicate balance between efficient H_2 generation and X_2 elimination must be achieved, and that overoptimization can render one of the two half-reactions inaccessible.

2.5 Experimental Methods

2.5.1 General Considerations

All reactions involving air-sensitive materials were executed in a nitrogen-filled glovebox using solvents previously dried by passage through an alumina column under argon, after sparging with argon. The starting materials bis(diphenylphosphino)methane (dppm), bis(dicyclohexylphosphino)methane (dcpm), and $[M^I(COD)Cl]_2$ ($M = Rh, Ir$; COD = 1,5-cyclooctadiene) were obtained from Strem. Bromine, $LiHBEt_3$ (1 M in THF), 2,6-lutidine, 2 M HCl/ Et_2O solution, ammonium hexafluorophosphate and sodium trifluoromethanesulfonate (NaOTf) were obtained from Sigma-Aldrich, whereas CO was purchased from BOC (Grade 2.3). Chlorine was delivered as the iodobenzene adduct $PhICl_2$.²⁶ $[Ir^I(dcpm)_2(CO)]Cl$ and $[Ir^I(dcpm)_2(CO)]Br$ were prepared in an analogous fashion to that described for

$[\text{Ir}^{\text{I}}(\text{dppm})_2(\text{CO})]\text{Cl}$.^{27,28} $[\text{Rh}^{\text{I}}(\text{COD})\text{Br}]_2$ was prepared according to the literature.²⁹ Gold(I) starting materials $\text{Au}^{\text{I}}(\text{tht})\text{Cl}$ (tht = tetrahydrothiophene) and $\text{Au}^{\text{I}}(\text{tht})\text{Br}$ were synthesized as previously described.³⁰ For additions of Br_2 to reactions, a stock solution was prepared using a weighed amount of bromine, and then an appropriate aliquot was added using an autopipet. 2,6-lutidinium hydrochloride (LutH^+Cl^-) was synthesized by reacting 2,6-lutidine with HCl (2 M Et_2O solution).

2.5.2 Physical Methods

NMR spectra were recorded at the MIT Department of Chemistry Instrumentation Facility on a Varian Mercury-300 NMR Spectrometer, operating at 121.5 MHz for ^{31}P acquisition, or a Varian Inova-500 NMR Spectrometer operating at 500 MHz for ^1H acquisition. $^{31}\text{P}\{^1\text{H}\}$ NMR spectra were referenced to an external standard of 85% D_3PO_4 and ^1H spectra were referenced to the residual proteo solvent resonances. UV-vis spectra were recorded at 293 K in CH_2Cl_2 solutions in quartz cuvettes on a Varian Cary 5000 UV-vis-NIR spectrophotometer. Extinction coefficients were determined over a concentration range of $\sim 2\text{--}50\ \mu\text{M}$, for which all compounds obeyed Beer's Law. Steady-state emission spectra were recorded on an automated Photon Technology International (PTI) QM 4 fluorimeter equipped with a 150 W Xe arc lamp and a Hamamatsu R928 photomultiplier tube. Excitation light was excluded with appropriate glass filters. Samples were housed in custom quartz EPR tubes with a ground-glass joint and Teflon plug. Solution samples were prepared in 1:1 CH_2Cl_2 / toluene and freeze-pump-thaw degassed (4 cycles, 1×10^{-5} torr). Solid samples were prepared by evaporation of a CH_2Cl_2 solution under vacuum; the resulting solid film was evacuated to $< 1 \times 10^{-5}$ torr. Spectra were recorded at 77 K by immersion of the sealed EPR tubes into a liquid-nitrogen-filled quartz dewar. Time resolved phosphorescence lifetimes were recorded on a nanosecond laser system described previously.³¹ IR spectra of powdered samples were recorded on a PerkinElmer Spectrum 400 FT-IR/FT-FIR Spectrometer outfitted with a Pike Technologies GladiATR attenuated total reflectance accessory with a monolithic diamond crystal stage and pressure clamp.

2.5.3 Photochemistry

Photochemical reactions were performed using a 1000 W high-pressure Hg/Xe arc lamp (Oriel). The beam was passed through a water-jacketed filter holder containing appropriate long-pass filters, an iris and collimating lens. Samples for all photolysis experiments were prepared in a nitrogen-filled glovebox in quartz cuvettes equipped with a magnetic stir bar and a threaded screw-cap and kept rigorously excluded from light until the start of irradiation. Monochromatic light was generated by combining the output from a long-pass filter with a Hg line filter of the appropriate wavelength. For quantum yield measurements, potassium ferrioxalate was synthesized via a published procedure and used as a chemical actinometer.³² The photon flux was determined from the average of the actinometric measurements collected before and after irradiation of a set of six samples. UV-vis spectra for steady-state photolysis experiments and quantum yield measurements were recorded on a Spectral Instruments 400 diode array spectrophotometer and were blanked to the appropriate solvent.

2.5.4 GC Measurements

Gas quantification measurements were performed on an Agilent 7890A GC System equipped with an Agilent G3432A EPC Thermal Conductivity Detector. The oven temperature was 150 °C, the rate of the N₂ makeup flow set to 3 ml/min, and the N₂ reference flow adjusted to 5 ml/min (N₂ was supplied by Airgas, UHP grade). A calibration curve was generated using gas mixtures of N₂/H₂ with known ratios.

2.5.5 Computational Methods

All calculations were performed using the Gaussian 03 program suite. Where possible, atomic coordinates for geometry optimizations originated from X-ray diffraction data. Cyclohexyl, phenyl, and *tert*-butyl groups were replaced with methyl groups, and counterions were omitted. DFT calculations were carried out using the three hybrid functionals of Becke³³ in conjunction with the correlation functional of Lee, Yang, and Parr (B3LYP).^{34,35} The 6-31G(p,d) basis set was applied to all non-metal atoms,³⁶ and the Stuttgart effective core potential and associated basis set was used for Ir and Au.³⁷ All calculations were spin-restricted on gas-phase molecules, with no imposed symmetry. Time-dependent calculations were initiated from the

optimized geometry using the B3LYP exchange and correlation functionals. Molecular orbitals were imaged in the program GaussView 3.0 with an isodensity of 0.04 applied.

2.5.6 Preparation of $[\text{Rh}^{\text{I}}\text{Au}^{\text{I}}(\text{dcpm})_2(\text{CO})\text{Cl}](\text{PF}_6)$ [1-(PF₆)]

A solution of $[\text{Rh}^{\text{I}}(\text{COD})\text{Cl}]_2$ (186 mg, 0.377 mmol, 1.00 eq) in 10 mL of CH_2Cl_2 was prepared in the glovebox and contained in a 100-mL Schlenk flask. A solution of dcpm (616 mg, 1.51 mmol, 4.00 eq) in 10 mL of CH_2Cl_2 was added dropwise to afford a bright orange solution. The solution was bubbled with CO gas for 10 min (oil bubbler pressure) with no noticeable color change. At this time, $\text{Au}^{\text{I}}(\text{tht})\text{Cl}$ (242 mg, 0.754 mmol, 2.00 eq) dissolved in 10 mL of CH_2Cl_2 was added, resulting in a lighter yellow-orange solution. The solution was stirred at room temperature for 30 min and then filtered through a plug of glass wool in open air. A solution of NH_4PF_6 (307 mg, 1.89 mmol, 5.00 eq) in 20 mL of MeOH was added with stirring. The resulting solution was concentrated by rotary evaporation to < 10 mL, resulting in the formation of a yellow-orange solid which was collected by filtration, washed with 10 mL of MeOH and dried in vacuo. Yield: 831 mg (83.1%). ^1H NMR (500 MHz, CD_2Cl_2) δ /ppm: 2.53–2.64 (m, 2H), 2.45–2.53 (br, m, 4H), 2.21–2.30 (m, 4H), 2.14–2.20 (br, d, 2H), 1.13–2.12 (br, m, 80H). $^{31}\text{P}\{^1\text{H}\}$ NMR (121.5 MHz, CD_2Cl_2) δ /ppm: 52.9 (m, 2P), 34.8 (dm, $^1J_{\text{Rh-P}} = 114$ Hz, 2P), -144.1 (sept., $^1J_{\text{F-P}} = 711$ Hz, 1P). UV-vis (CH_2Cl_2): λ /nm ($\epsilon/(\text{M}^{-1} \text{cm}^{-1})$) 263 (9700), 291 (sh) (5100), 418 (14000). IR (solid): $\tilde{\nu}_{\text{C=O}} = 1953 \text{ cm}^{-1}$. Anal. Calcd. for $\text{C}_{51}\text{H}_{92}\text{AuClF}_6\text{RhOP}_5$: C, 46.21; H, 7.00. Found: C, 46.28; H, 6.83.

2.5.7 Preparation of $[\text{Rh}^{\text{I}}\text{Au}^{\text{I}}(\text{dcpm})_2(\text{CO})\text{Br}](\text{PF}_6)$ [2-(PF₆)]

$[\text{Rh}^{\text{I}}(\text{COD})\text{Br}]_2$ (212 mg, 0.365 mmol, 1.00 eq) was dissolved in 10 mL of CH_2Cl_2 . With stirring, dcpm (596 mg, 1.46 mmol, 4.00 eq) in 10 mL of CH_2Cl_2 was added dropwise to give a bright orange solution. CO was bubbled through the solution for 15 min with no color change. Addition of $\text{Au}^{\text{I}}(\text{tht})\text{Br}$ (266 mg, 0.730 mmol, 2.00 eq) dissolved in 10 mL CH_2Cl_2 effected a color change to yellow. The solution was stirred under a CO atmosphere for 60 min and afterwards filtered through a plug of glass wool. A solution of NH_4PF_6 (300 mg, 1.82 mmol, 5.00 eq) in 20 mL of MeOH was added, stirred for 5 min and concentrated to < 10 mL by rotary evaporation. A light orange solid was collected by filtration, washed with MeOH and dried in vacuo. Yield: 832 mg (83.2%). ^1H NMR (500 MHz, CD_2Cl_2) δ /ppm:

2.55–2.73 (m, 6H), 2.12–2.36 (m, 6H), 1.10–2.12 (m, 80H). $^{31}\text{P}\{^1\text{H}\}$ NMR (121.5 MHz, CD_2Cl_2) δ/ppm : 52.5 (m, 2P), 33.7 (dm, $^1J_{\text{Rh-P}} = 113$ Hz, 2P), -144.1 (sept., $^1J_{\text{F-P}} = 711$ Hz, 1P). UV-vis (CH_2Cl_2): λ/nm ($\epsilon/(\text{M}^{-1} \text{cm}^{-1})$) 263 (9300), 305 (6000), 423 (14000). IR (solid): $\tilde{\nu}_{\text{C=O}} = 1955$ cm^{-1} . Anal. Calcd. for $\text{C}_{51}\text{H}_{92}\text{AuBrF}_6\text{RhOP}_5$: C, 44.71; H, 6.77; Found: C, 44.56; H, 6.65.

2.5.8 Preparation of $[\text{Rh}^{\text{I}}\text{Au}^{\text{I}}(\text{dppm})_2(\text{CO})\text{Cl}](\text{PF}_6)$ [3-(PF_6)]

In a Schlenk flask equipped with a stir bar, $[\text{Rh}^{\text{I}}(\text{COD})\text{Cl}]_2$ (186 mg, 0.377 mmol, 1.00 eq) was dissolved in 10 mL of CH_2Cl_2 with stirring giving a dark yellow solution. A sample of dppm (580 mg, 1.51 mmol, 4.00 eq) was dissolved in 10 mL of CH_2Cl_2 and added dropwise, causing a color change to orange. After stirring the solution at RT for 10 min, CO was bubbled through it for 15 min. $\text{Au}^{\text{I}}(\text{tht})\text{Cl}$ (242 mg, 0.754 mmol, 2.00 eq) dissolved in 10 mL CH_2Cl_2 was added and the solution stirred for 30 min. Addition of NH_4PF_6 (308 mg, 1.89 mmol, 5.00 eq) that was dissolved in 20 mL of MeOH gave an orange solution. Upon concentrating the solution to < 10 mL by rotary evaporation, an orange solid precipitated. The solid was collected by filtration, washed with methanol and dried in vacuo. Yield: 779 mg (80.9%). ^1H NMR (500 MHz, CD_3CN) δ/ppm : 7.89–7.91 (m, 4H), 7.79–7.86 (m, 4H), 7.64–7.71 (m, 4H), 7.39–7.60 (m, 22H), 7.21–7.27 (m, 2H), 7.05–7.12 (m, 4H), 4.15–4.30 (m, 4H). $^{31}\text{P}\{^1\text{H}\}$ NMR (121.5 MHz, CD_3CN) δ/ppm : 36.9 (m, 2P), 28.3 (dm, $^1J_{\text{Rh-P}} = 120$ Hz, 2P), -143.4 (sept., $^1J_{\text{F-P}} = 706$ Hz, 1P). UV-vis (CH_2Cl_2): λ/nm ($\epsilon/(\text{M}^{-1} \text{cm}^{-1})$) 424 (15000). IR (solid): $\tilde{\nu}_{\text{C=O}} = 1966$ cm^{-1} . Anal. Calcd. for $\text{C}_{51}\text{H}_{44}\text{AuClF}_6\text{RhOP}_5$: C, 47.96; H, 3.47; Found: C, 47.58; H, 3.45.

2.5.9 Preparation of $[\text{Rh}^{\text{I}}\text{Au}^{\text{I}}(\text{dppm})_2(\text{CO})\text{Br}](\text{CF}_3\text{SO}_3)$ [4-(OTf)]

In a Schlenk flask equipped with a stir bar, $[\text{Rh}^{\text{I}}(\text{COD})\text{Br}]_2$ (146 mg, 0.250 mmol, 1.00 eq) was dissolved in 6 mL of CH_2Cl_2 with stirring to afford a dark yellow solution. To this solution was added dppm (384 mg, 1 mmol, 4.00 eq) dissolved in 5 mL of CH_2Cl_2 , resulting in a color change to orange. After stirring the solution at RT for 10 min, CO was bubbled through it for 15 min. $\text{Au}^{\text{I}}(\text{tht})\text{Br}$ (183 mg, 0.500 mmol, 2.00 eq) dissolved in 5 mL CH_2Cl_2 was added and the solution stirred for 30 min. Addition of NaOTf (430 mg, 2.50 mmol, 10.0 eq) that was dissolved in 10 mL MeOH produced an orange solution. Concentrating the solution to < 10 mL by rotary evaporation caused an orange solid to

precipitate. The solid was collected by filtration, washed with methanol and dried in vacuo. Yield: 490 mg (73.9%). ^1H NMR (500 MHz, CD_2Cl_2) δ/ppm : 7.80–7.91 (m, 4H), 7.65–7.75 (m, 4H), 7.36–7.63 (m, 22H), 7.25–7.34 (m, 4H), 7.18–7.24 (m, 2H), 7.00–7.07 (m, 4H), 4.35–4.48 (m, 2H), 4.02–4.12 (m, 2H). $^{31}\text{P}\{^1\text{H}\}$ NMR (121.5 MHz, CD_2Cl_2) δ/ppm : 32.4 (m, 2P), 24.2 (dm, $^1J_{\text{Rh-P}} = 119$ Hz, 2P). UV-vis (CH_2Cl_2): λ/nm ($\epsilon/(\text{M}^{-1} \text{cm}^{-1})$) 430 (12000). IR (solid): $\tilde{\nu}_{\text{C=O}} = 1966 \text{ cm}^{-1}$. Anal. Calcd. for $\text{C}_{52}\text{H}_{44}\text{AuBrF}_3\text{RhO}_4\text{P}_4\text{S}$: C, 47.11; H, 3.35; Found: C, 46.86; H, 3.29.

2.5.10 Preparation of $[\text{Ir}^{\text{I}}\text{Au}^{\text{I}}(\text{dcpm})_2(\text{CO})\text{Cl}](\text{PF}_6)$ (5)

To a solution of $[\text{Ir}^{\text{I}}(\text{dcpm})_2(\text{CO})]\text{Cl}$ (1.00 g, 0.932 mmol, 1.00 eq) in 6 mL of CH_2Cl_2 was added a solution of $\text{Au}^{\text{I}}(\text{tht})\text{Cl}$ (299 mg, 0.932 mmol, 1.00 eq) in 8 mL of CH_2Cl_2 . The orange solution was stirred at room temperature for 1 h, at which time a solution of NH_4PF_6 (228 mg, 1.40 mmol, 1.50 eq) in 15 mL of methanol was added. The solution was concentrated to < 10 mL via rotary evaporation, during which time an orange solid precipitated. The solid was collected by filtration, washed with 5 mL of methanol and dried in vacuo. Yield: 1.04 g (78.8%). ^1H NMR (500 MHz, CD_2Cl_2) δ/ppm : 2.50–2.69 (br, m, 6H), 2.33 (br, d, 2H), 2.17–2.29 (br, m, 4H), 1.14–2.09 (br, m, 80H). $^{31}\text{P}\{^1\text{H}\}$ NMR (121.5 MHz, CD_2Cl_2) δ/ppm : 51.0 (m, 2P), 25.3 (m, 2P), -144.1 (sept., $^1J_{\text{F-P}} = 711$ Hz, 1P). UV-vis (CH_2Cl_2): λ/nm ($\epsilon/(\text{M}^{-1} \text{cm}^{-1})$) 300 (sh) (4300), 316 (5700), 355 (2500), 431 (17000), 517 (300). IR (solid): $\tilde{\nu}_{\text{C=O}} = 1944 \text{ cm}^{-1}$. Anal. Calcd. for $\text{C}_{51}\text{H}_{92}\text{AuClF}_6\text{IrOP}_5$: C, 43.30; H, 6.55. Found: C, 43.37; H, 6.51.

2.5.11 Preparation of $[\text{Ir}^{\text{I}}\text{Au}^{\text{I}}(\text{dcpm})_2(\text{CO})\text{Br}](\text{PF}_6)$ (6)

A solution of $\text{Au}^{\text{I}}(\text{tht})\text{Br}$ (327 mg, 0.895 mmol, 1.00 eq) in 8 mL of CH_2Cl_2 was added to a solution of $[\text{Ir}^{\text{I}}(\text{dcpm})_2(\text{CO})]\text{Br}$ (1.00 g, 0.895 mmol, 1.00 eq) in 6 mL of CH_2Cl_2 . The resulting dark orange solution was stirred for 90 min at room temperature and then filtered through a plug of glass wool. A solution of NH_4PF_6 (220 mg, 1.35 mmol, 1.51 eq) in 15 mL of methanol was added, and the resulting bright orange solution was stirred for 1 h. After concentrating to < 10 mL by rotary evaporation, an orange solid formed, which was collected by filtration, washed with 10 mL of methanol and dried in vacuo. Yield: 1.14 g (87.0%). ^1H NMR (500 MHz, CD_2Cl_2) δ/ppm : 2.50–2.82 (br, m, 6H), 2.15–2.40 (br, m, 6H), 1.00–2.10 (br, m, 80H). $^{31}\text{P}\{^1\text{H}\}$ NMR (121.5 MHz, CD_2Cl_2) δ/ppm : 50.4 (m, 2P), 23.2 (m, 2P), -144.2 (sept., $^1J_{\text{F-P}} = 711$ Hz, 1P).

UV-vis (CH₂Cl₂): λ/nm ($\epsilon/(\text{M}^{-1} \text{cm}^{-1})$) 307 (sh) (5800), 319 (6400), 360 (2600), 437 (18000), 526 (320). IR (solid): $\tilde{\nu}_{\text{C}=\text{O}} = 1945 \text{ cm}^{-1}$. Anal. Calcd. for C₅₁H₉₂AuBrF₆IrOP₅: C, 41.98; H, 6.35. Found: C, 41.90; H, 6.36.

2.5.12 Preparation of [Ir^IAu^I(dppm)₂(CN^tBu)₂](PF₆)₂ (7)

To a solution of [Ir(COD)Cl]₂ (149 mg, 0.222 mmol, 1.00 eq) in 5 mL of CH₂Cl₂ was added a solution of dppm (341 mg, 0.887 mmol, 4.00 eq) in 2 mL of CH₂Cl₂, giving a yellow solution. A solution of CN^tBu (73.7 mg, 0.887 mmol, 4.00 eq) was added immediately, initially causing a change to a lighter yellow color, which darkened to yellow-orange as the solution was stirred for 20 min. At this time, a solution of Au(tht)Cl (142 mg, 0.443 mmol, 2.00 eq) in 2 mL of CH₂Cl₂ was added, giving a deep red solution which was stirred for 45 min. Addition of a solution of NH₄PF₆ (180 mg, 1.10 mmol, 4.95 eq) in 20 mL of MeOH prompted an instantaneous color change to dark green. The solution was concentrated to 5 mL, and the resulting green solid was filtered and washed with 5 mL of methanol. The crude solid was dissolved in 2 mL of CH₂Cl₂ and recrystallized by layering with 1 mL of methanol followed by 17 mL of diethyl ether. After several hours, green microcrystals formed, which were separated from the supernatant by decantation and dried in vacuo. Yield: 382 mg (53.4%). ¹H NMR (500 MHz, CD₂Cl₂) δ/ppm : 7.84–7.90 (m, 8H), 7.68–7.74 (m, 8H), 7.52–7.63 (m, 12H), 7.44–7.50 (m, 4H), 7.38–7.43 (m, 8H), 4.10 (br, pseudoquintet, 4H), 0.63 (s, 18H). ³¹P{¹H} NMR (202.5 MHz, CD₂Cl₂) δ/ppm : 30.0 (m, 2P), 10.4 (m, 2P), -143.9 (sept., ¹J_{F-P} = 712 Hz, 2P). UV-vis (CH₂Cl₂): λ/nm ($\epsilon/(\text{M}^{-1} \text{cm}^{-1})$) 345 (11000), 402 (4400), 490 (26000), 606 (520). IR (solid): $\tilde{\nu}_{\text{C}=\text{N}} = 2138 \text{ cm}^{-1}$. Anal. Calcd. for C₆₀H₆₂AuF₁₂IrN₂P₆: C, 44.65; H, 3.87; N, 1.74. Found: C, 44.39; H, 3.82; N, 1.59.

2.5.13 Preparation of [Rh^{II}Au^{II}(dcpm)₂(CO)Cl₃](PF₆) [8-(PF₆)]

A sample of **1**-(PF₆) (100 mg, 0.0750 mmol, 1.00 eq) was dissolved in 10 mL of CH₂Cl₂ and frozen in the coldwell of the glovebox. Upon thawing a cold solution of PhICl₂ (22.0 mg 0.0800 mmol, 1.05 eq), dissolved in 10 mL of CH₂Cl₂, was added dropwise, giving a dark red solution that was stirred at RT for 30 min. Addition of 18 mL of pentane afforded a red solid which was isolated by decantation and washed with 10 mL of pentane twice. Yield: 102 mg (96.9%). ¹H NMR (500 MHz, CD₂Cl₂) δ/ppm : 3.40–3.55 (m, 2H), 3.19–3.32 (m, 2H), 2.83–3.02

(m, 4H), 2.68–2.80 (m, 2H), 2.49–2.63 (m, 4H), 1.20–2.40 (m, 78H). $^{31}\text{P}\{^1\text{H}\}$ NMR (121.5 MHz, CD_2Cl_2) δ/ppm : 37.8 (t, 2P), 20.2 (dt, $^1J_{\text{Rh-P}} = 74$ Hz, 2P), -144.1 (sept., $^1J_{\text{F-P}} = 711$ Hz, 1P). UV-vis (CH_2Cl_2): λ/nm ($\epsilon/(\text{M}^{-1} \text{cm}^{-1})$) 306 (26000), 372 (20000), 450 (6200). IR (solid): $\tilde{\nu}_{\text{C=O}} = 2030 \text{ cm}^{-1}$. Anal. Calcd. for $\text{C}_{51}\text{H}_{92}\text{AuCl}_3\text{F}_6\text{RhOP}_5$: C, 43.87; H, 6.64; Found: C, 44.51; H, 6.60.

2.5.14 Preparation of $[\text{Rh}^{\text{II}}\text{Au}^{\text{II}}(\text{dcpm})_2(\text{CO})\text{Br}_3](\text{PF}_6)$ [9-(PF₆)]

In 4 mL of CH_3CN **2**-(PF₆) (100 mg, 0.073 mmol, 1.00 eq) was dissolved. Br_2 (12.2 mg, 0.0763 mmol, 1.05 eq) that was dissolved in 157 μL of CH_3CN was added and the solution stirred at RT for 15 min during which time a solid started to precipitate. The solution was concentrated at the rotary evaporator and the resulting dark solid dried in vacuo. The solid was redissolved in 2 mL of CH_2Cl_2 and precipitated with Et_2O . The solvent was removed via pipet and the red solid dried in vacuo. Yield: 103 mg (92.2%). ^1H NMR (500 MHz, CD_2Cl_2) δ/ppm : 3.65–3.76 (m, 2H), 3.41–3.54 (m, 2H), 3.13–3.27 (m, 2H), 2.87–3.00 (m, 2H), 2.70–2.87 (m, 2H), 2.52–2.71 (m, 4H), 2.37 (br, d, 2H), 2.28 (br, d, 2H), 1.20–2.17 (m, 74H). $^{31}\text{P}\{^1\text{H}\}$ NMR (121.5 MHz, CD_2Cl_2) δ/ppm : 32.8 (t, 2P), 14.3 (dt, $^1J_{\text{Rh-P}} = 74$ Hz, 2P), -144.1 (sept., $^1J_{\text{F-P}} = 711$ Hz, 1P). UV-vis (CH_2Cl_2): λ/nm ($\epsilon/(\text{M}^{-1} \text{cm}^{-1})$) 335 (26000), 426 (13000). IR (solid): $\tilde{\nu}_{\text{C=O}} = 2028 \text{ cm}^{-1}$. Anal. Calcd. for $\text{C}_{51}\text{H}_{92}\text{AuBr}_3\text{F}_6\text{RhOP}_5$: C, 40.04; H, 6.06; Found: C, 40.17; H, 6.06.

2.5.15 Preparation of $[\text{Rh}^{\text{II}}\text{Au}^{\text{II}}(\text{dppm})_2(\text{CO})\text{Cl}_3](\text{PF}_6)$ [10-(PF₆)]

PhICl_2 (11.3 mg, 0.0411 mmol, 1.05 eq) was dissolved in 1 mL of CH_2Cl_2 and frozen in the coldwell of the glovebox. **3**-(PF₆) (50.0 mg, 0.0392 mmol, 1.00 eq) was dissolved in 5 mL of CH_2Cl_2 and likewise frozen. Upon thawing the solution of PhICl_2 was added dropwise, effecting a color change from yellow to deep red. The resulting solution was frozen in the coldwell again to avoid decomposition of the product which is stable below -20 °C but decomposes rapidly at RT. The instability of the product precluded determination of the isolated yield and further characterization, though NMR indicates a clean conversion. $^{31}\text{P}\{^1\text{H}\}$ NMR (121.5 MHz, CD_2Cl_2) δ/ppm : 27.7 (t, 2P), 11.3 (dt, $^1J_{\text{Rh-P}} = 78$ Hz, 2P), -143.4 (sept., $^1J_{\text{F-P}} = 708$ Hz, 1P).

2.5.16 Preparation of $[\text{Rh}^{\text{II}}\text{Au}^{\text{II}}(\text{dppm})_2(\text{CO})\text{Br}_3](\text{CF}_3\text{SO}_3)$ [11-(OTf)]

4-(OTf) (25.0 mg, 0.0188 mmol, 1.00 eq) was dissolved in 5 mL of CH_2Cl_2 and cooled to $-78\text{ }^\circ\text{C}$ with a dry ice/acetone bath. Br_2 (3.15 mg, 0.0197 mmol, 1.05 eq) in 0.167 mL of CH_2Cl_2 was added to the cold solution of **4** resulting in an immediate color change to dark red. The solution was kept in the cold to avoid decomposition of the product. Due to the thermal instability of the product it was not possible to determine the yield or perform further characterization. $^{31}\text{P}\{^1\text{H}\}$ NMR (121.5 MHz, CD_2Cl_2) δ/ppm : 20.5 (t, 2P), 3.4 (dt, $^1J_{\text{Rh-P}} = 79\text{ Hz}$, 2P).

2.5.17 Preparation of $[\text{Ir}^{\text{II}}\text{Au}^{\text{II}}(\text{dcpm})_2(\text{CO})\text{Cl}_3](\text{PF}_6)$ (12)

A solution of **5** (100 mg, 0.0707 mmol, 1.00 eq) in 1.5 mL of CH_2Cl_2 and a solution of PhICl_2 (23.3 mg, 0.0848 mmol, 1.20 eq) in 0.7 mL of CH_2Cl_2 were both chilled with liquid N_2 in the glovebox cold well. Once frozen, the two samples were removed, and upon melting the PhICl_2 solution was added dropwise to the solution of **5**. The color immediately faded to a lighter orange, and the solution was stirred at room temperature for 3 h. Dropwise addition of 15 mL of pentane to the stirred solution yielded a yellow-orange solid, which was separated from the supernatant by decantation and dried in vacuo. Yield: 104 mg (99.0%). ^1H NMR (500 MHz, CD_2Cl_2) δ/ppm : 3.62–3.73 (m, 2H), 3.08–3.22 (br, m, 4H), 2.81–2.90 (br, m, 2H), 2.68–2.77 (br, m, 2H), 2.54–2.64 (br, m, 2H), 2.44–2.51 (br, m, 2H), 2.08–2.32 (br, m, 6H), 1.20–2.05 (br, m, 72H). $^{31}\text{P}\{^1\text{H}\}$ NMR (121.5 MHz, CD_2Cl_2) δ/ppm : 31.6 (t, 2P), -11.0 (t, 2P), -144.1 (sept., $^1J_{\text{P-F}} = 714\text{ Hz}$, 1P). UV-vis (CH_2Cl_2): λ/nm ($\epsilon/(\text{M}^{-1}\text{ cm}^{-1})$) 266 (22000), 331 (23000), 396 (5800) 455 (sh) (1200). IR (solid): $\bar{\nu}_{\text{C=O}} = 2009\text{ cm}^{-1}$. Anal. Calcd. for $\text{C}_{51}\text{H}_{92}\text{AuCl}_3\text{F}_6\text{IrOP}_5$: C, 41.23; H, 6.24. Found: C, 40.96; H, 6.15.

2.5.18 Preparation of $[\text{Ir}^{\text{II}}\text{Au}^{\text{II}}(\text{dcpm})_2(\text{CO})\text{Br}_3](\text{PF}_6)$ (13)

A sample of **6** (100 mg, 0.0685 mmol, 1.00 eq) was dissolved in 4 mL of acetonitrile. A solution of Br_2 (11.5 mg, 0.0720 mmol, 1.05 eq) in 0.3 mL of acetonitrile was added dropwise. The resulting suspension was stirred at room temperature for 30 min. All volatiles were removed by rotary evaporation to afford an orange solid, which was suspended in 15 mL of diethyl ether and collected by filtration. The product was washed with 10 mL of diethyl ether and dried in vacuo. Yield: 97 mg (87%). ^1H NMR (500 MHz, CD_2Cl_2) δ/ppm : 3.84–3.94 (m, 2H), 3.35–3.49

(br, m, 4H), 2.88–2.96 (br, m, 2H), 2.73–2.81 (br, m, 2H), 2.33 (br, d, 2H) 2.24 (br, d, 2H), 2.08 (br, d, 2H), 1.21–2.05 (br, m, 76H). $^{31}\text{P}\{^1\text{H}\}$ NMR (121.5 MHz, CD_2Cl_2) δ/ppm : 25.7 (t, 2P), –18.6 (t, 2P), –144.2 (sept., $^1J_{\text{F-P}} = 711$ Hz, 1P). UV-vis (CH_2Cl_2): λ/nm ($\epsilon/(\text{M}^{-1} \text{cm}^{-1})$) 283 (sh) (16000), 305 (23000), 369 (15000), 416 (sh) (9400), 496 (sh) (1500). IR (solid): $\tilde{\nu}_{\text{C=O}} = 2007$ cm^{-1} . Anal. Calcd. for $\text{C}_{51}\text{H}_{92}\text{AuBr}_3\text{F}_6\text{IrOP}_5$: C, 37.83; H, 5.73. Found: C, 37.59; H, 5.64.

2.5.19 Preparation of $[\text{Ir}^{\text{II}}\text{Au}^{\text{II}}(\text{dppm})_2(\text{CN}^t\text{Bu})_2\text{Cl}_2](\text{PF}_6)_2$ (14)

A solution 7 (100 mg, 0.0620 mmol, 1.00 eq) in 1.5 mL of CH_2Cl_2 and a solution of PhICl_2 (18 mg, 0.065 mmol, 1.2 eq) in 1 mL of CH_2Cl_2 were prepared and frozen in the glovebox cold well. After removing from the cold well and allowing the solution to melt, the PhICl_2 solution was added dropwise, prompting an immediate color change from dark green to bright yellow. The reaction solution was stirred in the dark for 1 h. The yellow solution was filtered through a plug of glass wool into 18 mL of pentane, which resulted in the formation of a pale yellow powder. The supernatant was decanted and the remaining solid was washed with pentane and dried in vacuo. Yield: 94 mg (90%). ^1H NMR (500 MHz, CD_2Cl_2) δ/ppm : 7.61–7.70 (br, m, 16H), 7.46–7.56 (br, m, 24H), 5.24 (br, pseudoquintet, 4H), 1.01 (s, 18H). $^{31}\text{P}\{^1\text{H}\}$ NMR (121.5 MHz, CD_2Cl_2) δ/ppm : 7.7 (t, 2P), –17.6 (t, 2P), –143.9 (sept., $^1J_{\text{F-P}} = 711$ Hz, 2P). UV-vis (CH_2Cl_2): λ/nm ($\epsilon/(\text{M}^{-1} \text{cm}^{-1})$) 257 (34000), 320 (33000), 388 (sh) (2600). IR (solid): $\tilde{\nu}_{\text{C=N}} = 2192$ cm^{-1} . Anal. Calcd. for $\text{C}_{60}\text{H}_{62}\text{AuCl}_2\text{F}_{12}\text{IrN}_2\text{P}_6$: C, 42.77; H, 3.71; N, 1.66. Found: C, 42.43; H, 3.87; N, 1.60.

2.5.20 Preparation of $[\text{Ir}^{\text{II}}\text{Au}^{\text{II}}(\text{dppm})_2(\text{CN}^t\text{Bu})_2\text{Br}_2](\text{PF}_6)_2$ (15)

A 10-mL Schlenk tube was charged with a solution of 7 (100 mg, 0.0620 mmol, 1.00 eq) in 2 mL of CH_2Cl_2 and chilled to -78 °C under an argon atmosphere. A solution of Br_2 (10.4 mg, 0.0650 mmol, 1.05 eq) in 228 μL of CH_2Cl_2 was added dropwise, causing an immediate color change to pale orange. The solution was allowed to warm to room temperature and stirred for 15 min. Addition of 17 mL of pentane afforded a yellow-orange solid, which was separated by decanting the supernatant and dried in vacuo. Yield: 106 mg (96.4%). ^1H NMR (500 MHz, CD_2Cl_2) δ/ppm : 7.61–7.69 (br, m, 16H), 7.35–7.60 (br, m, 24H), 5.33–5.37 (br, m, 4H), 1.06 (s, 18H). $^{31}\text{P}\{^1\text{H}\}$ NMR (202.5 MHz, CD_2Cl_2) δ/ppm : 3.1 (t, 2P), –22.2 (t, 2P), –143.9 (sept., $^1J_{\text{F-P}} = 712$ Hz, 2P). UV-vis (CH_2Cl_2): λ/nm ($\epsilon/(\text{M}^{-1} \text{cm}^{-1})$) 255 (sh) (34000), 344

(38000). IR (solid): $\tilde{\nu}_{\text{C}=\text{N}} = 2189 \text{ cm}^{-1}$. Anal. Calcd. for $\text{C}_{60}\text{H}_{62}\text{AuBr}_2\text{F}_{12}\text{IrN}_2\text{P}_6$: C, 40.62; H, 3.52; N, 1.58. Found: C, 40.63; H, 3.62; N, 1.45.

2.5.21 Preparation of $[\text{Rh}^{\text{I}}\text{Au}^{\text{I}}(\text{dcpm})_2(\text{CO})\text{H}](\text{PF}_6)$ (**16**)

1-(PF_6) (300 mg, 0.226 mmol, 1.00 eq) was dissolved in 10 mL of THF and the solution frozen in the coldwell of the glovebox. Upon thawing a 1 M LiHBEt_3 solution in THF (0.238 mL, 0.238 mmol, 1.05 eq) was added. The solution was allowed to warm to RT and stirred for 1 h, giving a dark red solution. The solvent was removed in vacuo to afford a red-orange residue. The residue was triturated with 4 mL of Et_2O to afford an orange solid, and subsequently the Et_2O was removed in vacuo. The resulting solid was taken up in 6 mL of benzene and filtered through celite. Evaporation of the benzene yielded a red-orange solid, which was washed with 2×5 mL of Et_2O to remove a dark red impurity. The resulting orange solid was dried in vacuo. Yield: 250 mg (85.5%). ^1H NMR (500 MHz, C_6D_6) δ /ppm: 2.63–2.77 (m, 4H), 2.33–2.48 (m, 4H), 1.98–2.33 (m, 20H), 1.00–1.96 (m, 64H), –4.40 (nonet, $^1J_{\text{Rh-H}} = ^2J_{\text{P-H}} = 12$ Hz, $^3J_{\text{P-H}} = 6$ Hz, 1H). $^{31}\text{P}\{^1\text{H}\}$ NMR (C_6D_6) δ /ppm: 54.6 (m, 2P), 50.4 (dm, $^1J_{\text{Rh-P}} = 137$ Hz, 2P), –144.1 (sept., $^1J_{\text{P-F}} = 711$ Hz, 1P). UV-vis (C_6H_6): λ /nm ($\epsilon/(\text{M}^{-1} \text{ cm}^{-1})$) 359 (5000), 472 (16000). IR (solid): $\tilde{\nu}_{\text{C}=\text{O}} = 1948 \text{ cm}^{-1}$. Anal. Calcd. for $\text{C}_{51}\text{H}_{93}\text{AuF}_6\text{RhOP}_5$: C, 47.45; H, 7.26; Found: C, 47.49; H, 7.31.

2.5.22 Reactions of **16** with LutH^+Cl^- and PhICl_2

Samples for all experiments were prepared in a nitrogen-filled glovebox. In a typical experiment **16** (25 mg, 0.019 mmol, 1.0 eq) was weighed into a scintillation vial, dissolved in 2 mL of CH_3CN and sealed with a septum. 2,6-lutidinium chloride (3.0 mg 0.021 mmol, 1.1 eq) or PhICl_2 (2.9 mg, 0.010 mmol, 0.55 eq), dissolved in CH_3CN , were added via syringe from stock solutions prepared previously in the glovebox. The reaction was stirred for 5 min at RT before a 10 μL sample of the headspace gas was removed by syringe and injected directly into the GC.

2.5.23 X-Ray Crystallographic Details

Single crystals of **1**, **8**, **13**, **14**, and **15** were obtained by layering a CH_2Cl_2 solution with diethyl ether, crystals of **2**, **5**, and **6** were grown by vapor diffusion of diethyl ether into an acetonitrile solution, crystals of **3** and **4** were grown by layering CH_2Cl_2 solutions with pentane, crystals of **9** and **12** were obtained by layering a CH_2Cl_2 solution with methanol/diethyl ether,

and crystals of **16** were obtained from a C₆D₆ NMR sample layered with diethyl ether. The crystals were mounted on a Bruker three-circle goniometer platform equipped with an APEX detector. A graphite monochromator was employed for wavelength selection of the Mo K α radiation ($\lambda = 0.71073$ Å). The data were processed and refined using the program SAINT supplied by Siemens Industrial Automation. Structures were solved by direct methods in SHELXS and refined by standard difference Fourier techniques in the SHELXTL program suite (6.10 v., Sheldrick G. M., and Siemens Industrial Automation, 2000). Hydrogen atoms bonded to carbon were placed in calculated positions using the standard riding model and refined isotropically; all other atoms were refined anisotropically. The rhodium-bound hydrogen atom in **16** was located in the difference map and refined semifreely. A positional disorder of the CO ligand and the halide *trans* to it was present in the structures of **2**, **5**, **6**, **8**, **9**, **12** and **13**. The thermal displacement parameters of the CO ligand in the minor disordered component were constrained to be identical to those of the CO ligand in the major component. The structures of **1**, **4**, **8**, **9**, **13**, **14**, and **15** all contained one dichloromethane solvate molecule that was modeled as a two-part disorder. In **1**, **2**, and **16**, one of the cyclohexyl groups was found to be disordered over two sites, and an analogous two-part disorder was observed for one phenyl ring in **4**. In **14**, one of the two *tert*-butyl groups was found to be disordered over two sites. In **16**, the Rh \cdots Au core was found to be disordered over two sites. The (1,2) and (1,3) distances of all disordered parts were restrained to be similar using the SADI command; the rigid-bond restraints SIMU and DELU were also used on disordered parts. Crystallographic details for **1** (CCDC 789594), **2** (CCDC 789595), **3** (CCDC 789596), **4** (CCDC 789597), **5** (CCDC 786326), **6** (CCDC 786327), **8** (789598), **9** (CCDC 789599), **12** (CCDC 786328), **13** (CCDC 786329), **14** (CCDC 786330), **15** (CCDC 786331), and **16** (CCDC 789600) are summarized in Tables 2.2–2.6.

Table 2.2. Crystallographic summary for complexes **1** and **2**.

| | 1 -(PF ₆)·CH ₂ Cl ₂ | 2 -(PF ₆)·Et ₂ O |
|--|---|--|
| Formula | C ₅₂ H ₉₄ AuCl ₃ F ₆ OP ₅ Rh | C ₅₅ H ₁₀₂ AuBrF ₆ O ₂ P ₅ Rh |
| fw, g/mol | 1410.35 | 1444.00 |
| Temperature/K | 100(2) | 100(2) |
| cryst. syst. | Monoclinic | Monoclinic |
| space group | <i>P2₁/n</i> | <i>P2₁/n</i> |
| color | Orange | Orange |
| <i>a</i> /Å | 15.031(2) | 15.0137(12) |
| <i>b</i> /Å | 21.469(3) | 21.2486(17) |
| <i>c</i> /Å | 20.325(3) | 20.3833(16) |
| α /° | 90 | 90 |
| β /° | 102.251(2) | 102.5770(10) |
| γ /° | 90 | 90 |
| <i>V</i> /Å ³ | 6409.6(16) | 6346.6(9) |
| ρ (calc.)/(g cm ⁻³) | 1.462 | 1.511 |
| <i>Z</i> | 4 | 4 |
| no. refl. | 145895 | 147939 |
| no. unique refl. | 18727 | 19764 |
| <i>R</i> _{int} | 0.0514 | 0.0492 |
| <i>R</i> ₁ ^a (all data) | 0.0401 | 0.0390 |
| <i>wR</i> ₂ ^b (all data) | 0.0978 | 0.0640 |
| <i>R</i> ₁ [(<i>I</i> > 2σ)] | 0.0329 | 0.0279 |
| <i>wR</i> ₂ [(<i>I</i> > 2σ)] | 0.0930 | 0.0597 |
| <i>GOF</i> ^c | 1.071 | 1.034 |

^a $R_1 = \sum ||F_o - |F_c|| / \sum |F_o|$. ^b $wR_2 = (\sum (w(F_o^2 - F_c^2)^2) / \sum (w(F_o^2)^2))^{1/2}$. ^c $GOF = (\sum w(F_o^2 - F_c^2)^2 / (n - p))^{1/2}$ where *n* is the number of data and *p* is the number of parameters refined.

Table 2.3. Crystallographic summary for complexes **3** and **4**.

| | 3 -(OTf)·CH ₂ Cl ₂ | 4 -(OTf)·2CH ₂ Cl ₂ |
|--|--|--|
| Formula | C ₅₃ H ₄₆ AuCl ₃ F ₃ O ₄ P ₄ RhS | C ₅₄ H ₄₈ AuBrCl ₄ F ₃ O ₄ P ₄ RhS |
| fw, g/mol | 1366.06 | 1495.45 |
| Temperature/K | 100(2) | 100(2) |
| cryst. syst. | Orthorhombic | Monoclinic |
| space group | <i>P</i> 2 ₁ 2 ₁ 2 ₁ | <i>P</i> 2 ₁ / <i>c</i> |
| color | Orange | Orange |
| <i>a</i> /Å | 10.4553(11) | 19.5635(17) |
| <i>b</i> /Å | 19.2177(19) | 10.8423(10) |
| <i>c</i> /Å | 26.395(3) | 28.356(3) |
| α /° | 90 | 90 |
| β /° | 90 | 100.659(2) |
| γ /° | 90 | 90 |
| <i>V</i> /Å ³ | 5303.4(9) | 5910.9(9) |
| ρ (calc.)/(g cm ⁻³) | 1.711 | 1.680 |
| <i>Z</i> | 4 | 4 |
| no. refl. | 120893 | 122157 |
| no. unique refl. | 16512 | 17969 |
| <i>R</i> _{int} | 0.0440 | 0.0523 |
| <i>R</i> ₁ ^a (all data) | 0.0287 | 0.0698 |
| <i>wR</i> ₂ ^b (all data) | 0.0591 | 0.1681 |
| <i>R</i> ₁ [(<i>I</i> > 2σ)] | 0.0258 | 0.0572 |
| <i>wR</i> ₂ [(<i>I</i> > 2σ)] | 0.0583 | 0.1599 |
| <i>GOF</i> ^c | 1.041 | 1.074 |
| <i>Flack Param.</i> | 0.0089(21) | ----- |

^a $R_1 = \Sigma ||F_o - |F_c|| / \Sigma |F_o|$. ^b $wR_2 = (\Sigma (w(F_o^2 - F_c^2)^2) / \Sigma (w(F_o^2)^2))^{1/2}$. ^c $GOF = (\Sigma w(F_o^2 - F_c^2)^2 / (n - p))^{1/2}$ where *n* is the number of data and *p* is the number of parameters refined.

Table 2.4. Crystallographic summary for complexes **5**, **6**, and **8**.

| | 5 | 6 ·Et ₂ O | 8 ·(PF ₆)·CH ₂ Cl ₂ |
|--|--|---|---|
| Formula | C ₅₁ H ₉₂ AuClF ₆ IrOP ₅ | C ₅₅ H ₁₀₂ AuBrF ₆ IrO ₂ P ₅ | C ₅₂ H ₉₄ AuCl ₅ F ₆ OP ₅ Rh |
| fw, g/mol | 1414.71 | 1533.29 | 1481.25 |
| Temperature/K | 100(2) | 100(2) | 100(2) |
| cryst. syst. | Monoclinic | Monoclinic | Monoclinic |
| space group | <i>P</i> 2 ₁ / <i>c</i> | <i>P</i> 2 ₁ / <i>n</i> | <i>P</i> 2 ₁ / <i>c</i> |
| color | Orange | Orange | Orange |
| <i>a</i> /Å | 13.5909(13) | 15.0304(16) | 14.6050(13) |
| <i>b</i> /Å | 22.404(2) | 21.199(2) | 20.5013(17) |
| <i>c</i> /Å | 18.9079(17) | 20.366(2) | 20.6567(18) |
| α /° | 90 | 90 | 90 |
| β /° | 94.232(2) | 102.708(2) | 95.374(2) |
| γ /° | 90 | 90 | 90 |
| <i>V</i> /Å ³ | 5741.6(9) | 6330.3(11) | 6157.9(9) |
| ρ (calc.)/(g cm ⁻³) | 1.637 | 1.609 | 1.598 |
| <i>Z</i> | 4 | 4 | 4 |
| no. refl. | 131339 | 145929 | 122466 |
| no. unique refl. | 16785 | 19229 | 16655 |
| <i>R</i> _{int} | 0.0561 | 0.0511 | 0.0552 |
| <i>R</i> ₁ ^a (all data) | 0.0416 | 0.0356 | 0.0552 |
| <i>wR</i> ₂ ^b (all data) | 0.0702 | 0.0669 | 0.0899 |
| <i>R</i> ₁ [(<i>I</i> > 2σ)] | 0.0305 | 0.0278 | 0.0377 |
| <i>wR</i> ₂ [(<i>I</i> > 2σ)] | 0.0657 | 0.0636 | 0.0814 |
| <i>GOF</i> ^c | 1.070 | 1.049 | 1.060 |

^a $R_1 = \sum ||F_o - |F_c|| / \sum |F_o|$. ^b $wR_2 = (\sum (w(F_o^2 - F_c^2)^2) / \sum (w(F_o^2)^2))^{1/2}$. ^c $GOF = (\sum w(F_o^2 - F_c^2)^2 / (n - p))^{1/2}$ where *n* is the number of data and *p* is the number of parameters refined.

Table 2.5. Crystallographic summary for complexes **9**, **12**, and **13**.

| | 9 ·(PF ₆)·CH ₂ Cl ₂ | 12 ·CH ₂ Cl ₂ | 13 ·CH ₂ Cl ₂ |
|--|---|--|--|
| Formula | C ₅₂ H ₉₄ AuBr ₃ Cl ₂ F ₆ OP ₅ Rh | C ₅₂ H ₉₄ AuCl ₅ F ₆ IrOP ₅ | C ₅₂ H ₉₄ AuBr ₃ Cl ₂ F ₆ IrOP ₅ |
| fw, g/mol | 1614.63 | 1570.54 | 1703.92 |
| Temperature/K | 100(2) | 100(2) | 100(2) |
| cryst. syst. | Monoclinic | Monoclinic | Monoclinic |
| space group | <i>P2₁/c</i> | <i>P2₁/c</i> | <i>P2₁/c</i> |
| color | Red | Orange | Orange |
| <i>a</i> /Å | 14.6332(13) | 14.5925(16) | 14.6114(14) |
| <i>b</i> /Å | 20.6673(18) | 20.500(2) | 20.703(2) |
| <i>c</i> /Å | 20.6771(18) | 20.651(2) | 20.627(2) |
| <i>α</i> ° | 90 | 90 | 90 |
| <i>β</i> ° | 95.422(2) | 95.279(2) | 95.402(2) |
| <i>γ</i> ° | 90 | 90 | 90 |
| <i>V</i> /Å ³ | 6225.4(9) | 6151.7(11) | 6212.0(10) |
| <i>ρ</i> (calc.)/(g cm ⁻³) | 1.723 | 1.696 | 1.822 |
| <i>Z</i> | 4 | 4 | 4 |
| no. refl. | 143038 | 142362 | 124959 |
| no. unique refl. | 18943 | 18704 | 17446 |
| <i>R</i> _{int} | 0.0525 | 0.0596 | 0.0678 |
| <i>R</i> ₁ ^a (all data) | 0.0461 | 0.0474 | 0.0534 |
| <i>wR</i> ₂ ^b (all data) | 0.0829 | 0.0826 | 0.0839 |
| <i>R</i> ₁ [(<i>I</i> > 2σ)] | 0.0335 | 0.0348 | 0.0351 |
| <i>wR</i> ₂ [(<i>I</i> > 2σ)] | 0.0772 | 0.0765 | 0.0759 |
| <i>GOF</i> ^c | 1.041 | 1.051 | 1.012 |

^a $R_1 = \frac{\sum ||F_o| - |F_c||}{\sum |F_o|}$. ^b $wR_2 = \frac{(\sum (w(F_o^2 - F_c^2)^2))^{1/2}}{(\sum (w(F_o^2)^2))^{1/2}}$. ^c $GOF = \frac{(\sum (F_o^2 - F_c^2)^2 / (n - p))^{1/2}}{(\sum w(F_o^2)^2)^{1/2}}$ where *n* is the number of data and *p* is the number of parameters refined.

Table 2.6. Crystallographic summary for complexes **14–16**.

| | 14 ·2CH ₂ Cl ₂ | 15 ·2CH ₂ Cl ₂ | 16 ·2.5(C ₆ H ₆) |
|--|---|---|--|
| Formula | C ₆₂ H ₆₆ AuC ₁₆ F ₁₂ IrN ₂ P ₆ | C ₆₂ H ₆₆ AuBr ₂ Cl ₄ F ₁₂ IrN ₂ P ₆ | C ₆₆ H ₁₀₈ AuF ₆ OP ₅ Rh |
| fw, g/mol | 1854.85 | 1943.77 | 1486.25 |
| Temperature/K | 100(2) | 100(2) | 100(2) |
| cryst. syst. | Monoclinic | Monoclinic | Triclinic |
| space group | <i>P2₁/c</i> | <i>P2₁/c</i> | <i>PT</i> |
| color | Yellow | Orange | Orange |
| <i>a</i> /Å | 16.551(2) | 16.4460(18) | 13.5672(15) |
| <i>b</i> /Å | 20.888(3) | 20.891(2) | 14.0811(15) |
| <i>c</i> /Å | 21.963(3) | 22.145(2) | 19.974(2) |
| <i>α</i> /° | 90 | 90 | 76.123(2) |
| <i>β</i> /° | 106.100(2) | 105.181(2) | 82.666(2) |
| <i>γ</i> /° | 90 | 90 | 66.756(2) |
| <i>V</i> /Å ³ | 7295.4(17) | 7343.1(14) | 3401.4(6) |
| <i>ρ</i> (calc.)/(g cm ⁻³) | 1.689 | 1.758 | 1.451 |
| <i>Z</i> | 4 | 4 | 2 |
| no. refl. | 152587 | 159423 | 78297 |
| no. unique refl. | 18605 | 19773 | 19683 |
| <i>R</i> _{int} | 0.0625 | 0.0675 | 0.0395 |
| <i>R</i> ₁ ^a (all data) | 0.0582 | 0.0690 | 0.0394 |
| <i>wR</i> ₂ ^b (all data) | 0.1000 | 0.1070 | 0.0723 |
| <i>R</i> ₁ [(<i>I</i> > 2σ)] | 0.0399 | 0.0417 | 0.0325 |
| <i>wR</i> ₂ [(<i>I</i> > 2σ)] | 0.0894 | 0.0931 | 0.0698 |
| <i>GOF</i> ^c | 1.038 | 1.023 | 1.117 |

^a $R_1 = \frac{\sum ||F_o| - |F_c||}{\sum |F_o|}$. ^b $wR_2 = \frac{(\sum (w(F_o^2 - F_c^2)^2)/\sum (w(F_o^2)^2))^{1/2}}$. ^c $GOF = \frac{(\sum (w(F_o^2 - F_c^2)^2)/(n - p))^{1/2}}$ where *n* is the number of data and *p* is the number of parameters refined.

2.6 References

- (1) Heyduk, A. F.; Nocera, D. G. *Science* **2001**, *293*, 1639–1641.
- (2) Esswein, A. J.; Veige, A. S.; Nocera, D. G. *J. Am. Chem. Soc.* **2005**, *127*, 16641–16651.
- (3) Heyduk, A. F.; Macintosh, A. M.; Nocera, D. G. *J. Am. Chem. Soc.* **1999**, *121*, 5023–5032.
- (4) Odom, A. L.; Heyduk, A. F.; Nocera, D. G. *Inorg. Chim. Acta* **2000**, *297*, 330–337.
- (5) Cook, T. R.; Esswein, A. J.; Nocera, D. G. *J. Am. Chem. Soc.* **2007**, *129*, 10094–10095.
- (6) Cook, T. R.; Surendranath, Y.; Nocera, D. G. *J. Am. Chem. Soc.* **2009**, *131*, 28–29.
- (7) Heyduk, A. F.; Nocera, D. G. *J. Am. Chem. Soc.* **2000**, *122*, 9415–9426.
- (8) Hutton, A. T.; Pringle, P. G.; Shaw, B. L. *Organometallics* **1983**, *2*, 1889–1891.
- (9) Langrick, C. R.; Shaw, B. L. *J. Chem. Soc., Dalton Trans.* **1985**, 511–516.
- (10) Balch, A. L.; Catalano, V. J.; Olmstead, M. M. *Inorg. Chem.* **1990**, *29*, 585–586.
- (11) Balch, A. L.; Catalano, V. J. *Inorg. Chem.* **1991**, *30*, 1302–1308.
- (12) Striplin, D. R.; Brozik, J. A.; Crosby, G. A. *Chem. Phys. Lett.* **1994**, *231*, 159–163.
- (13) Striplin, D. R.; Crosby, G. A. *J. Phys. Chem.* **1995**, *99*, 7977–7984.
- (14) Liu, T.; Zhou, X.; Zhang, H.-X.; Xia, B.-H. *Dalton Trans.* **2008**, 1065–1072.
- (15) Balch, A. L.; Catalano, V. J. *Inorg. Chem.* **1992**, *31*, 2730–2734.
- (16) Balch, A. L.; Nagle, J. K.; Oram, D. E.; Reedy, P. E. *J. Am. Chem. Soc.* **1988**, *110*, 454–462.
- (17) Yip, H. K.; Lin, H. M.; Wang, Y.; Che, C. M. *Inorg. Chem.* **1993**, *32*, 3402–3407.
- (18) Striplin, D. R.; Crosby, G. A. *J. Phys. Chem.* **1995**, *99*, 11041–11045.
- (19) Esswein, A. J.; Dempsey, J. L.; Nocera, D. G. *Inorg. Chem.* **2007**, *46*, 2362–2364.
- (20) Tsui, E. Y.; Müller, P.; Sadighi, J. P. *Angew. Chem. Int. Ed.* **2008**, *47*, 8937–8940.
- (21) Chatt, J. *Science* **1968**, *160*, 723–729.
- (22) Harris, D. C.; Bertolucci, M. D. *Symmetry and spectroscopy: an introduction to vibrational and electronic spectroscopy*; Dover: New York, 1989.
- (23) Che, C. M.; Butler, L. G.; Gray, H. B.; Crooks, R. M.; Woodruff, W. H. *J. Am. Chem. Soc.* **1983**, *105*, 5492–5494.
- (24) Che, C. M.; Butler, L. G.; Gray, H. B. *J. Am. Chem. Soc.* **1981**, *103*, 7796–7797.
- (25) Fordyce, W. A.; Brummer, J. G.; Crosby, G. A. *J. Am. Chem. Soc.* **1981**, *103*, 7061–7064.

- (26) Zielinska, A.; Skulski, L. *Tetrahedron Lett.* **2004**, *45*, 1087–1089.
- (27) Miller, J. S.; Caulton, K. G. *J. Am. Chem. Soc.* **1975**, *97*, 1067–1073.
- (28) Vaska, L.; Catone, D. L. *J. Am. Chem. Soc.* **1966**, *88*, 5324–5325.
- (29) Giordano, G.; Crabtree, R. H. *Inorg. Synth.* **1990**, *28*, 88–90.
- (30) Uson, R.; Laguna, A.; Laguna, M.; *Inorg. Synth.* **1989**, *26*, 85–91.
- (31) McLaurin, E. J.; Greytak, A. B.; Bawendi, M. G.; Nocera, D. G. *J. Am. Chem. Soc.* **2009**, *131*, 12994–13001.
- (32) Montalti, M.; Murov, S. L. *Handbook of photochemistry.*; CRC/Taylor & Francis: Boca Raton, 2006.
- (33) Becke, A. D. *J. Chem. Phys.* **1993**, *98*, 5648–5652.
- (34) Lee, C.; Yang, W.; Parr, R. G. *Phys. Rev. B* **1988**, *37*, 785–789.
- (35) Miehlich, B.; Savin, A.; Stoll, H.; Preuss, H. *Chem. Phys. Lett.* **1989**, *157*, 200–206.
- (36) Hariharan, P. C.; Pople, J. A. *Theor. Chim. Acta* **1973**, 213–222.
- (37) Dolg, M.; Wedig, U.; Stoll, H.; Preuss, H. *J. Chem. Phys.* **1987**, *86*, 866–872.

Chapter 3 – Redox Chemistry, Acid Reactivity, and Hydrogenation Reactions of Two-Electron Mixed-Valent Dirhodium and Diiridium Complexes

Portions of this work have been previously published:

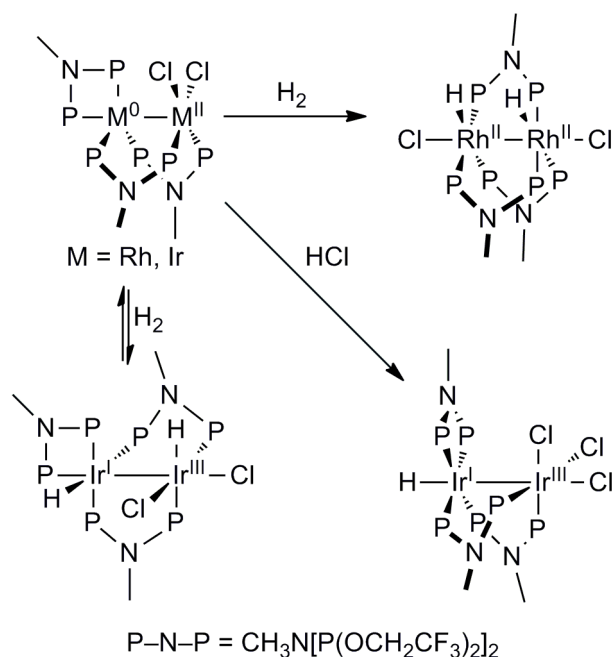
Reproduced in part with permission from Teets, T. S.; Cook, T. R.; McCarthy, B. D.; Nocera, D. G. *J. Am. Chem. Soc.* **2011**, *133*, 8114–8117. Copyright 2011 American Chemical Society.

Reproduced in part with permission from Teets, T. S.; Cook, T. R.; McCarthy, B. D.; Nocera, D. G. *Inorg. Chem.* **2011**, *50*, 5223–5233. Copyright 2011 American Chemical Society.

3.1 Introduction

The two half-reactions of HX splitting, formally the reduction of protons to H₂ and the oxidation of halides to X₂,^{1,2} each present their own unique set of challenges, which must be simultaneously overcome to design more efficient photocatalysts. Our interrogation of dirhodium catalysts affirmed that the sluggish halogen photoelimination limited the overall catalytic efficiency,^{3,4} motivating the study of more efficient halogen elimination from bimetallic and monometallic centers.⁵⁻⁹ In the first two chapters of this thesis, the focus was on photochemical halogen elimination, with studies on monometallic and bimetallic complexes of varying architectures geared towards improving and understanding the key design criteria that abet efficient halogen photoelimination. These previous results demonstrated success in designing systems which eliminate halogen with high quantum yields, in some cases not requiring a chemical trap, but to this date no one has been able to marry efficient X₂ (X = Cl, Br) elimination with hydrogen production in a molecular photocatalytic construct.¹⁰

In this chapter, the focus shifts to reactivity and small-molecule activation pertaining to the reductive half-reaction of HX splitting. The reductive half-reaction of HX splitting proceeds through hydrido-halide intermediates, generated by oxidative addition of HX. Early success in photocatalytic hydrogen production from HX solutions was realized with diphosphazane-bridged dirhodium complexes of the type Rh₂^{0,0}(dfpma)₃L₂ (dfpma = bis(difluorophosphino)methylamine, L = CO, PR₃),¹ which proceed via dihydride-dihalide Rh₂^{II,II} intermediates.² In this previous work, HX addition was found to be preceded by photochemical CO liberation from a five-coordinate Rh⁰ center, which generates a reactive four-coordinate center. This necessity to photoactivate the metal prior to HX addition translates to hydride-containing intermediates present in only minor quantities, and often these types of intermediates are unstable under the conditions used to generate them. Accordingly, these limitations complicate the structural and spectral characterization of key hydride intermediates of the catalytic cycle. Notwithstanding these limitations, several hydrido-halide model complexes have been prepared by either protonation or hydrogenation of two-electron mixed-valent cores, as summarized in Scheme 3.1. By using bulkier supporting ligands² and also preparing analogous diiridium species,¹¹ proposed catalytic intermediates have been characterized. The aforementioned hydride model complexes were all accessed by oxidative addition across



Scheme 3.1. Previous examples of dirhodium and diiridium hydride model complexes.

bimetallic cores which contain a saturated five-coordinate M^0 center and a reactive four-coordinate M^{II} center, a structure not known to be on the catalytic cycle. In addition, as shown in Scheme 3.1, the structural consequences of H_2 addition are disparate between the rhodium and iridium analogues, and all told it was unclear to what degree the structures of the model complexes in Scheme 3.1 were relevant to HX-splitting photocatalysis.

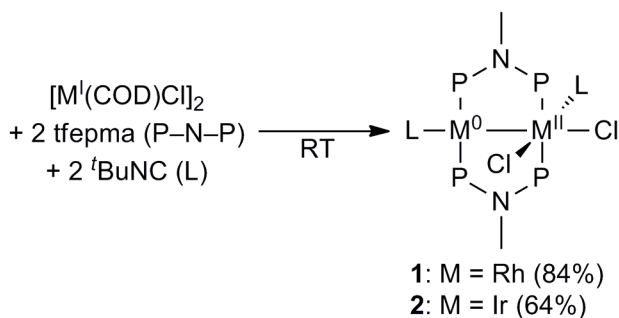
By avoiding high-coordination metal centers, key hydride intermediates may be generated by thermal addition of HX and H_2 to group 9 two-electron mixed-valent complexes that feature coordinatively unsaturated M^0 centers. As such, a long-standing goal in our group has been to prepare two-electron mixed-valent dirhodium and diiridium complexes which are structurally homologous to one another *and* feature stable four-coordinate M^0 centers in their ground states, allowing synthetic access to hydride-containing complexes via HX addition and/or hydrogenation. In addition to allowing the thorough characterization of ground- and excited-state reactivity as it pertains to HX splitting, the hydride complexes thus prepared are of potential interest to those studying hydrogenation,¹² O_2 reduction,¹³ aerobic oxidation,¹⁴⁻¹⁷ and CO_2 reduction chemistries,¹⁸ among others.¹⁹ In this chapter, the preparation and reactivity towards small molecules of a new class of two-electron mixed-valent complexes are described. The complexes $M_2^{0,II}(tfepma)_2(CN^tBu)_2Cl_2$ ($M = Rh$ (**1**), Ir (**2**); $tfepma = CH_3N[P(OCH_2CF_3)_2]_2$) are

structurally homologous and feature four-coordinate, unsaturated M^0 centers. The two-electron reduction and oxidation chemistries of **1** and **2** are described. Ligand-addition/substitution reactions of the complexes containing unsaturated M^0 centers are highlighted, and bimetallic hydride complexes are obtained by protonation of **1** and **2** and hydrogenation of **2**. The results described herein provide access to a new suite of dirhodium and diiridium hydride complexes, which are promising targets to further our understanding of both H_2 production and other small-molecule chemistries mediated by group 9 bimetallic complexes.

3.2 Results

3.2.1 Synthesis and Characterization of $M_2^{0,II}(tfepma)_2(CN^tBu)_2Cl_2$ ($M = Rh, Ir$)

Two-electron mixed-valent complexes $M_2^{0,II}(tfepma)_2(CN^tBu)_2Cl_2$ [$M = Rh$ (**1**), Ir (**2**)] are formed by treatment of $[M^I(COD)Cl]_2$ ($COD = 1,5$ -cyclooctadiene) with two equivalents of $tfepma$ and CN^tBu at room temperature, as outlined in Scheme 3.2. Note that in all schemes, P–N–P refers to the bridging ligand $tfepma$, and L refers to CN^tBu . Dirhodium complex **1** is isolated in 84.2% yield, whereas diiridium complex **2** is prepared in a lower isolated yield of 64.3%. The room-temperature $^{31}P\{^1H\}$ NMR spectra of **1** and **2** show two distinct signals, at 124.5 and 145.1 ppm for **1** and 85.9 and 132.3 ppm for **2**, indicative of the coordination asymmetry as a result of the two-electron mixed-valent core. The complex multiplicities in these spectra can be attributed to the AA'XX' spin system that arises from the four phosphorus atoms, with additional coupling to ^{103}Rh present in **1**. Further verification that the two-electron mixed valency persists in solution comes from the 1H NMR spectra, which each possess two distinct *tert*-butyl resonances, as well as in the IR spectra where two $C\equiv N$ stretching frequencies are observed. These spectral conclusions are verified by the X-ray crystal structures of **1** and **2**,



Scheme 3.2. Synthesis of $M_2^{0,II}$ complexes **1** and **2**. Isolated yields are listed in parentheses.

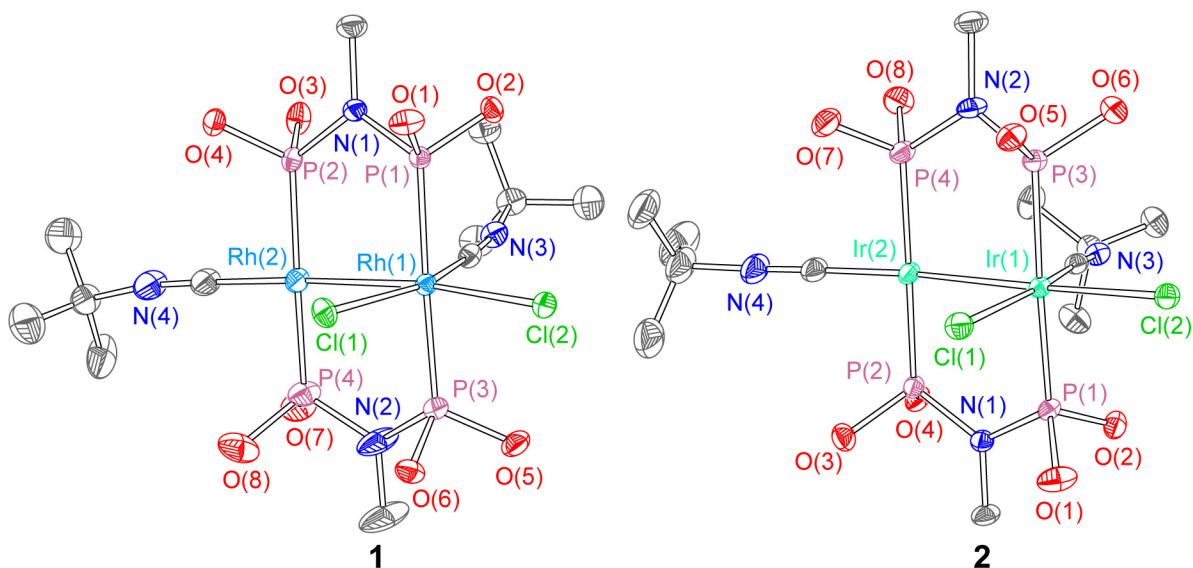
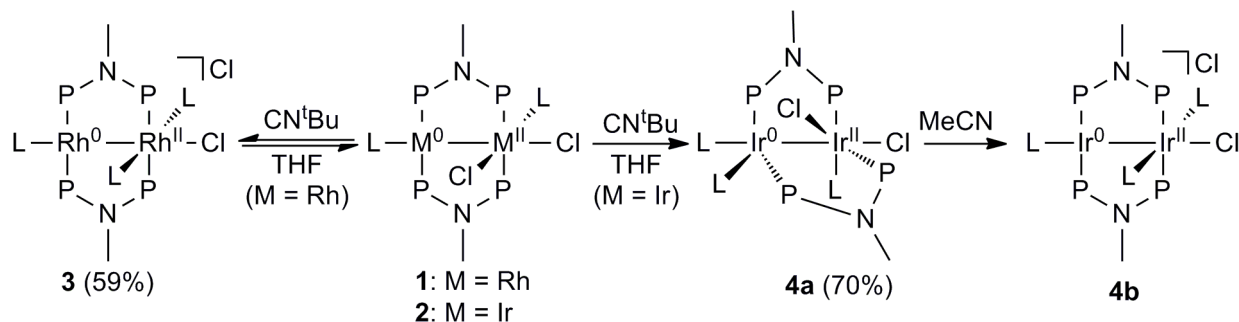


Figure 3.1. X-ray crystal structures of **1** and **2**. Ellipsoids are shown at the 50% probability level with $-\text{CH}_2\text{CF}_3$ groups and hydrogen atoms omitted for clarity.

which are shown in Figure 3.1. The respective square-planar and octahedral environments of the M^0 and M^{II} centers are evident; the Rh(1)–Rh(2) internuclear distance of 2.6807(3) Å in **1** and the Ir(1)–Ir(2) distance of 2.7112(3) Å in **2** indicate a formal metal–metal bond.

3.2.2 Addition of CN^tBu to **1** and **2**

As **1** and **2** feature coordinatively unsaturated M^0 centers, we sought to explore the possibility of occupying the vacant coordination site with an additional equivalent of CN^tBu . As shown in Scheme 3.3, different outcomes ensue when **1** and **2** are combined with CN^tBu . Treatment of $\text{Rh}_2^{0,\text{II}}$ complex **1** with one equivalent of CN^tBu leads to reversible association of the added ligand, as judged by NMR spectra. The $^{31}\text{P}\{^1\text{H}\}$ spectrum features broad resonances



Scheme 3.3. Addition of CN^tBu to **1** and **2**. Isolated yields are listed in parentheses.

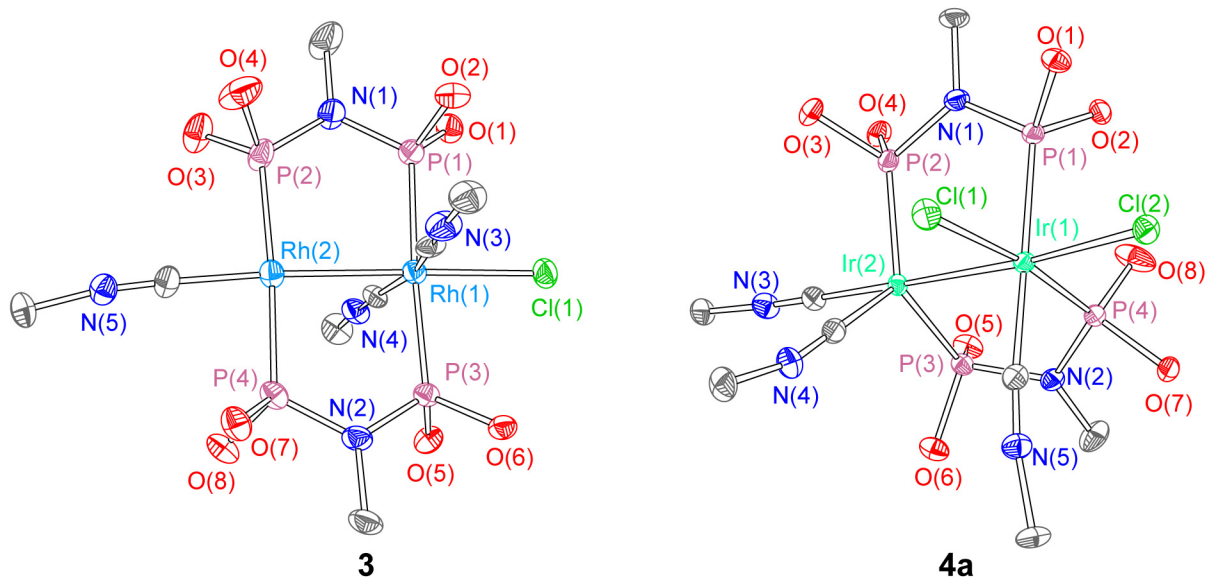


Figure 3.2. X-ray crystal structures of **3** and **4a**. Ellipsoids are shown at the 50% probability level with $-\text{CH}_2\text{CF}_3$ groups, CN^tBu methyl groups, outer-sphere anions and hydrogen atoms omitted for clarity.

whose chemical shifts are nearly identical to parent complex **1**. The ^1H spectrum is similarly broadened and only shows a single *tert*-butyl resonance, offering little insight to the structure. UV-vis spectra of the isolated product, recorded in the range of 3–50 μM , are identical to that of complex **1**, suggesting complete dissociation of the additional CN^tBu ligand at these low concentrations. X-ray crystallography reveals the structure of the addition product to be $[\text{Rh}_2^{0,\text{II}}(\text{tfepma})_2(\text{CN}^t\text{Bu})_3\text{Cl}]\text{Cl}$ (**3**), shown in Figure 3.2. The incoming CN^tBu ligand substitutes for one of the chloride ligands at the octahedral Rh^{II} center whereas the Rh^0 center is unperturbed. The intermetallic distances, 2.6847(10) Å and 2.6857(10) Å for the two crystallographically independent molecules, verify that the metal–metal bond and two-electron mixed valency are preserved upon ligand addition.

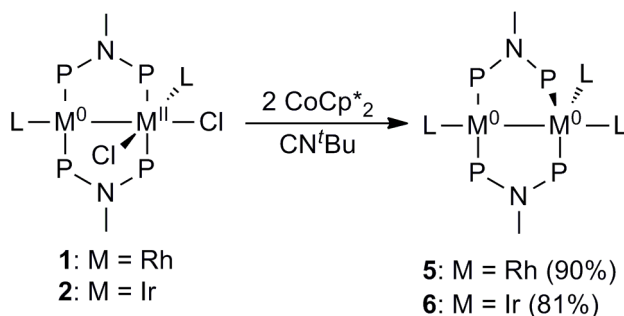
Treatment of $\text{Ir}_2^{0,\text{II}}$ complex **2** with one equivalent of CN^tBu in THF (Scheme 3.3) leads to a distinct outcome as compared to the addition chemistry of $\text{Rh}_2^{0,\text{II}}$ complex **1** with CN^tBu . After 21 h, the $^{31}\text{P}\{^1\text{H}\}$ NMR spectrum of the crude reaction mixture shows a major product with three resonances—a multiplet at 102.6 ppm integrating to two phosphorus nuclei, and multiplets at 80.6 and 69.6 ppm, each integrating to one phosphorus. These upfield resonances are attributed to the phosphorus nuclei coordinated to Ir^{II} , and their inequivalency suggests a *cis* arrangement of the phosphorus ligands at Ir^{II} . The solid-state structure of

$\text{Ir}_2^{0,\text{II}}(\text{tfepma})_2(\text{CN}^t\text{Bu})_3\text{Cl}_2$ (**4a**), shown in Figure 3.2, is consistent with this expectation. The Ir^0 center is now five-coordinate, distorted trigonal-bipyramidal, and at the octahedral Ir^{II} center the two phosphorus atoms are *cis* to one another. The metal–metal distance has lengthened by 0.08 Å to 2.7920(3) Å, though this distance suggests that the metal–metal bond is intact.

When crystals of **4a** are dissolved in acetonitrile, the NMR and UV-vis spectra suggest isomerization to a considerably more symmetric structure. The $^{31}\text{P}\{^1\text{H}\}$ NMR spectrum shows only two resonances, with an AA'XX' splitting pattern. The spectrum is similar to that of parent $\text{Ir}_2^{0,\text{II}}$ complex **2**, though the upfield resonance shifts by ca. 6 ppm and the multiplicity is distinct. The ^1H NMR spectrum features two closely spaced, sharp *tert*-butyl resonances with a 2:1 integration ratio, suggesting that all three CN^tBu ligands remain bound. Furthermore, the UV-vis spectra of **2** and **4** are decidedly similar in MeCN, with only slight 5–15 nm hypsochromic shifts of most peaks in the spectrum of **4** relative to that of **2**. These spectral data suggest that in acetonitrile solution, chloride dissociation from **4a** leads to the isomeric ionic complex $[\text{Ir}_2^{0,\text{II}}(\text{tfepma})_2(\text{CN}^t\text{Bu})_3\text{Cl}]\text{Cl}$ (**4b**), whose structure is analogous to **3**. The octahedral Ir^{II} and square-planar Ir^0 sites possess similar coordination environments to the parent $\text{Ir}_2^{0,\text{II}}$ complex **2**, giving rise to only slightly differing spectral features.

3.2.3 Chemical Reduction of **1** and **2**

Whereas treatment of $\text{M}_2^{0,\text{II}}$ complexes **1** and **2** with bis(cyclopentadienyl)cobalt(II) (CoCp_2 , $E^{\circ'} = -1.33$ V vs. ferrocene)²⁰ leads to incomplete reactions and mixtures of products, treatment with the stronger reducing agent bis(pentamethylcyclopentadienyl)cobalt(II) (CoCp_2^* , $E^{\circ'} = -1.94$ V)²⁰ completely consumes the $\text{M}_2^{0,\text{II}}$ starting material. Integration of the crude ^1H NMR spectra showed the major product of each reaction to contain three bound CN^tBu



Scheme 3.4. Synthesis of $\text{M}_2^{0,0}$ complexes **5** and **6**. Isolated yields are listed in parentheses.

ligands. The route shown in Scheme 3.4 gives optimized yields and purities of these major products, $M_2^{0,0}(\text{tfepma})_2(\text{CN}^t\text{Bu})_3$ [$M = \text{Rh}$ (**5**), Ir (**6**)], which are obtained when complexes **1** and **2** are treated with both two equivalents of CoCp^*_2 and one equivalent of CN^tBu . The solid-state structures of compounds **5** and **6** are shown in Figure 3.3. An asymmetric structure is observed, with a four-coordinate, square-planar environment about one M^0 center, and a five-coordinate, trigonal-bipyramidal structure about the other. Metal–metal distances of 2.7099(5) Å (**5**) and 2.7631(4) Å (**6**) are observed for these formally d^9 – d^9 complexes.

The room-temperature NMR spectra of **5** and **6** suggest conformational fluxionality in solution. Although the solid-state structure of both complexes would predict asymmetric $^{31}\text{P}\{^1\text{H}\}$ NMR spectra, they each show a single resonance, which appears as a symmetric multiplet in **5**

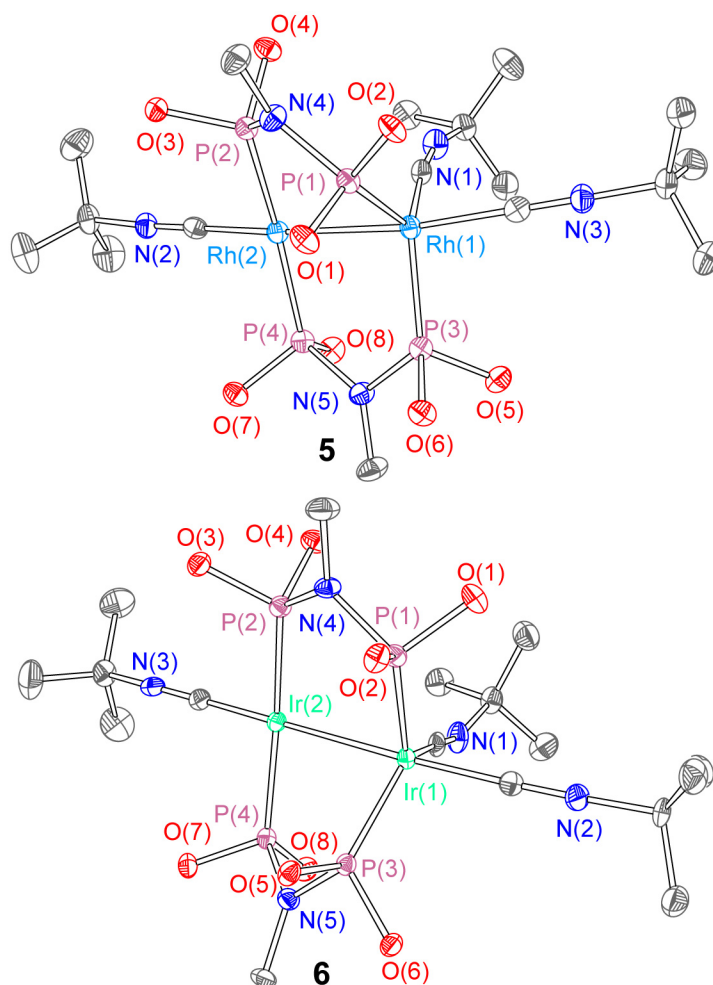


Figure 3.3. X-ray crystal structures of **5** and **6**. Ellipsoids are shown at the 50% probability level with $-\text{CH}_2\text{CF}_3$ groups and hydrogen atoms omitted for clarity.

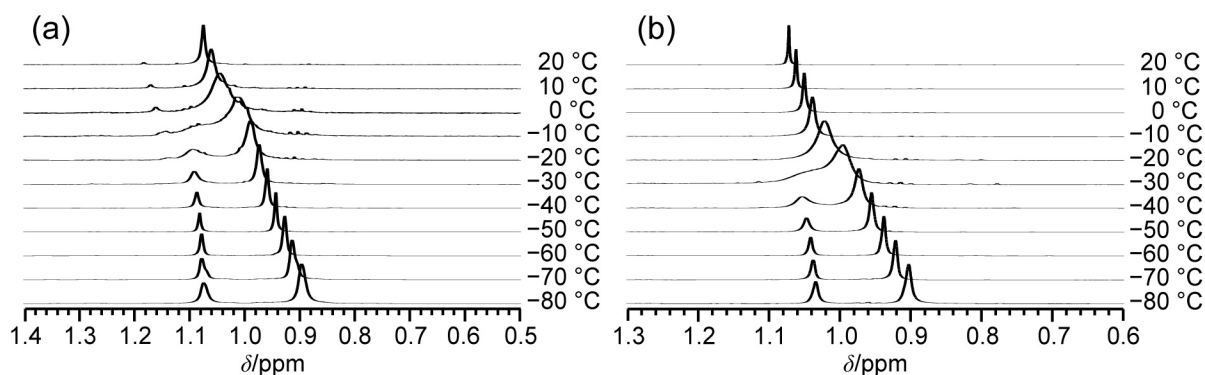
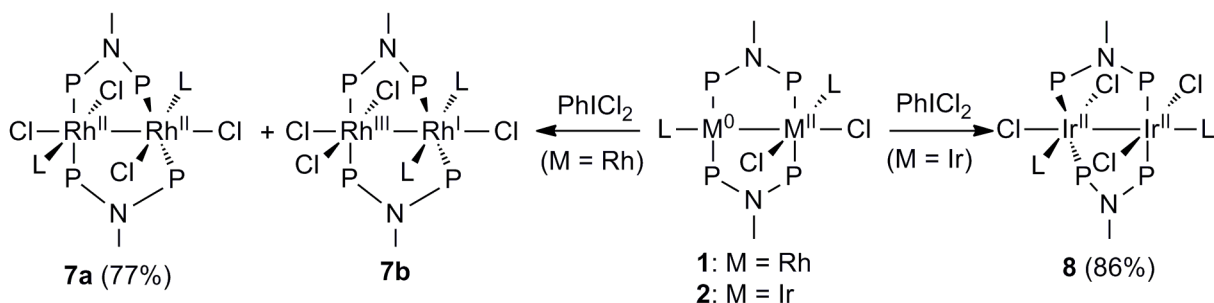


Figure 3.4. Variable-temperature ^1H NMR spectra for complex **5** (a) and **6** (b), showing the *tert*-butyl resonances. Spectra were recorded in toluene- d_8 at 500 MHz.

and a sharp singlet in **6**; the splitting in **5** arises from $J_{\text{Rh-P}}$ coupling. In addition, the room-temperature ^1H NMR spectra of **5** and **6** show a single *tert*-butyl resonance integrating to 27 protons, indicating that all three CN^tBu ligands remain bound in solution, albeit in a fluxional manner. Variable-temperature ^1H NMR, depicted in Figure 3.4 for the *tert*-butyl regions of complexes **5** and **6**, shows the evolution of two distinct *tert*-butyl resonances at low temperature, with a 2:1 (upfield: downfield) integration ratio. This behavior indicates that the four- and five-coordinate M^0 sites exchange slowly at low temperature, though even as low as $-80\text{ }^\circ\text{C}$ the two CN^tBu ligands at the five-coordinate site rapidly exchange. For both complexes the remaining ^1H resonances are minimally perturbed as the temperature is altered. Variable-temperature $^{31}\text{P}\{^1\text{H}\}$ NMR spectra demonstrate considerable broadening as the temperature is lowered, but a single resonance is observed over the entire temperature range.

3.2.4 Chlorine Oxidation of **1** and **2**

Chlorine oxidation of **1** and **2** was studied, using PhICl_2 as a solid chlorine surrogate, and disparate structures are observed in each case. Scheme 3.5 summarizes the products that are



Scheme 3.5. Oxidation of **1** and **2** with PhICl_2 . Isolated yields are listed in parentheses.

observed upon chlorine oxidation. Oxidation of dirhodium complex **1** produces a mixture of isomeric products in solution, of which two were crystallographically identified. The major product, which can be isolated in pure form as red crystals by selective crystallization (or as discussed in the next chapter, by aerobic oxidation), is the pseudo- C_{2h} -symmetric complex $\text{Rh}_2^{\text{II,II}}(\text{tfepma})_2(\text{CN}^t\text{Bu})_2\text{Cl}_4$ (**7a**). In both solution and the solid state, this $\text{Rh}_2^{\text{II,II}}$ complex (excluding $-\text{OCH}_2\text{CF}_3$ groups) adopts a nearly centrosymmetric structure where both Rh^{II} sites are equivalent. The $^{31}\text{P}\{\text{H}\}$ NMR spectrum of **7a**, recorded in CD_3CN , shows a single resonance, located at 113.8 ppm. In addition, the ^1H NMR spectrum, which contains a single *tert*-butyl resonance, and IR spectrum, which shows a single $\text{C}\equiv\text{N}$ stretch (2200 cm^{-1}), are indicative of oxidation of the complex to a valence-symmetric species. The crystal structure shown in Figure 3.5 confirms the spectral findings of a bimetallic core that possesses pseudo- C_{2h} symmetry, with two octahedral Rh^{II} centers related by an approximate inversion center at the metal–metal centroid. The $\text{Rh}(1)\text{--Rh}(2)$ distance of $2.7391(3)\text{ \AA}$ establishes that the rhodium–rhodium bond is maintained. A second two-electron oxidized isomer (**7b**) was obtained in one instance as dark green crystals, though its preparation was not reproducibly achieved. This isomer, whose structure was solved but did not refine satisfactorily, is formulated as the two-electron mixed-valent complex $\text{Rh}_2^{\text{I,III}}(\text{tfepma})_2(\text{CN}^t\text{Bu})_2\text{Cl}_4$ (**7b**). An asymmetric distribution

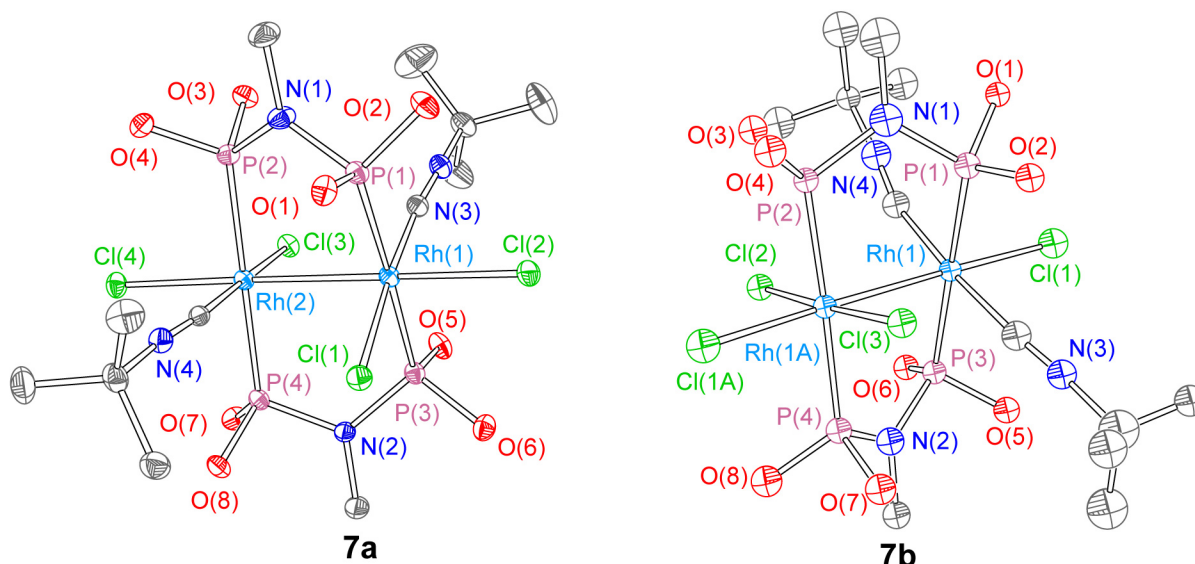


Figure 3.5. X-ray crystal structures of **7a** and **7b**. Ellipsoids are shown at the 50% probability level with $-\text{CH}_2\text{CF}_3$ groups and hydrogen atoms omitted for clarity. The atoms in **7b** are represented as isotropic spheres.

of the isocyanide and chloride ligands is evident in the preliminary isotropic crystal structure of Figure 3.5, which shows an approximate C_{2v} symmetry for the bimetallic core. The Rh(1)–Rh(1A) distance remains quite short, at 2.720(2) Å.

In contrast, treatment of diiridium complex **2** with PhICl_2 leads to formation of a valence-symmetric complex **8** which lacks the inversion center found in dirhodium analogue **7a**. The $^{31}\text{P}\{^1\text{H}\}$ NMR spectrum of $\text{Ir}_2^{\text{II,II}}(\text{tfepma})_2(\text{CN}^t\text{Bu})_2\text{Cl}_4$ (**8**) reveals two closely spaced multiplets, which are related by a mirror plane and suggestive of an AA'BB' spin system for which 12 of the possible 24 lines²¹ are resolved. A very minor product (< 5%), present in both the crude reaction mixture and isolated material, appears as a singlet in the $^{31}\text{P}\{^1\text{H}\}$ spectrum, consistent with a small amount of the centrosymmetric isomer being formed. The ^1H NMR spectrum also reveals asymmetry—two distinct *tert*-butyl peaks, each integrating to nine protons, are evident.

The solid-state X-ray structure of **8** presented in Figure 3.6 confirms the asymmetric structure predicted by NMR. Two nearly octahedral Ir^{II} centers separated by an intermetallic distance of 2.7774(3) Å are observed. The chloride ligands about Ir(1) maintain the *cis* arrangement found in $\text{Ir}_2^{0,\text{II}}$ complex **2** (see Figure 3.1), whereas on Ir(2) the chloride ligands are *trans* to one another, with an axial CN^tBu ligand. The complex has no symmetry element linking the two Ir^{II} centers, clearly lacking the inversion center found in the $\text{Rh}_2^{\text{II,II}}$ analogue **7a**.

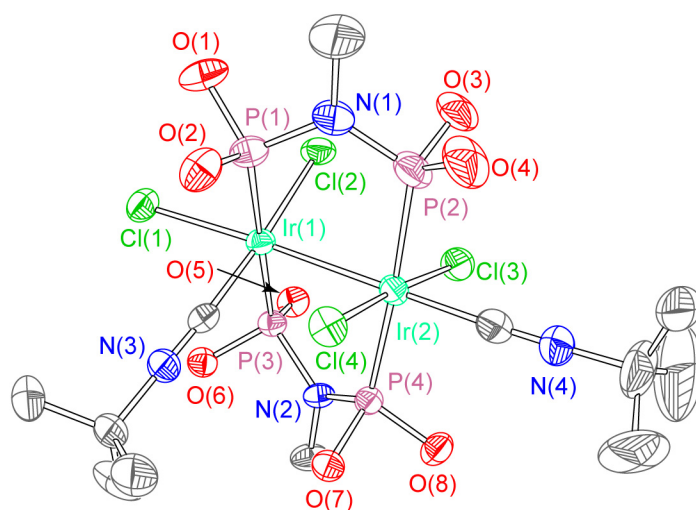
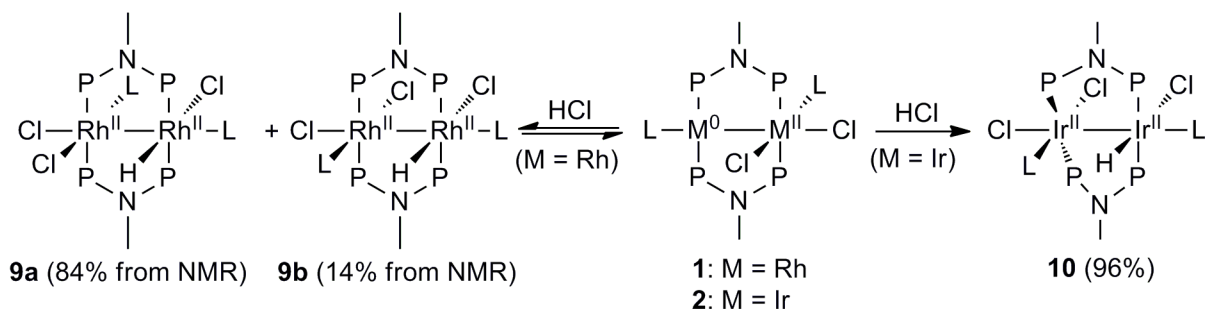


Figure 3.6. X-ray crystal structure of **8**. Ellipsoids are shown at the 50% probability level with $-\text{CH}_2\text{CF}_3$ groups and hydrogen atoms omitted for clarity.



Scheme 3.6. HCl addition to **1** and **2**. Yields are listed in parentheses; those for **9a/9b** are from a reaction with 25 eq of HCl.

3.2.5 Protonation of **1** and **2** with HX (X = Cl⁻, OTs⁻)

Complexes **1** and **2** oxidatively add HCl to form bimetallic hydrido-chloride complexes, as depicted in Scheme 3.6. In the case of dirhodium complex **1**, HCl addition is clearly reversible. Treatment of **1** with HCl results in an equilibrium between two isomeric hydride-containing products and **1**. With a single equivalent of HCl, only ~ 60% conversion is observed. By using an excess of HCl (25 eq), near quantitative conversion to Rh₂^{II,II}(tfepma)₂(CN^tBu)₂Cl₃H (**9a** and **9b**) results. The ³¹P{¹H} and partial ¹H NMR spectra of the reaction products are shown in Figure 3.7. Integration of the ¹H NMR spectrum reveals that the major isomer, **9a**, is formed in 84% yield along with 14% of **9b** and ~ 2% of unreacted **1**. The downfield region of the ¹H spectrum shows that each isomer contains two chemically inequivalent CN^tBu resonances. The Rh–H resonances shown in Figure 3.7 appear as doublets of triplets, arising from coupling to two phosphorus atoms and the 100% abundant *I* = 1/2 ¹⁰³Rh nucleus. The ¹J_{Rh–H} values are 13.3 Hz in

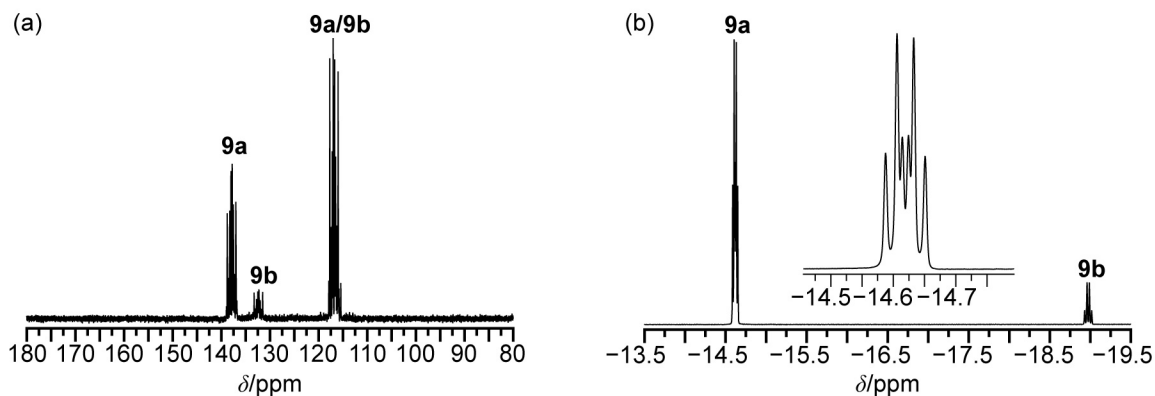


Figure 3.7. (a) ³¹P{¹H} and (b) low-frequency ¹H NMR spectra of **9a** and **9b**, prepared by treating **1** with 25 eq. of HCl gas in THF-d₈. The inset in (b) is an expansion of the Rh–H resonance of **9a**. Spectra were recorded at 20 °C at 202.5 MHz (³¹P) and 500 MHz (¹H).

9a and 14.5 Hz in **9b**, whereas $^2J_{\text{P-H}}$ coupling constants are 9.1 Hz in **9a** and 14.5 Hz in **9b**. By virtue of the equal $^1J_{\text{Rh-H}}$ and $^2J_{\text{P-H}}$ values, the hydride resonance for **9b** appears as a quartet. The observed splitting patterns with relatively small $^2J_{\text{P-H}}$ values indicate that the hydride ligand in both isomers is *cis* to two equivalent phosphorus nuclei.²² When a solution of **9a** and **9b** is concentrated to dryness and then redissolved, the $^{31}\text{P}\{^1\text{H}\}$ NMR spectrum shows a mixture of both isomers of **9** and $\text{Rh}_2^{0,\text{II}}$ complex **1** (ca. 40%), confirming the reversible nature of HCl addition to **1**.

The major isomer (**9a**) was crystallized; its structure is depicted in Figure 3.8. Two octahedral Rh^{II} centers are evident, and the $\text{Rh}(1)\text{--Rh}(2)$ distance of 2.7560(2) Å is once again consistent with a single bond. The hydride ligand on $\text{Rh}(2)$ is situated *trans* to a chloride and *syn* with respect to the chloride on $\text{Rh}(1)$. The second isomer **9b** was not crystallographically characterized, but the NMR data (vide infra) are consistent with an analogous structure where the hydride and chloride on $\text{Rh}(2)$ are exchanged with one another, though any structure featuring a hydride *cis* to both geminal phosphorus atoms is possible.

HCl addition to diiridium complex **2** is much more favorable thermodynamically, as compared to **1**. By treating **2** with either HCl or lutidinium hydrochloride (LutH^+Cl^-), a single

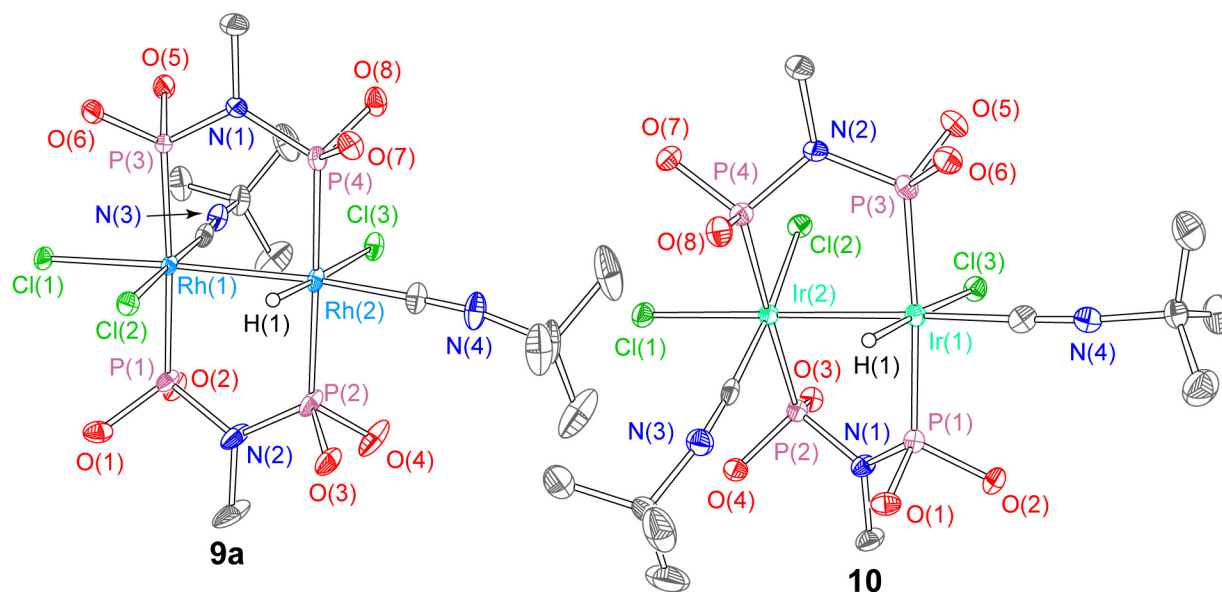
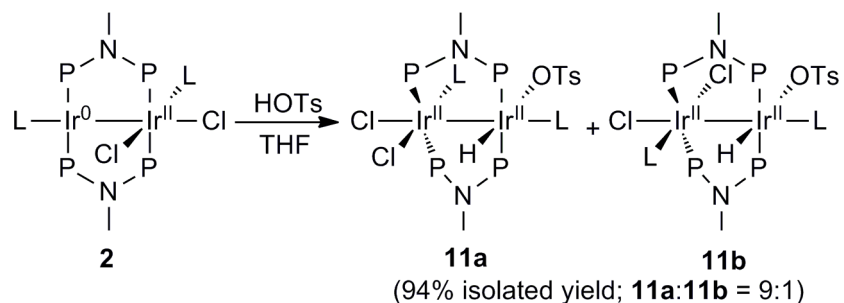


Figure 3.8. X-ray crystal structures of **9a** and **10**. Ellipsoids are drawn at the 50% probability level. Solvent molecules, carbon-bound hydrogen atoms and $-\text{CH}_2\text{CF}_3$ groups are omitted for clarity.

isomer of $\text{Ir}_2^{\text{II,II}}(\text{tfepma})_2(\text{CN}^t\text{Bu})_2\text{Cl}_3\text{H}$ (**10**) is formed rapidly and quantitatively. The $^{31}\text{P}\{^1\text{H}\}$ NMR spectrum shows two multiplets attributed to an AA'BB' spin system; in this case 20 of the 24 possible lines are resolved. The most definitive evidence for the presence of an iridium-bound hydride ligand comes from the ^1H NMR, which shows a 1:2:1 triplet at -20.69 ppm. This hydride peak integrates to one proton, and the observed $^2J_{\text{P-H}}$ of 16.0 Hz indicates that the hydride is positioned *cis* to two equivalent phosphorus atoms. The solid-state structure of **10**, also shown in Figure 3.8, is analogous to that of tetrachloride complex **8**, with a hydride replacing one of the chlorides. Both Ir^{II} centers are again octahedral, and hydride ligand H(1) is arranged *trans* to Cl(3) and *syn* with respect to the CN^tBu ligand on the adjacent Ir^{II} center. The metal–metal distance is $2.7821(3)$ Å, and the strong *trans*-influence of the hydride ligand is readily apparent. The Ir(1)–Cl(3) bond, situated *trans* to the hydride, has a distance of $2.5021(11)$ Å, which is substantially longer than the other equatorial chloride bond distance [Ir(2)–Cl(2)] ($d = 2.4002(10)$ Å). In comparing structures **9a** and **10**, it is worth noting the different stereochemistries of the crystalline isomers; the hydrides in **9a** and **10** reside on opposite sides of the metal–metal axis. In other words, the proposed *minor* dirhodium hydride isomer **9b**, which is unobserved crystallographically, is isostructural to **10**, the exclusive isomer that is formed by HCl addition to diiridium complex **2**.

Whereas dirhodium complex **1** is unreactive to *p*-toluenesulfonic acid (HOTs), showing no sign of hydride formation even with a tenfold excess of acid, addition of HOTs to **2** proceeds readily (Scheme 3.7). When the reaction between **2** and HOTs is carried out in acetonitrile, the ^1H NMR reveals two hydride-containing products in a ca. 1:1 ratio. By changing the reaction solvent to THF, a 9:1 ratio of the two products is isolated. The major isomer of $\text{Ir}_2^{\text{II,II}}(\text{tfepma})_2(\text{CN}^t\text{Bu})_2\text{Cl}_2\text{H}(\text{OTs})$ (**11**) can be crystallized. The structure of major product **11a**,



Scheme 3.7. Addition of HOTs to **2**.

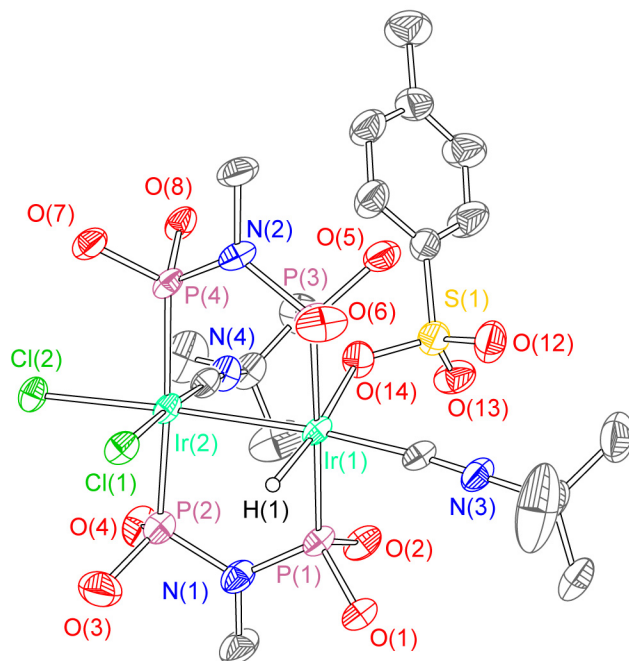
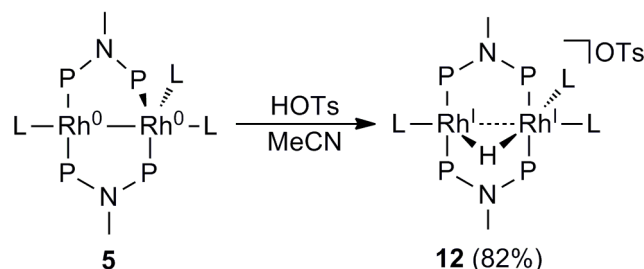


Figure 3.9. X-ray crystal structure of **11a**. Ellipsoids are shown at the 50% probability level with solvent molecules, $-\text{CH}_2\text{CF}_3$ groups and carbon-bound hydrogen atoms are omitted.

which is shown in Figure 3.9, bears many similarities to its HCl-addition analogue, namely an axial CN^tBu ligand and a *trans* arrangement of the H(1) and OTs^- ligands at the site of protonation. The major difference between the structures of **10** and **11a** is the position of the hydride relative to the CN^tBu ligand on the adjacent iridium; for **11a**, the hydride is in an *anti* conformation relative to the vicinal CN^tBu . Additionally, the metal–metal distance in **11a** of 2.7573(5) Å is slightly contracted relative to **10**. The $^{31}\text{P}\{^1\text{H}\}$ NMR spectrum of tosylate complex **11a** is again characteristic of an AA'BB' spin system, and its ^1H NMR spectrum shows an Ir–H resonance at –20.00 ppm, only marginally upfield relative to the hydride resonance of **10**. The observed $^2J_{\text{P-H}}$ coupling constant in **11a** is identical to that of **10** at 16.0 Hz. As alluded to above, when **11** is isolated ca. 10% of a minor isomer is present. The minor product **11b** shows a hydride resonance at –20.71 ppm in the ^1H spectrum, and yet again the two-bond proton-phosphorus coupling constant is 16.0 Hz, placing the hydride *cis* to its neighboring phosphorus nuclei. The remaining ^{31}P and ^1H NMR features of the minor isomer are virtually identical to those of the major product, suggesting an identical structure but with the hydride flipped to the other side of the metal–metal axis to position it *syn* to the vicinal CN^tBu . This isomerization will produce the same structure as that of hydrido-chloride complex **10**, but with



Scheme 3.8. Synthesis of **12** by HOTs addition to **5**. Isolated yield is listed in parentheses.

the chloride *trans* to the hydride substituted for OTs⁻. We cannot rule out other possibilities such as intermetallic exchange of Cl⁻ and OTs⁻, though the simple isomerization described above seems most plausible for the structure of the minor product.

3.2.6 Protonation of **5** with HOTs

Reactions involving M₂^{0,0} complexes **5** and **6** were explored with a variety of acids, though in most cases, complex and intractable mixtures of products were formed. The lone exception, described in Scheme 3.8, was the exclusive production of [Rh₂^{I,I}(tfepma)₂(CN^tBu)₃(μ-H)](OTs) (**12**), obtained from the treatment of Rh₂^{0,0} complex **5** with one equivalent of HOTs in thawing acetonitrile. The crystal structure of **12** is depicted in Figure 3.10. The position of the hydride ligand could not be located precisely, and the refinement statistics were indistinguishable if the hydride was modeled either as bridging or as a terminal

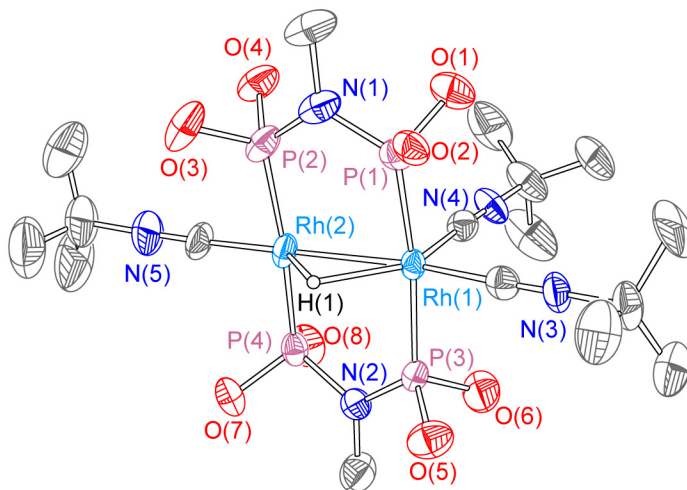


Figure 3.10. X-ray crystal structure of the cation of **12**. Ellipsoids are shown at the 50% probability level with -CH₂CF₃ groups, the outer-sphere tosylate anion and carbon-bound hydrogen atoms omitted for clarity.

hydride on Rh(1). However, on the basis of the NMR data (vide infra), complex **12** is assigned as a $\text{Rh}^{\text{I}}\cdots\text{Rh}^{\text{I}}$ μ -hydride species, as shown in Figure 3.10. All three CN^tBu ligands remain bound, and the intermetallic distance of 2.7449(11) Å compares favorably with other hydride-bridged dirhodium complexes spanned by two diphosphines.^{23–25} The OTs^- counterion is outer-sphere and does not interact with the cationic complex in the crystal structure.

Both the $^{31}\text{P}\{^1\text{H}\}$ and the ^1H NMR spectra support the assignment of a valence-symmetric structure for **12**. The ^{31}P NMR spectrum shows a single, symmetric multiplet centered at 150.7 ppm with a splitting pattern reminiscent of $\text{Rh}_2^{0,0}$ precursor **6**. This contrasts the expected four-spin, second-order system expected for a two-electron mixed-valent state (vide supra). In the room-temperature ^1H NMR spectrum, a single, sharp *tert*-butyl resonance is observed, which splits into two distinct peaks at low temperature, as shown in Figure 3.11. The most definitive evidence for a bridging hydride ligand comes from the low-frequency region of the ^1H NMR spectrum. As shown Figure 3.12a, in the ^1H NMR spectrum the rhodium hydride resonance appears as a complex, symmetric multiplet, with nine lines clearly resolved and an additional four lines appearing as shoulders. In the $^1\text{H}\{^{31}\text{P}\}$ spectrum (Figure 3.12b), only coupling to ^{103}Rh is observed, and a triplet splitting pattern results. This triplet multiplicity indicates equal coupling to both rhodium nuclei, with a $^1J_{\text{Rh-H}}$ of 14.8 Hz, and accordingly places the hydride in a bridging position. The remainder of the multiplet in the phosphorus-coupled ^1H spectrum is generated by considering equal coupling of the hydride nucleus to all four phosphorus nuclei, with an observed $^2J_{\text{P-H}}$ of 8.5 Hz. This value is considerably smaller than the $^2J_{\text{P-H}}$ coupling constants in bimetallic complexes of similar architectures featuring terminal

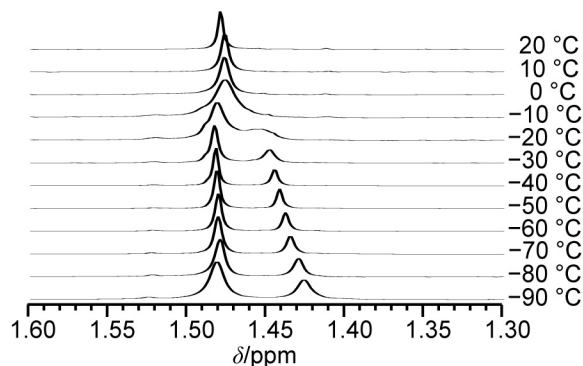


Figure 3.11. Variable-temperature ^1H NMR spectra for complex **12**, showing the *tert*-butyl resonances. Spectra were recorded in THF-d_8 at 500 MHz.

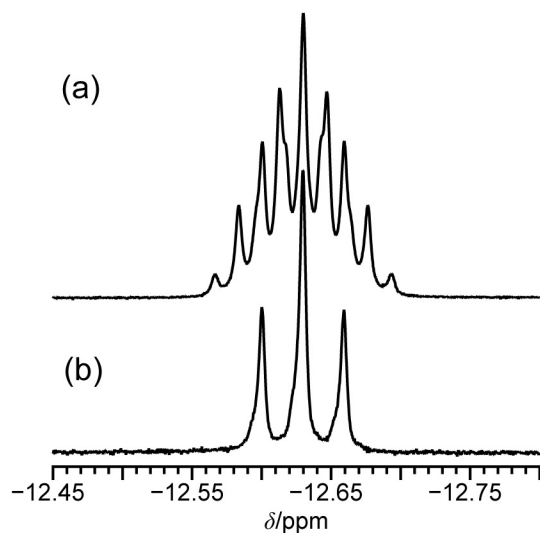
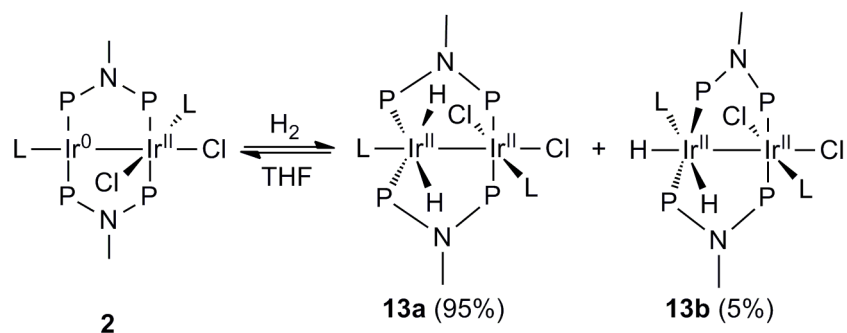


Figure 3.12. ^1H (a) and $^1\text{H}\{^{31}\text{P}\}$ (b) NMR spectra of **12**, showing the Rh–H resonance. Spectra were recorded in CD_3CN at 500 MHz and 293 K.

hydride ligands.^{9,26} This arrangement of coupling constants would give a maximum of 15 lines in a triplet-of-quintets pattern, 13 of which are resolved in the phosphorus-coupled spectrum.

3.2.7 Hydrogenation of **2**

When a solution of **2** in THF-d_8 is introduced to ca. 1.5 atm of H_2 , the bright orange color rapidly fades to give a nearly colorless solution. Scheme 3.9 summarizes the outcome of this reversible hydrogenation reaction. $^{31}\text{P}\{^1\text{H}\}$ and ^1H NMR spectroscopy clearly show clean conversion to two isomers of $\text{Ir}_2^{\text{II,II}}(\text{tfepma})_2(\text{CN}^t\text{Bu})_2\text{Cl}_2(\text{H})_2$ (**13**), with the two isomers forming in a ca. 19:1 ratio. The low-frequency region of the ^1H NMR spectrum, reproduced in Figure 3.13, gives some insight into the structural differences between the two isomers. The major product (**13a**) shows a complex, asymmetric multiplet integrating to two protons centered at ca.



Scheme 3.9. Hydrogenation of **2**. NMR yields are listed in parentheses.

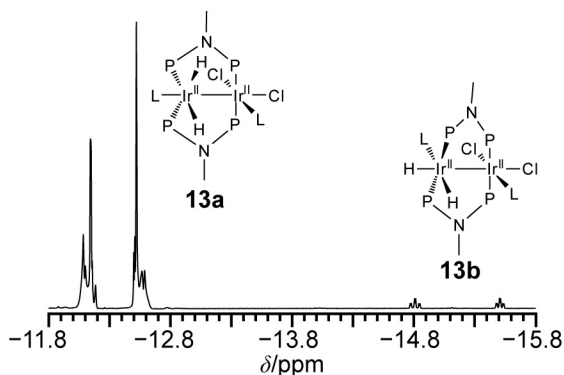


Figure 3.13. Low-frequency region of the ^1H NMR spectrum of **13**, showing the Ir–H resonances for the major and minor isomers. The structure of the major isomer and a likely structure of the minor isomer are shown near the peaks they are assigned to.

–12.3 ppm. The large 187 Hz splitting between the two most intense peaks suggests the presence of *trans* $^2J_{\text{P-H}}$ coupling. Though the precise structure of **13a** was not elucidated from NMR spectra, it has been structurally characterized by X-ray crystallography, described below.

For the minor product (**13b**), the two hydride ligands are chemically inequivalent, with a straightforward triplet-of-doublets splitting pattern for each resonance. The two peaks have slightly different $^2J_{\text{P-H}}$ coupling constants—the downfield resonance (–14.80 ppm) has a value of 17.9 Hz whereas the upfield resonance (–15.50 ppm) is coupled to phosphorus with a 13.8 Hz coupling constant. These two values indicate that each of the inequivalent hydrides is arranged *cis* to the two adjacent phosphorus nuclei. The doublet splitting results from $^2J_{\text{H-H}}$ coupling of the two hydride ligands and a coupling constant of 4.6 Hz indicates a *cis* arrangement of the two hydrides, as observed for numerous other *cis*-dihydride complexes of iridium.^{27–31} One of the two resonances for this minor isomer is clearly visible in the $^{31}\text{P}\{^1\text{H}\}$ NMR spectrum, and its appearance as an AA'XX' multiplet suggests a *trans* arrangement of the two phosphorus nuclei at each iridium. A likely structure for this minor product is included in Scheme 3.9 and Figure 3.13, though a structure in which the equatorial hydride is switched with the CN^tBu (L) *trans* to it would also be consistent with the spectral data. Solutions of **13** are unstable with respect to H₂ loss. The orange color and NMR features of Ir₂^{0,II} complex **2** are restored by repeated freeze-pump-thaw cycling of a solution of **13** or by removing all volatiles and drying in vacuo.

The major isomer **13a** was crystallized from CD₃CN under an H₂ atmosphere and its structure has been determined unequivocally by single-crystal X-ray diffraction, as shown in

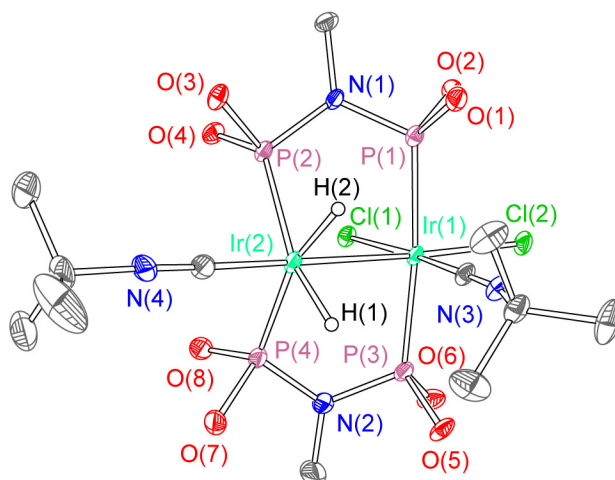
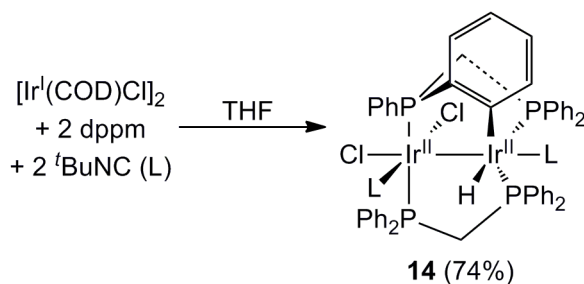


Figure 3.14. X-ray crystal structure of **13a**. Ellipsoids are shown at the 50% probability level with $-\text{CH}_2\text{CF}_3$ groups and carbon-bound hydrogen atoms omitted for clarity.

Figure 3.14. Both iridium centers are six-coordinate, with a *cis*- P_2 , *cis*- H_2 geometry at Ir(2). The geometry about Ir(2) is substantially distorted from octahedral, marked by a $\text{P}(2)\text{--Ir}(2)\text{--P}(4)$ angle of $118.46(5)^\circ$ and a $\text{H}(1)\text{--Ir}(2)\text{--H}(2)$ angle of $79(3)^\circ$. The $\text{H}(1)\text{--H}(2)$ distance is $2.04(7) \text{ \AA}$, with an $\text{Ir}(1)\text{--Ir}(2)$ bond distance of $2.7487(3) \text{ \AA}$ similar to the other metal–metal-bonded $\text{Ir}_2^{\text{II,II}}$ complexes described herein.

3.2.8 Formation of a Bimetallic Iridium Hydride Complex by Cyclometallation

In the course of preparing $\text{M}_2^{0,\text{II}}$ complexes **1** and **2**, we sought similar complexes bearing other bridging phosphine ligands. Reaction of $[\text{Ir}^{\text{I}}(\text{COD})\text{Cl}]_2$ with two equivalents of *dppm* and two equivalents of CN^tBu in THF leads to immediate formation of a dark green solution, followed by the gradual deposition of a cream-colored solid, identified spectroscopically and crystallographically as $\text{Ir}_2^{\text{II,II}}(\text{dppm})(\text{PPh}(o\text{-C}_6\text{H}_4)\text{CH}_2\text{PPh}_2)(\text{CN}^t\text{Bu})_2\text{Cl}_2\text{H}$ (**14**). This reaction is shown in Scheme 3.10. Complex **14** bears the expected stoichiometry but involves an



Scheme 3.10. Synthesis of cyclometallated complex **14**.

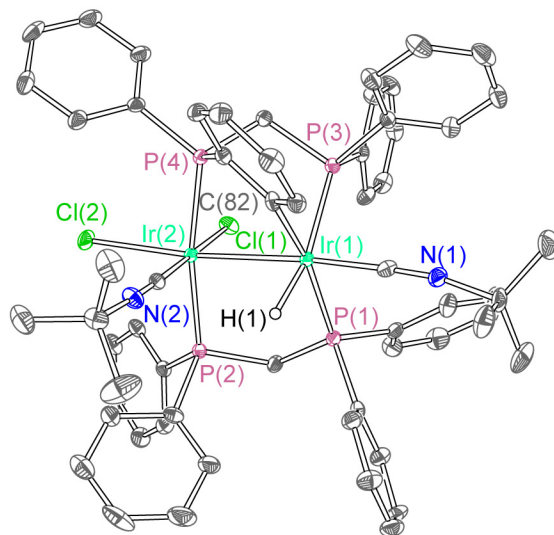


Figure 3.15. X-ray crystal structure of **14**. Ellipsoids are shown at the 50% probability level with the solvent molecule, $-\text{CH}_2\text{CF}_3$ groups and carbon-bound hydrogen atoms omitted for clarity.

intermetallic cyclometallation of one dppm ligand. The solid-state structure is depicted in Figure 3.15. The most noteworthy feature is the orthometallation of a phenyl ring bonded to P(4) onto the opposite iridium site, Ir(1). The phenyl and hydride ligands are arranged *cis* to one another, and again the geometry is distorted from octahedral. The P(1)–Ir(1)–P(3) angle is $109.83(3)^\circ$ whereas the C(82)–Ir(1)–H(1) angle is $81.4(13)^\circ$, giving a coordination geometry similar to that of **13a**. The Ir(1)–Ir(2) distance is $2.7928(4) \text{ \AA}$.

Complex **14** suffers from limited solution stability, decomposing to an intractable mixture of products within hours. However, the NMR spectra of **14** do suggest that prior to decomposition, the solid-state structure is maintained in solution, and that the C–H activation is irreversible at room temperature. The $^{31}\text{P}\{^1\text{H}\}$ NMR spectrum shows three distinct chemical environments for the phosphorus nuclei, with complex multiplicity in all of the peaks. In addition to the expected ^1H NMR resonances arising from dppm and CN^tBu protons, a doublet of doublets integrating to one proton is seen at -10.69 ppm for the iridium hydride. The $^2J_{\text{P-H}}$ values of 163 Hz and 19.1 Hz are indicative of coupling of the hydride nucleus to a *trans* and *cis* phosphorus nucleus, respectively. Furthermore, the dppm $-\text{CH}_2-$ resonances are each split into two distinct frequencies, suggestive of the very rigid binding mode of the bridging ligands.

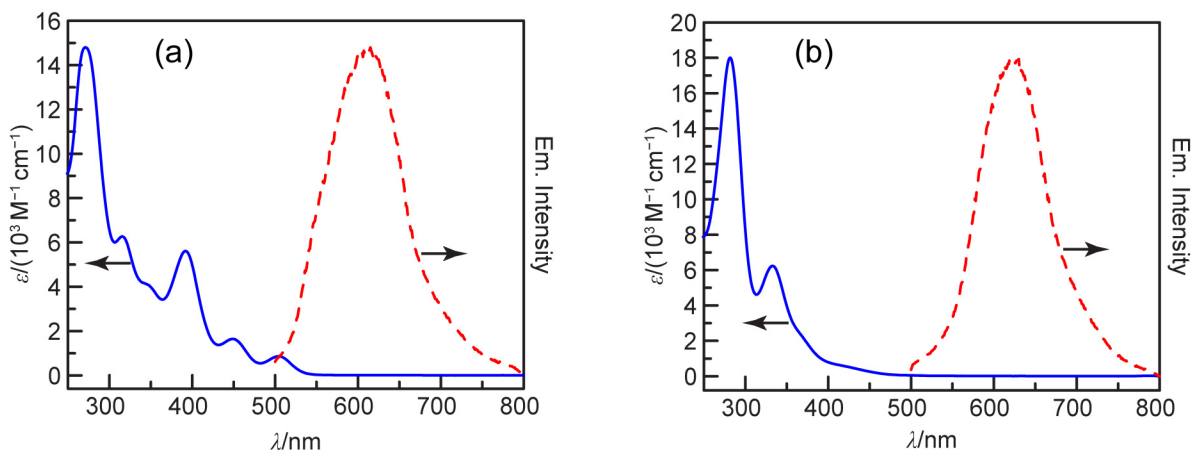


Figure 3.16. Electronic absorption (—, blue) and emission (---, red) spectra of **2** (a) and **8** (b). The absorption spectra were recorded at 295 K in CH₃CN, the emission spectra were recorded at 77 K in 2-MeTHF with $\lambda_{\text{ex}} = 325$ nm (a) and 280 nm (b).

3.2.9 Electronic Absorption and Emission Spectra

Excepting complexes **3** and **14**, which are unstable in dilute solution, the UV-vis absorption features of all new compounds were collected, and a brief summary is provided here. The electronic spectrum of Ir₂^{0,II} complex **2** (Figure 3.16a) is decidedly more complex than that of dirhodium analogue **1**. The former shows 6 closely spaced, overlapping but resolved bands, whereas the latter only has three distinct maxima. This complexity is mirrored in Ir₂^{0,II} complex **4** which is prepared by CN^tBu addition to **2** and presumed to have a similar solution structure in acetonitrile, giving rise to similar absorption features as discussed above. The absorption spectra of M₂^{0,0} complexes **5** and **6** also share similarities with one another, showing a maximum at 379 nm in dirhodium complex **5** and 383 nm in diiridium complex **6**, along with a shoulder towards the visible region and intense UV features. Complexes **8**, **10**, **11**, and **13** all feature a d⁷-d⁷ Ir₂^{II,II} core and have largely analogous absorption profiles. All show two distinct maxima and a shoulder, whose positions are marginally responsive to the ligand environment. As a representative example, the spectrum of Ir₂^{II,II}Cl₄ complex **8** is also shown in Figure 3.16b. In all cases the highest-energy peak is the wavelength of maximum absorption, which ranges between 267 nm (**13**) and 285 nm (**10**). In addition to the electronic absorption features described above, the Ir₂^{0,II} and Ir₂^{II,II} complexes **2**, **3**, **8**, **10** and **11** are emissive at 77 K in 2-methyltetrahydrofuran solution. The emission bands are at ca. 600 nm, with maxima at 613 nm (**2**), 598 nm (**3**), 624 nm (**8**), 641 nm (**10**) and 582 nm (**11**). For the Ir₂^{II,II} complexes, the relative energies of the emission

maxima track well with the energy of the absorption maxima, and in all cases the large Stokes shifts suggest emission from a triplet excited state.

3.3 Discussion

Two-electron mixed-valent dirhodium and diiridium complexes can serve as platforms for a diverse range of chemistries, including photocatalytic H₂ production,^{1,2} multi-electron photochemistry,^{3,4} reversible H₂ addition,¹¹ C–H activation,³² and other organometallic chemistry.³³ In all of these previous examples, the M₂^{0,II} complexes contain M⁰ centers that are five-coordinate, precluding reactivity at this reduced metal site. It was reasoned that addition reactions could be facilitated by preparing two-electron mixed-valent group 9 bimetallic complexes with four-coordinate M⁰ sites. Complexes **1** and **2**, which meet this criterion, assemble readily when [M^I(COD)Cl]₂ (M = Rh, Ir) is treated with two equivalents of tfepma and two equivalents of CN^tBu. The net result is valence disproportionation of the M₂^{I,I} precursor to yield M₂^{0,II}(tfepma)₂(CN^tBu)₂Cl₂ [M = Rh (**1**), Ir (**2**)]. The coordinative unsaturation at the Ir⁰ site in **2** drives the binding of donor ligands such as CN^tBu to furnish complex **4a**. In the solid state, **4a** contains three bound CN^tBu molecules, indicating that the open coordination site at the Ir⁰ center in **2** can accept an additional ligand. However, the solution behavior of **4**, and the disparate reactivity of Rh₂^{0,II} complex **1** towards CN^tBu revealed some unexpected results concerning ligand addition and substitution. When **1** is treated with CN^tBu, the broadened NMR features suggest reversible binding to form **3**. Crystals of **3** revealed the unexpected structure shown in Figure 3.2, where the reaction results in ligand substitution instead of addition. The equatorial Cl[−] ligand at the Rh^{II} site is displaced by the incoming CN^tBu, maintaining the square-planar Rh⁰ and octahedral Rh^{II} geometries that are found in **1**. This suggests that the electrophilicity of the Rh^{II} center dictates the reactivity, as opposed to the vacant coordination site at Rh⁰. When crystals of **4a** are dissolved in acetonitrile, the NMR and electronic absorption spectra suggest isomerization to a structure analogous to **3**, giving monocationic complex **4b** which retains a four-coordinate Ir⁰ center. These results reveal that in the two-electron mixed-valent state a four-coordinate M⁰ center is quite favorable, even when the possibility of forming a five-coordinate center exists.

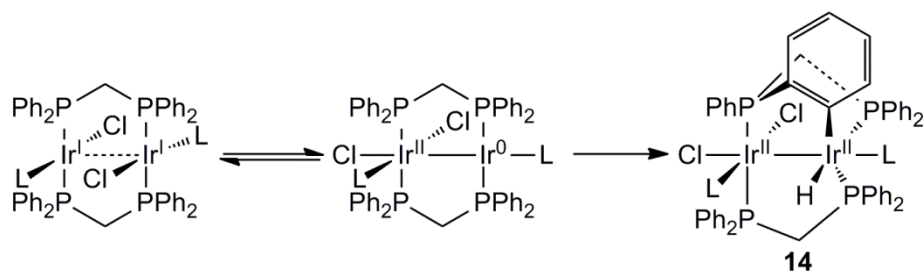
Our group has demonstrated that multi-electron photocatalytic processes are enabled when the bimetallic catalyst can span multiple oxidation states differing by two electrons each.^{1,2}

Thus, the ability to prepare a homologous series of d^7-d^7 , d^7-d^9 , and d^9-d^9 complexes motivates future studies of multi-electron catalysis supported on the complexes described here. Indeed, $M_2^{0,II}$ complexes **1** and **2** may be both reduced and oxidized by two electrons to prepare the full suite of oxidation states. The initial goal was to reduce **1** and **2** to complexes of the stoichiometry $M_2^{0,0}(tfepma)_2(CN^tBu)_2$, which would feature two four-coordinate M^0 sites. However, such species are not observed, and isostructural complexes $M_2^{0,0}(tfepma)_2(CN^tBu)_3$ [$M = Rh$ (**5**), Ir (**6**)], are instead obtained where an additional equivalent of CN^tBu is required to stabilize the fully reduced core. Nevertheless, the structures of **5** and **6** (Figure 3.3) each reveal a single four-coordinate M^0 center, motivating further study of demanding addition reactions on these highly reducing species. Oxidation of **1** and **2** with $PhICl_2$ produces complexes with three distinct geometries. In the case of the dirhodium system, two valence isomers are observed, where one is best formulated as retaining two-electron mixed valency in a $Rh_2^{1,III}$ core (**7b**), and the other is a pseudocentrosymmetric $Rh_2^{II,II}$ core (**7a**). Oxidation of diiridium complex **2**, on the other hand, furnishes $Ir_2^{II,II}(tfepma)_2(CN^tBu)_2Cl_4$ (**8**), which is valence-symmetric but is structurally distinct from its dirhodium analogue **7a**.

Having established a redox chemistry of **1** and **2**, routes for the preparation of hydride-containing complexes are available. Protonation reactions of isoelectronic valence-symmetric dirhodium A-frame complexes have been shown to give products featuring a bridging hydride, where the net reaction is the protonation of the metal-metal bond.²⁴ The reactivity of our first-generation $Ir_2^{0,II}$ complexes¹¹ arises from a vacant axial site on the M^{II} center. Addition of reagents such as HX and H_2 results in oxidative addition across the metal-metal bond, with the two-electron mixed valency being preserved in the products (see Scheme 3.1). In contrast, addition of HCl (to **1** and **2**), $HOTs$ (to **2**) or H_2 (to **2**) furnishes products suggestive of addition to the M^0 site, with the M^{II} center unperturbed. As seen in the crystal structures of $M_2^{II,II}(tfepma)_2(CN^tBu)_2Cl_2HX$ [$M = Rh$: $X = Cl$ (**9a**); $M = Ir$: $X = Cl^-$ (**10**), OTs^- (**11a**)], the hydride and X^- ligand situate in a *trans* configuration on the same metal center, and a valence-symmetric $M_2^{II,II}$ core ensues. Only terminal hydride products are observed for these acid-addition reactions to the two-electron mixed-valent precursors. $Ir_2^{0,II}$ complex **2** reacts much more readily with HX than its dirhodium analogue **1**. HCl addition to **1** to furnish hydride complexes **9a/b** is decidedly reversible whereas in the case of **2** a single equivalent of HCl begets quantitative formation of hydride-containing **10**. In addition, $Ir_2^{II,II}Cl_3H$ complex **10** is

conveniently prepared by protonation of **2** with solid HCl surrogate LutH^+Cl^- , though dirhodium complex **1** is completely unreactive to this reagent. This difference in reactivity is likely tied to the stronger iridium–hydride bond strengths as compared to rhodium.³⁴ Attempted protonation reactions of $\text{M}_2^{0,0}$ complexes **5** and **6** were generally not fruitful, though $\text{Rh}_2^{0,0}$ complex **5** does react readily with HOTs to furnish μ -hydride complex **12** (Scheme 3.8 and Figure 3.10). This outcome is largely reminiscent of earlier examples of protonation reactions involving other group 9 $\text{M}_2^{0,0}$ complexes, where the addition of acid also gives a hydride-bridged product and an outer-sphere conjugate base anion.^{23,35,36}

The hydrogenation reaction of **2** is also distinct from that of previous diiridium constructs. Several products have been identified from hydrogenation reactions of valence-symmetric diiridium complexes, as reported primarily by the groups of Eisenberg and Cowie. Hydrogenation of a face-to-face diiridium(I) complex yields a vicinal dihydride product, where the two terminal hydride ligands are *syn* with respect to each other.³⁷ When diiridium A-frame complexes are treated with H_2 the thermodynamically stable species is once again a vicinal dihydride, though in this case the two H^- ligands occupy axial positions,^{37,38} it has since been shown that a geminal *cis*-dihydride forms initially which rearranges to this final product.^{39,40} In our earlier work on two-electron mixed-valent complexes,¹¹ summarized in Scheme 3.1, hydrogenation of the iridium–iridium bond was observed, producing a vicinal dihydride where the two-electron mixed valency was preserved in a formally $\text{Ir}^{\text{I}} \rightarrow \text{Ir}^{\text{III}}$ core. The addition of H_2 to **2**, where the coordinative unsaturation resides at the four-coordinate Ir^0 center, produces a result distinct from these previously characterized reactions. In the same vein as the HX-addition reactions, H_2 adds to a single metal center, resulting in two isomeric $\text{Ir}_2^{\text{II,II}}$ geminal *cis*-dihydride products **13a** and **13b**; the structure of major product **13a** is depicted in Figure 3.14. The minor product **13b** also features a *cis*-dihydride arrangement, as determined by the $^2J_{\text{H-H}}$ coupling constants in the ^1H NMR. On the basis of X-ray crystallography and ^1H NMR spectroscopy there is no evidence for rearrangement to vicinal dihydride isomers. The observed distance between the two hydrogen atoms is 2.04(7) Å, which represents a lower limit for this true interatomic distance, given the systematically short bonds to hydrogen that are observed in X-ray crystallography. Nonetheless, this value shows that the H–H bond is cleaved completely, and that the description of **13a** as a dihydride complex (and not an $\eta^2\text{-H}_2$ adduct) is valid, on the basis of comparisons to numerous other metal- H_2 structures.⁴¹ The *cis* arrangement of the



Scheme 3.11. Proposed cyclometallation mechanism for **14**.

hydride ligands in **13**, compared to the *trans* HX complexes described above, suggests the possibility of a different mechanism for H₂ and HX oxidative additions. H₂ addition is clearly reversible, and removal of the H₂ headspace from a solution of **13a/b** regenerates complex **2** cleanly.

A route to a diiridium hydride complex is also achieved from intramolecular cyclometallation (Scheme 3.10). With the bridging ligand dppm and reaction conditions otherwise identical to the synthesis of **2**, the complex Ir₂^{II,II}(dppm)(PPh(*o*-C₆H₄)CH₂PPh₂)(CN^tBu)₂Cl₂H (**14**) is formed as the final product. At early reaction time a dark green solution is observed, which is qualitatively indicative of an initial Ir^I...Ir^I product prior to the cyclometallation. The final product possesses an Ir^{II,II} core oxidation state with the expected stoichiometry (Figure 3.15). The cyclometallated binding mode of dppm seen in the structure of **14** has been observed in a Cp^{*}-ligated diiridium complex,⁴² where an *ortho* C–H bond was activated in a base-assisted fashion. Although the mechanism of cyclometallation of **14** has not been probed in detail, a plausible route is shown in Scheme 3.11. The initially formed Ir^I...Ir^I complex rearranges to an Ir₂^{0,II} state, and cyclometallation at the reactive Ir⁰ center yields **14**. Direct cyclometallation of Ir^I...Ir^I cannot be explicitly ruled out, though a more complex mechanism involving chloride-bridged intermediates and/or phosphine dissociation would be required to avoid hypercoordinate intermediate species.

3.4 Conclusions

The work contained in this chapter demonstrates a multifaceted reaction chemistry centered around coordinatively unsaturated two-electron mixed-valent dirhodium and diiridium complexes. It has been shown that stable complexes with d⁹–d⁹, d⁷–d⁹, and d⁷–d⁷ electron counts can all be prepared with the ligand framework employed here. In both the fully reduced d⁹–d⁹

and mixed-valent d^7 – d^9 states, a four-coordinate, unsaturated M^0 center is present, providing enticing platforms for the study of small-molecule activation chemistry, extending beyond the work presented here. In this chapter, three distinct routes to access hydride-containing products are outlined: addition of HX ($X = Cl^-$, OTs^-), addition of H_2 , and intramolecular cyclometallation. On account of the coordinative unsaturation at M^0 , both HX and H_2 oxidative addition furnish hydride-containing products with novel structures; these complexes are candidates for future HX-splitting schemes. In addition, many of the dirhodium and diiridium complexes described here, including hydrido-halide complexes **9** and **10**, are structurally analogous to one another, allowing for meaningful comparisons of their structures and reactivities. Though some stereochemical differences between dirhodium and diiridium complexes do present themselves in this new class of complexes, it may be possible to use the diiridium complexes, typically more stable and thermally robust, as structural analogues for more reactive and difficult-to-observe dirhodium complexes. With our previous suite of two-electron mixed-valent dirhodium and diiridium complexes, such structural homology was not achieved, and it was likely that the model complexes that were prepared were not faithful structural models to the catalytically active species. Our interest in bimetallic hydride-containing complexes is ongoing, as we continue to explore their reactivity and unveil new routes for their facile preparation, and the complexes whose preparations are described in this chapter further motivate these continued studies.

3.5 Experimental Details

3.5.1 General Considerations

All reactions involving air-sensitive materials were executed in a nitrogen-filled glovebox or on a high-vacuum manifold using solvents previously dried by passage through an alumina column under argon, after sparging with argon. The starting materials $[M^I(COD)Cl]_2$ ($M = Rh, Ir$; COD = 1,5-cyclooctadiene) and bis(diphenylphosphino)methane (dppm) were obtained from Strem Chemicals. 2,6-lutidine, HCl (1 M in Et_2O), bis(pentamethylcyclopentadienyl)cobalt(II) ($CoCp^*_2$), *p*-toluenesulfonic acid hydrate ($HOTs \cdot H_2O$), and *tert*-butylisocyanide (CN^tBu) were obtained from Sigma-Aldrich, whereas H_2 was purchased from Airgas. Anhydrous 2,6-lutidinium hydrochloride ($LutH^+Cl^-$) was prepared by adding anhydrous 2,6-lutidine to 1 M HCl/ Et_2O under nitrogen. The ligand

bis(bis(trifluoroethoxy)phosphino)methylamine (tfepma),⁴³ and PhICl_2 ⁴⁴ were prepared as described in the literature. Elemental analyses were performed by Midwest Microlab LLC or Quantitative Technologies Incorporated.

3.5.2 Physical Methods

NMR spectra were recorded at the MIT Department of Chemistry Instrumentation Facility on a Varian Mercury-300 NMR Spectrometer, operating at 121.5 MHz for ^{31}P acquisition, or a Varian Inova-500 NMR Spectrometer operating at 500 MHz for ^1H acquisition. $^{31}\text{P}\{^1\text{H}\}$ NMR spectra were referenced to an external standard of 85% D_3PO_4 and ^1H spectra were referenced to the residual proteo solvent resonances. UV-vis samples were prepared in a nitrogen-filled glovebox and spectra were recorded at 293 K in THF solutions in quartz cuvettes on a Varian Cary 5000 UV-vis-NIR spectrophotometer. Extinction coefficients were determined over a concentration range of $\sim 10^{-6}$ to 10^{-4} M, for which all compounds obeyed Beer's Law. IR spectra were recorded on a PerkinElmer Spectrum 400 FT-IR/FT-FIR Spectrometer outfitted with a Pike Technologies GladiATR attenuated total reflectance accessory with a monolithic diamond crystal stage and pressure clamp. Samples were suspended in Nujol® mineral oil for all IR measurements. Steady-state emission spectra were recorded on an automated Photon Technology International (PTI) QM 4 fluorimeter equipped with a 150 W Xe arc lamp and a Hamamatsu R928 photomultiplier tube. Excitation light was excluded with appropriate glass filters. Samples were housed in custom quartz EPR tubes with a ground-glass joint and Teflon plug. Solution samples were prepared in 2-methyltetrahydrofuran and freeze-pump-thaw degassed (4 cycles, 1×10^{-5} torr). The sample tubes were immersed in liquid N_2 in a quartz finger dewar prior to measurement.

3.5.3 Preparation of $\text{Rh}_2^{0,\text{II}}(\text{tfepma})_2(\text{CN}^t\text{Bu})_2\text{Cl}_2$ (1)

$[\text{Rh}^{\text{I}}(\text{COD})\text{Cl}]_2$ (348 mg, 0.706 mmol, 1.00 eq) was dissolved in 3 mL of CH_2Cl_2 in a 20-mL scintillation vial. A solution of tfepma (687 mg, 1.41 mmol, 2.00 eq) in 2 mL of CH_2Cl_2 was added at a fast dropwise rate, followed immediately by a solution of CN^tBu (117 mg, 1.41 mmol, 2.00 eq) in 2 mL of CH_2Cl_2 , added in a similar fashion. An additional 2 mL of CH_2Cl_2 was used to dissolve the residual tfepma and CN^tBu and ensure quantitative transfer to the reaction vessel. The resulting deep red solution was stirred for 3 h at room temperature,

during which time it lightened and some orange solid precipitated. The mixture was concentrated to < 3 mL in vacuo, and 17 mL of pentane was added to the stirred suspension to separate a light orange solid. The supernatant was decanted and the product dried in vacuo. Yield: 842 mg (84.2%). ^1H NMR (500 MHz, CD_2Cl_2) δ/ppm : 4.22–5.20 (br, m, 16H), 2.86 (pseudoquintet, 6H), 1.41 (br, s, 9H), 1.38 (br, s, 9H). $^{31}\text{P}\{^1\text{H}\}$ NMR (121.5 MHz, CD_2Cl_2) δ/ppm : 145.1 (m, 2P), 124.5 (m, 2P). UV-vis (THF): λ/nm ($\epsilon/(\text{M}^{-1} \text{cm}^{-1})$) 295 (19000), 328 (sh) (11000), 388 (4700). IR (Nujol): $\tilde{\nu}_{\text{C}\equiv\text{N}} = 2122, 2143 \text{ cm}^{-1}$. Anal. Calcd. For $\text{C}_{28}\text{H}_{40}\text{Cl}_2\text{F}_{24}\text{N}_4\text{O}_8\text{P}_4\text{Rh}_2$: C, 23.73; H, 2.84; N, 3.95. Found: C, 23.70; H, 2.73; N, 3.85.

3.5.4 Preparation of $\text{Ir}_2^{0,\text{II}}(\text{tfepma})_2(\text{CN}^t\text{Bu})_2\text{Cl}_2$ (2)

$[\text{Ir}^{\text{I}}(\text{COD})\text{Cl}]_2$ (421 mg, 0.627 mmol, 1.00 eq) was suspended in 3 mL of Et_2O in a 20-mL scintillation vial. A solution of tfepma (611 mg, 1.25 mmol, 2.00 eq), dissolved in 2 mL of Et_2O , was added at a fast dropwise rate to give a dark yellow/brown solution. A solution of CN^tBu (104 mg, 1.25 mmol, 2.00 eq) in 2 mL of Et_2O was added immediately, giving a dark red solution. The reaction mixture was stirred at room temperature for 22 h, during which time some orange solid had formed. The mixture was concentrated to dryness, leaving an orange solid and a red residue. The product was resuspended in 2 mL of Et_2O , and 16 mL of pentane was added to the stirred mixture, liberating a light orange solid. The supernatant was decanted, and the solid briefly dried in vacuo. The product was dissolved in 10 mL of CH_2Cl_2 and filtered, removing a small amount of a brown impurity. The solvent was removed in vacuo, and the resulting solid was resuspended in 1 mL of $\text{CH}_2\text{Cl}_2/15 \text{ mL}$ of pentane. The mixture was chilled overnight at $-20 \text{ }^\circ\text{C}$, at which time the supernatant was decanted and the light orange product dried in vacuo. Yield: 643 mg (64.3%). ^1H NMR (500 MHz, CD_2Cl_2) δ/ppm : 4.96–5.13 (m, 4H), 4.77–4.88 (m, 2H), 4.47–4.64 (m, 4H), 4.29–4.46 (m, 6H), 2.87 (pseudoquintet, 6H), 1.38 (s, 9H), 1.33 (s, 9H). $^{31}\text{P}\{^1\text{H}\}$ NMR (121.5 MHz, CD_2Cl_2) δ/ppm : 132.3 (m, 2P), 85.9 (m, 2P). UV-vis (CH_3CN): λ/nm ($\epsilon/(\text{M}^{-1} \text{cm}^{-1})$) 271 (15000), 315 (6300), 338 (sh) (4100), 392 (5600), 449 (1600), 504 (860). IR (Nujol): $\tilde{\nu}_{\text{C}\equiv\text{N}} = 2071 \text{ (sh), } 2100, 2132 \text{ (sh) cm}^{-1}$. Anal. Calcd. for $\text{C}_{28}\text{H}_{40}\text{Cl}_2\text{F}_{24}\text{N}_4\text{O}_8\text{P}_4\text{Ir}_2$: C, 21.07; H, 2.53; N, 3.51. Found: C, 20.97; H, 2.49; N, 3.27.

3.5.5 Preparation of $[\text{Rh}_2^{0,\text{II}}(\text{tfepma})_2(\text{CN}^t\text{Bu})_3\text{Cl}]\text{Cl}$ (**3**)

To a solution of **1** (100 mg, 0.0706 mmol, 1.00 eq) in 2 mL of THF was added a solution of CN^tBu (6.2 mg, 0.074 mmol, 1.1 eq) in 0.5 mL of THF, causing the color to darken slightly. The reaction was stirred at room temperature for 2.5 h, following which the solvent was removed in vacuo. The residue was washed with 4 mL of Et_2O and 2 mL of hexane, leaving a yellow solid which was dried in vacuo. The product was dissolved in 1.5 mL of THF and layered with 15 mL of hexane to recrystallize. After ca. 48 h the supernatant was decanted and the product dried in vacuo. Yield: 63 mg (59%). Repeated attempts to obtain analytically pure material by various recrystallization procedures were unsuccessful, likely due to the reversible nature of the reaction, i.e. dissociation of CN^tBu . ^1H NMR (500 MHz, CD_3CN) δ/ppm : 4.15–5.15 (m, 16H), 2.95 (br, s, 6H), 1.47 (br, s, 27H). $^{31}\text{P}\{^1\text{H}\}$ NMR (121.5 MHz, CD_3CN) δ/ppm : 144.0 (br, m, 2P), 125.7 (br, m, 2P). IR (Nujol): $\tilde{\nu}_{\text{C}\equiv\text{N}} = 2131, 2160 \text{ cm}^{-1}$. Anal. Calcd. for $\text{C}_{33}\text{H}_{49}\text{Cl}_2\text{F}_{24}\text{N}_5\text{O}_8\text{P}_4\text{Rh}_2$: C, 26.42; H, 3.29; N, 4.67. Found: C, 25.04; H, 3.17; N, 4.49.

3.5.6 Preparation of $\text{Ir}_2^{0,\text{II}}(\text{tfepma})_2(\text{CN}^t\text{Bu})_3\text{Cl}_2$ (**4**)

A sample of **2** (100 mg, 0.0627 mmol, 1.00 eq) was dissolved in 1.5 mL of THF. A solution of CN^tBu (5.7 mg, 0.068 mmol, 1.1 eq) in 0.5 mL of THF was added, and the yellow-orange solution was stirred at room temperature for 24 h. The solution was concentrated in vacuo to give a yellow-orange residue, which was suspended in 1 mL of CH_2Cl_2 /15 mL of pentane and chilled at -20°C for 24 h. The supernatant was decanted and the resulting yellow product dried in vacuo. Yield: 73 mg (70%). Analytically pure material was obtained in much lower yields (< 50%) by recrystallization from a concentrated CH_2Cl_2 solution layered with pentane. ^1H NMR (500 MHz, CD_3CN) δ/ppm : 4.86–4.97 (m, 4H), 4.44–4.69 (m, 12H), 2.94 (pseudoquintet, 6H), 1.45 (s, 9H), 1.43 (s, 18H). $^{31}\text{P}\{^1\text{H}\}$ NMR (121.5 MHz, CD_3CN) δ/ppm : 132.3 (m, 2P), 79.8 (m, 2P). UV-vis (CH_3CN): λ/nm ($\epsilon/(\text{M}^{-1} \text{cm}^{-1})$) 271 (16000), 307 (5300), 325 (sh) (3700), 382 (6400), 444 (1800), 496 (960). IR (Nujol): $\tilde{\nu}_{\text{C}\equiv\text{N}} = 2116, 2159, 2181 \text{ cm}^{-1}$. Anal. Calcd. for $\text{C}_{33}\text{H}_{49}\text{Cl}_2\text{F}_{24}\text{N}_5\text{O}_8\text{P}_4\text{Ir}_2$: C, 23.61; H, 2.94; N, 4.17. Found: C, 22.95; H, 2.85; N, 4.05.

3.5.7 Preparation of $\text{Rh}_2^{0,0}(\text{tfepma})_2(\text{CN}^t\text{Bu})_3$ (**5**)

A mixture of **1** (475 mg, 0.335 mmol, 1.00 eq) and CN^tBu (27.9 mg, 0.336 mmol, 1.00 eq) was dissolved in 6 mL of THF, giving a red-orange solution and

a small amount of yellow precipitate. The mixture was added via pipet to a stirred solution of CoCp^*_2 (221 mg, 0.671 mmol, 2.00 eq) in 2 mL of THF. Yellow $[\text{CoCp}^*_2]\text{Cl}$ formed immediately, and the mixture was allowed to stir at room temperature for 3 h. A yellow-green solid was removed by filtration through a plug of glass wool, and the volatiles were removed from the supernatant in vacuo to afford a dark red residue. The product was dissolved in a mixture of 2 mL of Et_2O /2 mL of hexanes, and upon concentrating in vacuo an orange solid was obtained. The solid was suspended in 8 mL of hexanes at $-20\text{ }^\circ\text{C}$ overnight. The supernatant was decanted, and the solid was dried in vacuo. Yield: 432 mg (90.2%). ^1H NMR (500 MHz, C_6D_6) δ/ppm : 4.13–4.40 (br, m, 16H), 2.80 (br, pseudoquintet, 6H), 1.04 (br, s, 27H). $^{31}\text{P}\{^1\text{H}\}$ NMR (121.5 MHz, C_6D_6) δ/ppm : 156.0 (m, 4P). UV-vis (THF): λ/nm ($\epsilon/(\text{M}^{-1}\text{ cm}^{-1})$) 285 (19000), 379 (6200). IR (Nujol): $\tilde{\nu}_{\text{C}\equiv\text{N}}$ = 2042 (sh), 2074 (sh), 2098 cm^{-1} . Anal. Calcd. for $\text{C}_{33}\text{H}_{49}\text{F}_{24}\text{N}_5\text{O}_8\text{P}_4\text{Rh}_2$: C, 27.73; H, 3.46; N, 4.90. Found: C, 27.80; H, 3.37; N, 4.80.

3.5.8 Preparation of $\text{Ir}_2^{0,0}(\text{tfepma})_2(\text{CN}^t\text{Bu})_3$ (6)

A suspension of **2** (500 mg, 0.313 mmol, 1.00 eq) in 6 mL of Et_2O was combined with a solution of CN^tBu (26.0 mg, 0.313 mmol, 1.00 eq) in 2 mL of Et_2O . Most of the solid was drawn into solution, with only a small amount of undissolved orange solid remaining. The mixture was added to CoCp^*_2 (206 mg, 0.627 mmol, 2.00 eq) in 2 mL of Et_2O . A yellow solid formed immediately, and the mixture was stirred for 3 h, at which time the precipitate was removed by filtration through glass wool. The solution was concentrated to dryness, and the resulting orange solid was suspended in 6 mL of pentane at $-20\text{ }^\circ\text{C}$ overnight. The supernatant was decanted, and the bright orange solid dried in vacuo. Yield: 410 mg (81.3%). ^1H NMR (500 MHz, C_6D_6) δ/ppm : 4.15–4.39 (br, m, 16H), 2.74 (pseudoquintet, 6H), 1.03 (s, 27H). $^{31}\text{P}\{^1\text{H}\}$ NMR (202.5 MHz, C_6D_6) δ/ppm : 126.1 (s, 4P). UV-vis (THF): λ/nm ($\epsilon/(\text{M}^{-1}\text{ cm}^{-1})$) 266 (sh) (16000), 383 (4300). IR (Nujol): $\tilde{\nu}_{\text{C}\equiv\text{N}}$ = 2038 (sh), 2088 (sh), 2113 cm^{-1} . Anal. Calcd. for $\text{C}_{33}\text{H}_{49}\text{F}_{24}\text{N}_5\text{O}_8\text{P}_4\text{Ir}_2$: C, 24.65; H, 3.07; N, 4.36. Found: C, 24.72; H, 3.14; N, 4.27.

3.5.9 Preparation of $\text{Rh}_2^{\text{II,II}}(\text{tfepma})_2(\text{CN}^t\text{Bu})_2\text{Cl}_4$ (7a)

A sample of **1** (100 mg, 0.0706 mmol, 1.00 eq) was suspended in 1 mL of toluene in a scintillation vial. A solution of PhICl_2 (20.4 mg, 0.0741 mmol, 1.05 eq) dissolved in 1.5 mL of toluene was added dropwise to give a red solution. The vial was immediately removed from

stirring and allowed to stand at room temperature for 24 h, during which time the red product crystallized. The supernatant was decanted, and the product was washed with pentane and dried in vacuo. Yield: 81 mg (77%). ^1H NMR (500 MHz, CD_3CN) δ/ppm : 5.05–5.16 (m, 4H), 4.89–5.03 (m, 8H), 4.55–4.66 (m, 4H), 3.04 (pseudoquintet, 6H), 1.45 (s, 18H). $^{31}\text{P}\{^1\text{H}\}$ NMR (121.5 MHz, CD_3CN) δ/ppm : 113.8 (m, 4P). UV-vis (THF): λ/nm ($\epsilon/(\text{M}^{-1} \text{cm}^{-1})$) 287 (12000), 352 (32000), 473 (2600). IR (Nujol): $\tilde{\nu}_{\text{C}\equiv\text{N}} = 2200 \text{ cm}^{-1}$. Anal. Calcd. For $\text{C}_{28}\text{H}_{40}\text{Cl}_4\text{F}_{24}\text{N}_4\text{O}_8\text{P}_4\text{Rh}_2$: C, 22.60; H, 2.71; N, 3.76. Found: C, 23.22; H, 2.82; N, 3.77.

3.5.10 Preparation of $\text{Ir}_2^{\text{II,II}}(\text{tfepma})_2(\text{CN}^t\text{Bu})_2\text{Cl}_4$ (**8**)

In a 20-mL scintillation vial, **2** (100 mg, 0.0627 mmol, 1.00 eq) was dissolved in 2 mL of CH_2Cl_2 . In a separate vial, PhICl_2 (19.0 mg, 0.0691 mmol, 1.10 eq) was dissolved in 2 mL of CH_2Cl_2 . Both solutions were frozen in the glovebox coldwell. They were removed, and upon thawing the PhICl_2 solution was added dropwise to the solution of **2**. The color immediately lightened to canary yellow, and the reaction was allowed to warm to room temperature and stirred for 1 h. The resulting solution was concentrated in vacuo and triturated with 4 mL of hexane to yield a bright yellow solid. The product was washed with 2 mL of hexane and dried in vacuo. Yield: 90 mg (86%). ^1H NMR (500 MHz, CD_3CN) δ/ppm : 5.34–5.45 (m, 2H), 5.00–5.11 (m, 2H), 4.55–4.93 (m, 12H), 2.90 (pseudoquintet, 6H), 1.61 (s, 9H), 1.38 (s, 9H). $^{31}\text{P}\{^1\text{H}\}$ NMR (121.5 MHz, CD_3CN) δ/ppm : 76.1–77.6 (m, 2P), 70.3–71.8 (m, 2P) (AA'BB', 12 lines resolved, $\delta_{\text{avg}} = 73.9 \text{ ppm}$). UV-vis (CH_3CN): λ/nm ($\epsilon/(\text{M}^{-1} \text{cm}^{-1})$) 282 (18000), 333 (6200), 364 (sh) (2500). IR (Nujol): $\tilde{\nu}_{\text{C}\equiv\text{N}} = 2186 \text{ cm}^{-1}$. Anal. Calcd. for $\text{C}_{28}\text{H}_{40}\text{Cl}_4\text{F}_{24}\text{N}_4\text{O}_8\text{P}_4\text{Ir}_2$: C, 20.18; H, 2.42; N, 3.36. Found: C, 20.37; H, 2.41; N, 3.35.

3.5.11 Preparation and NMR Characterization of $\text{Rh}_2^{\text{II,II}}(\text{tfepma})_2(\text{CN}^t\text{Bu})_2\text{Cl}_3\text{H}$ (**9a** and **9b**)

A J. Young NMR tube was charged with a solution of **1** (25 mg, 0.018 mmol, 1.0 eq) in 0.7 mL of THF-d_8 . The tube was frozen in liquid N_2 and evacuated to $< 3 \times 10^{-6}$ torr. Anhydrous HCl gas (0.44 mmol, 24 eq) was generated by treating anhydrous NaCl (26 mg, 0.44 mmol, 24 eq) with 0.5 mL of concentrated sulfuric acid and transferred under vacuum into the NMR tube. After completing the HCl transfer and while still frozen, the J. Young tube was evacuated to $< 2 \times 10^{-6}$ torr, sealed, and then thawed. After 30 minutes, the NMR spectra were recorded. The instability of **9a** and **9b** in the absence of excess HCl precluded

product isolation. **9a**: Yield (from ^1H NMR): 84%. ^1H NMR (500 MHz, THF- d_8) δ /ppm: 5.31–5.39 (m, 2H), 5.12–5.28 (m, 4H), 4.86–5.02 (m, 4H), 4.48–4.69 (m, 4H), 4.32–4.42 (m, 2H), 2.95 (pseudoquintet, 6H), 1.52 (br, s, 9H), 1.49 (s, 9H), –14.62 (dt, $^2J_{\text{P-H}} = 9.1$ Hz, $^1J_{\text{Rh-H}} = 13.3$ Hz, 1H). $^{31}\text{P}\{^1\text{H}\}$ NMR (202.5 MHz, THF- d_8) δ /ppm: 137.9 (m, 2P), 116.8 (m, 2P). **9b**: Yield (from ^1H NMR): 14%. ^1H NMR (500 MHz, THF- d_8) δ /ppm: 4.30–5.49 (m, 16H) (overlap with peaks from major isomer), 3.00 (pseudoquintet, 6H), 1.54 (s, 9H), 1.50 (s, 9H), –18.97 (dt (apparent quartet), $^2J_{\text{P-H}} = ^1J_{\text{Rh-H}} = 14.5$ Hz, 1H). $^{31}\text{P}\{^1\text{H}\}$ NMR (202.5 MHz, THF- d_8) δ /ppm: 132.4 (m, 2P), ca. 116.3 (m, 2P) (overlap with major isomer). The ^1H NMR spectrum also shows unreacted HCl (δ 8.04 ppm) and a small amount (ca. 2%) of unreacted **1**.

3.5.12 Crystallization and IR Characterization of $\text{Rh}_2^{\text{II,II}}(\text{tfepma})_2(\text{CN}^t\text{Bu})_2\text{Cl}_3\text{H}$ (**9a**)

In a septum-capped NMR tube, a sample of **1** (25 mg, 0.018 mmol, 1.0 eq) was dissolved in 0.5 mL of 2.18 M HCl/Et₂O solution. The resulting solution was layered with hexane and stored at –20 °C. Over a period of 2 days, yellow crystals formed. An X-ray quality crystal was selected for crystallographic characterization. The remaining material was suspended in oil for IR analysis. IR: $\tilde{\nu}_{\text{Rh-H}} = 2137$ cm^{–1} (weak); $\tilde{\nu}_{\text{C=N}} = 2186$ (sh), 2196 cm^{–1}.

3.5.13 Preparation of $\text{Ir}_2^{\text{II,II}}(\text{tfepma})_2(\text{CN}^t\text{Bu})_2\text{Cl}_3\text{H}$ (**10**)

In a 20-mL scintillation vial, **2** (100 mg, 0.0627 mmol, 1.00 eq) was dissolved in 2 mL of acetonitrile. A solution of LuH^+Cl^- (11.2 mg, 0.0780 mmol, 1.24 eq) in 1 mL of acetonitrile was added, causing the color to fade to pale yellow. The solution was stirred at room temperature for 30 min, and then the solvent was removed in vacuo to give a cream-colored solid. The solid was taken up in 8 mL of Et₂O and filtered through a plug of glass wool to remove unreacted LuH^+Cl^- . To the resulting solution was added 2 mL of hexane, and concentration in vacuo left a light yellow solid, which was suspended in hexane and stored at –20 °C overnight. The supernatant was decanted and the product dried in vacuo. Yield: 98 mg (96%). ^1H NMR (500 MHz, C₆D₆) δ /ppm: 5.93 (m, 2H), 5.62 (m, 2H), 5.44 (m, 2H), 4.96 (m, 2H), 4.80 (m, 2H), 4.64 (m, 2H), 3.93 (m, 4H), 2.54 (pseudoquintet, 6H), 1.08 (s, 9H), 1.03 (s, 9H), –20.69 (t, $^2J_{\text{P-H}} = 16.0$ Hz, 1H). $^{31}\text{P}\{^1\text{H}\}$ NMR (121.5 MHz, C₆D₆) δ /ppm: 89.0–91.5 (m, 2P), 77.8–80.3 (m, 2P) (AA'BB', 20 lines resolved, $\delta_{\text{avg}} = 84.7$ ppm). UV-vis (THF): λ/nm ($\epsilon/(\text{M}^{-1} \text{cm}^{-1})$) 285

(12000), 322 (8300), 360 (sh) (2400). IR (Nujol): $\tilde{\nu}_{\text{C}\equiv\text{N}} = 2170 \text{ cm}^{-1}$. Anal. Calcd. for $\text{C}_{28}\text{H}_{41}\text{Cl}_3\text{F}_{24}\text{N}_4\text{O}_8\text{P}_4\text{Ir}_2$: C, 20.60; H, 2.53; N, 3.43. Found: C, 21.29; H, 2.31; N, 3.28.

3.5.14 Preparation of $\text{Ir}_2^{\text{II,II}}(\text{tfepma})_2(\text{CN}^t\text{Bu})_2\text{Cl}_2\text{H}(\text{OTs})$ (**11**)

Solid **2** (100 mg, 0.0627 mmol, 1.00 eq) was dissolved in 2 mL of THF. A solution of $\text{HOTs}\cdot\text{H}_2\text{O}$ (12.5 mg, 0.0657 mmol, 1.05 eq) in 1 mL of THF was added, giving a nearly colorless solution. After 48 h, the solvent was removed in vacuo. The product was redissolved in 4 mL of hexane/6 mL of Et_2O , and the resulting solution was concentrated in vacuo to leave a white solid, which was treated with 4 mL of hexane and stored at $-20 \text{ }^\circ\text{C}$ overnight. The supernatant was decanted and the product dried in vacuo. Yield: 104 mg (93.7%). **11a** (89%): ^1H NMR (500 MHz, CD_3CN) δ/ppm : 7.60 (d, $^3J_{\text{H-H}} = 8.5 \text{ Hz}$, 2H), 7.16 (d, $^3J_{\text{H-H}} = 8.5 \text{ Hz}$, 2H), 5.23 (m, 2H), 4.60–5.00 (m, 10H), 4.37–4.45 (m, 4H), 2.92 (pseudoquintet, 6H), 2.33 (s, 3H), 1.55 (s, 9H), 1.43 (s, 9H), -20.00 (t, $^2J_{\text{P-H}} = 16.0 \text{ Hz}$, 1H). $^{31}\text{P}\{^1\text{H}\}$ NMR (121.5 MHz, CD_3CN) δ/ppm : 91.1–93.9 (m, 2P), 77.7–80.5 (m, 2P) (AA'BB', 18 lines resolved, $\delta_{\text{avg}} = 85.8 \text{ ppm}$). **11b** (11%): ^1H NMR (500 MHz, CD_3CN) δ/ppm : 7.60 (d, $^3J_{\text{H-H}} = 8.5 \text{ Hz}$, 2H) (coincident with major isomer), 7.16 (d, $^3J_{\text{H-H}} = 8.5 \text{ Hz}$, 2H) (coincident with major isomer), 4.28–5.12 (m, 16H) (overlap with peaks from major isomer), 2.98 (pseudoquintet, 6H), 2.33 (s, 3H) (coincident with major isomer), 1.56 (s, 9H), 1.44 (s, 9H), -20.71 (t, $^2J_{\text{P-H}} = 16.0 \text{ Hz}$, 1H) $^{31}\text{P}\{^1\text{H}\}$ NMR (121.5 MHz, CD_3CN) δ/ppm : ~ 92.7 (m, 2P), ~ 78.9 (m, 2P) (peaks are completely overlapped with those of major isomer). UV-vis (CH_3CN) (mixture of isomers): λ/nm ($\epsilon/(\text{M}^{-1} \text{ cm}^{-1})$) 270 (17000), 320 (5300), 348 (3500). IR (Nujol) (mixture of isomers): $\tilde{\nu}_{\text{C}\equiv\text{N}} = 2171, 2181$ (sh), 2189 (sh) cm^{-1} . Anal. Calcd. for $\text{C}_{35}\text{H}_{48}\text{Cl}_2\text{F}_{24}\text{N}_4\text{O}_{11}\text{P}_4\text{SIr}_2$: C, 23.78; H, 2.74; N, 3.17. Found: C, 24.15; H, 2.42; N, 3.05.

3.5.15 Preparation of $[\text{Rh}_2^{\text{I,I}}(\text{tfepma})_2(\text{CN}^t\text{Bu})_3(\mu\text{-H})](\text{OTs})$ (**12**)

Separate solutions of **5** (100 mg, 0.0700 mmol, 1.00 eq) in 2 mL of CH_3CN and $\text{HOTs}\cdot\text{H}_2\text{O}$ (13.3 mg, 0.699 mmol, 0.999 eq) in 1 mL of CH_3CN were prepared and frozen in the glovebox coldwell. The solutions were removed, and upon thawing the HOTs solution was added dropwise to the stirred solution of **5**, giving a red-orange solution, which was allowed to warm to room temperature and stirred for 1 h. The solution was concentrated to dryness in vacuo, yielding a red residue. Trituration with 2 mL of Et_2O afforded a yellow solid, and the

resulting suspension was placed in the freezer at $-20\text{ }^{\circ}\text{C}$ overnight. The product was isolated by decantation and dried in vacuo. Yield: 92 mg (82%). ^1H NMR (500 MHz, CD_3CN) δ/ppm : 7.59 (d, $^3J_{\text{H-H}} = 8.0\text{ Hz}$, 2H), 7.14 (d, $^3J_{\text{H-H}} = 8.0\text{ Hz}$, 2H), 4.28–4.50 (br, m, 16H), 2.80 (pseudoquintet, 6H), 2.32 (s, 3H), 1.45 (s, 27H), -12.63 (tquint, $^1J_{\text{Rh-H}} = 14.8\text{ Hz}$, $^2J_{\text{P-H}} = 8.5\text{ Hz}$, 1H). $^{31}\text{P}\{^1\text{H}\}$ NMR (121.5 MHz, CD_3CN) δ/ppm : 150.7 (m, 4P). UV-vis (CH_3CN): λ/nm ($\epsilon/(\text{M}^{-1}\text{ cm}^{-1})$) 270 (13000), 283 (sh) (12000), 339 (sh) (4400), 376 (sh) (3900), 443 (sh) (1400). IR (Nujol): $\tilde{\nu}_{\text{C=N}} = 2135, 2164\text{ cm}^{-1}$. Anal. Calcd. for $\text{C}_{40}\text{H}_{57}\text{F}_{24}\text{N}_5\text{O}_{11}\text{P}_4\text{SRh}_2$: C, 30.00; H, 3.59; N, 4.37. Found: C, 29.65; H, 3.31; N, 4.27.

3.5.16 Preparation of $\text{Ir}^{\text{II}}(\text{tfepma})_2(\text{CN}^t\text{Bu})_2\text{Cl}_2(\text{H})_2$ (**13**)

A J. Young NMR tube was charged with **2** (25 mg, 0.016 mmol, 1.0 eq) dissolved in 0.7 mL of THF-d_8 . The solution was freeze-pump-thaw degassed three times on a high vacuum manifold. The tube was pressurized with ca. 1.5 atm of H_2 and upon shaking the tube a nearly colorless solution was obtained. The NMR spectra were immediately recorded. Compound **13** is unstable in the absence of H_2 , losing H_2 and reverting back to **2**. This instability precluded isolation of solid material for microanalysis. Crystals for X-ray diffraction and IR analysis were obtained by conducting an analogous preparation in CD_3CN and chilling the solution to $-20\text{ }^{\circ}\text{C}$ overnight in the presence of H_2 . For the UV-vis measurement, a solution of **2** (63 μM in THF) was prepared in a septum-sealed cuvette, and 2 mL of H_2 was injected via gastight syringe. **13a** (*cis*- H_2 , *cis*- P_2): Yield (from NMR): 95%. ^1H NMR (500 MHz, THF-d_8) δ/ppm : 5.60 (m, 2H), 4.84 (m, 2H), 4.68 (m, 4H), 4.42–4.56 (m, 4H), 4.29 (m, 2H), 4.13 (m, 2H), 2.82 (m, 6H), 1.48 (s, 9H), 1.46 (s, 9H), -12.63 to -12.03 (m, 2H). $^{31}\text{P}\{^1\text{H}\}$ NMR (121.5 MHz, THF-d_8) δ/ppm : 93.4–97.8 (m, 2P), 88.2–90.4 (m, 2P). IR (Nujol): $\tilde{\nu}_{\text{Ir-H}} = 2036, 2065\text{ cm}^{-1}$, $\tilde{\nu}_{\text{C=N}} = 2161\text{ cm}^{-1}$. **13b** (*cis*- H_2 , *trans*- P_2): Yield (from NMR): 5%. ^1H NMR (500 MHz, THF-d_8) δ/ppm : 5.26 (m, 2H), 5.13 (m, 4H), ca. 4.84 (m, 2H) (overlap with major isomer), ca. 4.68 (m, 4H) (overlap with major isomer), 4.39 (m, 4H), 2.86 (pseudoquintet, 6H), 1.44 (s, 9H), 1.41 (s, 9H), -14.80 (td, $^2J_{\text{P-H}} = 17.9\text{ Hz}$, $^2J_{\text{H-H}} = 4.6\text{ Hz}$, 1H) -15.50 (td, $^2J_{\text{P-H}} = 13.8\text{ Hz}$, $^2J_{\text{H-H}} = 4.6\text{ Hz}$, 1H). $^{31}\text{P}\{^1\text{H}\}$ NMR (121.5 MHz, THF-d_8) δ/ppm : 109.6 (m, 2P), ca. 95.0 (m, 2P), (overlap with major isomer). UV-vis (THF) (both isomers present): λ/nm ($\epsilon/(\text{M}^{-1}\text{ cm}^{-1})$) 267 (16000), 313 (4800), 342 (3300).

3.5.17 Preparation of Ir₂^{II,II}(dppm)(PPh(*o*-C₆H₄)CH₂PPh₂)(CN^{*t*}Bu)₂Cl₂H (**14**)

[Ir^I(COD)Cl]₂ (242 mg, 0.360 mmol, 1.00 eq) was dissolved in 8 mL of THF to give an orange solution. A solution of dppm (276 mg, 0.718 mmol, 1.99 eq) in 6 mL of THF was added, followed by CN^{*t*}Bu (60 mg, 0.72 mmol, 2.0 eq) in 6 mL of THF. The resulting dark green solution gradually faded to pale yellow, and over the course of 72 h stirring at room temperature a white solid precipitated from solution. The solid was collected by vacuum filtration, washed with 10 mL of THF and 10 mL of Et₂O and dried in vacuo. Yield: 374 mg (74.0%). ¹H NMR (500 MHz, CD₂Cl₂) δ/ppm: 8.02 (m, 2H), 7.89 (m, 4H), 7.64–7.71 (m, 3H), 7.48–7.58 (m, 3H), 7.34–7.44 (m, 3H), 7.15–7.25 (m, 7H), 6.93–7.12 (m, 10H), 6.72–6.81 (m, 4H), 6.59 (m, 1H), 6.51 (m, 2H), 4.69 (m, 1H), 4.47 (m, 1H), 4.39 (m, 1H), 3.86 (m, 1H), 1.09 (s, 9H), 0.73 (s, 9H), –10.69 (dd, ²J_{P-H} = 163 Hz, 19.1 Hz, 1H). ³¹P{¹H} NMR (121.5 MHz, CD₂Cl₂) δ/ppm: –9.8 to 1.5 (m, 2P), –20.7 to –19.6 (m, 1P), –33.4 (m, 1P). IR (Nujol): $\tilde{\nu}_{\text{Ir-H}} = 2097 \text{ cm}^{-1}$, $\tilde{\nu}_{\text{C}\equiv\text{N}} = 2134, 2162 \text{ cm}^{-1}$. Anal. Calcd. for C₆₀H₆₂Cl₂N₂P₄Ir₂: C, 51.83; H, 4.49; N, 2.01. Found: C, 51.76; H, 4.25; N, 2.02.

3.5.18 X-Ray Crystallographic Details

Single crystals of **1**, **2**, **3**, **4**, and **7a** were obtained by layering a CH₂Cl₂ solution with pentane, crystals of **5** and **6** were obtained from a toluene/pentane solution at –20 °C, crystals of **7b** deposited from toluene at room temperature, crystals of **8** and **11** deposited from CH₂Cl₂/hexane at –20 °C, crystals of **9a** were grown from Et₂O/hexane as described above, crystals of **10** were grown in Et₂O/pentane at –20 °C, crystals of **12** were obtained from THF/hexane at –20 °C, crystals of **13a** were grown from a CD₃CN NMR sample at –20 °C, and crystals of **14** deposited from THF at room temperature. The crystals were mounted on a Bruker three-circle goniometer platform equipped with an APEX detector. A graphite monochromator was employed for wavelength selection of the Mo K α radiation ($\lambda = 0.71073 \text{ \AA}$). The data were processed and refined using the program SAINT supplied by Siemens Industrial Automation. Structures were solved by Patterson methods in SHELXS and refined by standard difference Fourier techniques in the SHELXTL program suite (6.10 v., Sheldrick G. M., and Siemens Industrial Automation, 2000). Hydrogen atoms bonded to carbon were placed in calculated positions using the standard riding model and refined isotropically; all non-hydrogen atoms were refined anisotropically. The metal-bound hydrogen atoms in **9a**, **10**, **11**, **13** and **14** were located

in the difference map, restrained to a distance of 1.60 Å from the metal, and refined isotropically. The bridging hydride in **12** was restrained to be equidistant from the two rhodium nuclei. The crystal of **3** was a nonmerohedral twin; two unit-cell domains were located using the program CELL_NOW and used for integration in SAINT. The absorption correction was performed with TWINABS, and the structure was refined against the major twin component. The structures of **1**, **4**, **7a**, **9a**, **12** and **13** all had one or more disordered $-\text{OCH}_2\text{CF}_3$ groups, and the structures of **8** and **13** had a disordered *tert*-butyl group. In addition, the structures of **4** and **11** also contained a disordered dichloromethane, and the structure of **9a** also contained an *n*-hexane molecule disordered about an inversion center. The (1,2) and (1,3) distances of all disordered parts were restrained to be similar using the SADI command; the rigid-bond restraints SIMU and DELU were also used on disordered parts. Crystallographic details for **1** (CCDC 839883), **2** (CCDC 852644), **3** (CCDC 852645), **4a** (CCDC 852646), **5** (CCDC 852647), **6**, (CCDC 852648), **7a** (CCDC 839884), **8** (CCDC 852649), **9a** (CCDC 839885), **10** (CCDC 852650), **11a** (CCDC 852651), **12** (CCDC 852652), **13a** (CCDC 852653), and **14** (CCDC 852654) are summarized in Tables 3.1–3.5.

Table 3.1. Crystallographic summary for **1–3**.

| | 1 | 2 | 3·0.5CH₂Cl₂ |
|--|--|--|--|
| Formula | C ₂₈ H ₄₀ Cl ₂ F ₂₄ N ₄ O ₈ P ₄ Rh ₂ | C ₂₈ H ₄₀ Cl ₂ F ₂₄ Ir ₂ N ₄ O ₈ P ₄ | C _{33.5} H ₅₀ Cl ₃ F ₂₄ N ₅ O ₈ P ₄ Rh ₂ |
| fw, g/mol | 1417.24 | 1595.82 | 1542.83 |
| Temperature/K | 100(2) | 100(2) | 100(2) |
| cryst. syst. | Monoclinic | Monoclinic | Monoclinic |
| space group | <i>P2₁/n</i> | <i>P2₁/n</i> | <i>P2₁/c</i> |
| color | Orange | Orange | Yellow |
| <i>a</i> /Å | 12.8443(11) | 12.7757(15) | 23.342(6) |
| <i>b</i> /Å | 16.7085(15) | 16.831(2) | 23.350(6) |
| <i>c</i> /Å | 24.735(2) | 24.504(3) | 23.863(6) |
| α /° | 90 | 90 | 90 |
| β /° | 104.723(2) | 103.753(2) | 114.407(4) |
| γ /° | 90 | 90 | 90 |
| <i>V</i> /Å ³ | 5134.0(8) | 5118.1(10) | 11844(5) |
| <i>Z</i> | 4 | 4 | 8 |
| ρ (calc.)/(g cm ⁻³) | 1.834 | 2.071 | 1.730 |
| no. refl. | 118868 | 113463 | 314109 |
| no. unique refl. | 15573 | 14349 | 27273 |
| <i>R</i> _{int} | 0.0468 | 0.0614 | 0.1031 |
| <i>R</i> ₁ ^a (all data) | 0.0468 | 0.0448 | 0.0963 |
| <i>wR</i> ₂ ^b (all data) | 0.0958 | 0.0786 | 0.1568 |
| <i>R</i> ₁ [(<i>I</i> > 2σ)] | 0.0368 | 0.0317 | 0.0614 |
| <i>wR</i> ₂ [(<i>I</i> > 2σ)] | 0.0883 | 0.0712 | 0.1341 |
| <i>GOF</i> ^c | 1.045 | 1.042 | 1.093 |

^a $R_1 = \Sigma ||F_o - |F_c|| / \Sigma |F_o|$. ^b $wR_2 = (\Sigma (w(F_o^2 - F_c^2)^2) / \Sigma (w(F_o^2)^2))^{1/2}$. ^c $GOF = (\Sigma w(F_o^2 - F_c^2)^2 / (n - p))^{1/2}$ where *n* is the number of data and *p* is the number of parameters refined.

Table 3.2. Crystallographic summary for **4a**, **5**, and **6**.

| | 4a ·CH ₂ Cl ₂ | 5 | 6 |
|--|--|--|--|
| Formula | C ₃₄ H ₅₁ Cl ₄ F ₂₄ Ir ₂ N ₅ O ₈ P ₄ | C ₃₃ H ₄₉ F ₂₄ N ₅ O ₈ P ₄ Rh ₂ | C ₃₃ H ₄₉ F ₂₄ Ir ₂ N ₅ O ₈ P ₄ |
| fw, g/mol | 1763.88 | 1429.47 | 1608.05 |
| Temperature/K | 100(2) | 100(2) | 100(2) |
| cryst. syst. | Monoclinic | Triclinic | Triclinic |
| space group | P2 ₁ /n | PI | PI |
| color | Yellow | Yellow | Yellow |
| <i>a</i> /Å | 14.1247(12) | 11.4612(12) | 11.4559(19) |
| <i>b</i> /Å | 19.1523(16) | 11.9197(13) | 11.936(2) |
| <i>c</i> /Å | 22.2083(19) | 21.769(3) | 21.746(4) |
| <i>α</i> ° | 90 | 98.562(3) | 98.676(3) |
| <i>β</i> ° | 92.009(2) | 97.729(2) | 97.678(3) |
| <i>γ</i> ° | 90 | 108.231(2) | 108.068(2) |
| <i>V</i> /Å ³ | 6004.1(9) | 2740.8(6) | 2742.6(8) |
| <i>ρ</i> (calc.)/(g cm ⁻³) | 1.951 | 1.732 | 1.947 |
| <i>Z</i> | 4 | 2 | 2 |
| no. refl. | 118286 | 45473 | 57220 |
| no. unique refl. | 18204 | 11607 | 14837 |
| <i>R</i> _{int} | 0.0600 | 0.0675 | 0.0498 |
| <i>R</i> ₁ ^a (all data) | 0.0487 | 0.0683 | 0.0464 |
| <i>wR</i> ₂ ^b (all data) | 0.0805 | 0.1086 | 0.0694 |
| <i>R</i> ₁ [(<i>I</i> > 2σ)] | 0.0339 | 0.0436 | 0.0314 |
| <i>wR</i> ₂ [(<i>I</i> > 2σ)] | 0.0735 | 0.0961 | 0.0632 |
| <i>GOF</i> ^c | 1.033 | 1.037 | 1.030 |

^a $R_1 = \frac{\sum ||F_o| - |F_c||}{\sum |F_o|}$. ^b $wR_2 = \frac{(\sum (w(F_o^2 - F_c^2)^2)/\sum (w(F_o^2)^2))^{1/2}}$. ^c $GOF = \frac{(\sum w(F_o^2 - F_c^2)^2/(n - p))^{1/2}}$ where *n* is the number of data and *p* is the number of parameters refined.

Table 3.3. Crystallographic summary for **7a**, **8**, and **9a**.

| | 7a | 8 | 9a ·0.5(C ₆ H ₁₄) |
|--|--|--|---|
| Formula | C ₂₈ H ₄₀ Cl ₄ F ₂₄ N ₄ O ₈ P ₄ Rh ₂ | C ₂₈ H ₄₀ Cl ₄ F ₂₄ Ir ₂ N ₄ O ₈ P ₄ | C ₃₁ H _{47.50} Cl ₃ F ₂₄ N ₄ O ₈ P ₄ Rh ₂ |
| fw, g/mol | 1488.14 | 1666.72 | 1496.28 |
| Temperature/K | 100(2) | 183(2) | 100(2) |
| cryst. syst. | Monoclinic | Monoclinic | Monoclinic |
| space group | <i>P2₁/c</i> | <i>P2₁/n</i> | <i>C2/c</i> |
| color | Orange | Yellow | Yellow |
| <i>a</i> /Å | 12.7491(12) | 17.810(2) | 44.021(3) |
| <i>b</i> /Å | 19.5900(18) | 13.7756(16) | 11.0442(7) |
| <i>c</i> /Å | 21.030(2) | 22.387(3) | 25.8534(16) |
| α /° | 90 | 90 | 90 |
| β /° | 98.354(2) | 95.925(2) | 120.8920(10) |
| γ /° | 90 | 90 | 90 |
| <i>V</i> /Å ³ | 5196.5(8) | 5463.1(11) | 10786.1(11) |
| ρ (calc.)/(g cm ⁻³) | 1.902 | 2.026 | 1.843 |
| <i>Z</i> | 4 | 4 | 8 |
| no. refl. | 119995 | 115190 | 125079 |
| no. unique refl. | 15814 | 14135 | 16465 |
| <i>R</i> _{int} | 0.0577 | 0.0532 | 0.0397 |
| <i>R</i> ₁ ^a (all data) | 0.0506 | 0.0530 | 0.0372 |
| <i>wR</i> ₂ ^b (all data) | 0.0845 | 0.0896 | 0.0758 |
| <i>R</i> ₁ [(<i>I</i> > 2σ)] | 0.0346 | 0.0338 | 0.0290 |
| <i>wR</i> ₂ [(<i>I</i> > 2σ)] | 0.0757 | 0.0781 | 0.0702 |
| <i>GOF</i> ^c | 1.060 | 1.043 | 1.047 |

^a $R_1 = \Sigma ||F_o - |F_c|| / \Sigma |F_o|$. ^b $wR_2 = (\Sigma (w(F_o^2 - F_c^2)^2) / \Sigma (w(F_o^2)^2))^{1/2}$. ^c $GOF = (\Sigma w(F_o^2 - F_c^2)^2 / (n - p))^{1/2}$ where *n* is the number of data and *p* is the number of parameters refined.

Table 3.4. Crystallographic summary for **10** and **11a**.

| | 10 | 11a ·1.25CH ₂ Cl ₂ |
|--|--|--|
| Formula | C ₂₈ H ₄₁ Cl ₃ F ₂₄ Ir ₂ N ₄ O ₈ P ₄ | C _{36.25} H _{50.5} Cl _{4.5} F ₂₄ Ir ₂ N ₄ O ₁₁ P ₄ S |
| fw, g/mol | 1542.83 | 1874.17 |
| Temperature/K | 100(2) | 175(2) |
| cryst. syst. | Triclinic | Monoclinic |
| space group | <i>P</i> <i>T</i> | <i>C</i> 2/ <i>c</i> |
| color | Colorless | Colorless |
| <i>a</i> /Å | 11.9690(10) | 29.043(3) |
| <i>b</i> /Å | 12.9308(11) | 29.565(3) |
| <i>c</i> /Å | 18.8604(16) | 19.9842(18) |
| α /° | 86.6610(10) | 90 |
| β /° | 82.4840(10) | 130.3560(10) |
| γ /° | 66.6980(10) | 90 |
| <i>V</i> /Å ³ | 2657.8(4) | 13076(2) |
| ρ (calc.)/(g cm ⁻³) | 2.040 | 1.904 |
| <i>Z</i> | 2 | 8 |
| no. refl. | 25417 | 107930 |
| no. unique refl. | 11643 | 11581 |
| <i>R</i> _{int} | 0.0320 | 0.0570 |
| <i>R</i> ₁ ^a (all data) | 0.0400 | 0.0639 |
| <i>wR</i> ₂ ^b (all data) | 0.0760 | 0.1263 |
| <i>R</i> ₁ [(<i>I</i> > 2σ)] | 0.0307 | 0.0426 |
| <i>wR</i> ₂ [(<i>I</i> > 2σ)] | 0.0712 | 0.1066 |
| <i>GOF</i> ^c | 1.049 | 1.088 |

^a $R_1 = \sum ||F_o - |F_c|| / \sum |F_o|$. ^b $wR_2 = (\sum (w(F_o^2 - F_c^2)^2) / \sum (w(F_o^2)^2))^{1/2}$. ^c $GOF = (\sum w(F_o^2 - F_c^2)^2 / (n - p))^{1/2}$ where *n* is the number of data and *p* is the number of parameters refined.

Table 3.5. Crystallographic summary for **12**, **13a**, and **14**.

| | 12 | 13a | 14·THF |
|--|---|--|--|
| Formula | C ₄₀ H ₅₇ F ₂₄ N ₅ O ₁₁ P ₄ Rh ₂ S | C ₂₈ H ₄₂ Cl ₂ F ₂₄ Ir ₂ N ₄ O ₈ P ₄ | C ₆₄ H ₇₀ Cl ₂ Ir ₂ N ₂ OP ₄ |
| fw, g/mol | 1601.67 | 1597.84 | 1462.40 |
| Temperature/K | 100(2) | 100(2) | 100(2) |
| cryst. syst. | Monoclinic | Triclinic | Orthorhombic |
| space group | <i>P2₁/n</i> | <i>PI</i> | <i>P2₁2₁2₁</i> |
| color | Yellow | Colorless | Yellow |
| <i>a</i> /Å | 12.9771(14) | 10.6705(9) | 13.4826(16) |
| <i>b</i> /Å | 22.103(2) | 13.3913(11) | 18.813(2) |
| <i>c</i> /Å | 22.523(2) | 19.0514(16) | 23.724(3) |
| α /° | 90 | 96.0920(10) | 90 |
| β /° | 93.474(2) | 99.0260(10) | 90 |
| γ /° | 90 | 99.4350(10) | 90 |
| <i>V</i> /Å ³ | 6448.3(12) | 2627.8(4) | 6017.6(12) |
| ρ (calc.)/(g cm ⁻³) | 1.650 | 2.019 | 1.614 |
| <i>Z</i> | 4 | 2 | 4 |
| no. refl. | 94961 | 60163 | 141265 |
| no. unique refl. | 10253 | 15167 | 18296 |
| <i>R</i> _{int} | 0.0733 | 0.0352 | 0.0613 |
| <i>R</i> ₁ ^a (all data) | 0.1133 | 0.0465 | 0.0297 |
| <i>wR</i> ₂ ^b (all data) | 0.2192 | 0.0941 | 0.0546 |
| <i>R</i> ₁ [(<i>I</i> > 2σ)] | 0.0963 | 0.0412 | 0.0252 |
| <i>wR</i> ₂ [(<i>I</i> > 2σ)] | 0.2099 | 0.0920 | 0.0528 |
| <i>GOF</i> ^c | 1.179 | 1.228 | 1.039 |
| <i>Flack param.</i> | ----- | ----- | -0.068(30) |

^a $R_1 = \frac{\sum ||F_o| - |F_c||}{\sum |F_o|}$. ^b $wR_2 = \frac{(\sum (w(F_o^2 - F_c^2)^2)/\sum (w(F_o^2)^2))^{1/2}}$. ^c $GOF = \frac{(\sum w(F_o^2 - F_c^2)^2/(n - p))^{1/2}}$ where *n* is the number of data and *p* is the number of parameters refined.

3.6 References

- (1) Heyduk, A. F.; Nocera, D. G. *Science* **2001**, *293*, 1639–1641.
- (2) Esswein, A. J.; Veige, A. S.; Nocera, D. G. *J. Am. Chem. Soc.* **2005**, *127*, 16641–16651.
- (3) Heyduk, A. F.; Macintosh, A. M.; Nocera, D. G. *J. Am. Chem. Soc.* **1999**, *121*, 5023–5032.
- (4) Odom, A. L.; Heyduk, A. F.; Nocera, D. G. *Inorg. Chim. Acta* **2000**, *297*, 330–337.
- (5) Cook, T. R.; Esswein, A. J.; Nocera, D. G. *J. Am. Chem. Soc.* **2007**, *129*, 10094–10095.
- (6) Cook, T. R.; Surendranath, Y.; Nocera, D. G. *J. Am. Chem. Soc.* **2009**, *131*, 28–29.
- (7) Teets, T. S.; Nocera, D. G. *J. Am. Chem. Soc.* **2009**, *131*, 7411–7420.
- (8) Teets, T. S.; Lutterman, D. A.; Nocera, D. G. *Inorg. Chem.* **2010**, *49*, 3035–3043.
- (9) Teets, T. S.; Neumann, M. P.; Nocera, D. G. *Chem. Commun.* **2011**, *47*, 1485–1487.
- (10) Teets, T. S.; Nocera, D. G. *Chem. Commun.* **2011**, *47*, 9268–9274.
- (11) Heyduk, A. F.; Nocera, D. G. *J. Am. Chem. Soc.* **2000**, *122*, 9415–9426.
- (12) Roseblade, S. J.; Pfaltz, A. *Acc. Chem. Res.* **2007**, *40*, 1402–1411.
- (13) Heiden, Z. M.; Rauchfuss, T. B. *J. Am. Chem. Soc.* **2007**, *129*, 14303–14310.
- (14) Wick, D. D.; Goldberg, K. I. *J. Am. Chem. Soc.* **1999**, *121*, 11900–11901.
- (15) Denney, M. C.; Smythe, N. A.; Cetto, K. L.; Kemp, R. A.; Goldberg, K. I. *J. Am. Chem. Soc.* **2006**, *128*, 2508–2509.
- (16) Konnick, M. M.; Gandhi, B. A.; Guzei, I. A.; Stahl, S. S. *Angew. Chem. Int. Ed.* **2006**, *45*, 2904–2907.
- (17) Konnick, M. M.; Stahl, S. S. *J. Am. Chem. Soc.* **2008**, *130*, 5753–5762.
- (18) Morris, A. J.; Meyer, G. J.; Fujita, E. *Acc. Chem. Res.* **2009**, *42*, 1983–1994.
- (19) McGrady, G. S.; Guilera, G. *Chem. Soc. Rev.* **2003**, *32*, 383–392.
- (20) Connelly, N. G.; Geiger, W. E. *Chem. Rev.* **1996**, *96*, 877–910.
- (21) Hesse, M.; Meier, H.; Zeeh, B.; Dunmur, R. E. *Spectroscopic methods in organic chemistry*; Thieme: Stuttgart, 2008.
- (22) Kaesz, H. D.; Saillant, R. B. *Chem. Rev.* **1972**, *72*, 231–281.
- (23) Kubiak, C. P.; Woodcock, C.; Eisenberg, R. *Inorg. Chem.* **1982**, *21*, 2119–2129.
- (24) Sutherland, B. R.; Cowie, M. *Inorg. Chem.* **1984**, *23*, 1290–1297.
- (25) Werner, H.; Manger, M.; Laubender, M.; Teichert, M.; Stalke, D. *J. Organomet. Chem.* **1998**, *569*, 189–194.

- (26) Teets, T. S.; Cook, T. R.; McCarthy, B. D.; Nocera, D. G. *J. Am. Chem. Soc.* **2011**, *133*, 8114–8117.
- (27) Gründemann, S.; Kovacevic, A.; Albrecht, M.; Faller, J. W.; Crabtree, R. H. *J. Am. Chem. Soc.* **2002**, *124*, 10473–10481.
- (28) Clot, E.; Chen, J.; Lee, D.-H.; Sung, S. Y.; Appelhans, L. N.; Faller, J. W.; Crabtree, R. H.; Eisenstein, O. *J. Am. Chem. Soc.* **2004**, *126*, 8795–8804.
- (29) Clarke, Z. E.; Maragh, P. T.; Dasgupta, T. P.; Gusev, D. G.; Lough, A. J.; Abdur-Rashid, K. *Organometallics* **2006**, *25*, 4113–4117.
- (30) Atkinson, K. D.; Cowley, M. J.; Duckett, S. B.; Elliott, P. I. P.; Green, G. G. R.; López-Serrano, J.; Khazal, I. G.; Whitwood, A. C. *Inorg. Chem.* **2009**, *48*, 663–670.
- (31) Nishihara, Y.; Takemura, M.; Osakada, K. *Inorg. Chim. Acta* **2009**, *362*, 2951–2956.
- (32) Esswein, A. J.; Veige, A. S.; Piccoli, P. M. B.; Schultz, A. J.; Nocera, D. G. *Organometallics* **2008**, *27*, 1073–1083.
- (33) Veige, A. S.; Gray, T. G.; Nocera, D. G. *Inorg. Chem.* **2005**, *44*, 17–26.
- (34) Pearson, R. G. *Chem. Rev.* **1985**, *85*, 41–49.
- (35) Sutherland, B. R.; Cowie, M. *Organometallics* **1985**, *4*, 1637–1648.
- (36) Jenkins, J. A.; Cowie, M. *Organometallics* **1992**, *11*, 2767–2774.
- (37) Sutherland, B. R.; Cowie, M. *Organometallics* **1985**, *4*, 1801–1810.
- (38) Kubiak, C. P.; Woodcock, C.; Eisenberg, R. *Inorg. Chem.* **1980**, *19*, 2733–2739.
- (39) Vaartstra, B. A.; O'Brien, K. N.; Eisenberg, R.; Cowie, M. *Inorg. Chem.* **1988**, *27*, 3668–3672.
- (40) Oldham, S. M.; Houllis, J. F.; Sleigh, C. J.; Duckett, S. B.; Eisenberg, R. *Organometallics* **2000**, *19*, 2985–2993.
- (41) Weller, A. S.; McIndoe, J. S. *Eur. J. Inorg. Chem.* **2007**, *2007*, 4411–4423.
- (42) Fujita, K.; Takahashi, Y.; Nakaguma, H.; Hamada, T.; Yamaguchi, R. *J. Organomet. Chem.* **2008**, *693*, 3375–3382.
- (43) Teets, T. S.; Cook, T. R.; Nocera, D. G. *Inorg. Synth.* **2010**, *35*, 164–168.
- (44) Zielinska, A.; Skulski, L. *Tetrahedron Lett.* **2004**, *45*, 1087–1089.

Chapter 4 – Oxygen Reduction Effected by Group 9 Bimetallic Hydride Complexes

Portions of this work have been previously published:

Reproduced in part with permission from Teets, T. S.; Cook, T. R.; McCarthy, B. D.; Nocera, D. G. *J. Am. Chem. Soc.* **2011**, *133*, 8114–8117. Copyright 2011 American Chemical Society.

Reproduced in part with permission from Teets, T. S.; Nocera, D. G. *J. Am. Chem. Soc.* **2011**, *133*, 17796–17806. Copyright 2011 American Chemical Society.

4.1 Introduction

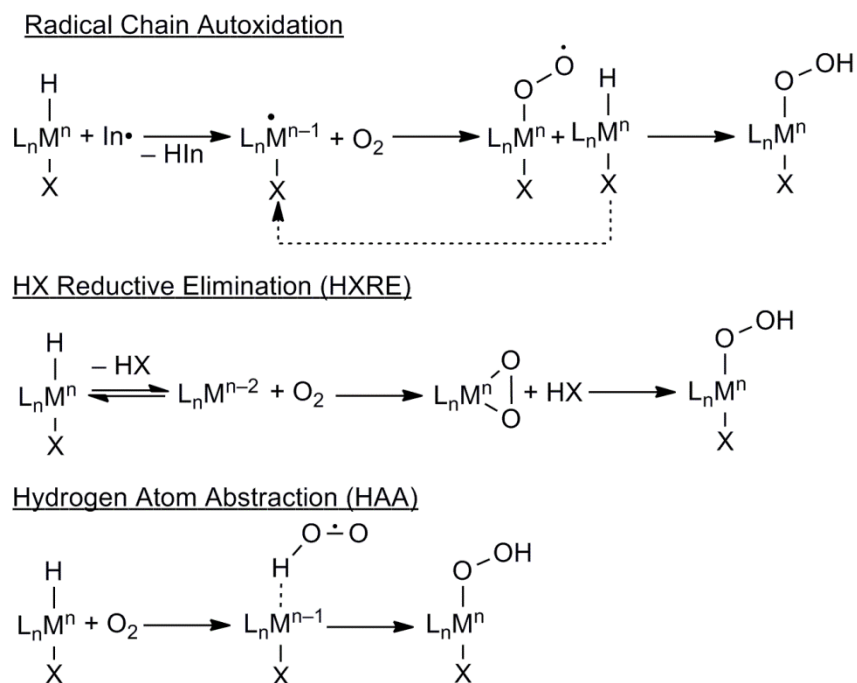
Oxidase enzymes direct a series of four-proton, four-electron events in the reduction of molecular oxygen to water.¹ This same energy-conversion chemistry is crucial to synthetic catalysts that recover the stored energy from water splitting²⁻⁵ again with much complexity to be considered.⁶ The mechanistic richness of the multi-proton, multi-electron reaction, coupled with its relevance to energy conversion, has led our group⁷⁻¹¹ and others¹²⁻¹⁷ to explore molecular catalysts in homogeneous solution because characterization of the catalytic species, the ability to tune catalytic properties, and the mechanism of action are in principle more easily investigated. The palette of molecular O₂-reduction chemistries reveals that the reduction of oxygen to water is favored in complexes that (i) are able to bind O₂ (ii) react in multi-electron steps and (iii) can couple this multi-electron chemistry to proton transfer. For these reasons, hangerman porphyrins with an appended acid or base functionality are especially effective O₂-reduction catalysts because they promote the requisite coupling of multi-electron chemistry to proton transfer.^{9,10,18,19}

A complementary strategy for multi-electron, multi-proton chemistry is to exploit bimetallic cooperativity using late transition-metal bimetallic complexes,²⁰⁻²² and especially complexes that feature a stable two-electron mixed-valent state. Until very recently, the multi-electron chemistry of this broad class of bimetallic complexes has been focused on photocatalytic H₂ production,²³⁻²⁵ halogen photoelimination,²⁶⁻³⁰ and organometallic transformations.^{31,32} Many of these topics have been elaborated further in the preceding chapters of this thesis, and in the immediately preceding chapter a new structural class of bimetallic rhodium and iridium complexes was unveiled. In working with these compounds their proclivity for oxygen reactivity became apparent. In the first part of this chapter, the reduction of O₂ to water mediated by a dirhodium hydride complex is described. The two-electron mixed-valent complex Rh₂^{0,II}(tfepma)₂(CN^tBu)₂Cl₂ (**1**) reacts reversibly in its ground state with HCl to furnish Rh₂^{II,II}(tfepma)₂(CN^tBu)₂Cl₃H (**2**), as has been demonstrated in the preceding chapter. Once formed, hydrido-chloride complex **2** reacts with O₂ in the presence of additional HCl, producing Rh₂^{II,II}(tfepma)₂(CN^tBu)₂Cl₄ (**3**) and one equivalent of H₂O.

Having discovered the O₂-reduction chemistry mediated by dirhodium hydride complex **2**, attention was immediately given to deducing mechanistic details of this intriguing

transformation. The efforts which were devoted to uncovering mechanistic insights into this chemistry comprise the majority of this chapter, and literature precedent provided important considerations to begin with. A rhodium-bound hydroperoxo is a plausible intermediate in the conversion of O₂ to water by **2**, and Fukuzumi and co-workers have shown via kinetic studies that peroxy complexes are competent intermediates for oxygen reduction promoted by iridium complexes.³³ In other synthetic systems, the insertion of O₂ into metal hydride bonds prevails for late transition metals,^{34–42} and such reactivity has been heavily studied, especially in the context of aerobic oxidation catalysis.^{43–45} Mechanistic studies and computations reveal three common mechanistic pathways for the insertion of O₂, which are summarized in Scheme 4.1: (i) radical chain autoxidation,^{37,43} (ii) HX dissociation followed by O₂ binding,⁴⁶ commonly referred to as the “HX Reductive-Elimination (HXRE)” pathway, and (iii) direct H-atom abstraction (HAA) by O₂.^{44,47–49} In one case it was found that pathways (ii) and (iii) operate in parallel.⁴⁵

The mechanism of O₂ activation by dirhodium hydride complex **2** was studied on two fronts. Model diiridium compounds were synthesized to gain structural insight into the primary products of oxygen activation. The third row analogue of **2**, Ir₂^{II,II}(tfepma)₂(CN^tBu)₂Cl₃H (**6**),⁵⁰ reacts cleanly with O₂ to form hydroperoxo complex Ir₂^{II,II}(tfepma)₂(CN^tBu)₂Cl₃(OOH) (**7**),



Scheme 4.1. Established mechanisms for aerobic oxidation of metal hydrides.

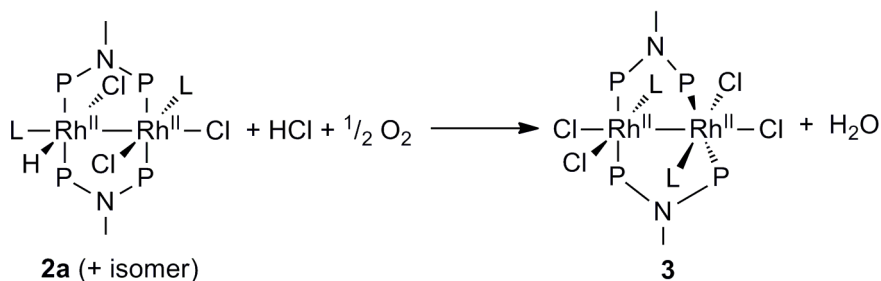
which is isolable and is amenable to structural and spectroscopic characterization. A side-on peroxo complex results if the hydride is not present; $\text{Ir}_2^{\text{II,II}}(\text{tfepma})_2(\text{CN}^t\text{Bu})_2\text{Cl}_2(\eta^2\text{-O}_2)$ (**8**) is obtained from the reaction of O_2 with $\text{Ir}_2^{0,\text{II}}(\text{tfepma})_2(\text{CN}^t\text{Bu})_2\text{Cl}_2$ (**5**). In addition to the synthetic models, detailed kinetic studies of the oxygen-reduction reactions of rhodium complex **2** and iridium complex **6** provide insight into the mechanistic details of O_2 activation. The kinetic profile for the O_2 -reduction reaction mediated by rhodium hydride complex **2** is consistent with the intermediacy of peroxo and hydroperoxo complexes akin to iridium models **7** and **8**. The results described here provide a mechanistic framework for O_2 reduction by bimetallic group 9 hydride complexes and they show that O_2 insertion into metal hydride bonds can be a key step in the reduction of O_2 to water.

4.2 Results

4.2.1 Oxygen Reduction by Dirhodium Hydride Complex **2**

As described in Chapter 3, the complex $\text{Rh}_2^{\text{II,II}}(\text{tfepma})_2(\text{CN}^t\text{Bu})_2\text{Cl}_3\text{H}$ (**2**) forms reversibly in two isomeric forms (**2a/2b**) when $\text{Rh}_2^{0,\text{II}}(\text{tfepma})_2(\text{CN}^t\text{Bu})_2\text{Cl}_2$ (**1**) is treated with an excess of HCl. The equilibrium constant for the addition of HCl to complex **1** (K_{HCl}) is determined to be 1.8×10^2 by ^1H NMR integration. Similarly, treatment of **1** with excess DCl cleanly furnishes two isomers of $\text{Rh}_2^{\text{II,II}}(\text{tfepma})_2(\text{CN}^t\text{Bu})_2\text{Cl}_3\text{D}$, **4a** and **4b**. The NMR spectra suggest that **4a** and **4b** are structurally analogous to their hydride analogs and formed in the same ratio. Degassed solutions of hydride species **2a** and **2b** display indefinite thermal stability in the presence of excess HCl. However, when a solution of **1** is treated with excess HCl to furnish the hydride and O_2 is subsequently introduced, clean conversion to $\text{Rh}_2^{\text{II,II}}\text{Cl}_4$ complex **3** is observed over the course of a few hours, as determined by $^{31}\text{P}\{^1\text{H}\}$ and ^1H NMR spectroscopic monitoring. During the course of the reaction, no intermediate species are observed by NMR, and the ratio of **2a:2b** stays virtually constant. The reaction sequence is given in Scheme 4.2.

Analogous oxygen reactivity is observed for the deuteride complexes **4a** and **4b**. Treatment with O_2 in THF results in quantitative formation of **3** on a comparable timescale, as confirmed by $^{31}\text{P}\{^1\text{H}\}$ NMR. Following neutralization of the unreacted DCl with 2,6-lutidine, which precipitates the deuteriochloride salt, the ^2H NMR spectrum, Figure 4.1, clearly shows the formation of one equivalent of D_2O , as determined by integration of the broad D_2O resonance



Scheme 4.2. Oxygen reduction to water mediated by complex **2a/b**.

(2.7 ppm) against an internal standard of C_6D_6 . A control experiment, treated in an identical fashion but without any rhodium complex **1** present at the start, showed negligible amounts of D_2O in the ^2H NMR spectrum. These results confirm that hydride complex **2** promotes the four-electron, four-proton reduction of O_2 yielding one equivalent of water per equivalent of **2**.

The reaction of **2** with O_2 and HCl can be monitored by UV-vis absorption spectroscopy. The electronic spectra of authentic samples of **2** and **3** are depicted in Figure 4.2a for reference. The spectrum of **2** consists of 3 distinct maxima at 270, 317 and 414 nm. Figure 4.2b shows the spectral evolution when complex **2**, in the presence of 55 mM HCl , is treated with 0.80 atm of O_2 at 293 K. Over the time course of the 70-min reaction, features attributed to $\text{Rh}_2^{\text{II,II}}\text{Cl}_4$ complex **3** grow in, with isosbestic points maintained at 256, 276, 292, 330, 394 and 447 nm, in good agreement with the predicted isosbestic values from the authentic spectra shown in Figure 4.2a.

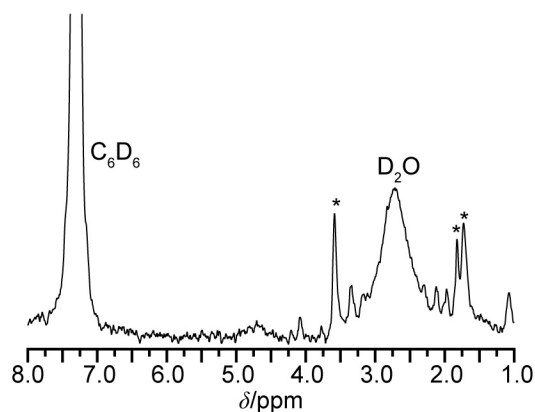


Figure 4.1. ^2H NMR spectrum of the reaction of **1** with 10 eq. of DCl and 2.3 eq. of O_2 , after consumption of excess DCl by treatment with 2,6-lutidine. The spectrum shows the presence of 1 eq. of D_2O , as judged by integration against the internal C_6D_6 standard. Peaks marked with an asterisk (*) are minor impurities resulting from solvent decomposition caused by DCl ; these peaks are also present in the control sample (no **1** present). The spectrum was recorded at 77.8 MHz in THF at 293 K.

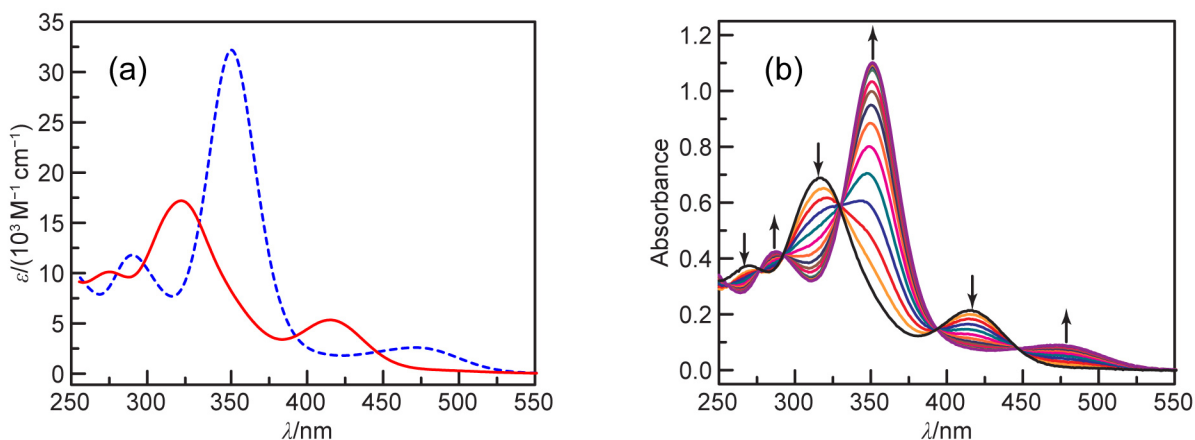


Figure 4.2. (a) Overlaid electronic absorption spectra of **2** (—, red) and **3** (---, blue), recorded at 295 K in THF. (b) Spectral evolution during the reaction of **2** (40 μM) with O_2 (0.80 atm) in the presence of HCl (55 mM). The reaction was carried out in THF at 293 K, and spectra were recorded every 5 min.

The final spectrum, which is a good match for that of an authentic sample of **3**, indicates near quantitative conversion to **3**. These observations suggest clean conversion of **2** to **3** at micromolar concentrations, and the presence of the isosbestic points indicates that substantial concentrations of intermediate species do not accrue during the course of the reaction.

The $\text{Rh}_2^{\text{II,II}}$ product **3** generated in the reaction given in Scheme 4.2 can be converted back to **1** photolytically. The UV-vis spectral features of **1** and **3** (Figure 4.3a) are similar to other metal–metal-bonded late transition-metal complexes,^{26,28,29} and can be attributed to states

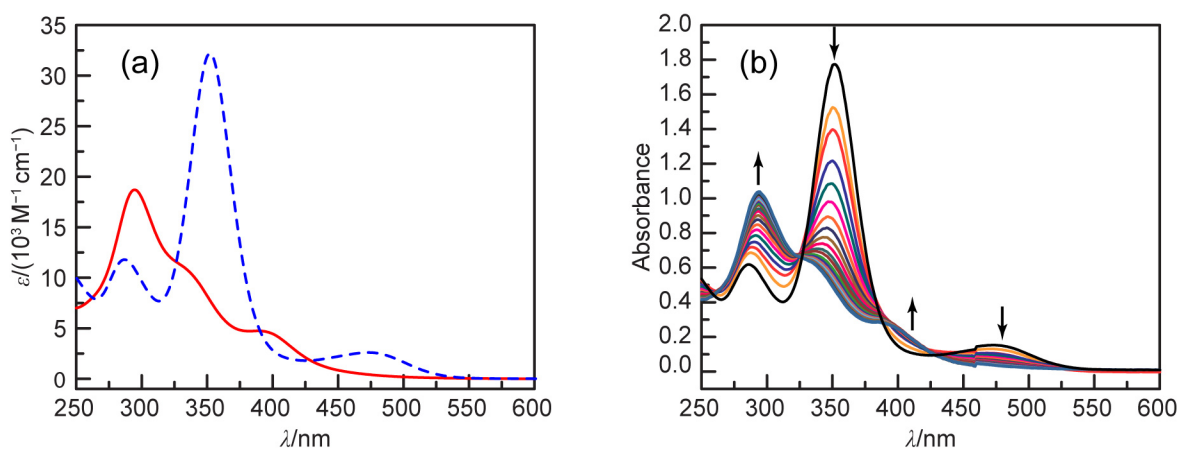
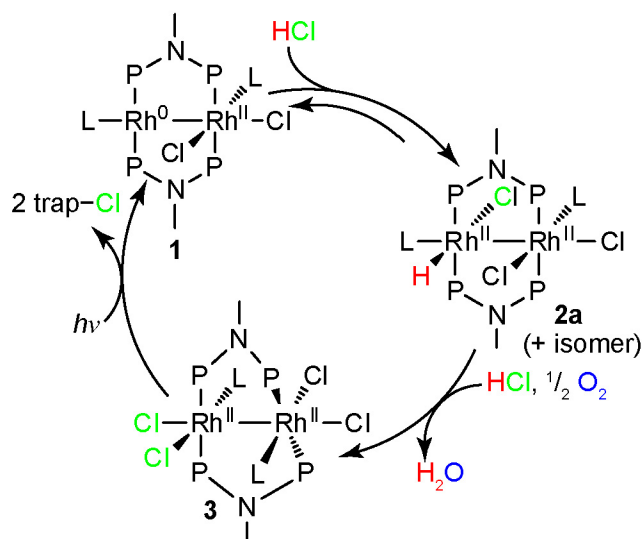


Figure 4.3. (a) Electronic absorption spectra of **1** (—, red) and **3** (---, blue) recorded in THF at 295 K. (b) Spectral evolution for the photolysis of **3** (56 μM) in THF, using broadband light with $\lambda > 313$ nm. Spectra were recorded every 2 min for a total of 40 min.



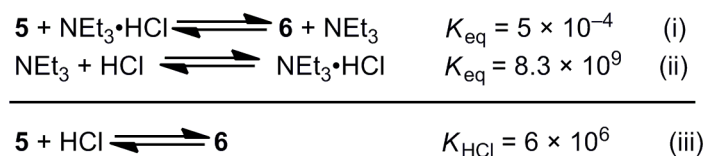
Scheme 4.3. Synthetic cycle for O₂ reduction mediated by **2**.

arising from the promotion of electrons into the $d\sigma^*$ LUMO. Irradiation of **3** ($\lambda_{\text{ex}} > 313$ nm) in THF begets smooth conversion to Rh₂^{0,II} complex **1**, which is stable under these photochemical conditions. The UV-vis spectral evolution of the photolysis, shown in Figure 4.3b, clearly indicates the formation of complex **1**. Isosbestic points at 261, 325, 391 and 431 nm attest to the quantitative photoconversion, and the final spectrum is identical to an authentic sample of **1**. The product-formation quantum yield, Φ_p , was found to be 0.0063(2) at $\lambda_{\text{ex}} = 320$ nm. This value for chlorine photoelimination is somewhat lower than that observed for d^7 – d^7 dirhodium complexes bridged by three dfpma ligands,⁵¹ which have quantum yields of 0.05(1) when irradiated at 334 nm.

By photochemically regenerating **1** from **3**, the synthetic photocycle shown in Scheme 4.3 is established. The cycle in Scheme 4.3 must be carried out in a stepwise fashion owing to the photochemical instability of hydride complexes **2a** and **2b**, as well as deleterious side reactions when **3** is photolyzed in the presence of oxygen and water, which build in concentration over the course of the reaction.

4.2.2 HCl Addition to Ir₂^{0,II} Complex **5**

Treatment of Ir₂^{0,II}(tfepma)₂(CN^{*t*}Bu)₂Cl₂ (**5**) with HCl forms the isolable iridium analogue to **2**, Ir₂^{II,II}(tfepma)₂(CN^{*t*}Bu)₂Cl₃H (**6**). The synthesis, spectroscopic properties and solid-state structure of **6** were discussed in the previous chapter; here a more quantitative



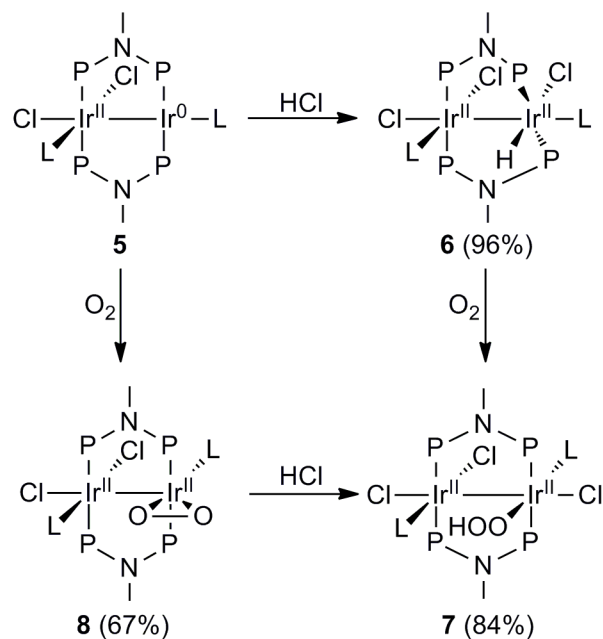
Scheme 4.4. Thermodynamic cycle for the determination of K_{HCl} for the addition of HCl to **5**.

treatment of the HCl addition to **5** is presented. The equilibrium constant for HCl addition to **5** to form **6**, K_{HCl} , was measured using the thermodynamic cycle shown in Scheme 4.4, analogous to a method used by Bercaw and DuBois to determine protonation equilibria for monometallic rhodium hydride complexes.⁵² The equilibrium constant was measured in acetonitrile, owing to the sufficient solubility of amine hydrochloride salts and the ready availability of the relevant acid-dissociation constants in this solvent. The equilibrium constant for (i) in Chart 1 was determined by ¹H NMR integration after treating Ir₂^{0,II} complex **5** with NEt₃·HCl in CD₃CN. The equilibrium constant of (ii) is calculated from known p*K*_a values of HCl⁵³ and triethylammonium⁵⁴ in acetonitrile. Reaction (iii) in Chart 1 is simply the sum of (i) and (ii), such that the HCl-addition equilibrium constant is the product of the K_{eq} 's for (i) and (ii). In this manner, a K_{HCl} of 4×10^6 is obtained for the addition of HCl to diiridium complex **5** to furnish **6**.

4.2.3 Reaction of **6** with O₂ to Form Ir₂^{II,II}(tfepma)₂(CN^{*t*}Bu)₂Cl₃(OOH) (**7**)

Scheme 4.5 summarizes the aerobic oxidation chemistry of diiridium complexes **5** and **6**. Hydride complex **6** (with no additional HCl), reacts cleanly with O₂ to form Ir₂^{II,II}(tfepma)₂(CN^{*t*}Bu)₂Cl₃(OOH) (**7**), which can be isolated in 84% yield and is determined to be pure by multinuclear NMR and elemental analysis. The ³¹P{¹H} NMR spectrum of **7**, recorded in CD₃CN, shows two closely spaced multiplets best described as arising from an AA'BB' spin system; this type of splitting has been observed in other asymmetric Ir₂^{II,II} complexes (see Chapter 3). The ¹H NMR spectrum shows the expected resonances from ligand protons, with two distinct *tert*-butyl resonances indicating chemical inequivalency of the two *tert*-butyl isocyanide ligands. In addition, a singlet at 7.32 ppm is attributed to the OO-*H* proton. The IR spectrum shows a single resolvable $\tilde{\nu}_{\text{C}=\text{N}}$ stretch at 2185 cm⁻¹ and a weak, broad $\tilde{\nu}_{\text{O}-\text{H}}$ stretch at 3355 cm⁻¹.

Hydroperoxo complex **7** has been crystallographically characterized, and its structure is shown in Figure 4.4. The structure of **7** contains a crystallographically imposed inversion center,



Scheme 4.5. Aerobic oxidation chemistry of **5** and **6**. Isolated yields are listed in parentheses.

such that half of the molecule is present in the asymmetric unit and the hydroperoxo ligand is disordered with the equatorial chloride ligand. The resulting structure shows two octahedral Ir^{III} centers, where the octahedra are eclipsed and the Ir(1)–Ir(1A) distance is 2.7492(8) Å. The O(5)–O(6) distance is 1.509(19) Å, similar to but slightly longer than other structurally characterized transition-metal terminal hydroperoxo complexes.^{44,45,55–62} The poor O–O bond-

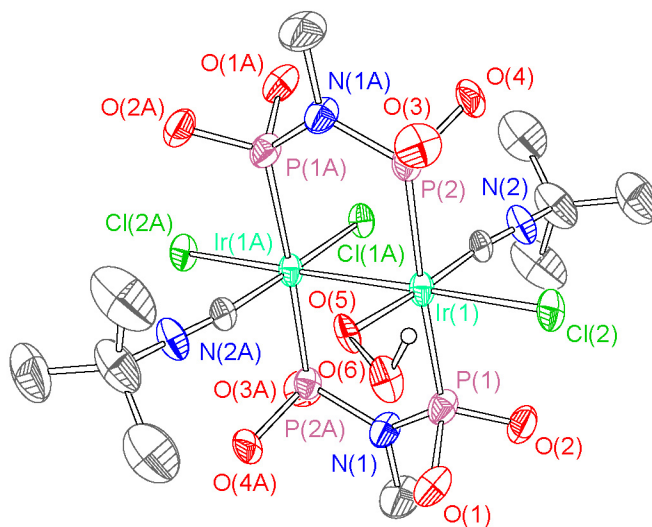


Figure 4.4. X-ray crystal structure of **7**. Ellipsoids are shown at the 50% probability level with $-\text{CH}_2\text{CF}_3$ groups and carbon-bound hydrogen atoms omitted for clarity.

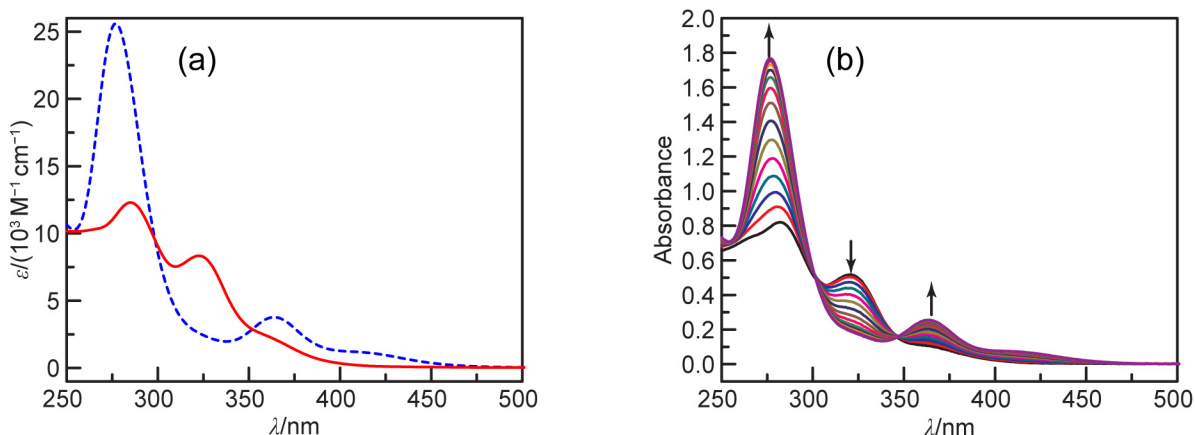


Figure 4.5. (a) Overlaid electronic absorption spectra of **6** (—, red) and **7** (---, blue), recorded at 295 K in THF. (b) Spectral evolution during the reaction of **6** (67 μM) with O_2 (0.40 atm). The reaction was carried out in THF at 293 K, and spectra were recorded every 5 min.

length precision results from the aforementioned disorder, but nonetheless this distance is consistent with an oxygen–oxygen single bond. The structure of **7** represents the first example of a structurally characterized iridium hydroperoxo complex.

The reaction of iridium hydride complex **6** with O_2 to form hydroperoxo **7** is also conveniently monitored by UV-vis absorption spectroscopy. The overlaid spectra of **6** and **7** are depicted in Figure 4.5a, showing that the absorption maxima are similar [$\lambda_{\text{max}} = 285 \text{ nm}$ (**6**), 277 nm (**7**)], though for the wavelength of maximum absorbance the molar absorptivity in hydroperoxo complex **7** is much greater [$\epsilon = 12000 \text{ M}^{-1} \text{ cm}^{-1}$ (**6**), $26000 \text{ M}^{-1} \text{ cm}^{-1}$ (**7**)]. After introduction of 0.40 atm of O_2 to a 67 μM solution of **6**, the absorption spectra evolve as shown in Figure 4.5b. Over time, the features of **7** appear; the final spectrum ($t = 65 \text{ min}$) is a good match to the authentic spectrum of **7** (Figure 4.5a). Isosbestic points maintained at 301 and 347 nm are in good agreement with their expected positions, and once again their presence shows that intermediate species persist at very low concentrations during the course of the reaction, or that no intermediates are involved in the conversion.

4.2.4 Reaction of **5** with O_2 to form $\text{Ir}_2^{\text{II,II}}(\text{tfepma})_2(\text{CN}^t\text{Bu})_2\text{Cl}_2(\eta^2\text{-O}_2)$ (**8**)

As shown in Scheme 4.5, $\text{Ir}_2^{0,\text{II}}$ complex **5** reacts directly with O_2 to form a side-on peroxo complex, $\text{Ir}_2^{\text{II,II}}(\text{tfepma})_2(\text{CN}^t\text{Bu})_2\text{Cl}_2(\eta^2\text{-O}_2)$ (**8**). The reaction is quite rapid, and within minutes $^{31}\text{P}\{^1\text{H}\}$ NMR of the crude reaction mixture reveals complete conversion. Analytically pure **8** is isolated in 67% yield and can withstand several hours of in vacuo drying without O_2

loss. The $^{31}\text{P}\{^1\text{H}\}$ NMR spectrum shows two closely spaced multiplets suggestive of an AA'BB' spin system, where in this case the ν_A and ν_B values are nearly coincident. The ^1H NMR spectrum shows the expected resonances arising from tfepma and CN^tBu ligands, with only minimal shifting relative to $\text{Ir}_2^{0,\text{II}}$ precursor **5**. The IR spectrum shows two closely spaced $\tilde{\nu}_{\text{C}\equiv\text{N}}$ stretching frequencies at 2148 and 2174 cm^{-1} , though the $\tilde{\nu}_{\text{O}=\text{O}}$ stretch, expected to occur in the range of 800–900 cm^{-1} , is obscured by strong features from the supporting ligands. The electronic absorption spectrum reveals three closely spaced bands characteristic of d^7-d^7 $\text{Ir}_2^{\text{II,II}}$ complexes.

X-ray crystallography confirms the structure of **8**, as shown in Figure 4.6. Complex **8** represents the first structurally characterized example of O_2 binding by a two-electron mixed-valent diiridium complex. The $\eta^2\text{-O}_2$ binding mode is reminiscent of the uptake of dioxygen by Vaska's complex^{63–65} and other related Ir^{I} complexes,^{66–70} as opposed to the $\mu\text{-O}_2$ diiridium peroxo cyclic motif that results when an $\text{Ir}^{\text{I}}\cdots\text{Ir}^{\text{I}}$ complex is treated with O_2 .^{71,72} The O(1)–O(2) internuclear distance of 1.480(5) Å is consistent with these previous examples and is demonstrative of a fully reduced O_2^{2-} ligand. It should be noted that librational disorder can lead to inaccuracies in crystallographically determined O–O bond distances in $\eta^2\text{-O}_2$ complexes; in particular the observation of abnormally short O–O bonds is a recurring problem.⁷³ However, the reported O–O bond distance in **8** is not noticeably short for a peroxo moiety, and the low temperature of the data collection (100 K) should minimize these effects. The O(1)–O(2)–Ir(1)

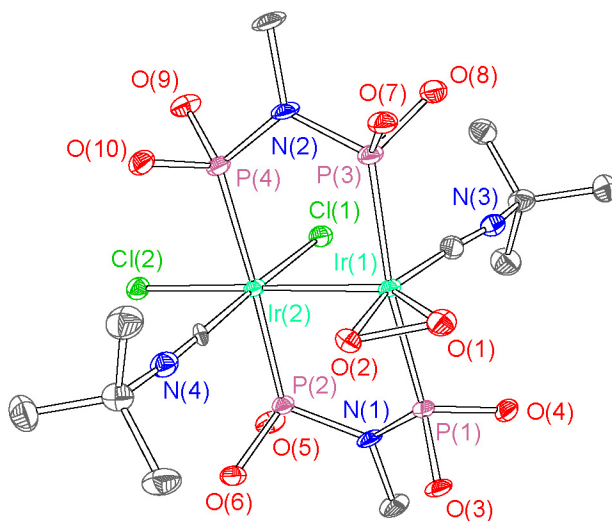


Figure 4.6. X-ray crystal structure of **8**. Ellipsoids are shown at the 50% probability level with $-\text{CH}_2\text{CF}_3$ groups and hydrogen atoms omitted for clarity.

and O(2)–O(1)–Ir(1) bond angles of 70.6(2)° and 67.6(2)°, respectively, necessitate a severe distortion from octahedral geometry at the Ir(1) center. In fact, if the O(1)–O(2) centroid is taken to occupy a single coordination site, the geometry about Ir(1) is better described as trigonal-bipyramidal. The Ir(1)–Ir(2) distance is 2.7498(4) Å, nearly identical to that of **6** and **7** and falling in line with other Ir₂^{II,II} complexes characterized recently.

Peroxo complex **8** is reactive toward HCl, forming hydroperoxo **7** as the major product as judged by the ³¹P{¹H} NMR spectrum of the reaction mixture. Several side products are also observed, though they can be attributed to HCl-induced decomposition of hydroperoxo complex **7**, as determined from an independent reaction of **7** with HCl. This reactivity establishes the bottom reaction pathway shown in Scheme 4.5, and gives the possibility that peroxo complex **8** forms as an intermediate during the direct oxygenation of hydride complex **6** to hydroperoxo **7**.

4.2.5 Rate Law for the Reaction of Rh₂^{II,II}Cl₃H (**2**) with HCl and O₂ to Form Rh₂^{II,II}Cl₄ (**3**)

The kinetic profile for the reaction of dirhodium hydride complex **2** with HCl and O₂ was determined. Based on previous NMR experiments, described in the preceding chapter, complex **2** exists as a mixture of two isomers in a ca. 7:1 ratio. The equilibrium between the two isomers is established within minutes, and the ratio of the two isomers does not change noticeably throughout the course of the experiment, suggesting that interconversion is able to keep up with O₂ activation and the two geometric isomers can be considered to remain in equilibrium throughout the reaction. This also establishes that it is not necessary (or for that matter possible) to determine separate rate laws for the two individual isomers. The reaction proceeds as described in Scheme 4.2, and it is conveniently monitored by tracking the production of **3** as indicated by the growth of the absorbance at 350 nm. Figure 4.7 shows a representative kinetic trace for the reaction of **2** with O₂ and HCl, in this case with 1.6 atm of O₂ and 5.5 mM of HCl and at 20 °C. As expected, the absorbance at 350 nm grows in over time, and with these pseudo-first-order conditions a monoexponential time course is observed. With these conditions, $k_{\text{obs}} = 0.12 \text{ min}^{-1}$.

Figure 4.8a shows the dependence of k_{obs} on the partial pressure of O₂, $p(\text{O}_2)$, at four different HCl concentrations. The values for k_{obs} depend on both O₂ partial pressure and HCl

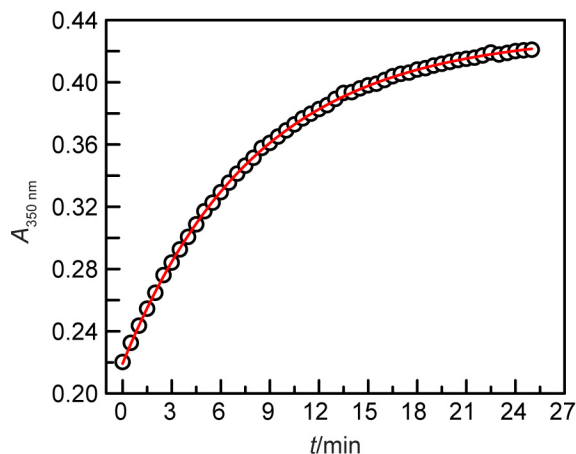


Figure 4.7. Representative kinetic trace for the reaction of **2** with O_2 (1.6 atm) and HCl (5.5 mM), showing the change in the absorbance at 350 nm ($A_{350\text{ nm}}$) vs. time. The solid line shows the best-fit monoexponential curve. The reaction was executed at 20 °C in THF, and was preceded by ~ 2 min of manual shaking to ensure equilibration of dissolved O_2 .

concentration. At a constant [HCl], the value of k_{obs} varies linearly with $p(O_2)$, though in all cases a nonzero y -intercept is observed. By inspection of Figure 4.8a, it is clear that the y -intercept of the four plots is invariant to the [HCl], and best-fit lines yield y -intercepts ranging between 0.050 and 0.055 min^{-1} , with no systematic trend. As shown in Figure 4.8b, the slopes of the plots in Figure 4.8a vary linearly with $[\text{HCl}]^{-1}$, with a nonzero intercept of 0.008(2) $\text{atm}^{-1} \text{min}^{-1}$. This shows that there are two first-order O_2 terms in the rate law, one which is inverse-first-order in

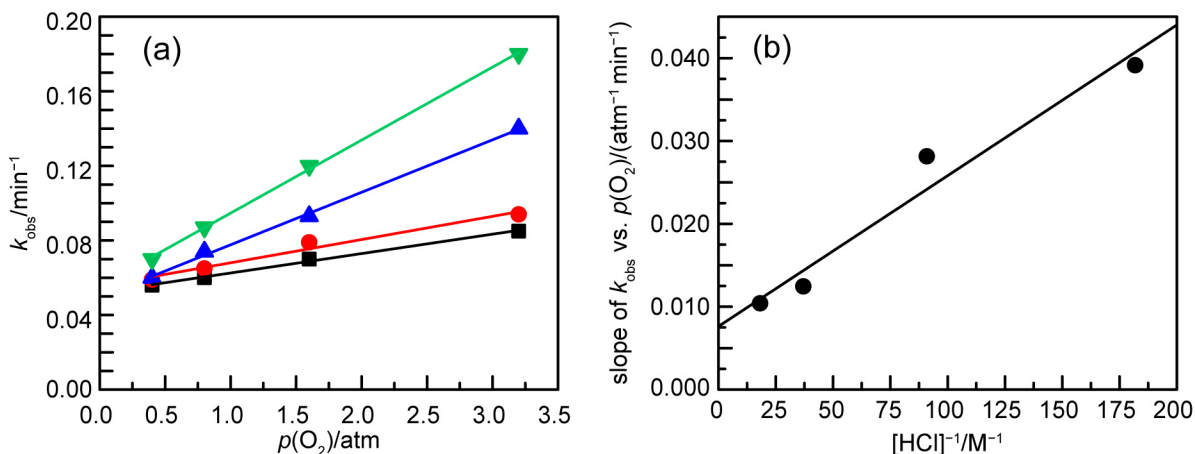


Figure 4.8. (a) Dependence of k_{obs} on $p(O_2)$ for the reaction of **2** with O_2 and HCl, with the [HCl] at 5.5 mM (∇), 11 mM (\blacktriangle), 27 mM (\bullet) and 55 mM (\blacksquare). The solid lines show the best-fit lines for each dataset. (b) The slopes of the best-fit lines of k_{obs} vs. $p(O_2)$ from (a) are plotted against $[\text{HCl}]^{-1}$. The best-fit line is shown.

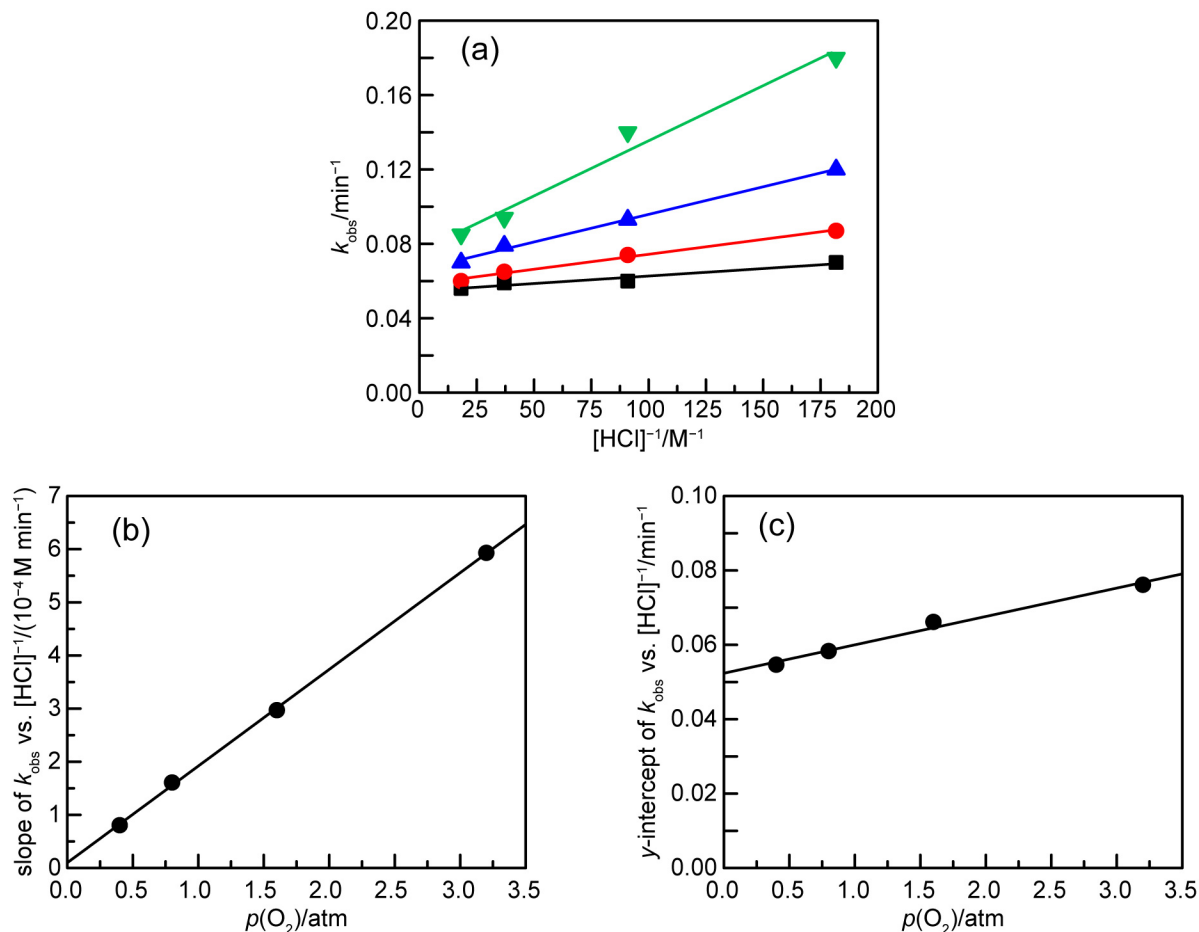


Figure 4.9. (a) Dependence of k_{obs} on $[\text{HCl}]^{-1}$ for the reaction of **2** with O₂ and HCl, with $p(\text{O}_2)$ at 0.4 atm (■), 0.8 atm (●), 1.6 atm (▲) and 3.2 atm (▼). Data are the same as those depicted in Figure 4.8. The solid red lines show the best-fit lines for each dataset. (b) The slopes of the best-fit lines of k_{obs} vs. $[\text{HCl}]^{-1}$ from (a) are plotted against $p(\text{O}_2)$. The best-fit line is shown. (c) The y-intercepts of the best-fit lines of k_{obs} vs. $[\text{HCl}]^{-1}$ from (a) are plotted against $p(\text{O}_2)$. The best-fit line is shown.

HCl, the other zero-order. Further insight is provided by plotting k_{obs} vs. $[\text{HCl}]^{-1}$, as shown in Figure 4.9a. Qualitative visual inspection of Figure 4.9a reveals that both the slopes and intercepts of the depicted plots vary with $p(\text{O}_2)$. Figure 4.9b shows the dependence of the slopes on $p(\text{O}_2)$, and a strict first-order trend is observed, dictating that there is a single inverse-first-order HCl term in the rate law which is also first-order in O₂. In Figure 4.9c, the y-intercepts from Figure 4.9a are plotted vs. $p(\text{O}_2)$. A linear dependence with a nonzero y-intercept is seen, suggesting two HCl-independent terms in the rate law.

Taken together, the data in Figures 4.8 and 4.9 give rise to a three-term rate law, whose form is given by,

$$\text{Rate} = k_1[\mathbf{2}][\text{O}_2][\text{HCl}]^{-1} + k_1'[\mathbf{2}][\text{O}_2] + k_1''[\mathbf{2}] \quad (4.1)$$

The best-fit lines in Figures 4.8 and 4.9 provide estimates for the three rate constants. The first rate constant, k_1 , is determined from the slope of either Figure 4.8b or 4.9b, and is found to be $1.8(3) \times 10^{-4} \text{ M atm}^{-1} \text{ min}^{-1}$. The rate constant k_1' is readily determined from the slope of Figure 4.9c, with a value of $0.0076(6) \text{ atm}^{-1} \text{ min}^{-1}$. And finally, the y-intercept of Figure 4.9c gives the zero-order rate constant k_1'' , which has a value of $0.052(1) \text{ min}^{-1}$, matching the average value of the y-intercepts from the individual plots in Figure 4.8a.

In addition to the dependencies described above, the reaction of **2** with O_2 and HCl was conducted in the presence of the radical inhibitor BHT (1 mM), which was found to have a minimal effect on the observed kinetics. In the absence of BHT, the reaction of **2** with 3.2 atm of O_2 and 55 mM of HCl gives a k_{obs} of 0.085 min^{-1} , whereas in the presence of 1 mM of BHT the observed pseudo-first-order rate constant was 0.077 min^{-1} . Furthermore, it should be noted that the kinetic traces do not show any deviations at later time points attributed to the formation of the product water. Thus, at least at the concentrations that are formed during the conversion of **2** to **3**, the evolved H_2O has no effect on the observed kinetics.

4.2.6 Rate Law for the Reaction of $\text{Ir}_2^{\text{II,II}}\text{Cl}_3\text{H}$ (**6**) with O_2 to form $\text{Ir}_2^{\text{II,II}}\text{Cl}_3(\text{OOH})$ (**7**)

The reaction rate of $\text{Ir}_2^{\text{II,II}}(\text{tfepma})_2(\text{CN}^t\text{Bu})_2\text{Cl}_3\text{H}$ (**6**) with O_2 was monitored as a function

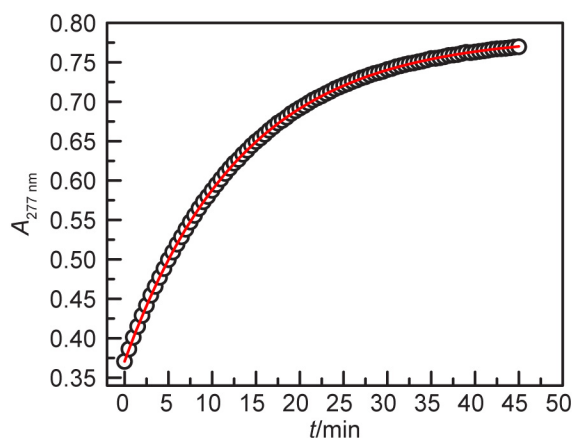


Figure 4.10. Representative kinetic trace for the reaction of **6** with O_2 (3.2 atm) at $20 \text{ }^\circ\text{C}$, showing the change in the absorbance at 277 nm ($A_{277 \text{ nm}}$) vs. time. The solid line shows the best-fit monoexponential curve.

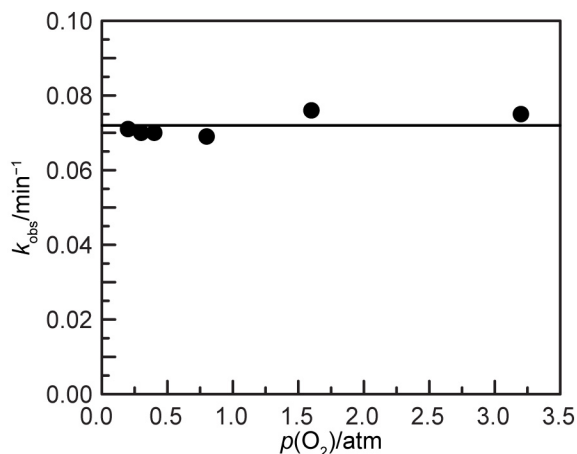


Figure 4.11. Dependence of k_{obs} on $p(\text{O}_2)$ for the reaction of **6** with O_2 . The horizontal line is drawn at the average of value of $k_{\text{obs}} = 0.072 \text{ min}^{-1}$.

of O_2 partial pressure. Figure 4.10 shows a representative trace for the conversion of **6** to **7** with 3.2 atm of O_2 and in the absence of HCl. The reaction is monitored at 277 nm, where **7** absorbs strongly. The data in Figure 4.10 can be satisfactorily fit to a monoexponential function, as shown by the best-fit monoexponential curve. Figure 4.11 shows that the observed rate constant, k_{obs} , has a zero-order dependence on O_2 concentration. The average value is 0.072 min^{-1} with no systematic variation in the range of 0.20 to 3.2 atm of O_2 . Thus, for reaction of **6** with O_2 to form **7**, a simple rate law is obtained,

$$\text{Rate} = k_2[\mathbf{6}] \quad (4.2)$$

The reaction of **6** with O_2 is strongly inhibited by added HCl, as determined from initial reaction rates with varying HCl concentrations. Figure 4.12a shows the dependence of k_{obs} (determined from initial rates) as a function of inverse HCl concentration. The data are clearly linear at the upper range of HCl concentrations, indicative of a concentration regime where the reaction is inverse-first-order in HCl. With added HCl, the reaction becomes first-order in O_2 , as indicated by the initial rate data in Figure 4.12b. A linear dependence is observed, and the y -intercept is very nearly zero, suggesting a single term in the rate law. The above indicate that, in the presence of HCl, the conversion of **6** to **7** exhibits the following rate law,

$$\text{Rate} = k_3[\mathbf{6}][\text{O}_2][\text{HCl}]^{-1} \quad (4.3)$$

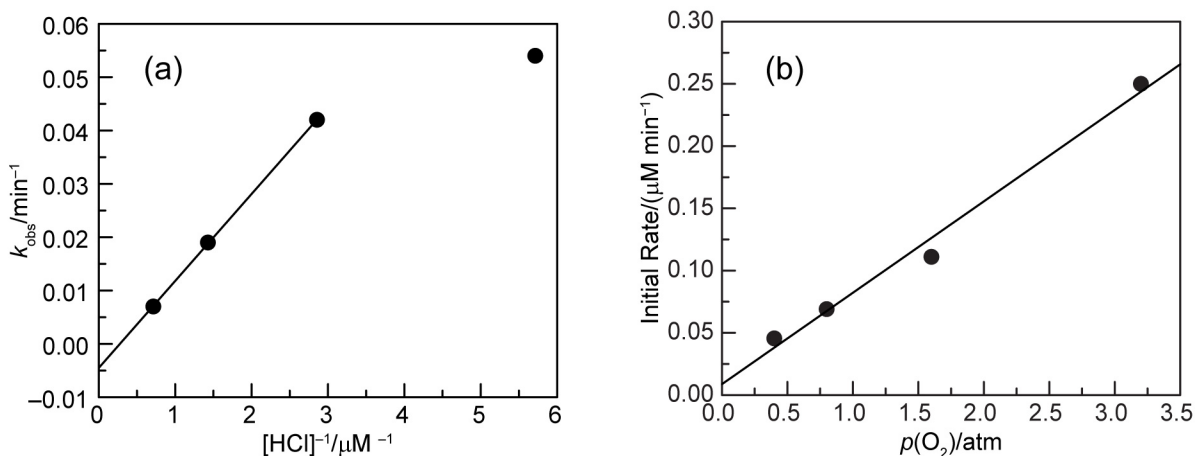


Figure 4.12. (a) Plot of k_{obs} vs. $[\text{HCl}]^{-1}$ for the reaction of **6** with O_2 (0.80 atm). Rate constants were calculated from initial rate data. A best-fit line to the three highest $[\text{HCl}]$ values is shown. (b) Plot of initial rate vs. $p(\text{O}_2)$ for the reaction of **6** with O_2 in the presence of HCl (1.4 μM). The $[\text{6}]_0$ is 9.7 μM .

The value of k_3 , determined from Figure 4.12b, is $2.0 \times 10^{-8} \text{ M atm}^{-1} \text{ min}^{-1}$.

Radical inhibitors have minimal effect on the observed rate constants. Addition of 1 mM of BHT gave k_{obs} of 0.070 min^{-1} , and with 1 mM of 1,4-cyclohexadiene $k_{\text{obs}} = 0.069 \text{ min}^{-1}$, with 0.80 atm of O_2 . These values are nearly identical to the average value of 0.072 min^{-1} over the range of O_2 concentrations (Figure 4.11). The radical initiator AIBN has a slight inhibitory effect on the reaction—at 80 μM AIBN, $k_{\text{obs}} = 0.064 \text{ min}^{-1}$, and at 1 mM AIBN $k_{\text{obs}} = 0.050 \text{ min}^{-1}$.

4.3 Discussion

4.3.1 Reactivity of Diiridium Complexes with O_2

With the goal of understanding the mechanism of O_2 reduction mediated by dirhodium hydride complex **2**, we first investigated oxygenation reactions with diiridium complexes. $\text{Ir}_2^{0,\text{II}}$ complex **5** and its corresponding protonation product **6** are structurally analogous to their dirhodium brethren **1** and **2**. In addition, diiridium hydride complex **6**, unlike its dirhodium relative **2**, is thermally stable in the absence of HCl and as such is readily isolated. This feature allowed for an isolated study of the reactivity of **6** with O_2 , without interference of subsequent HCl reactivity.

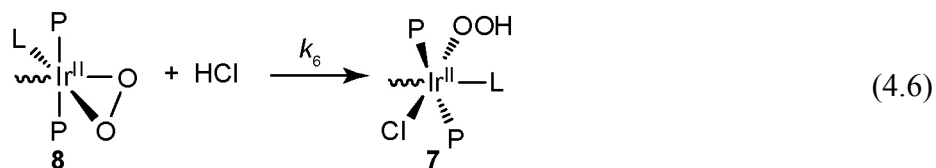
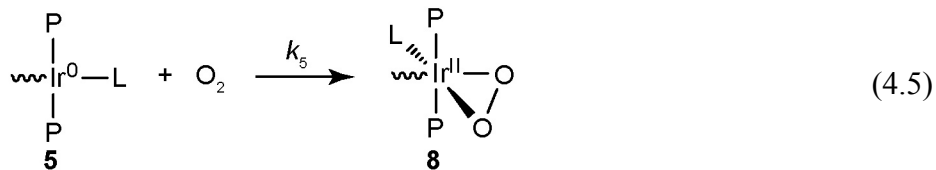
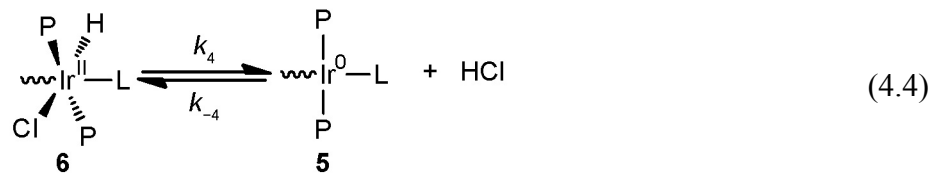
Addition of O_2 to **6** gives hydroperoxo complex **7**, which itself can be isolated. Recognizing the possibility of binding of O_2 by the M^0 center, the reactions of O_2 with $\text{M}_2^{0,\text{II}}$

complexes **1** and **5** were investigated. The reaction of dirhodium complex **1** with O₂ under ambient conditions fails to produce a stable O₂ adduct, and a gradual and nonspecific decomposition is observed. However, diiridium complex **5** reacts rapidly and cleanly with O₂, forming the isolable η^2 -peroxide complex **8**. Taken together, complexes **7** and **8** represent plausible structural models for intermediate species involved in the reduction of O₂ mediated by dirhodium complex **2**. As is shown below, they are indeed kinetically reasonable intermediates for the reaction sequence.

4.3.2 Mechanism of Formation of Iridium Hydroperoxo **7**

The discussion begins with the reaction of the diiridium hydride complex **6** with O₂ to form hydroperoxo complex **7**. The mechanistic considerations for this reaction will serve as a framework for interpreting the results of the dirhodium system. Radical-based mechanisms, which have been invoked previously in select examples of O₂-insertion chemistry,^{37,43,74} can be excluded. The reaction of **6** with O₂ is unaffected by the radical inhibitors BHT and 1,4-cyclohexadiene; the reaction is actually slightly inhibited by AIBN, which should accelerate a radical reaction.

The kinetic profile for the conversion of **6** to **7** takes on two different forms, depending on whether HCl is present as an additive. In all cases, the conversion is found to be first-order in **6**, removing the possibility of bimolecular reactivity as part of the mechanistic sequence. The reaction is zero-order in O₂ with no added HCl, as determined from the data of Figure 4.11. Under these conditions, the chemistry prior to the rate-determining step must be in net unimolecular in **6**. HCl is not consumed in the reaction, but the kinetic studies reveal an inverse-first-order HCl dependence, Figure 4.12a, suggesting a pre-equilibrium loss of HCl prior to the rate-determining step. And finally, with HCl present the reaction becomes first-order in O₂, as demonstrated in Figure 4.12b. This latter observation suggests that under conditions of added HCl, reaction with O₂ is the rate-determining step. All of the observations described above are consistent with the HX reductive-elimination (HXRE) mechanism that is summarized by the reaction sequence of Equations (4.4)–(4.6),



Reversible HCl elimination from hydride complex **6** produces Ir₂^{0,II} complex **5**, which binds O₂ via the reactive Ir⁰ center to yield η²-peroxo complex **8**. Our ability to isolate complex **8**, and its apparent thermal stability even under vacuum, suggest irreversible binding of O₂. Complex **8** is protonated by HCl to form the hydroperoxo complex **7**. The rate law for the three-step mechanism described by Eqs. (4.4)–(4.6) is,

$$\frac{d[\mathbf{7}]}{dt} = \frac{k_4 k_5 [\mathbf{6}] [\text{O}_2]}{k_{-4} [\text{HCl}] + k_5 [\text{O}_2]} \quad (4.7)$$

In the absence of HCl, the $k_{-4}[\text{HCl}]$ term in the denominator approaches zero, equivalent to the HCl-elimination step (4) becoming irreversible and rate-limiting. In this case, the rate law becomes,

$$\frac{d[\mathbf{7}]}{dt} = \frac{k_4 k_5 [\mathbf{6}] [\text{O}_2]}{k_5 [\text{O}_2]} = k_4 [\mathbf{6}] \quad (4.8)$$

equivalent to the rate law shown in Eq. (4.2), with $k_2 = k_4$. When HCl is present, the $k_{-4}[\text{HCl}]$ term becomes large relative to $k_5[\text{O}_2]$, and O₂-binding becomes the rate-determining step, leading to the following rate law,

$$\frac{d[7]}{dt} = \frac{k_4 k_5 [6][O_2]}{k_{-4} [HCl]} \quad (4.9)$$

This simplified rate law is equivalent to that of Eq. (4.3), with $k_3 = k_4 k_5 / k_{-4}$. The data in Figure 4.12 predict a first-order dependence on O₂ and an inverse-first-order dependence on HCl, when **6** is reacted with O₂ in the presence of added HCl. Thus the rate behavior predicted from the sequence of reactions in Eqs. (4.4)–(4.6) is realized experimentally, where the O₂ order depends on the presence or absence of added HCl, which itself exhibits an inverse-first order.

The reactivity that we have established here, and summarized in Scheme 4.5, lends credence to the proposed mechanism for the conversion of **6** to **7**. We predict the equilibrium constant $K_4 = k_4/k_{-4}$, to be quite small on the basis that: (i) the formation of hydride complex **6** from Ir₂^{0,II} complex **5** and HCl appears quantitative, and (ii) complex **6** is readily isolated and found to be stable in the absence of HCl,⁵⁰ as was described in the previous chapter. Indeed, the measured value for K_4 , the inverse of HCl-addition equilibrium constant (K_{HCl} , Scheme 4.4), is 2.5×10^{-7} . Nonetheless, the kinetic studies suggested HCl reductive elimination prior to oxygenation. Motivated by these results, we have independently verified that Ir₂^{0,II} complex **5**, formed by HCl elimination from **6**, reacts rapidly and quantitatively with O₂. The reaction forms the isolable complex Ir₂^{II,II}(tfepma)₂(CN^tBu)₂Cl₂(η²-O₂) (**8**), which can be treated with HCl to form hydroperoxo complex **7** as the major product. Thus, the intermediate species **5** and **8** have both been isolated, and their reactivity is consistent with the proposed mechanism that is constructed from kinetic rate profiles.

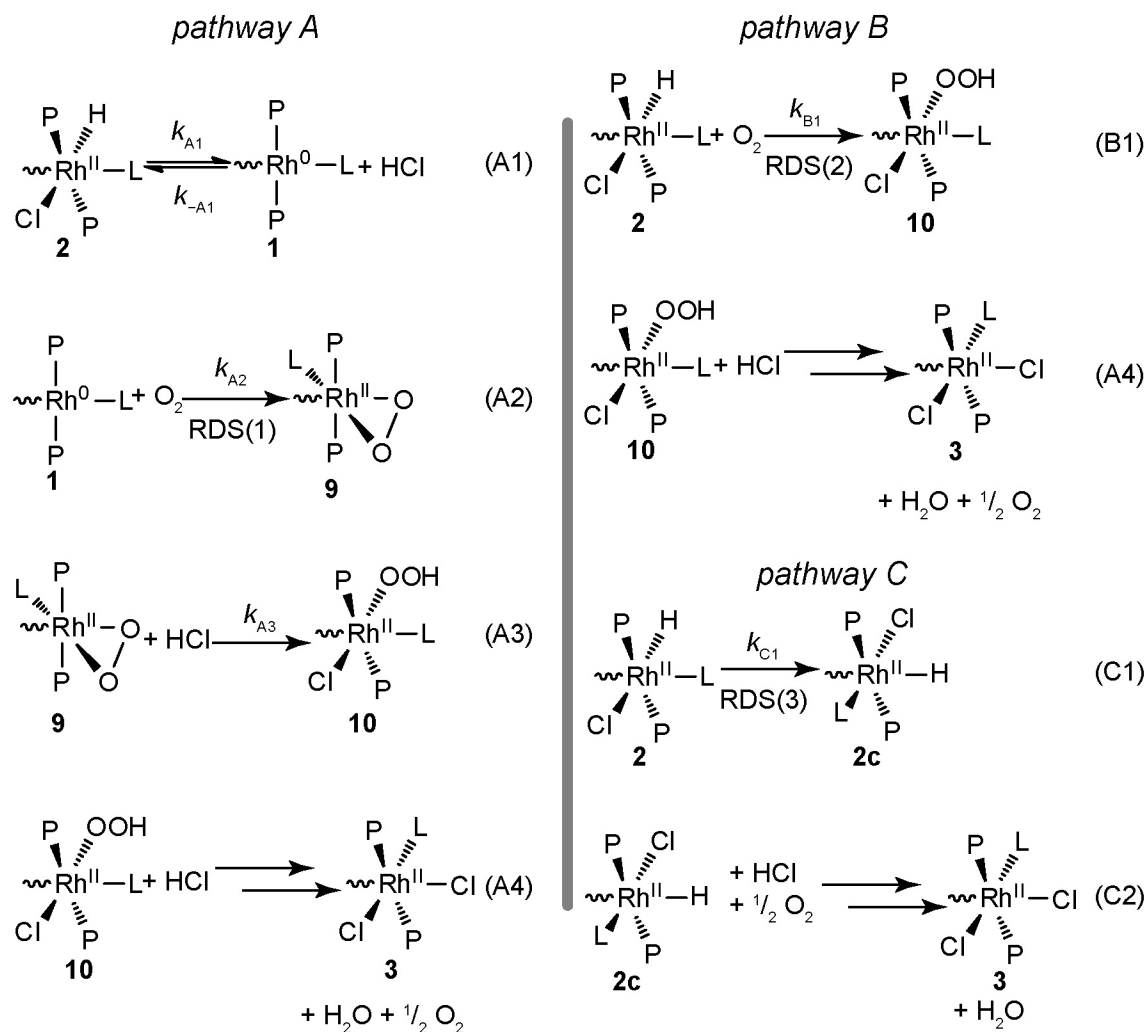
4.3.3 Mechanism of O₂ Reduction by Dirhodium Complex **2**

The foregoing mechanistic studies on the diiridium analogs provide a framework for interpreting the dirhodium system, for which no intermediate species can be isolated. The kinetic studies of the dirhodium system described above revealed a complex three-term rate law, given in Eq. (4.1). The rate law indicates that three distinct reaction pathways operate in parallel for the conversion of **2** to **3** when reacted with O₂ and HCl. The three parallel reaction pathways shown in Scheme 4.6 fit well with the kinetic data and furnish the rate law,

$$\frac{d[\mathbf{3}]}{dt} = \frac{k_{A1}k_{A2}[\mathbf{2}][O_2]}{k_{-A1}[HCl]} + k_{B1}[\mathbf{2}][O_2] + k_{C1}[\mathbf{2}] \quad (4.10)$$

Eq. (4.10) is equivalent to Eq. (4.1), with $k_1 = k_{A1}k_{A2}/k_{-A1}$, $k_1' = k_{B1}$ and $k_1'' = k_{C1}$. We will first focus on the first term of the rate law, which is consistent with the reaction sequence labeled “pathway A” of Scheme 4.6. This mechanism is analogous to that of the diiridium analogs [Eqs. (4.4)–(4.6)]. The inverse HCl dependence dictates an HCl-elimination reaction prior to the rate-determining step, and the first-order O_2 term mandates that the reaction with O_2 is rate-limiting. These results are consistent with the formation of peroxo complex **9**. Subsequent elementary steps occur beyond the rate-determining step and as such have no kinetic impact, though the protonation of **9**, reaction (A3), would seem likely based on the reactivity characterized for the diiridium analogs. Another possibility, which cannot be discounted on the basis of the kinetics data, is that the proposed peroxo intermediate **9** continues on to produce water without being protonated to a hydroperoxo, as has been suggested by Fukuzumi and collaborators in work on iridium complexes.³³ However, such a scheme would require liberation of OH^- and formation of a high-valent rhodium oxo, leading us to still favor the route we have proposed in Scheme 4.6.

The second term in the rate law is first-order in O_2 , and requires an alternate reaction sequence to occur in parallel. A likely possibility for this second pathway is given in pathway B of Scheme 4.6. Here again, the formation of hydroperoxo intermediate **10** is invoked, in this case via direct reaction of hydride complex **2** and O_2 [Eq. (B1)]. Hydroperoxo formation via direct H-atom abstraction has been implied from kinetic studies on Pd^{II} complexes,⁴⁴ and has been described computationally.^{47,48} Other computational⁴⁹ and experimental⁷⁵ studies have also shown that the HCl reductive elimination and H-atom abstraction pathways are close in energy and can operate competitively, as observed here. The subsequent reactivity of **10** to result in the production of H_2O with concomitant formation of $Rh^{II,II}Cl_4$ complex **3** occurs after the rate-determining steps for these two pathways. Thus we cannot speak definitively about the precise nature of reaction (A4). We speculate two possibilities: (i) evolution of a rhodium hydroxide complex followed by protonolysis to release H_2O , or (ii) protonation of **10** to release H_2O_2 ,



Scheme 4.6. Proposed mechanisms for O_2 reduction mediated by hydride complex **2**.

which is rapidly dismutated to O_2 and H_2O . Additional studies will be required to lend credence to either of these suggestions.

The third term of the rate law in Eq. (4.1), which dictates the mechanism for the other parallel reaction pathway that results in the conversion of **2** to **3**, is zero-order with respect to both O_2 and HCl . Accordingly there is little that can be said definitively about this parallel pathway, other than that the net conversion prior to the rate-determining step is a unimolecular reaction of **2**. One plausible sequence is shown in pathway C of Scheme 4.6, involving rate-limiting isomerization to form hydride complex **2c**. We observed previously by NMR studies that solutions of **2** contain $\sim 14\%$ of a minor product (**2b**), which rapidly equilibrates with the major species. However, there is the possibility that a third isomer, perhaps involving an axial

hydride, is formed in minor equilibrium and is reactive towards O₂. Other possibilities for the rate-limiting unimolecular step involve dissociation of either a chloride or CN^tBu ligand to open up a coordination site at one of the rhodium centers and cannot be explicitly ruled out. Addition of (NBu₄)Cl or CN^tBu to reaction mixtures causes deleterious side reactions of **2**, making it impossible to assess an inhibitory effect of either of these ligands on any of the parallel pathways in the reaction sequence. Reaction (C2), leading to the conversion of **2a** to **3**, is necessarily ill-defined since it occurs past the unimolecular rate-limiting step and as such does not give rise to an observed order in either HCl or O₂. Reaction (C2) may involve H-atom abstraction by O₂, which must be faster in pathway C than in pathway B. We have not crystallographically observed axial hydride ligands in any related complexes, though it is worth noting that in the previously reported crystal structures of dirhodium complexes **1–3**, the axial Rh–Cl bond distances are consistently 0.08–0.12 Å longer than the adjacent equatorial Rh–Cl. This observation confirms a sizeable *trans* influence of the Rh–Rh bond, which would weaken the Rh–H bond in an axial isomer and could lead to a lower activation barrier for H-atom abstraction subsequent to formation of a minor axial hydride isomer. One final possibility, which also cannot be ruled out, is that one of the spectroscopically observed isomers of **2** (**2a** or **2b**) also undergoes the HCl reductive-elimination pathway, but with HCl-elimination as the rate-determining step. This final possibility has been suggested by some ongoing transition-state computations for these various mechanisms. This pathway would be identical to pathway A, but would effectively involve irreversible, rate-determining HCl elimination, as opposed to pre-equilibrium HCl loss. This would give rise to a term in the rate law which is only first-order in complex **2**, with no O₂ or HCl dependence, and would require that the barrier for reductive elimination of one isomer of **2** be larger than the other. In this way, both **2a** and **2b** undergo the HXRE mechanism, but for one the HCl reductive elimination is rate-determining, and for the other O₂ binding is rate-determining. Furthermore, the interconversion of **2a** and **2b**, which likely also involves reductive HCl elimination, must occur at a comparable rate to pathways A and C such that **2a** and **2b** remain in equilibrium.

With these mechanistic proposals in hand, some quantitative differences between the dirhodium and diiridium O₂-activation chemistries become apparent. In particular, the protonation equilibrium constants and O₂-binding rate constants are distinct between the dirhodium and diiridium complexes. As described earlier, the equilibrium constant for HCl

addition (K_{HCl}) to $\text{Rh}_2^{0,\text{II}}$ complex **1** is 1.8×10^2 , whereas for $\text{Ir}_2^{0,\text{II}}$ complex **5** the analogous K_{HCl} is over four orders of magnitude higher at 4×10^6 . The observed rate constants for the HCl-reductive-elimination pathways (Eq. (4.4)–(4.6) and Scheme 3A) are given by $k_{\text{O}_2}/K_{\text{HCl}}$, where k_{O_2} is the rate constant for O_2 binding to the $\text{M}_2^{0,\text{II}}$ complex. Provided that HCl is present in sufficient quantities such that HCl-elimination is reversible and not rate-determining, the values for the O_2 -binding rate constants, k_5 and $k_{\text{A}2}$, can be extracted. For $\text{Ir}_2^{0,\text{II}}$ complex **5**, the O_2 -binding rate constant $k_5 = 8 \times 10^{-2} \text{ atm}^{-1} \text{ min}^{-1}$, whereas for $\text{Rh}_2^{0,\text{II}}$ complex **1** the analogous rate constant is quite similar at $k_{\text{A}2} = 3.2 \times 10^{-2} \text{ atm}^{-1} \text{ min}^{-1}$. Thus the major kinetic difference between the HCl reductive-elimination pathways for the dirhodium and diiridium complexes is found in the equilibrium constants for HCl elimination, and not in intrinsic differences in the rate constant for binding of O_2 to form the metal peroxo intermediate.

4.4 Conclusions

In this chapter, oxygen reduction and activation chemistry of bimetallic rhodium and iridium complexes was established, with coordinatively unsaturated $\text{M}_2^{0,\text{II}}$ complexes playing key roles in the observed reactivity. $\text{Rh}_2^{0,\text{II}}$ complex **1** reacts with HCl in an equilibrium fashion to furnish isomeric hydrido-chloride complexes **2a** and **2b**. The coordinative unsaturation of the Rh^0 center in **1** facilitates the thermal oxidative addition of HCl. The hydride complexes are resistant to protonolysis by additional HCl, but react smoothly with O_2 and HCl to furnish $\text{Rh}_2^{\text{II,II}}\text{Cl}_4$ complex **3**, with concomitant generation of H_2O . By using deuterated analogs, the production of one equivalent of water is confirmed. Product **3** can be photolytically converted back to **1** to complete a catalytic cycle, provided that the excess reactants (HCl and O_2) and the product water are first removed.

The sequence shown in Scheme 4.2 provides an unprecedented example of oxygen reduction facilitated by a two-electron mixed-valent complex. The molecular nature of this transformation permits the clear definition of reaction steps and intermediates, and in the majority of this chapter efforts to unveil mechanistic details were described. Considerable insight into the mechanism of O_2 reduction mediated by the dirhodium hydride complex $\text{Rh}_2^{\text{II,II}}(\text{tfepma})_2(\text{CN}^t\text{Bu})_2\text{Cl}_3\text{H}$ (**2**) is acquired by examining its diiridium congeners, owing to the ability to isolate and characterize plausible reaction intermediates. Particularly, with the diiridium suite both peroxo (**8**) and hydroperoxo (**7**) complexes can be isolated, their structure

and reactivity providing insight into unobserved intermediates in the dirhodium system. The results of synthesis and kinetics, taken together, permit the delineation of pathways for the insertion of O₂ into the metal hydride bonds. It has been determined that, as part of the HXRE pathway for oxygen insertion, O₂ binding by the M⁰ center, to furnish an η²-O₂ complex, is a key step in these transformations. The O₂ reactivity at the square-planar Rh⁰ and Ir⁰ centers is facilitated by the unsaturated coordination environment. In the case of the dirhodium system, kinetic studies reveal two additional competing pathways for O₂ insertion, one involving direct H-atom abstraction and the other proceeding through an isomeric species. In all cases, the step(s) leading to cleavage of the O–O bond and liberation of water occur beyond the rate-determining step, and as such no definitive insight into these key steps is provided by the present results. Subsequent work will aim to unveil pathways by which the hydroperoxo intermediates selectively liberate H₂O as the reduced oxygen species, and the initial findings of these efforts are disclosed in the next chapter of this thesis.

4.5 Experimental Details

4.5.1 General Considerations

All reactions involving air-sensitive materials were executed in a nitrogen-filled glovebox or on a high-vacuum manifold using solvents previously dried by passage through an alumina column under argon. The complexes Rh₂^{0,II}(tfepma)₂(CN^tBu)₂Cl₂ (**1**), Ir₂^{0,II}(tfepma)₂(CN^tBu)₂Cl₂ (**5**), and Ir₂^{II,II}(tfepma)₂(CN^tBu)₂HCl₃ (**6**) were prepared as described in Chapter 3. HCl (4 M in dioxane), 1,4-cyclohexadiene, BHT, and 2,2'-azobis(2-methylpropionitrile) (AIBN) were obtained from Sigma-Aldrich, whereas O₂ was purchased from Airgas and used as received. Elemental analyses were performed by Midwest Microlab LLC.

4.5.2 Physical Methods

NMR spectra were recorded at the MIT Department of Chemistry Instrumentation Facility on a Varian Mercury-300 NMR Spectrometer operating at 121.5 MHz for ³¹P acquisition, or a Varian Inova-500 NMR Spectrometer operating at 202.5 MHz for ³¹P acquisition, 76.8 MHz for ²H acquisition, or 500 MHz for ¹H acquisition. ³¹P{¹H} NMR spectra were referenced to an external standard of 85% D₃PO₄ and ¹H spectra were referenced to the residual proteo solvent resonances. UV-vis spectra were recorded at 293 K in THF solutions in

quartz cuvettes on a Varian Cary 5000 UV-vis-NIR spectrophotometer. Extinction coefficients were determined over a concentration range of $\sim 10^{-6}$ to 10^{-4} M, for which all compounds obeyed Beer's Law. IR spectra were recorded on a PerkinElmer Spectrum 400 FT-IR/FT-FIR Spectrometer outfitted with a Pike Technologies GladiATR attenuated total reflectance accessory with a monolithic diamond crystal stage and pressure clamp. Samples were suspended in Nujol[®] for all IR measurements, unless otherwise noted.

4.5.3 Preparation and NMR Characterization of $\text{Rh}_2^{\text{II,II}}(\text{tfepma})_2(\text{CN}^t\text{Bu})_2\text{Cl}_3\text{D}$ (**4a** and **4b**)

In a septum-capped NMR tube, a solution of **1** (25 mg, 0.018 mmol, 1.0 eq) was prepared in 0.5 mL of THF with 2.5 μL of C_6D_6 as an internal standard. A solution of 0.97 M DCl in Et_2O (180 μL , 0.176 mmol, 10 eq) was added via syringe. The NMR spectra were recorded immediately. **4a**: Yield (from ^2H NMR): 88%. ^2H NMR (76.8 MHz, THF) δ/ppm : -14.6 (br, s, 1D). $^{31}\text{P}\{^1\text{H}\}$ NMR (121.5 MHz, THF) δ/ppm : 138.1 (m, 2P), 116.9 (m, 2P). **4b**: Yield (from NMR): 12%. ^2H NMR (76.8 MHz, THF- d_8) δ/ppm : -18.8 (br, s, 1D). $^{31}\text{P}\{^1\text{H}\}$ NMR (121.5 MHz, THF- d_8) δ/ppm : 132.4 (m, 2P), ca. 116.3 (m, 2P) (overlap with major isomer). The ^2H NMR spectrum also shows unreacted DCl (δ 7.5 ppm).

4.5.4 O_2 -Reduction Reaction of **2a** and **2b**

A sample of **1** (25 mg, 0.018 mmol, 1.00 eq) was dissolved in 0.7 mL of THF and transferred to a septum-capped NMR tube. A solution of 4.31 M HCl in dioxane (40 μL , 0.172 mmol, 9.6 eq) was added via syringe, and the NMR tube was inverted several times to ensure complete mixing. $^{31}\text{P}\{^1\text{H}\}$ NMR confirmed clean formation of **2a** and **2b** in a ca. 7:1 ratio. Using a gas-tight syringe, O_2 (1.0 mL, 1 atm, 0.041 mmol, 2.3 eq) was injected into the headspace of the NMR tube. The tube was shaken periodically to mix, and within 1–3 h $^{31}\text{P}\{^1\text{H}\}$ NMR showed clean formation of **3**. ^1H NMR analysis of the isolated product confirmed that **3** was formed quantitatively. The product **3** is stable to both O_2 and HCl, so longer reaction times can be used without detriment to the observed yield of **3**.

4.5.5 O_2 -Reduction Reaction of **4a** and **4b** and Detection of D_2O

A solution of **4a/4b** was prepared as described above, with 2.5 μL of C_6D_6 as an internal standard. Using a gas-tight syringe, O_2 (1.0 mL, 1 atm, 0.041 mmol, 2.3 eq) was injected, and the solution shaken vigorously to mix. After standing for several hours, ^{31}P NMR shows clean

conversion to **3**. An aliquot of 2,6-lutidine (20 μ L, 0.172 mmol, 10 eq) was injected via syringe to consume the unreacted DCl. The ^2H NMR revealed the formation of 1.0 ± 0.1 eq of D_2O , as determined by integration against the internal C_6D_6 standard. A control sample, prepared in the same fashion but with no **1** present, showed a negligible amount of D_2O in the ensuing ^2H NMR spectrum.

4.5.6 Kinetic Measurements

All kinetic experiments were monitored by UV-vis spectroscopy. Samples of appropriate concentrations were prepared in a nitrogen-filled glovebox and housed in quartz cuvettes sealed with a septum cap and containing a Teflon-coated magnetic stir bar. HCl solutions were introduced to the cuvette by syringe, and measured amounts of O_2 were injected using a gas-tight syringe. Samples were manually shaken to ensure complete mixing and equilibration of O_2 . The cuvette was placed in a temperature-controlled cuvette holder with magnetic stirrer, and reactions were monitored at 293 K by collecting single-wavelength absorption data every 15 or 30 seconds, depending on the rate of the reaction. Data fitting and analysis was performed with the aid of the software OriginPro[®] 8.

4.5.7 Preparation of $\text{Ir}_2^{\text{II,III}}(\text{tfepma})_2(\text{CN}^t\text{Bu})_2\text{Cl}_3(\text{OOH})$ (**7**)

A J. Young NMR tube was charged with a solution of $\text{Ir}_2^{\text{II,III}}(\text{tfepma})_2(\text{CN}^t\text{Bu})_2\text{HCl}_3$ (**6**) (42 mg, 0.026 mmol, 1.0 eq) in 0.7 mL of THF. The solution was freeze-pump-thaw degassed three times and then backfilled with ca. 1.5 atm of O_2 . The reaction was monitored by $^{31}\text{P}\{^1\text{H}\}$ NMR, and after 2 h complete conversion was noted. The tube was freeze-pump-thaw degassed once to remove headspace O_2 and in the glovebox the contents were transferred to a 20-mL scintillation vial. The solvent was removed to afford a yellow solid, which was washed with 2 mL of hexane and dried in vacuo. Yield: 36 mg (84%). ^1H NMR (500 MHz, CD_3CN) δ/ppm : 7.32 (s, 1H), 5.34 (m, 2H), 4.99–5.15 (m, 4H) 4.94 (m, 4H), 4.77 (m, 2H), 4.68 (m, 2H), 4.62 (m, 2H), 2.93 (pseudoquintet, 6H), 1.45 (s, 9H), 1.41 (s, 9H). $^{31}\text{P}\{^1\text{H}\}$ NMR (202.5 MHz, CD_3CN) δ/ppm : 78.4–79.5 (m, 2P), 75.9–77.0 (m, 2P) (AA'BB', 20 lines resolved, $\delta_{\text{avg}} = 77.7$ ppm). UV-vis (THF): λ/nm ($\epsilon/(\text{M}^{-1} \text{cm}^{-1})$) 277 (26000), 364 (3800), 402 (sh) (1200). IR (Nujol): $\tilde{\nu}_{\text{C}=\text{N}} = 2185 \text{ cm}^{-1}$, $\tilde{\nu}_{\text{O}-\text{H}} = 3355 \text{ cm}^{-1}$. Anal. Calcd. for $\text{C}_{28}\text{H}_{41}\text{Cl}_3\text{F}_{24}\text{N}_4\text{O}_{10}\text{P}_4\text{Ir}_2$: C, 20.21; H, 2.48; N, 3.37. Found: C, 20.41; H, 2.49; N, 3.25.

4.5.8 Preparation of Ir₂^{II,II}(tfepma)₂(CN^tBu)₂Cl₂(η²-O₂) (**8**)

Ir₂^{0,II}(tfepma)₂(CN^tBu)₂Cl₂ (**5**) (50 mg, 0.031 mmol, 1.0 eq) was dissolved in 0.7 mL of THF and transferred to a J. Young NMR tube. The sample was degassed by three freeze-pump-thaw cycles and backfilled with ca. 1.5 atm of O₂. Upon mixing the tube manually, the color rapidly faded to a dull yellow-orange. The excess O₂ was removed by two freeze-pump-thaw cycles, and in the glovebox the contents of the NMR tube were transferred to a 20-mL scintillation vial. The solvent was removed in vacuo to afford a yellow-orange solid, which was redissolved in 2 mL of Et₂O/2 mL of hexane. Concentration in vacuo afforded a dark yellow solid, which was washed with 2 × 2 mL of hexane and dried in vacuo. Yield: 34 mg (67%). ¹H NMR (500 MHz, CD₃CN) δ/ppm: 5.05–5.14 (m, 4H), 4.95 (m, 4H) 4.52–4.78 (m, 8H), 2.85 (pseudoquintet, 6H), 1.46 (s, 9H), 1.43 (s, 9H). ³¹P{¹H} NMR (121.5 MHz, CD₃CN) δ/ppm: 82.1 (m, 4P) (AA'BB', 16 lines resolved, δ_{avg} = 82.1 ppm). UV-vis (THF): λ/nm (ε/(M⁻¹ cm⁻¹)) 294 (12000), 338 (sh) (7700), 397 (sh) (1600). IR (Nujol): ν_{C=N} = 2148, 2174 cm⁻¹. Anal. Calcd. for C₂₈H₄₀Cl₂F₂₄N₄O₁₀P₄Ir₂: C, 20.66; H, 2.48; N, 3.44. Found: C, 20.83; H, 2.37; N, 3.29.

4.5.9 X-Ray Crystallographic Details

Single crystals of **7** were obtained by synthesizing the complex in CD₃CN and allowing the sample to stand at room temperature, and crystals of **8** were obtained in an analogous fashion from Et₂O. The crystals were mounted on a Bruker three-circle goniometer platform equipped with an APEX detector. A graphite monochromator was employed for wavelength selection of the Mo Kα radiation (λ = 0.71073 Å). The data were processed and refined using the program SAINT supplied by Siemens Industrial Automation. Structures were solved by Patterson methods in SHELXS and refined by standard difference Fourier techniques in the SHELXTL program suite (6.10 v., Sheldrick G. M., and Siemens Industrial Automation, 2000). Hydrogen atoms bonded to carbon were placed in calculated positions using the standard riding model and refined isotropically; all non-hydrogen atoms were refined anisotropically. In the structure of **7**, the O–H proton was tentatively located in the difference map, restrained to a distance of 0.84 Å from the oxygen nucleus and refined isotropically. In the structure of **7**, the (OOH)⁻ ligand and equatorial Cl⁻ ligand were disordered about a crystallographically imposed inversion center, and three of the four crystallographically independent –OCH₂CF₃ groups were modeled as two-part disorders. The (1,2) and (1,3) distances of all disordered parts were restrained to be similar using

the SADI command; the rigid-bond restraints SIMU and DELU were also used on disordered parts. Crystallographic details for **7** (CCDC 856949) and **8** (CCDC 856950) are summarized in Table 4.1.

Table 4.1. Crystallographic summary for **7** and **8**.

| | 7 | 8 |
|---|---|---|
| Formula | C ₂₈ H ₄₁ Cl ₃ F ₂₄ Ir ₂ N ₄ O ₁₀ P ₄ | C ₂₈ H ₄₀ Cl ₂ F ₂₄ Ir ₂ N ₄ O ₁₀ P ₄ |
| fw, g/mol | 1664.28 | 1627.82 |
| Temperature/K | 100(2) | 100(2) |
| cryst. syst. | Monoclinic | Monoclinic |
| space group | <i>P2₁/n</i> | <i>P2₁</i> |
| color | Yellow | Yellow |
| <i>a</i> /Å | 13.003(2) | 12.4449(13) |
| <i>b</i> /Å | 10.798(2) | 18.0315(19) |
| <i>c</i> /Å | 18.699(4) | 12.9712(13) |
| α /° | 90 | 90 |
| β /° | 91.086(3) | 117.313(2) |
| γ /° | 90 | 90 |
| <i>V</i> /Å ³ | 2625.0(8) | 2586.2(5) |
| ρ (calc.)/(g cm ⁻³) | 2.106 | 2.090 |
| <i>Z</i> | 2 | 2 |
| no. refl. | 50603 | 57482 |
| no. unique refl. | 4479 | 15121 |
| <i>R</i> _{int} | 0.0911 | 0.0566 |
| <i>R</i> ₁ ^{<i>a</i>} (all data) | 0.0645 | 0.0434 |
| <i>wR</i> ₂ ^{<i>b</i>} (all data) | 0.1216 | 0.0797 |
| <i>R</i> ₁ [(<i>I</i> > 2σ)] | 0.0493 | 0.0353 |
| <i>wR</i> ₂ [(<i>I</i> > 2σ)] | 0.1175 | 0.0760 |
| <i>GOF</i> ^{<i>c</i>} | 1.079 | 0.995 |
| Formula | — | -0.0100(42) |

^{*a*} $R_1 = \Sigma||F_o - |F_c||/\Sigma|F_o|$. ^{*b*} $wR_2 = (\Sigma(w(F_o^2 - F_c^2)^2)/\Sigma(w(F_o^2)^2))^{1/2}$. ^{*c*} $GOF = (\Sigma w(F_o^2 - F_c^2)^2/(n - p))^{1/2}$ where *n* is the number of data and *p* is the number of parameters refined.

4.6 References

- (1) Kaila, V. R. I.; Verkhovsky, M. I.; Wikström, M. *Chem. Rev.* **2010**, *110*, 7062–7081.
- (2) Cook, T. R.; Dogutan, D. K.; Reece, S. Y.; Surendranath, Y.; Teets, T. S.; Nocera, D. G. *Chem. Rev.* **2010**, *110*, 6474–6502.
- (3) Nocera, D. G. *Inorg. Chem.* **2009**, *48*, 10001–10017.
- (4) Lewis, N. S.; Nocera, D. G. *Proc. Natl. Acad. Sci. U.S.A.* **2006**, *103*, 15729–15735.
- (5) Winter, M.; Brodd, R. J. *Chem. Rev.* **2004**, *104*, 4245–4270.
- (6) Adler, S. B. *Chem. Rev.* **2004**, *104*, 4791–4844.
- (7) Chang, C. J.; Deng, Y.; Nocera, D. G.; Shi, C.; Anson, F. C.; Chang, C. K. *Chem. Commun.* **2000**, 1355–1356.
- (8) Chang, C. J.; Loh, Z.-H.; Shi, C.; Anson, F. C.; Nocera, D. G. *J. Am. Chem. Soc.* **2004**, *126*, 10013–10020.
- (9) Rosenthal, J.; Nocera, D. G. *Acc. Chem. Res.* **2007**, *40*, 543–553.
- (10) McGuire Jr., R.; Dogutan, D. K.; Teets, T. S.; Suntivich, J.; Shao-Horn, Y.; Nocera, D. G. *Chem. Sci.* **2010**, *1*, 411–414.
- (11) Dogutan, D. K.; Stoian, S. A.; McGuire, R.; Schwalbe, M.; Teets, T. S.; Nocera, D. G. *J. Am. Chem. Soc.* **2011**, *133*, 131–140.
- (12) Chang, C. K.; Liu, H. Y.; Abdalmuhdi, I. *J. Am. Chem. Soc.* **1984**, *106*, 2725–2726.
- (13) Collman, J. P.; Wagenknecht, P. S.; Hutchison, J. E. *Angew. Chem. Int. Ed.* **1994**, *33*, 1537–1554.
- (14) Anson, F. C.; Shi, C.; Steiger, B. *Acc. Chem. Res.* **1997**, *30*, 437–444.
- (15) Fukuzumi, S.; Kotani, H.; Lucas, H. R.; Doi, K.; Suenobu, T.; Peterson, R. L.; Karlin, K. D. *J. Am. Chem. Soc.* **2010**, *132*, 6874–6875.
- (16) Soo, H. S.; Komor, A. C.; Iavarone, A. T.; Chang, C. J. *Inorg. Chem.* **2009**, *48*, 10024–10035.
- (17) Halime, Z.; Kotani, H.; Li, Y.; Fukuzumi, S.; Karlin, K. D. *Proc. Natl. Acad. Sci. U.S.A.* **2011**, *108*, 13990–13994.
- (18) Rosenthal, J. R.; Nocera, D. G. In *Progress in inorganic chemistry*; John Wiley and Sons: New York, 2007; pp. 483–544.
- (19) Dogutan, D. K.; Bediako, D. K.; Teets, T. S.; Schwalbe, M.; Nocera, D. G. *Org. Lett.* **2010**, *12*, 1036–1039.
- (20) *Multimetallic catalysts in organic synthesis*; Shibasaki, M.; Yamamoto, Y., Eds.; Wiley-VCH: Weinheim; [Germany], 2004.

- (21) Broussard, M. E.; Juma, B.; Train, S. G.; Peng, W.-J.; Laneman, S. A.; Stanley, G. G. *Science* **1993**, *260*, 1784–1788.
- (22) Gray, T. G.; Veige, A. S.; Nocera, D. G. *J. Am. Chem. Soc.* **2004**, *126*, 9760–9768.
- (23) Heyduk, A. F.; Nocera, D. G. *Science* **2001**, *293*, 1639–1641.
- (24) Esswein, A. J.; Veige, A. S.; Nocera, D. G. *J. Am. Chem. Soc.* **2005**, *127*, 16641–16651.
- (25) Heyduk, A. F.; Nocera, D. G. *J. Am. Chem. Soc.* **2000**, *122*, 9415–9426.
- (26) Heyduk, A. F.; Macintosh, A. M.; Nocera, D. G. *J. Am. Chem. Soc.* **1999**, *121*, 5023–5032.
- (27) Cook, T. R.; Esswein, A. J.; Nocera, D. G. *J. Am. Chem. Soc.* **2007**, *129*, 10094–10095.
- (28) Cook, T. R.; Surendranath, Y.; Nocera, D. G. *J. Am. Chem. Soc.* **2009**, *131*, 28–29.
- (29) Teets, T. S.; Lutterman, D. A.; Nocera, D. G. *Inorg. Chem.* **2010**, *49*, 3035–3043.
- (30) Teets, T. S.; Neumann, M. P.; Nocera, D. G. *Chem. Commun.* **2011**, *47*, 1485–1487.
- (31) Esswein, A. J.; Veige, A. S.; Piccoli, P. M. B.; Schultz, A. J.; Nocera, D. G. *Organometallics* **2008**, *27*, 1073–1083.
- (32) Veige, A. S.; Gray, T. G.; Nocera, D. G. *Inorg. Chem.* **2005**, *44*, 17–26.
- (33) Fukuzumi, S.; Kobayashi, T.; Suenobu, T. *J. Am. Chem. Soc.* **2010**, *132*, 11866–11867.
- (34) Roberts, H. L.; Symes, W. R. *J. Chem. Soc. A* **1968**, 1450–1453.
- (35) Johnston, L. E.; Page, J. A. *Can. J. Chem.* **1969**, *47*, 4241–4246.
- (36) Gillard, R. D.; Heaton, B. T.; Vaughan, D. H. *J. Chem. A* **1970**, 3126–3130.
- (37) Endicott, J. F.; Wong, C.-L.; Inoue, T.; Natarajan, P. *Inorg. Chem.* **1979**, *18*, 450–454.
- (38) Atlay, M. T.; Preece, M.; Strukul, G.; James, B. R. *J. Chem. Soc., Chem. Commun.* **1982**, 406–407.
- (39) Atlay, M. T.; Preece, M.; Strukul, G.; James, B. R. *Can. J. Chem.* **1983**, *61*, 1332–1338.
- (40) Bakac, A. *J. Am. Chem. Soc.* **1997**, *119*, 10726–10731.
- (41) Thyagarajan, S.; Incarvito, C. D.; Rheingold, A. L.; Theopold, K. H. *Chem. Commun.* **2001**, 2198–2199.
- (42) Cui, W.; Wayland, B. B. *J. Am. Chem. Soc.* **2006**, *128*, 10350–10351.
- (43) Wick, D. D.; Goldberg, K. I. *J. Am. Chem. Soc.* **1999**, *121*, 11900–11901.
- (44) Denney, M. C.; Smythe, N. A.; Cetto, K. L.; Kemp, R. A.; Goldberg, K. I. *J. Am. Chem. Soc.* **2006**, *128*, 2508–2509.

- (45) Konnick, M. M.; Gandhi, B. A.; Guzei, I. A.; Stahl, S. S. *Angew. Chem. Int. Ed.* **2006**, *45*, 2904–2907.
- (46) Konnick, M. M.; Stahl, S. S. *J. Am. Chem. Soc.* **2008**, *130*, 5753–5762.
- (47) Keith, J. M.; Nielsen, R. J.; Oxgaard, J.; Goddard, W. A. *J. Am. Chem. Soc.* **2005**, *127*, 13172–13179.
- (48) Keith, J. M.; Muller, R. P.; Kemp, R. A.; Goldberg, K. I.; Goddard, W. A.; Oxgaard, J. *Inorg. Chem.* **2006**, *45*, 9631–9633.
- (49) Popp, B. V.; Stahl, S. S. *J. Am. Chem. Soc.* **2007**, *129*, 4410–4422.
- (50) Teets, T. S.; Cook, T. R.; McCarthy, B. D.; Nocera, D. G. *Inorg. Chem.* **2011**, *50*, 5223–5233.
- (51) Odom, A. L.; Heyduk, A. F.; Nocera, D. G. *Inorg. Chim. Acta* **2000**, *297*, 330–337.
- (52) Wilson, A. D.; Miller, A. J. M.; DuBois, D. L.; Labinger, J. A.; Bercaw, J. E. *Inorg. Chem.* **2010**, *49*, 3918–3926.
- (53) Izutsu, K. *Electrochemistry in nonaqueous solutions*; Wiley-VCH: Weinheim, Germany, 2002.
- (54) Kaljurand, I.; Kütt, A.; Sooväli, L.; Rodima, T.; Mäemets, V.; Leito, I.; Koppel, I. A. *J. Org. Chem.* **2005**, *70*, 1019–1028.
- (55) Carmona, D.; Lamata, M. P.; Ferrer, J.; Modrego, J.; Perales, M.; Lahoz, F. J.; Atencio, R.; Oro, L. A. *J. Chem. Soc., Chem. Commun.* **1994**, 575–576.
- (56) Wada, A.; Harata, M.; Hasegawa, K.; Jitsukawa, K.; Masuda, H.; Mukai, M.; Kitagawa, T.; Einaga, H. *Angew. Chem. Int. Ed.* **1998**, *37*, 798–799.
- (57) Takahashi, Y.; Hashimoto, M.; Hikichi, S.; Akita, M.; Moro-oka, Y. *Angew. Chem. Int. Ed.* **1999**, *38*, 3074–3077.
- (58) Akita, M.; Miyaji, T.; Hikichi, S.; Moro-oka, Y. *Chem. Lett.* **1999**, 813–814.
- (59) Guzei, I. A.; Bakac, A. *Inorg. Chem.* **2001**, *40*, 2390–2393.
- (60) Miyaji, T.; Kujime, M.; Hikichi, S.; Moro-oka, Y.; Akita, M. *Inorg. Chem.* **2002**, *41*, 5286–5295.
- (61) Rostovtsev, V. V.; Henling, L. M.; Labinger, J. A.; Bercaw, J. E. *Inorg. Chem.* **2002**, *41*, 3608–3619.
- (62) Ahijado, M.; Braun, T.; Noveski, D.; Kocher, N.; Neumann, B.; Stalke, D.; Stammler, H.-G. *Angew. Chem. Int. Ed.* **2005**, *44*, 6947–6951.
- (63) Vaska, L. *Science* **1963**, *140*, 809–810.
- (64) La Placa, S. J.; Ibers, J. A. *J. Am. Chem. Soc.* **1965**, *87*, 2581–2586.

- (65) Lebel, H.; Ladjel, C.; Bélanger-Gariépy, F.; Schaper, F. *J. Organomet. Chem.* **2008**, *693*, 2645–2648.
- (66) McGinnety, J. A.; Doedens, R. J.; Ibers, J. A. *Inorg. Chem.* **1967**, *6*, 2243–2250.
- (67) Wang, H. H.; Pignolet, L. H.; Reedy, P. E.; Olmstead, M. M.; Balch, A. L. *Inorg. Chem.* **1987**, *26*, 377–383.
- (68) Barbaro, P.; Bianchini, C.; Laschi, F.; Midollini, S.; Moneti, S.; Scapacci, G.; Zanello, P. *Inorg. Chem.* **1994**, *33*, 1622–1630.
- (69) Doux, M.; Ricard, L.; Le Floch, P.; Jean, Y. *Organometallics* **2005**, *24*, 1608–1613.
- (70) Crestani, M. G.; Steffen, A.; Kenwright, A. M.; Batsanov, A. S.; Howard, J. A. K.; Marder, T. B. *Organometallics* **2009**, *28*, 2904–2914.
- (71) Vaartstra, B. A.; Xiao, J.; Cowie, M. *J. Am. Chem. Soc.* **1990**, *112*, 9425–9426.
- (72) Xiao, J.; Santarsiero, B. D.; Vaartstra, B. A.; Cowie, M. *J. Am. Chem. Soc.* **1993**, *115*, 3212–3220.
- (73) Cramer, C. J.; Tolman, W. B.; Theopold, K. H.; Rheingold, A. L. *Proc. Natl. Acad. Sci.* **2003**, *100*, 3635–3640.
- (74) Boisvert, L.; Denney, M. C.; Hanson, S. K.; Goldberg, K. I. *J. Am. Chem. Soc.* **2009**, *131*, 15802–15814.
- (75) Konnick, M. M.; Decharin, N.; Popp, B. V.; Stahl, S. S. *Chem. Sci.* **2011**, *2*, 326–330.

**Chapter 5 –
Reactivity of a Diiridium Hydroperoxo Complex:
Acidolysis and Oxygen-Atom Transfer**

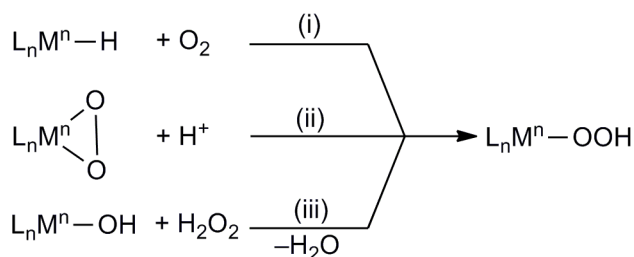
Portions of this work are pending for publication:

Teets, T. S.; Nocera, D. G. *Chem. Sci.*, submitted for publication. Reproduced by permission of the Royal Society of Chemistry.

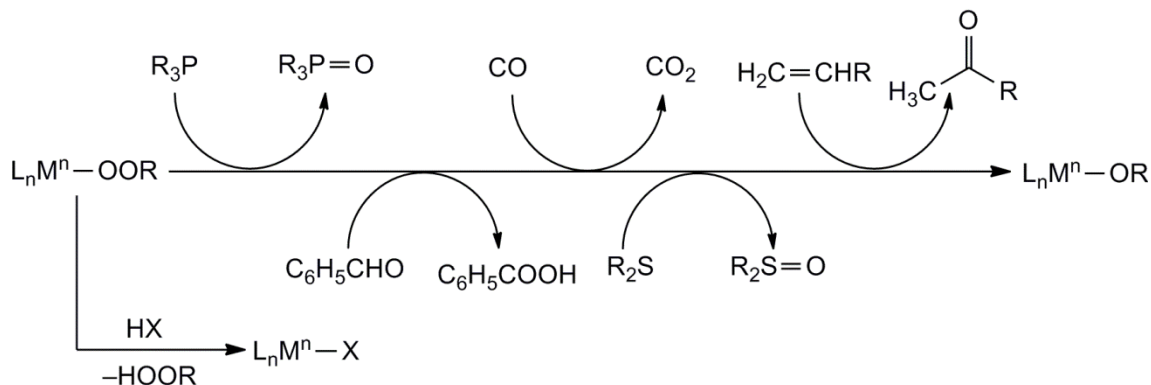
5.1 Introduction

In Chapter 4, detailed studies of O₂-reduction reactions, mediated by dirhodium and diiridium hydride complexes, were described. As part of this work, it was shown that HCl addition to the mixed-valent complex Ir₂^{0,II}(tfepma)₂(CN^tBu)₂Cl₂ (**1**, tfepma = CH₃N[P(OCH₂CF₃)₂]₂) produces an isolable diiridium hydride complex, Ir₂^{II,II}(tfepma)₂(CN^tBu)₂Cl₃H (**2**), which inserts O₂ to form Ir₂^{II,II}(tfepma)₂(CN^tBu)₂Cl₃(OOH) (**3**), the first isolable iridium hydroperoxo complex. In Chapter 4, mechanistic details for the formation of **3** were described, and compared directly to the dirhodium system, which reduces O₂ to water and likely proceeds through an analogous hydroperoxo complex. In the work presented in this chapter, complex **3** is interrogated further, and some key reactions of this novel hydroperoxo complex are described.

The synthesis and reactivity of O₂ complexes of transition metals has garnered widespread interest, owing to the prominence of such complexes in the fields of bioinorganic chemistry,¹⁻³ O₂-reduction electrocatalysis,⁴ and aerobic oxidation catalysis.⁵ One such class of reduced-oxygen complexes are metal hydroperoxos, which are commonly prepared by (i) aerobic oxidation of metal hydrides,⁶⁻²⁴ (ii) protonation of peroxo complexes,²⁵ or (iii) by addition of hydrogen peroxide to a terminal metal hydroxide,²⁶⁻²⁸ as summarized in Scheme 5.1. A wide range of supporting ligands have been used for late-metal hydroperoxo complexes, including phosphines, tris(pyrazolyl)borates, chelating pyridyl-amine ligands, and nitrogen-based planar macrocycles, among others. Although much of the interest in metal hydroperoxo complexes centers around the mechanisms of their formation, reactivity of these species has also been interrogated for select systems. Oxygen-atom-transfer (OAT) reactions are among the most prevalent.²⁶⁻³² Oxygenation of phosphines to phosphine oxides, sulfides to sulfoxides, olefins to carbonyl compounds, carbon monoxide to carbon dioxide, and benzaldehyde to benzoic acid



Scheme 5.1. Synthetic routes to late-metal hydroperoxo complexes.



Scheme 5.2. Previously characterized reactions of late-metal hydroperoxo and alkylperoxo complexes.

have all been reported for late-metal hydroperoxo and alkylperoxo complexes. Although acidolysis reactions of coordinated hydroperoxos are less heavily studied, there are several examples of hydrogen or alkyl peroxide liberation upon treatment of a hydroperoxo or alkylperoxo complex with acid; in all of these cases the O–O bond was reported to remain intact, with no other reduced oxygen species detected.^{25,30,31} Scheme 5.2 summarizes some of the key reactions of late-metal hydroperoxo and alkylperoxo complexes. Note that the series of reactions is not general to all such complexes, and the accessibility of different reactions frequently depends on the choice of metal and supporting ligands, particularly for the oxygen-atom-transfer reactions. Also, in some cases the organic product undergoes an additional insertion reaction with the hydroxo (or alkoxo) product, but in all cases OAT is proposed to initiate with the hydroperoxo (or alkylperoxo) complex.

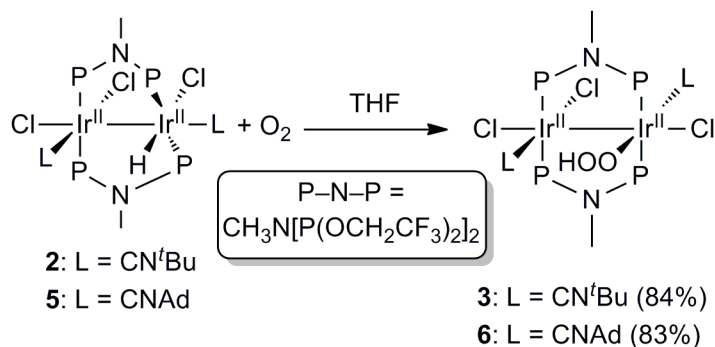
Having established a synthetic route to prepare $\text{Ir}_2^{\text{II,II}}(\text{tfepma})_2(\text{CN}^t\text{Bu})_2\text{Cl}_3(\text{OOH})$ (**3**), we became interested in interrogating its reactivity on two fronts: (i) its ability to transfer oxygen atoms to various substrates, and (ii) its reactions with acid sources, leading to an understanding of the O–O bond-cleavage step in the O_2 -reduction chemistry of the analogous dirhodium system. The kinetic studies described in Chapter 4 are consistent with a scenario where the transformations of the putative hydroperoxo intermediate occur beyond the rate-determining step, and as such, nothing was revealed about the types of reactions that lead to liberation of water. Also as part of this study, we aimed to prepare analogous iridium hydroperoxo complexes with altered ligand architectures, thinking that the mechanism of formation and subsequent reactivity could depend on the choice of supporting ligands. Though this final pursuit led to

minimal new insight, the initial results of efforts in all of these areas are disclosed here. Diiridium hydroperoxo complex **3** transfers an oxygen atom to phosphines, generating a novel diiridium hydroxo complex, and treatment of **3** with acids induces rapid O–O bond cleavage and formation of water. The exact fate of the acidolysis reaction depends on the strength of the acid used. These latter results provide some insight into the mode by which water is produced in the oxygen-reduction chemistry mediated by dirhodium hydride complexes.

5.2 Results

5.2.1 Synthesis of Iridium Hydroperoxo Complexes

As was detailed in Chapter 4, the high-yielding synthesis of hydroperoxo complex **3** proceeds by oxygenation of hydride complex **2** in THF. In an analogous fashion, Ir₂^{0,II}(tfepma)₂(CNAd)₂Cl₂ (**4**, CNAd = 1-adamantylisocyanide) is converted to hydride complex **5**, which also inserts O₂ to form isostructural hydroperoxo complex **6**. Scheme 5.3 summarizes the syntheses of hydroperoxo complexes **3** and **6**, which are isolated in yields of 84% and 83%, respectively. Complex **6** is structurally analogous to **3**, and its X-ray crystal structure is depicted in Figure 5.1. Complexes **3** and **6** are stereochemically identical, with the hydroperoxo ligand situated on the same side of the metal–metal axis as the isocyanide on the adjacent metal center. In **6**, the hydroperoxo hydrogen atom was tentatively located in the difference map and assigned as a two-part disorder. Relevant bond metrics for **3** and **6** are quite similar. The Ir–Ir bond distance of 2.7492(8) Å in **3** is nearly identical in **6**, at 2.7462(4) Å. The hydroperoxo O–O distance of 1.509(19) Å in **3**, which includes some uncertainty brought on by disorder, is noticeably shorter at 1.471(3) Å in **6**. However, this latter value is still clearly indicative of a



Scheme 5.3. Synthesis of diiridium hydroperoxo complexes **3** and **6**. Isolated yields are listed in parentheses.

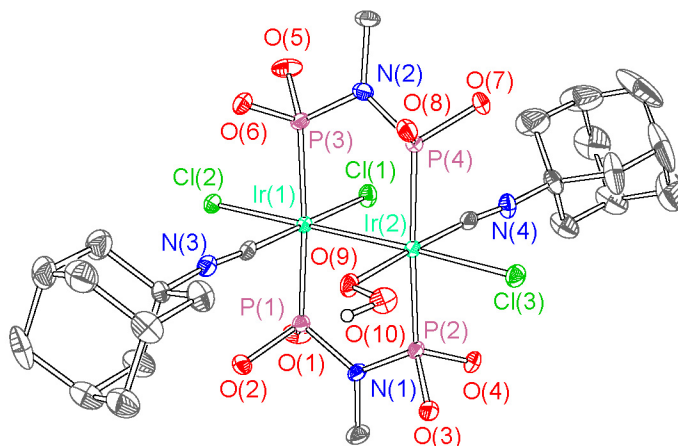
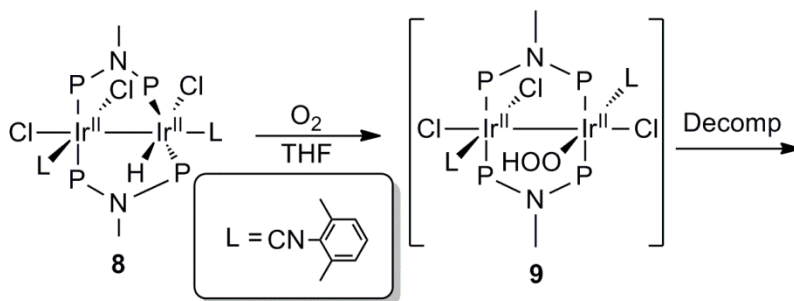


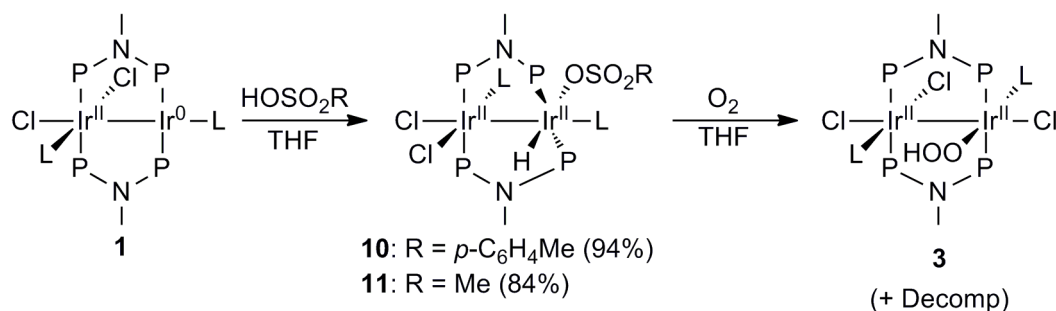
Figure 5.1. X-ray crystal structure of **6**. Ellipsoids are shown at the 50% probability level, with solvent molecules, $-\text{CH}_2\text{CF}_3$ groups and carbon-bound hydrogen atoms omitted for clarity.

formal oxygen–oxygen single bond. It was reasoned that in replacing CN^tBu with CN^iAd , some of the side reactions that plague the reactivity studies of **3** (see Sections 5.2.2 and 5.2.3) would be avoided, since CN^iAd is incapable of forming planar tertiary sp^2 carbocations or radicals, which may be involved in degradation pathways. However, preliminary reactivity studies show no noticeable differences between **3** and **6**, so the reactivity of complex **6** will not be considered further.

Two other modifications to complex **3** were sought, but neither resulted in the formation of stable hydroperoxo complexes. HCl addition to $\text{Ir}_2^{0,\text{II}}(\text{tfepma})_2(\text{CNXy})_2\text{Cl}_2$ (**7**, $\text{CNXy} = 2,6\text{-dimethylphenylisocyanide}$) gives hydride complex $\text{Ir}_2^{\text{II},\text{II}}(\text{tfepma})_2(\text{CNXy})_2\text{Cl}_3\text{H}$ (**8**) in an analogous fashion to **2** and **5**. However, as described in Scheme 5.4, oxygenation of **8** produces hydroperoxo **9**, which is found to be unstable at room temperature and decompose to a slew of intractable products. At early time points, a small amount of **9** is observed in the $^{31}\text{P}\{^1\text{H}\}$



Scheme 5.4. Synthesis of thermally unstable hydroperoxo complex **9**.



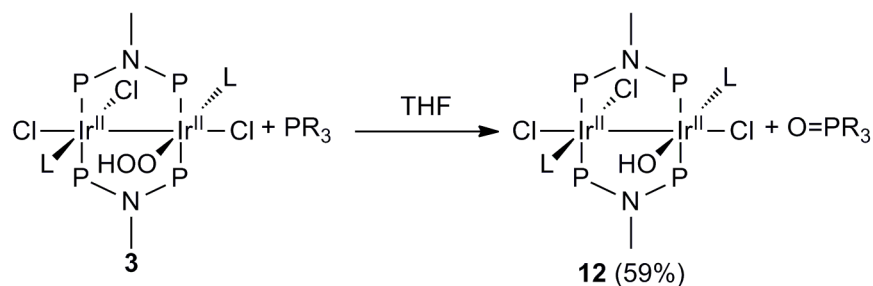
Scheme 5.5. O₂ reactivity of hydrido-sulfonate complexes **10** and **11**. Isolated yields are listed in parentheses.

NMR spectra, as indicated by a set of multiplets centered at 75.3 ppm, attributed to an AA'BB' spin system. Notably, hydride **8** is consumed at a substantially slower rate than **2** and **5** under similar conditions, but the instability of the product precluded detailed kinetic studies.

Similarly, attempts to substitute the chloride anions in **3** with sulfonate anions were unsuccessful. Addition of sulfonic acids to Ir₂^{0,II} complex **1** produces hydride complexes Ir₂^{II,II}(tfepma)₂(CN^tBu)₂Cl₂(H)(OSO₂R) [R = *p*-C₆H₄Me (**10**); Me (**11**)], which were isolated and found to be reactive towards O₂. Solutions of **10** and **11** were treated with ~ 1 atm of O₂ overnight, and the resulting NMR spectra (³¹P{¹H} and ¹H) indicate that hydroperoxo-trichloro product **3** is the only hydroperoxo-containing product, along with several intractable decomposition products. These results, summarized in Scheme 5.5, seem to suggest that the lability of the sulfonate anions induces scrambling of chloride and sulfonate anions. Complexes **10** and **11** are stable in anaerobic solutions, suggesting that the anion scrambling which leads to the formation of **3** occurs after O₂ insertion. Nevertheless, attempted partial anion substitution failed to produce a stable and isolable hydroperoxo species whose mechanism of formation and reactivity could be investigated.

5.2.2 Oxygen-Atom-Transfer Reactivity of **3**

Once prepared as described in Scheme 5.3, hydroperoxo complex **3** persists for some time in THF solution, both in the presence or absence of additional O₂. Under an inert atmosphere, **3** decomposes to a complex mixture of products with a half-life of approximately 2 weeks at room temperature. Complex **3** is unreactive towards organic substrates similar to those given in Scheme 5.2, including the alkene cyclohexene, the more electrophilic alkene 2-cyclohexen-1-one, benzaldehyde, and potent hydrogen-atom donor 1,4-cyclohexadiene.



Scheme 5.6. Oxygen-atom-transfer reactivity of **3**, generating **12**. Isolated yield is listed in parentheses.

Treatment of **3** with 5–10 eq of these substrates at room temperature gives no evidence for product formation after prolonged time periods. Attempts to heat reaction mixtures led to the decomposition of hydroperoxo complex **3** to a bevy of intractable products, with no evidence of substrate oxygenation in any case. Complex **3** undergoes nonspecific decomposition in the presence of dimethylsulfide at room temperature, again with no evidence for oxygen-atom transfer.

In contrast to these previous substrates, treatment of **3** with PPh₃ leads to clean oxygen-atom transfer, producing O=PPh₃ and Ir₂^{II,II}(tfepma)₂(CN^tBu)₂Cl₃(OH) (**12**) as major products. Scheme 5.6 depicts this transformation, which only proceeds cleanly with ca. 2 equivalents of PPh₃; stoichiometric reaction conditions result in significant decomposition in addition to the desired products. The initial NMR spectra (³¹P{¹H} and ¹H) for the reaction mixture are consistent with a weak interaction of **3** with PPh₃, as evidenced by the substantial broadening of the free PPh₃ resonances, with no apparent change in the spectral features attributed to **3**. The

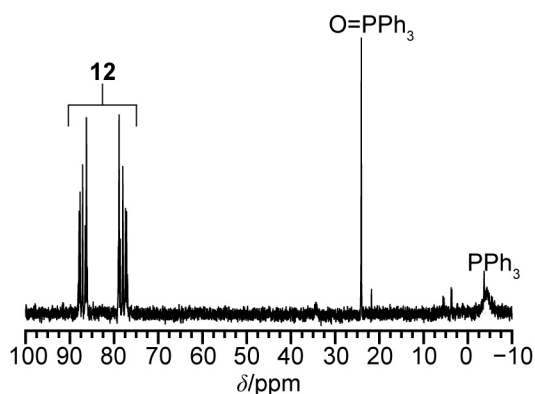


Figure 5.2. ³¹P{¹H} NMR spectrum recorded of the product mixture isolated from the reaction of **3** with 2 eq. of PPh₃ for 12 h. The spectrum was recorded at 121.5 MHz in THF-d₈. Peaks corresponding to O=PPh₃, unreacted PPh₃, and **12** are marked accordingly.

reaction of Scheme 5.6 is complete within 12 h, and furnishes the $^{31}\text{P}\{^1\text{H}\}$ NMR spectrum displayed in Figure 5.2. The $^{31}\text{P}\{^1\text{H}\}$ NMR spectrum of the hydroxo product **12** is consistent with an AA'BB' spin system, with chemical shifts and splitting patterns reminiscent of other $\text{Ir}_2^{\text{II,II}}$ complexes we have recently described.^{33,34} Two distinct $\text{C}\equiv\text{NC}(\text{CH}_3)_3$ resonances in the ^1H NMR spectrum provide further evidence for an asymmetric complex. Also in the ^1H NMR spectrum, a slightly broadened singlet at 6.96 ppm (THF- d_8), integrating to one proton, is assigned to the O–H group of **12**. The NMR spectra also clearly show the presence of $\text{O}=\text{PPh}_3$ and unreacted PPh_3 , with the latter resonances remaining broadened in the final product spectra. The IR spectrum of the isolated product contains a weak resonance at 3336 cm^{-1} attributed to the O–H stretch, which occurs at a slightly lower energy than that of hydroperoxo complex **3** (3355 cm^{-1}). Complex **12** can be prepared in pure form by using PEt_3 instead of PPh_3 as the O-atom acceptor. The crude NMR spectra show numerous minor side products, in addition to **12**, PEt_3 and $\text{O}=\text{PEt}_3$, though all are quite soluble and recrystallization removes all other products, allowing **12** to be obtained in 59% isolated yield, with purity verified by NMR and elemental analysis.

The structure of complex **12** was verified by single-crystal X-ray diffraction and is displayed in Figure 5.3. A crystallographically imposed inversion center defines two disordered

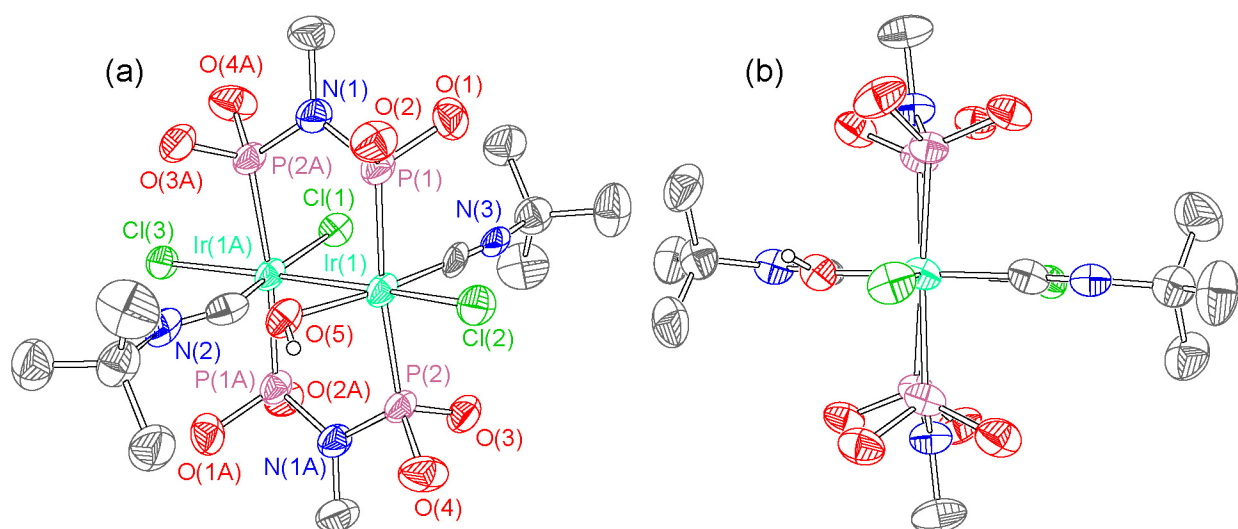


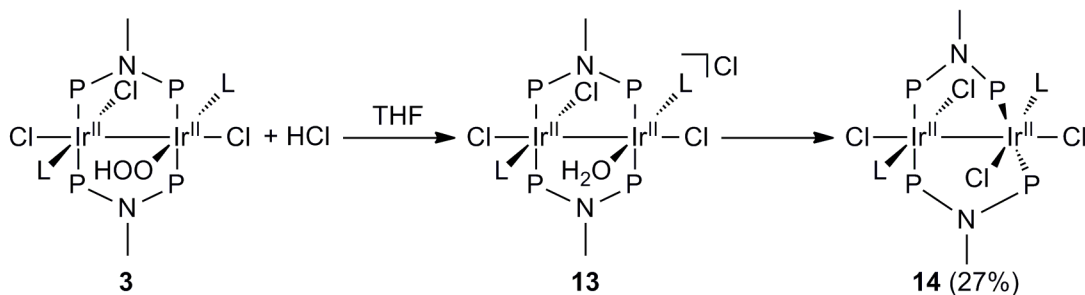
Figure 5.3. X-ray crystal structure of **12**, with ellipsoids shown at the 50% probability level. In (a) all non-carbon atoms are labeled, whereas in (b) a view down the metal–metal axis with an analogous color scheme is shown. Solvent molecules, carbon-bound hydrogen atoms, and $-\text{CH}_2\text{CF}_3$ groups are omitted for clarity. Only one of the two disordered orientations is shown.

orientations of the six monodentate ligands (three chlorides, two isocyanides, and one hydroxide) that surround the metal–metal axis. The relative configuration of the ligands is identical to that of hydroperoxo complex **3**, i.e. the hydroxide in **12** occupies the former site of the hydroperoxide, with no structural rearrangement upon oxygen-atom transfer. The Ir(1)–O(5) distance of 2.054(10) Å is consistent with a single bond, and though a definitive maximum for the O–H hydrogen atom was not located, owing to the aforementioned disorder, the spectroscopic data described above are consistent with the presence of a bound hydroxide ligand. The Ir(1)–Ir(1A) distance of 2.6584(5) Å is ca. 0.1 Å shorter than our other recent Ir₂^{II,II} complexes, but nonetheless is suggestive of a metal–metal single bond. As shown in Figure 5.3b, the two equatorial coordination spheres about the iridium atoms are very nearly eclipsed, as judged by the two independent P–Ir–Ir–P torsion angles, one of which is fixed at 180° by the inversion center, with the other quite small at 4.40(7)°.

5.2.3 Acidolysis Reactions of **3**

In the previously reported O₂-reduction chemistry of dirhodium hydride complexes³⁴ (see also Chapter 4), it was found that the activation of O₂ was the rate-determining step, and that beyond this rate-determining step the putative hydroperoxo intermediate reacted further with acid, inducing cleavage of the O–O bond to release water. It was reasoned that some insight into the O–O bond cleavage could be gained by studying the reactivity of the isolable iridium hydroperoxo complex **3** with acidic reagents. The reactivity of **3** with two acids, HCl and 2,6-lutidinium chloride, is summarized in this section.

As shown in Scheme 5.7, the reaction of hydroperoxo **3** with HCl proceeds in two distinct steps. Immediately upon addition of HCl, oxygen–oxygen bond cleavage is induced, and



Scheme 5.7. Reaction of **3** with HCl. Isolated yield is listed in parentheses.

an unstable species grows in which is assigned as the cationic complex $[\text{Ir}_2^{\text{II,II}}(\text{tfepma})_2(\text{CN}^t\text{Bu})_2\text{Cl}_3(\text{OH}_2)]\text{Cl}$ (**13**), on the basis of NMR spectroscopy. The temporal progression of the $^{31}\text{P}\{^1\text{H}\}$ NMR spectrum is given in Figure 5.4, and at early time shows a slightly broadened AA'BB' splitting pattern, suggestive of an $\text{Ir}_2^{\text{II,II}}$ complex but distinct from the spectrum of **3**. In the ^1H NMR spectrum, the expected resonances assigned to tfepma and CN^tBu are present, but in addition a broad resonance at ~ 7.8 ppm, integrating to two protons, is present and is assigned to a bound water molecule. This resonance persists in the isolated product, and diminishes at a rate commensurate with the disappearance of the other resonances of **13**, verifying that this broad resonance is indeed attributed to bound O–H protons (i.e. and not to H_2O_2 or some other free species in solution). Analysis of headspace gases by gas chromatography did not show any evidence for the formation of O_2 gas. Over the course of ca. 48 h, the NMR resonances attributed to **13** give way to a symmetric product, with a singlet in the $^{31}\text{P}\{^1\text{H}\}$ NMR spectrum (76.8 ppm, see Figure 5.4) and a single CN^tBu resonance in the ^1H spectrum. The disappearance of **13** is independent of the presence of added acid, and the final ^1H NMR spectrum also shows a broad singlet at ~ 2.6 ppm, which overlaps some of the peaks for side products but is tentatively assigned to free H_2O . The final diiridium product is assigned to be the centrosymmetric pseudo- C_{2h} isomer of $\text{Ir}_2^{\text{II,II}}(\text{tfepma})_2(\text{CN}^t\text{Bu})_2\text{Cl}_4$ (**14**), distinct from the asymmetric isomer that is prepared by halogen oxidation³³ (see also Chapter 3). Complex **14** was isolated in pure form in low yield (27%) by recrystallization, and determined to be pure by NMR and elemental analysis.

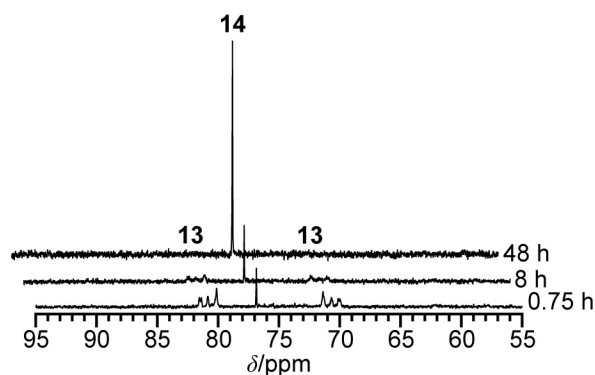


Figure 5.4. Evolution of the $^{31}\text{P}\{^1\text{H}\}$ NMR spectrum upon treatment of **3** with HCl (1.1 eq) at room temperature. The time is indicated at the right, and the resonances attributed to **13** and **14** are denoted. The spectra were recorded at 121.5 MHz in THF-d_8 .

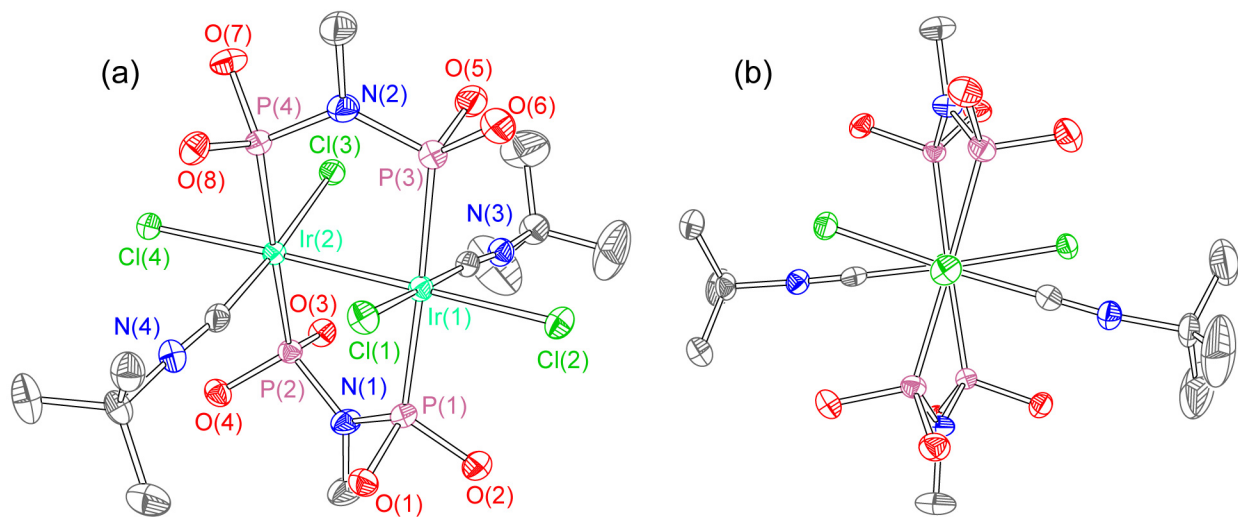
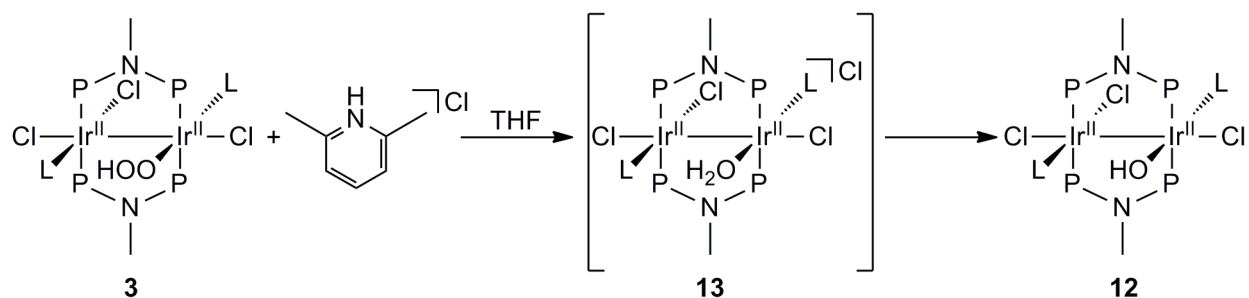


Figure 5.5. X-ray crystal structure of **14**, with ellipsoids shown at the 50% probability level. In (a) all non-carbon atoms are labeled, whereas in (b) a view down the metal–metal axis with an analogous color scheme is shown. Carbon-bound hydrogen atoms and $-\text{CH}_2\text{CF}_3$ groups are omitted for clarity.

The structure of **14** was validated by X-ray crystallography, as shown in Figure 5.5. The symmetric nature of the complex is evident, and the Ir(1)–Ir(2) bond distance of 2.7586(3) Å is consistent with a metal–metal bond. Notably, an approximate (though not crystallographic) inversion center is situated at the metal–metal centroid, consistent with the highly symmetric NMR resonances observed in solution. Evident from the side view given in Figure 5.5b, the equatorial coordination planes are twisted relative to one another, with four independent P–Ir–Ir–P dihedral angles of 25.66(4), 22.61(4), 156.13(4) and 155.60(4)°. These values indicate a substantial deviation from the eclipsed configuration that is observed in the structure of **12** discussed earlier. Complex **14** is crystallographically isostructural with the previously reported dirhodium analogue³⁵ (see also Chapter 3) of **14**, with nearly identical unit-cell dimensions and the same space group ($P2_1/c$).

As outlined in Scheme 5.8, the outcome is different if hydroperoxo complex **3** is treated with the weaker acid 2,6-lutidinium chloride. At early time points a small amount of aqua complex **13** is evident, but over the course of 15 h hydroxo complex **12** grows in as the major product, as is evident in the ^1H NMR spectrum, with none of the $\text{Ir}_2^{\text{II,II}}\text{Cl}_4$ product **14** detected. This suggests that 2,6-lutidinium is a strong enough acid to protonate the hydroperoxo ligand, but that the ensuing aqua complex **13** is deprotonated by the free lutidine, at a rate exceeding the



Scheme 5.8. Reaction of complex **3** with 2,6-lutidinium chloride.

substitution of Cl^- for the bound water. Such a reaction sequence should be catalytic in 2,6-lutidinium, although the final ^1H NMR spectrum after treating **3** with 2,6-lutidinium chloride suggests a mixture of 2,6-lutidinium and 2,6-lutidine. It is not clear by what means the acid is being consumed, though it is worth noting that there is a substantial yield of side products in these reactions, making it seem likely that some of the 2,6-lutidinium is consumed in an undesirable side reaction.

5.3 Discussion

Complex **3** represents the first isolable diiridium hydroperoxo complex, and its mechanism of formation was crucial to interpreting the mechanism of oxygen reduction mediated by dirhodium hydride complexes. Further insight, both into the mechanism of formation and the subsequent reactivity, could be gained by making analogs of **3** with altered ligand environments. However, the initial efforts described in section 5.2.1 showed that the stability of diiridium hydroperoxo complexes akin to **3** is exceptionally sensitive to ligand modification. Complex **6**, where the trivial substitution of the CN^tBu ligand in **3** for CN^{Ad} is made, was accessed and found to be thermally stable. But when more substantial modifications were sought, such as substituting the isocyanide for the *aryl* isocyanide CN^{Xy} , the resulting hydroperoxo complex was found to be thermally unstable, and along the way to consuming the hydride starting material complete decomposition to a mixture of spectroscopically intractable products was noted. In the case of anion substitutions, attempts to utilize hydrides originating from sulfonic acids failed to produce novel hydroperoxo complexes. The acid strengths of *p*-tosic acid and methanesulfonic acid are comparable to HCl , and the hydride complexes **10** and **11** generated from them can be accessed in pure form and are stable. However, aerobic oxidation reactions of **10** and **11** produce **3** as the only spectroscopically identifiable product, with

numerous decomposition products also evident. These observations suggest that diiridium hydroperoxo complexes featuring one or more weakly coordinating anionic ligands are inherently unstable.

In spite of the inability to make meaningful modifications to hydroperoxo complex **3**, the work described in this chapter does unveil two key classes of reactions for **3**. Oxygen-atom transfer to phosphines is facile, generating the corresponding phosphine oxide and a novel diiridium hydroxo complex **12**, which was spectroscopically and structurally characterized. The reaction between **3** and PPh₃ is complete within 12 h, and shows some broadening of the PPh₃ NMR resonances that likely indicates some association between **3** and PPh₃. The production of **12** occurs much more rapidly when the more electron-rich PEt₃ is used to accept the oxygen atom. This latter route, while resulting in numerous side products, allows for successful separation of **12** from the other reaction products and proved to be a viable synthetic route to pure **12**. The oxygen-atom-transfer reactivity of **3** is quite limited however, and no success was found with other substrates commonly utilized in such transformations (see Scheme 5.2). The inability of complex **3** to oxidize unsaturated organic substrates may be in part due to its coordinatively saturated octahedral geometry—previous examples of olefin oxygenation involved square-planar hydroperoxo complexes,^{26,28} and in a related study of alkylperoxo complexes it was explicitly shown that coordination of the alkene precedes oxygen-atom transfer.³⁶ It seems unlikely that the substrates considered here would displace one of the ligands from **3**, and indeed the NMR spectra of reaction mixtures show no shifts in the resonances of either **3** or the substrate that would suggest such an association. Without such a pre-coordination, oxygen-atom transfer would not occur, provided the mechanistic insights disclosed previously are general to these classes of reactions.³⁶

More relevant to the reduction of oxygen to water mediated by dirhodium hydride complexes, the reactivity of hydroperoxo complex **3** with acids was explored. The previous studies on oxygen-reduction chemistry (see Chapter 4) suggested intermediacy of hydroperoxo complexes, but their subsequent reactivity occurred beyond the rate-determining steps and could not be elucidated. Notable here is that treatment of **3** with either HCl or the weaker HCl-surrogate 2,6-lutidinium chloride induced scission of the oxygen-oxygen bond and formation of water, in the form of a bound aqua complex **13**. The fate of **13** depends on the choice of acid;

with HCl the aqua is gradually displaced by chloride to form the symmetric $\text{Ir}_2^{\text{II,II}}\text{Cl}_4$ product **14**, and with a weaker acid source, 2,6-lutidinium, intermediate **13** is intercepted by the conjugate base and instead forms hydroxo complex **12** as the major product. Hydrogen peroxide was not observed as a product of any of the acidolysis reactions, in stark contrast to the reactivity of previously reported hydroperoxo complexes, which are described to release H_2O_2 upon protonolysis.^{25,26,30} There are still some unknown details related to this reactivity, and there is particular interest in defining any short-lived intermediates that are involved in the oxygen–oxygen bond-cleavage reaction. In addition, though the gas chromatography studies described briefly above can rule out formation of one-half of an equivalent of O_2 , the fate of the second oxygen atom in the oxygen–oxygen bond-cleavage reaction remains unclear.

5.4 Conclusions

The synthesis and reactivity of diiridium hydroperoxo complexes was described. Although recalcitrant to synthetic modifications, hydroperoxo complex **3** does show some notable reactivity. Oxygen-atom transfer to phosphines occurs readily, giving a diiridium hydroxo complex in good yields. Complex **3** was found to be unreactive towards other electron-rich organic substrates, namely alkenes and aldehydes, likely due to the coordinative saturation at the iridium centers in **3**. Reactions of **3** with acids were also explored, and they provide insight into the oxygen–oxygen bond-cleaving elementary steps in the reduction of O_2 to water mediated by structurally analogous dirhodium complexes. Addition of acids results in cleavage of the O–O bond and formation of water, a distinct departure from reported reactivity of group 10 hydroperoxo and alkylperoxo complexes. Though unanswered questions remain regarding this acidolysis chemistry, it does provide further confirmation that hydroperoxo complexes are involved in the O_2 -reduction chemistry, and that their subsequent reactions with acid are responsible for the formation of water as the final reduced oxygen species.

5.5 Experimental Details

5.5.1 General Considerations

All reactions involving air-sensitive materials were executed in a nitrogen-filled glovebox using solvents previously dried by passage through an alumina column under argon. HCl (4 M in dioxane), methanesulfonic acid, and 2,6-dimethylphenylisocyanide (CNXy) were obtained from

Sigma-Aldrich, whereas $[\text{Ir}^{\text{I}}(\text{COD})\text{Cl}]_2$ (COD = 1,5-cyclooctadiene), PPh_3 and PEt_3 were obtained from Strem. Anhydrous 2,6-lutidinium chloride was prepared by adding anhydrous 2,6-lutidine to 1 M $\text{HCl}/\text{Et}_2\text{O}$ under nitrogen, as described previously.³³ The ligands $\text{CH}_3\text{N}[\text{P}(\text{OCH}_2\text{CF}_3)_2]_2$ (tfepma)³⁷ and 1-adamantylisocyanide (CNAd)³⁸ were prepared by a literature procedure. The complexes **1–3** and **10** were prepared as previously described^{33,34} (see also Chapters 3 and 4).

5.5.2 Physical Methods

NMR spectra were recorded at the MIT Department of Chemistry Instrumentation Facility on a Varian Mercury-300 NMR Spectrometer operating at 121.5 MHz for ^{31}P acquisition, or a Varian Inova-500 NMR Spectrometer operating at 500 MHz for ^1H acquisition. $^{31}\text{P}\{^1\text{H}\}$ NMR spectra were referenced to an external standard of 85% D_3PO_4 and ^1H spectra were referenced to the residual proteo solvent resonances. IR spectra were recorded on a PerkinElmer Spectrum 400 FT-IR/FT-FIR Spectrometer outfitted with a Pike Technologies GladiATR attenuated total reflectance accessory with a monolithic diamond crystal stage and pressure clamp.

5.5.3 Preparation of $\text{Ir}_2^{0,\text{II}}(\text{tfepma})_2(\text{CNAd})_2\text{Cl}_2$ (**4**)

$[\text{Ir}^{\text{I}}(\text{COD})\text{Cl}]_2$ (421 mg, 0.627 mmol, 1.00 eq) was suspended in 2 mL of Et_2O . A solution of tfepma (611 mg, 1.25 mmol, 2.00 eq) in 2 mL of Et_2O was added to leave a dark red solution. Addition of CNAd (202 mg, 1.25 mmol, 2.00 eq) in 6 mL of Et_2O caused the color to gradually lighten, and over the course of 40 h an orange solid precipitated. The suspension was concentrated in vacuo to leave an orange solid/red residue. The product was redissolved in 12 mL of CH_2Cl_2 , filtered and concentrated in vacuo. The solid was resuspended in a mixture of 2 mL of CH_2Cl_2 and 16 mL of hexane to liberate an orange solid, which was separated from the red supernatant by decantation, washed with 2×4 mL of hexane and dried in vacuo. Yield: 712 mg (64.8%). ^1H NMR (500 MHz, CD_2Cl_2) δ/ppm : 5.04 (m, 4H), 4.86 (m, 2H), 4.32–4.62 (m, 10H), 2.87 (pseudoquintet, 6H), 2.08 (br, m, 6H), 1.94 (br, d, 6H), 1.84 (br, d, 6H), 1.53–1.72 (br, m, 12H). $^{31}\text{P}\{^1\text{H}\}$ NMR (121.5 MHz, CD_2Cl_2) δ/ppm : 132.4 (m, 2P), 85.8 (m, 2P).

5.5.4 Preparation of Ir₂^{II,II}(tfepma)₂(CNAd)₂Cl₃H (5)

Complex 4 (75 mg, 0.043 mmol, 1.0 eq) was suspended in 1 mL of CH₃CN. A solution of 2,6-lutidinium chloride (7.7 mg, 0.054 mmol, 1.2 eq) in 2 mL of CH₃CN was added, drawing all solids into solution and yielding a pale yellow solution. After stirring for 1 h at room temperature, the solution was concentrated in vacuo to leave a yellow-orange residue. The product was redissolved in 6 mL of Et₂O and filtered to remove unreacted 2,6-lutidinium chloride. The resulting solution was combined with 4 mL of hexane and concentrated in vacuo. The nearly colorless solid was washed with 2 mL of cold hexane and dried in vacuo. Yield: 72 mg (95%). ¹H NMR (500 MHz, THF-d₈) δ/ppm: 5.53 (m, 2H), 5.28–5.43 (m, 4H), 4.74–4.97 (m, 6H), 4.25 (m, 4H), 2.84 (pseudoquintet, 6H), 2.08–2.18 (br, m, 12H), 2.04 (br, d, 6H), 1.63–1.78 (br, m, 12H), –20.69 (t, ²J_{P-H} = 16.2 Hz, 1H). ³¹P{¹H} NMR (121.5 MHz, CD₃CN) δ/ppm: 88.7–91.2 (m, 2P), 78.1–80.6 (m, 2P).

5.5.5 Preparation of Ir₂^{II,II}(tfepma)₂(CNAd)₂Cl₃(OOH) (6)

A solution of 5 (100 mg, 0.0559 mmol, 1.00 eq) was dissolved in 0.7 mL of THF and transferred to a J. Young NMR tube. The solution was freeze-pump-thaw degassed three times, then backfilled with O₂. The tube was shaken vigorously to mix, and then allowed to stand for 5 min. This process was repeated three times, at which time a crude ³¹P{¹H} NMR spectrum showed complete conversion. The solution was transferred to a scintillation vial, and concentrated in vacuo to produce a yellow solid. The solid was redissolved in 2 mL Et₂O/2 mL of hexane, concentrated to dryness in vacuo, washed with 1 mL of hexane and dried in vacuo. Yield: 85 mg (83%). ¹H NMR (500 MHz, THF-d₈) δ/ppm: 7.57 (s, 1H), 5.43 (m, 2H), 5.21 (m, 4H), 4.99(m, 4H), 4.85 (m, 2H), 4.77 (m, 2H), 4.68 (m, 2H), 2.96 (pseudoquintet, 6H), 2.03–2.11 (br, m, 12H), 1.59–1.75 (br, m, 18H). ³¹P{¹H} NMR (121.5 MHz, CD₃CN) δ/ppm: 77.1–79.0 (m, 2P), 73.8–75.9 (m, 2P).

5.5.6 Preparation of Ir₂^{0,II}(tfepma)₂(CNXy)₂Cl₂ (7)

To a suspension of [Ir^I(COD)Cl]₂ (79 mg, 0.12 mmol, 1.0 eq) in 1 mL of Et₂O was added a solution of tfepma (115 mg, 0.236 mmol, 2.0 eq) in 1 mL of Et₂O, producing a dark red solution. Addition of CNXy (31 mg, 0.24 mmol, 2.0 eq) in 1 mL of Et₂O left a dark brown solution, which was stirred for 24 h at room temperature. During this time, the color lightened

considerably. The mixture was concentrated in vacuo and triturated with pentane to give a pale orange solid. The solid was washed with 2 mL of cold hexane, decanted and dried in vacuo. Yield: 149 mg (74.5%) (Product is contaminated with ca. 10% Ir^I(κ²-tfepma)(CNXy)Cl). ¹H NMR (500 MHz, CD₃CN) δ/ppm: 7.25 (t, ³J_{H-H} = 7.6 Hz, 1H), 7.20 (m, 1H), 7.12 (m, 2H), 7.08 (d, ³J_{H-H} = 7.6 Hz, 2H), 5.13–5.23 (m, 2H), 5.01–5.11 (m, 2H), 4.92 (m, 2H), 4.73 (m, 2H), 4.51–4.67 (m, 6H), 4.42 (m, 2H), 2.90 (pseudoquintet, 6H), 2.35 (s, 6H), 2.28 (s, 6H). ³¹P{¹H} NMR (121.5 MHz, CD₃CN) δ/ppm: 131.5 (m, 2P), 85.2 (m, 2P).

5.5.7 Preparation of Ir₂^{II,II}(tfepma)₂(CNXy)₂Cl₃H (8)

A sample of **7** (75 mg, 0.044 mmol, 1.0 eq) was dissolved in 1 mL of CH₃CN. A solution of 2,6-lutidinium chloride (8.0 mg, 0.055 mmol, 1.2 eq) in 2 mL of CH₃CN was added to give a yellow solution. After 2 h, the solution was concentrated in vacuo to give a mixture of white and yellow solids. The product was redissolved in 6 mL of Et₂O and filtered. The colorless solution was combined with 4 mL of hexane and concentrated in vacuo to leave a light yellow solid. The solid was washed with 2 × 2 mL of hexane and dried in vacuo. Yield: 62 mg (80%). ¹H NMR (500 MHz, THF-d₈) δ/ppm: 7.28 (m, 1H), 7.16–7.24 (m, 5H), 5.65 (m, 2H), 5.44 (m, 4H), 4.94 (m, 4H), 4.75 (m, 2H), 4.12–4.28 (m, 4H), 2.90 (pseudoquintet, 6H), 2.49 (s, 6H), 2.44 (s, 6H), –19.77 (distorted t, ²J_{P-H} ~ 15 Hz, 1H). ³¹P{¹H} NMR (121.5 MHz, CD₃CN) δ/ppm: 85.5–87.8 (br, m, 2P), 77.0–78.6 (br, m, 2P).

5.5.8 Preparation of Ir₂^{II,II}(tfepma)₂(CN^tBu)₂Cl₂H(OSO₂Me) (11)

In a scintillation vial, complex **1** (100 mg, 0.0627 mmol, 1.00 eq) was dissolved in 2 mL of THF. In a separate vial, a stock solution containing 64.3 mg of methanesulfonic acid in 3 mL of THF was prepared. A 0.295-mL aliquot of this solution, corresponding to 1.05 eq of MeSO₃H, was added dropwise to the stirred solution of **1**. An immediate color change to light yellow occurred, and the solution was stirred for a total of 2 h. At this time, it was concentrated in vacuo to leave a pale residue, which was redissolved in 1 mL Et₂O/2 mL of hexane. The solution was concentrated to less than one-half the original volume, decanted and dried in vacuo. Yield: 89 mg (84%). ¹H NMR (500 MHz, THF-d₈) δ/ppm: 5.35 (m, 2H), 4.99–5.25 (m, 6H), 4.35–4.68 (m, 8H), 2.92 (pseudoquintet, 6H), 2.65 (s, 3H), 1.56 (s, 9H), 1.52 (s, 9H), –24.94 (t, ²J_{P-H} = 16.7 Hz, 1H). ³¹P{¹H} NMR (121.5 MHz, CD₃CN) δ/ppm: 100.0–102.3 (m, 2P), 80.7–83.0 (m, 2P).

5.5.9 Preparation of $\text{Ir}_2^{\text{II,II}}(\text{tfepma})_2(\text{CN}^t\text{Bu})_2\text{Cl}_3(\text{OH})$ (**12**) by Reaction of $\text{Ir}_2^{\text{II,II}}(\text{tfepma})_2(\text{CN}^t\text{Bu})_2\text{Cl}_3(\text{OOH})$ (**3**) with PPh_3

A sample of **3** (25 mg, 0.015 mmol, 1.0 eq) was dissolved in 0.7 mL of THF. This solution was used to dissolve solid PPh_3 (8 mg, 0.03 mmol, 2 eq). The solution was transferred to a J. Young NMR tube and held at room temperature for 12 h. At this time, $^{31}\text{P}\{^1\text{H}\}$ NMR indicates the formation of **12** and $\text{O}=\text{PPh}_3$ as major products, along with unreacted PPh_3 and some minor side products. The solution was concentrated in vacuo to yield a yellow residue, which was redissolved in ~ 2 mL of 1:1 Et_2O /hexane. This solution was concentrated in vacuo to leave a yellow solid. The solid was washed with hexane and dried in vacuo. It was not possible to satisfactorily separate **12** from the $\text{O}=\text{PPh}_3$ and unreacted PPh_3 , precluding suitable elemental analysis by this method. Crystals of **12** suitable for X-ray diffraction were grown from CH_2Cl_2 /hexane at -20 °C and manually separated from the $\text{O}=\text{PPh}_3/\text{PPh}_3$ also present. Spectroscopic data for **12**: ^1H NMR (500 MHz, THF-d_8) δ /ppm: 6.96 (br, s, 1H), 5.48 (m, 2H), 5.26 (m, 2H), 4.98 (m, 4H), 4.84 (m, 2H), 4.76 (m, 2H), 4.66 (m, 2H), 4.47 (m, 2H), 2.93 (pseudoquintet, 6H), 1.49 (s, 9H), 1.29 (s, 9H). $^{31}\text{P}\{^1\text{H}\}$ NMR (121.5 MHz, THF-d_8) δ /ppm: 86.0–88.2 (m, 2P), 76.9–79.1 (m, 2P) (AA'BB', 21 lines resolved, $\delta_{\text{avg}} = 82.6$ ppm). IR (Nujol): $\tilde{\nu}_{\text{O-H}} = 3336 \text{ cm}^{-1}$, $\tilde{\nu}_{\text{C=N}} = 2187 \text{ cm}^{-1}$.

5.5.10 Preparation and Isolation of $\text{Ir}_2^{\text{II,II}}(\text{tfepma})_2(\text{CN}^t\text{Bu})_2\text{Cl}_3(\text{OH})$ (**12**)

In the glovebox, **3** (37 mg, 0.022 mmol, 1.0 eq) was dissolved in 1 mL of THF in a scintillation vial. In a separate vial, a stock solution of PEt_3 (20 μL , 0.14 mmol) in 0.20 mL of THF was prepared. An aliquot of this stock solution (66 μL), corresponding to 2.0 eq of PEt_3 , was added to the stirring solution of **3**. The yellow solution was stirred for 2 h at room temperature, at which time the crude $^{31}\text{P}\{^1\text{H}\}$ NMR spectrum shows a mixture of **12**, $\text{O}=\text{PEt}_3$, PEt_3 , and several side products. The solution was concentrated in vacuo to leave a yellow residue. The residue was taken up in 4 mL of 1:1 Et_2O /hexane, and concentrated in vacuo to leave a yellow solid. The solid was recrystallized from 3 mL of 1:2 CH_2Cl_2 /hexane at -35 °C. The supernatant was decanted, and the yellow microcrystals were washed with 2 mL of hexane and dried in vacuo. Yield: 22 mg (59%). ^1H NMR (500 MHz, CD_2Cl_2) δ /ppm: 6.88 (br, s, 1H), 5.26 (m, 2H), 5.08 (m, 2H), 4.76–4.91 (m, 4H), 4.68 (m, 4H), 4.52 (m, 2H), 4.35 (m, 2H), 2.86 (pseudoquintet, 6H), 1.46 (s, 9H), 1.23 (s, 9H). $^{31}\text{P}\{^1\text{H}\}$ NMR (121.5 MHz, CD_2Cl_2) δ /ppm:

85.7–87.9 (m, 2P), 77.0–79.2 (m, 2P) (AA'BB', 20 lines resolved, $\delta_{\text{avg}} = 82.5$ ppm). Anal. Calcd. for $\text{C}_{28}\text{H}_{41}\text{Cl}_4\text{F}_{24}\text{Ir}_2\text{N}_4\text{O}_9\text{P}_4$: C, 20.40; H, 2.51; N, 3.40. Found: C, 20.74; H, 2.55; N, 3.22.

5.5.11 Reaction of $\text{Ir}_2^{\text{II,II}}(\text{tfepma})_2(\text{CN}^t\text{Bu})_2\text{Cl}_3(\text{OOH})$ (**3**) with HCl

Complex **3** (15 mg, 0.0090 mmol, 1.0 eq) was dissolved in 0.68 mL of THF- d_8 . A solution of HCl (0.48 M, 20 μL , 0.0097 mmol, 1.1 eq) in THF- d_8 (prepared by diluting a 4.2 M HCl/dioxane solution) was introduced via autopipet. The solution lightened in color slightly, and was immediately transferred to a J. Young NMR tube. Initial NMR spectra indicate complete consumption of **3**, with $[\text{Ir}_2^{\text{II,II}}(\text{tfepma})_2(\text{CN}^t\text{Bu})_2\text{Cl}_3(\text{OH}_2)]\text{Cl}$ (**13**) as the major species. After 48 h, the NMR spectra show complete conversion to the pseudo- C_{2h} isomer of $\text{Ir}_2^{\text{II,II}}(\text{tfepma})_2(\text{CN}^t\text{Bu})_2\text{Cl}_4$ (**14**), with several side products evident in the ^1H NMR spectrum. Crystals of **14** suitable for X-ray diffraction were obtained from this mixture by removing the solvent in vacuo, redissolving in 2 mL of ca. 1:3 CH_2Cl_2 /hexane and chilling to -35 $^\circ\text{C}$ overnight. Spectroscopic data for **13**: ^1H NMR (500 MHz, THF- d_8) δ/ppm : 7.83 (br, s, 2H), 4.45–5.45 (m, 16H), 3.14 (pseudoquintet, 6H), 1.60 (s, 9H), 1.47 (s, 9H). $^{31}\text{P}\{^1\text{H}\}$ NMR (121.5 MHz, THF- d_8) δ/ppm : 79.9–81.7 (br, m, 2P), 69.8–71.6 (br, m, 2P) (AA'BB', 8 lines resolved, $\delta_{\text{avg}} = 75.8$ ppm). IR (solid): $\tilde{\nu}_{\text{C}=\text{N}} = 2193$ cm^{-1} . Spectroscopic data for **14**: ^1H NMR (500 MHz, THF- d_8) δ/ppm : 5.18 (m, 4H), 5.04 (m, 8H), 4.62 (m, 4H), 3.03 (pseudoquintet, 6H), 1.50 (s, 18H). $^{31}\text{P}\{^1\text{H}\}$ NMR (121.5 MHz, THF- d_8) δ/ppm : 76.8 (s, 4P). IR (Nujol): $\tilde{\nu}_{\text{C}=\text{N}} = 2188$ cm^{-1} .

5.5.12 Preparation and Isolation of $\text{Ir}_2^{\text{II,II}}(\text{tfepma})_2(\text{CN}^t\text{Bu})_2\text{Cl}_4$ (**14**) (pseudo- C_{2h} isomer)

A sample of **3** (45 mg, 0.027 mmol, 1.0 eq) was dissolved in 2 mL of THF and sealed in a septum-capped vial. An aliquot of HCl in dioxane (4.2 M, 13 μL , 0.054 mmol, 2.0 eq) was introduced via syringe. The solution lightened in color, and after ~ 15 min an aliquot of the headspace gas was withdrawn for GC analysis, which showed no gaseous reaction products. The solution was concentrated in vacuo to leave a yellow residue, which was redissolved in Et_2O /hexane. Removal of the solvents in vacuo left a pale yellow solid, which was redissolved in THF- d_8 . At this stage, ^1H NMR showed a majority of aqua product **13**, as described above. After 48 h, the crude ^1H NMR spectrum indicated complete consumption of **13**, with the desired product **14** as the major species (ca. 60% crude yield). The solution was concentrated in vacuo,

and the resulting residue suspended in Et₂O/hexane. Removal of the solvents in vacuo left a yellow solid, which was redissolved in 1.5 mL of CH₂Cl₂/3 mL of hexane. The yellow solution was chilled at -35 °C for 24 h, producing pure product **14** as yellow microcrystals. Yield: 12 mg (27%). Spectral data are identical to those given above. Anal. Calcd. for C₂₈H₄₀Cl₄F₂₄Ir₂N₄O₈P₄: C, 20.18; H, 2.42; N, 3.36. Found: C, 20.41; H, 2.44; N, 3.22.

5.5.13 Reaction of Ir₂^{II,III}(tfepma)₂(CN^tBu)₂Cl₃(OOH) (**3**) with 2,6-Lutidinium Chloride

A solution of **3** (10 mg, 0.0060 mmol, 1.0 eq) in 0.7 mL of THF was prepared in a J. Young NMR tube. In a scintillation vial, a stock solution of 2,6-lutidinium chloride (10.5 mg in 0.50 mL of CD₃CN) was prepared. A 41-μL aliquot of this stock solution, corresponding to 1 eq. of 2,6-lutidinium chloride, was added to the NMR tube. Initially some of the 2,6-lutidinium hydrochloride precipitated, but with occasional shaking all solids dissolved after ~ 2 h. After 40 h, the ¹H NMR spectrum indicated the formation of **12** as the major product, with some unreacted **3** also present (ca. 15% relative to **12**). In addition to several metal-containing side products, the NMR spectrum also indicated a mixture of 2,6-lutidinium chloride and free 2,6-lutidine in the product mixture. The reaction can also be executed in the same manner with a molar excess (2 eq) of 2,6-lutidinium chloride, and in this case all of **3** is consumed within 15 h, with a similar distribution of side products.

5.5.14 X-Ray Crystallographic Details

Single crystals of **6** were grown from Et₂O/hexane at -20 °C, crystals of **12** were obtained from CH₂Cl₂/hexane at -20 °C, and crystals of **14** were grown from the same solvent system at -35 °C. The crystals were mounted on a Bruker three-circle goniometer platform equipped with an APEX detector. A graphite monochromator was employed for wavelength selection of the Mo K α radiation ($\lambda = 0.71073$ Å). The data were processed and refined using the program SAINT supplied by Siemens Industrial Automation. Structures were solved by Patterson methods in SHELXS and refined by standard difference Fourier techniques in the SHELXTL program suite (6.10 v., Sheldrick G. M., and Siemens Industrial Automation, 2000). Hydrogen atoms bonded to carbon were placed in calculated positions using the standard riding model and refined isotropically; all other atoms were refined anisotropically. A disordered Et₂O solvent molecule was present in the structure of **6**, and was modeled as a two-part disorder about

a special position. Also in this structure, the oxygen-bound hydrogen atom was tentatively located with two distinct maxima in the difference map, and as such was modeled as a two-part disorder with the O–H distance restrained to be 0.84 Å. The oxygen-bound hydrogen atom in **12** was tentatively located in the difference map, but owing to the substantial disorder in the crystal was constrained using a standard riding model for O–H protons. The crystal of **12** was found to be a nonmerohedral twin; two domains of the unit cell were located, the absorption correction was applied using the program TWINABS, and for the final refinement cycles the model was refined against both twin domains. In addition, the structure of **12** was substantially disordered. By virtue of a crystallographically imposed inversion center at the molecule's centroid, two orientations of the six monodentate ligands were present. In addition, three of the four crystallographically independent –CF₃ groups were disordered about two positions, and the dichloromethane solvent molecule was disordered about a special position. In the structure of **14**, one of the –CF₃ groups was modeled as a two-part disorder. The (1,2) and (1,3) distances of all disordered parts were restrained to be similar using the SADI command; the rigid-bond restraints SIMU and DELU were also used on disordered parts. Crystallographic details for **6**, **12**, and **14** are summarized in Table 5.1.

Table 5.1. Crystallographic summary for **6**, **12**, and **14**.

| | 6 ·0.5Et ₂ O | 12 ·CH ₂ Cl ₂ | 14 |
|---|---|--|---|
| Formula | C ₄₂ H ₅₈ Cl ₃ F ₂₄ Ir ₂ N ₄ O _{10.5} P ₄ | C ₂₉ H ₄₃ Cl ₅ F ₂₄ Ir ₂ N ₄ O ₉ P ₄ | C ₂₈ H ₄₀ Cl ₄ F ₂₄ Ir ₂ N ₄ O ₁₀ P ₄ |
| fw, g/mol | 1857.55 | 1 1733.20 | 1666.72 |
| Temperature/K | 100(2) | 175(2) | 100(2) |
| cryst. syst. | Triclinic | Triclinic | Monoclinic |
| space group | <i>P</i> <i>T</i> | <i>P</i> <i>T</i> | <i>P</i> 2 ₁ / <i>c</i> |
| color | Yellow | Yellow | Yellow |
| <i>a</i> /Å | 12.6295(19) | 10.4031(11) | 12.7559(9) |
| <i>b</i> /Å | 15.778(2) | 12.5695(13) | 19.5938(14) |
| <i>c</i> /Å | 17.895(3) | 12.6361(13) | 21.0181(15) |
| <i>α</i> /° | 84.570(2) | 65.033(2) | 90 |
| <i>β</i> /° | 80.215(2) | 70.612(2) | 97.9880(10) |
| <i>γ</i> /° | 70.494(2) | 84.392(2) | 90 |
| <i>V</i> /Å ³ | 3309.6(9) | 1411.2(3) | 5202.2(6) |
| <i>ρ</i> (calc.)/(g cm ⁻³) | 1.864 | 2.039 | 2.128 |
| <i>Z</i> | 2 | 1 | 4 |
| no. refl. | 76039 | 64399 | 117116 |
| no. unique refl. | 19179 | 8499 | 15213 |
| <i>R</i> _{int} | 0.0474 | 0.0557 | 0.0527 |
| <i>R</i> ₁ ^{<i>a</i>} (all data) | 0.0456 | 0.0638 | 0.0483 |
| <i>wR</i> ₂ ^{<i>b</i>} (all data) | 0.0769 | 0.1362 | 0.0811 |
| <i>R</i> ₁ [(<i>I</i> > 2σ)] | 0.0309 | 0.0521 | 0.0318 |
| <i>wR</i> ₂ [(<i>I</i> > 2σ)] | 0.0709 | 0.1294 | 0.0718 |
| <i>GOF</i> ^{<i>c</i>} | 1.043 | 1.098 | 1.040 |

^{*a*} $R_1 = \sum ||F_o - |F_c|| / \sum |F_o|$. ^{*b*} $wR_2 = (\sum (w(F_o^2 - F_c^2)^2) / \sum (w(F_o^2)^2))^{1/2}$. ^{*c*} $GOF = (\sum w(F_o^2 - F_c^2)^2 / (n - p))^{1/2}$ where *n* is the number of data and *p* is the number of parameters refined.

5.6 References

- (1) Costas, M.; Mehn, M. P.; Jensen, M. P.; Que, L. *Chem. Rev.* **2004**, *104*, 939–986.
- (2) Mirica, L. M.; Ottenwaelder, X.; Stack, T. D. P. *Chem. Rev.* **2004**, *104*, 1013–1046.
- (3) Lewis, E. A.; Tolman, W. B. *Chem. Rev.* **2004**, *104*, 1047–1076.
- (4) Rosenthal, J.; Nocera, D. G. *Acc. Chem. Res.* **2007**, *40*, 543–553.
- (5) Stahl, S. S. *Angew. Chem. Int. Ed.* **2004**, *43*, 3400–3420.
- (6) Roberts, H. L.; Symes, W. R. *J. Chem. Soc. A* **1968**, 1450–1453.
- (7) Johnston, L. E.; Page, J. A. *Can. J. Chem.* **1969**, *47*, 4241–4246.
- (8) Gillard, R. D.; Heaton, B. T.; Vaughan, D. H. *J. Chem. Soc. A* **1970**, 3126–3130.
- (9) Endicott, J. F.; Wong, C.-L.; Inoue, T.; Natarajan, P. *Inorg. Chem.* **1979**, *18*, 450–454.
- (10) Atlay, M. T.; Preece, M.; Strukul, G.; James, B. R. *J. Chem. Soc., Chem. Commun.* **1982**, 406–407.
- (11) Atlay, M. T.; Preece, M.; Strukul, G.; James, B. R. *Can. J. Chem.* **1983**, *61*, 1332–1338.
- (12) Bakac, A. *J. Am. Chem. Soc.* **1997**, *119*, 10726–10731.
- (13) Thyagarajan, S.; Incarvito, C. D.; Rheingold, A. L.; Theopold, K. H. *Chem. Commun.* **2001**, 2198–2199.
- (14) Cui, W.; Wayland, B. B. *J. Am. Chem. Soc.* **2006**, *128*, 10350–10351.
- (15) Wick, D. D.; Goldberg, K. I. *J. Am. Chem. Soc.* **1999**, *121*, 11900–11901.
- (16) Konnick, M. M.; Gandhi, B. A.; Guzei, I. A.; Stahl, S. S. *Angew. Chem. Int. Ed.* **2006**, *45*, 2904–2907.
- (17) Denney, M. C.; Smythe, N. A.; Cetto, K. L.; Kemp, R. A.; Goldberg, K. I. *J. Am. Chem. Soc.* **2006**, *128*, 2508–2509.
- (18) Szajna-Fuller, E.; Bakac, A. *Inorg. Chem.* **2010**, *49*, 781–785.
- (19) Keith, J. M.; Nielsen, R. J.; Oxgaard, J.; Goddard, W. A. *J. Am. Chem. Soc.* **2005**, *127*, 13172–13179.
- (20) Keith, J. M.; Muller, R. P.; Kemp, R. A.; Goldberg, K. I.; Goddard, W. A.; Oxgaard, J. *Inorg. Chem.* **2006**, *45*, 9631–9633.
- (21) Konnick, M. M.; Stahl, S. S. *J. Am. Chem. Soc.* **2008**, *130*, 5753–5762.
- (22) Konnick, M. M.; Decharin, N.; Popp, B. V.; Stahl, S. S. *Chem. Sci.* **2011**, *2*, 326–330.
- (23) Decharin, N.; Stahl, S. S. *J. Am. Chem. Soc.* **2011**, *133*, 5732–5735.
- (24) Decharin, N.; Popp, B. V.; Stahl, S. S. *J. Am. Chem. Soc.* **2011**, *133*, 13268–13271.

- (25) Konnick, M. M.; Guzei, I. A.; Stahl, S. S. *J. Am. Chem. Soc.* **2004**, *126*, 10212–10213.
- (26) Strukul, G.; Ros, R.; Michelin, R. A. *Inorg. Chem.* **1982**, *21*, 495–500.
- (27) Karlin, K. D.; Ghosh, P.; Cruse, R. W.; Farooq, A.; Gultneh, Y.; Jacobson, R. R.; Blackburn, N. J.; Strange, R. W.; Zubieta, J. *J. Am. Chem. Soc.* **1988**, *110*, 6769–6780.
- (28) Miyaji, T.; Kujime, M.; Hikichi, S.; Moro-oka, Y.; Akita, M. *Inorg. Chem.* **2002**, *41*, 5286–5295.
- (29) Wang, W.-D.; Bakac, A.; Espenson, J. H. *Inorg. Chem.* **1995**, *34*, 4049–4056.
- (30) Mirza, S. A.; Bocquet, B.; Robyr, C.; Thomi, S.; Williams, A. F. *Inorg. Chem.* **1996**, *35*, 1332–1337.
- (31) Pestovsky, O.; Bakac, A. *J. Am. Chem. Soc.* **2003**, *125*, 14714–14715.
- (32) Man; Zhu, J.; Man, S. M.; Zhou, Z.; Yin, C.; Lin, Z.; Lau, C. P. *Organometallics* **2004**, *23*, 6214–6220.
- (33) Teets, T. S.; Cook, T. R.; McCarthy, B. D.; Nocera, D. G. *Inorg. Chem.* **2011**, *50*, 5223–5233.
- (34) Teets, T. S.; Nocera, D. G. *J. Am. Chem. Soc.* **2011**, *133*, 17796–17806.
- (35) Teets, T. S.; Cook, T. R.; McCarthy, B. D.; Nocera, D. G. *J. Am. Chem. Soc.* **2011**, *133*, 8114–8117.
- (36) Mimoun, H.; Charpentier, R.; Mitschler, A.; Fischer, J.; Weiss, R. *J. Am. Chem. Soc.* **1980**, *102*, 1047–1054.
- (37) Teets, T. S.; Cook, T. R.; Nocera, D. G. *Inorg. Synth.* **2010**, *35*, 164–168.
- (38) Sasaki, T.; Nakanishi, A.; Ohno, M. *J. Org. Chem.* **1981**, *46*, 5445–5447.

**Chapter 6 –
Oxygen-Reduction Reactions of Monometallic
Rhodium Hydride Complexes**

Portions of this work have been previously published:

Reproduced in part with permission from Teets, T. S.; Nocera, D. G. *Inorg. Chem.*, submitted for publication. Unpublished work copyright 2012 American Chemical Society.

6.1 Introduction

In Chapter 4, oxygen-reduction chemistry of dirhodium and diiridium hydride complexes was considered, which was further expounded in Chapter 5 with a discussion of the reactivity of a novel diiridium hydroperoxo complex. In considering the reaction chemistry that was described in these preceding chapters, all mechanistic sequences could be rationalized by considering only one of the two centers of the bimetallic complexes, with no explicit bimetallic cooperativity proposed. It is true that the metal–metal-bonding motif stabilized the formally M^0 and M^{II} oxidation states that were involved in the oxygen-reduction chemistry, but it was unclear if the role of the second metal extended beyond this electronic stabilization. As such, an immediate goal upon unveiling the oxygen-reduction chemistry of the dirhodium and diiridium complexes was to explore analogous chemistry on mononuclear metal complexes. In addition, monometallic systems offer enhanced prospects for tunability. As was briefly mentioned in the last chapter, the bimetallic complexes suffer from poor synthetic generality, and attempts to make substantial ligand substitutions were met with failure. With monometallic complexes, ligand architectures can be systematically tuned, enabling detailed studies of electronic-structure effects on the observed oxygen-reduction mechanisms.

The immense field of oxygen-activation chemistry was introduced in Chapters 4 and 5, and will be briefly reconsidered here to contextualize the content of this chapter. The fundamental reactivity of O_2 at transition-metal centers is at the nexus of bioenergy^{1,2} and chemical energy^{3,4} conversion. In nature, oxidase⁵ and oxygenase^{6,7} enzymes utilize O_2 as the oxidant in crucial respiratory and biosynthetic catalyses by managing both the proton and electron inventory. With an eye towards designing biomimetic catalysts and gaining a more thorough understanding of energy-conversion mechanisms, numerous model complexes designed to retain key features of the enzyme active sites have appeared.^{8–10} By appending either Brønsted acids^{11,12} or auxiliary metal centers^{9,13–17} in the secondary coordination sphere of a metallomacrocycle, biofunctional O_2 -reduction catalysts have been realized. In addition, because of oxygen's abundance and environmental compatibility, in the realm of synthetic chemistry there is considerable appeal in developing catalytic systems that utilize O_2 as the sole oxidizing species.^{18,19} Complexes of iron,²⁰ copper,²¹ rhodium,²² and select other metals^{23–25} can catalyze aerobic oxidation reactions, though palladium catalysis is the most widespread.^{18,26–28}

The insertion of O₂ into metal–hydride bonds often plays a key role in its activation especially if the reactions occur in acidic media and/or are attendant to C–H activation. As such, in-depth studies of the reactions of O₂ with metal hydride complexes are germane to numerous topics in catalysis. There are many examples of O₂ insertion into metal hydrides to furnish hydroperoxo complexes,^{29–41} and in recent years mechanistic studies of the aerobic oxidation of group 10 hydrides and especially those involving palladium have proliferated in the context of the aerobic oxidation catalysis.^{42–48} In previous years, mechanistic studies of O₂ reactivity with group 9 metal hydrides were less numerous.^{32,35,41} But as was described in Chapter 4 of this thesis, dirhodium hydride complexes, accessed by reversible HCl addition to two-electron mixed-valent centers, promote the reduction of oxygen to water.⁴⁹ Mechanistic studies of this transformation were undertaken, leading to the discovery that the analogous diiridium hydride complex inserts O₂ to form an isolable hydroperoxo complex.⁵⁰ This finding, coupled with kinetic⁵⁰ and as yet unpublished computational analyses of both the dirhodium and diiridium systems, fostered the conclusion that a hydroperoxo complex is a key intermediate in the 4e⁻/4H⁺ oxygen-reduction reaction (ORR) of O₂ to water. Though some examples involve radical chain mechanisms,^{32,51} most of these recent mechanistic studies reveal two common pathways for the insertion of O₂ into a metal hydride bond: (i) the “HX reductive-elimination” (HXRE) mechanism,^{41,45,48} where reductive elimination precedes reaction of the reduced metal center with O₂, and (ii) “H-atom abstraction” (HAA),⁴² where O₂ reacts directly with the metal hydride. It has been observed experimentally that it is possible in some systems for these two mechanisms to be competitive and occur simultaneously.^{46,50}

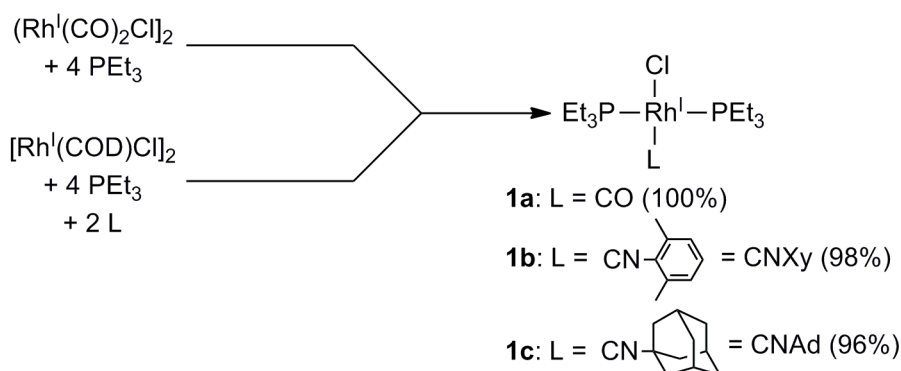
The proclivity of the HXRE and HAA mechanisms to compete in O₂ activation offers the opportunity to assess the electronic factors that are the determinants of the HXRE and HAA pathways, and thus provide further insight into the preferred mechanism(s) of the aerobic oxidation reactions. Such a line of inquiry thus demanded the construction of new transition-metal scaffolds to effect ORR activity. Another outstanding goal was to better understand the role of the second metal in the O₂-activation chemistry of bimetallic centers and to determine whether bimetallic cooperativity at two-electron mixed-valent centers⁵² offered any benefits for the ORR. Accordingly interrogation of O₂ activation and reduction at monometallic rhodium hydride complexes commenced, and the initial findings are disclosed herein. Three isostructural rhodium hydride complexes of the type *cis-trans*-Rh^{III}Cl₂H(L)(PEt₃)₂, (where L = CO,

2,6-dimethylphenylisocyanide (CNXy) or 1-adamantylisocyanide (CNAAd)) are found to promote the ORR in the presence of HCl with the attendant production of the corresponding *trans*-Rh^{III}Cl₃(L)(PEt₃)₂. Alteration of L has a dramatic effect on both the HCl-addition equilibrium constant and on the O₂-binding thermodynamics of the parent Rh^I complexes. It is shown that when L is an isocyanide, an aqua-rhodium(III) intermediate forms prior to generation of the final product. By interrogating the reactivity of the O₂ adducts *trans*-Rh^{III}Cl(CNR)(η²-O₂)(PEt₃)₂ (R = 2,6-dimethylphenyl, 1-adamantyl) it is also demonstrated that these η²-peroxo complexes and the spectroscopically unobserved hydroperoxo complexes are plausible intermediates in the ORR of the hydride complexes.

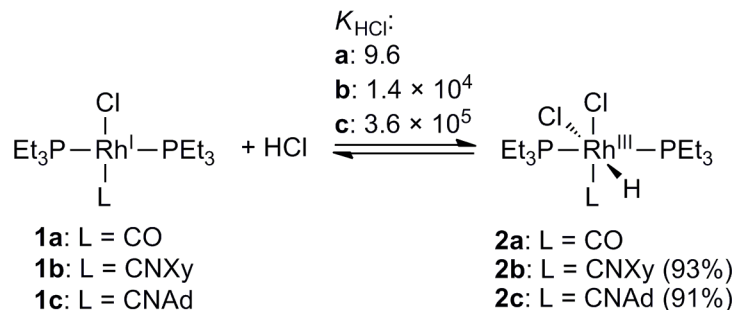
6.2 Results

6.2.1 HCl Addition to Rh^I Complexes to Furnish Rh^{III} Hydride Complexes

A series of Rh^I complexes of the type *trans*-Rh^ICl(L)(PEt₃)₂ was prepared to provide precursors to the desired hydride-containing complexes. Scheme 6.1 describes the syntheses of these complexes. The *trans*-Rh^ICl(CO)(PEt₃)₂ (**1a**) precursor complex was accessed by a stoichiometric reaction of [Rh^I(CO)₂Cl]₂ with PEt₃, as described previously.⁵³ Complexes **1b** (L = CNXy) and **1c** (L = CNAAd) were prepared in a stepwise manner, successively adding stoichiometric amounts of PEt₃ and the isocyanide to [Rh^ICl(COD)]₂. A similar strategy has been employed to prepare close variants of **1b** and **1c**.⁵⁴ Use of PEt₃ as the supporting phosphine resulted in greater solubility than that for the more common PPh₃ analogs,^{55–57} thereby facilitating studies in ethereal solvents, which is a solvent of choice for O₂-reduction reactions of the type described herein.^{49,50}



Scheme 6.1. Synthesis of Rh^I precursors **1a–c**. Isolated yields are listed in parentheses.



Scheme 6.2. HCl addition to form hydride complexes **2a–c**. Isolated yields are listed in parentheses.

Hydride complexes *cis-trans*-Rh^{III}Cl₂H(L)(PEt₃)₂ (**2a–c**) were prepared by HCl addition to Rh^I complexes **1a–c**, as depicted in Scheme 6.2. Treatment of **1a** with a large excess of HCl results in the growth of new NMR features attributable to **2a**. The ³¹P{¹H} NMR spectrum in THF-*d*₈ shows a slight downfield shift, from 25.0 ppm for **1a** to 26.4 ppm in **2a**, as well as a decrease in the ¹J_{Rh–P} from 117 Hz in **1a** to 81 Hz in **2a**, characteristic of oxidation of the rhodium center. The ¹H NMR spectrum shows, in addition to the expected resonances arising from PEt₃, growth of a new doublet-of-triplets resonance in the low-frequency region, centered at –13.16 ppm and indicative of the rhodium-bound hydride. HCl addition to **1a** to form **2a** is reversible,⁵⁸ such that removal of HCl from **2a** results in complete reversion to **1a**. Complexes **2b** and **2c** featuring isocyanide ligands have not been previously described, though an isolated example of a close relative prepared by hydride transfer from an alcoholic reaction medium is known.⁵⁹ Hydride complexes **2b** and **2c** were found to form quantitatively upon treatment of **1b** and **1c** with HCl. Furthermore, these complexes are isolable, and can be obtained in pure form as colorless solids. Characteristic NMR features, similar to those described for **2a**, are observed for **2b** and **2c** as well. Specifically, the ³¹P{¹H} NMR doublet (in C₆D₆) downshifts slightly upon HCl addition, from 23.6 ppm (**1b**) and 22.8 ppm (**1c**) to 24.7 ppm (**2b**) and 24.1 ppm (**2c**). Even more definitive is the almost 40-Hz decrease in the ¹J_{Rh–P} coupling constant, from 124 Hz (**1b**) and 127 Hz (**1c**) to 86 Hz (**2b**) and 88 Hz (**2c**). And once again, the low-frequency region of the ¹H NMR spectrum clearly indicates the presence of a rhodium-bound hydride, with ¹J_{Rh–H} values of 18.1 Hz (**2b**) and 17.9 Hz (**2c**). The additional splitting in the doublet-of-triplets splitting pattern for this hydride resonance is brought on by coupling to two equivalent phosphorus nuclei, with ²J_{P–H} values of 11.4 Hz (**1b**) and 11.6 Hz (**1c**) indicating a *cis* arrangement of the hydride relative to the phosphine ligands.

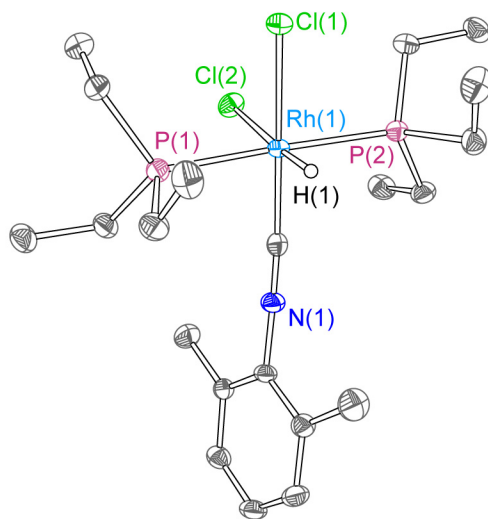
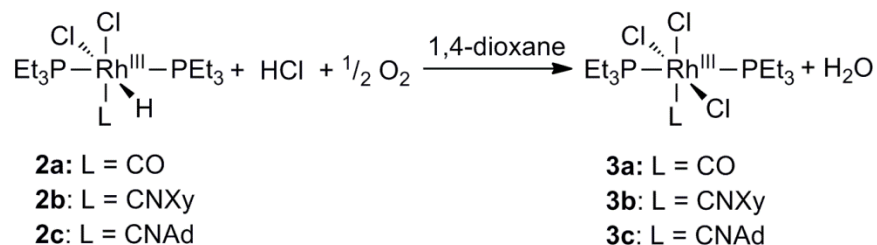


Figure 6.1. X-ray crystal structure of **2b**. Ellipsoids are shown at the 50% probability level with all carbon-bound hydrogen atoms omitted for clarity.

The stereochemistry of **2b** was confirmed by single-crystal X-ray diffraction. The structure of the complex is shown in Figure 6.1. The geometry of the Rh^{III} center is octahedral with a *trans* arrangement of the two PEt₃ ligands and a *cis* arrangement of the two Cl⁻ ligands. Of note is the disparity of the two Rh–Cl bond distances. The strong *trans* influence of the hydride ligand causes the Rh(1)–Cl(2) distance (2.4947(5) Å) to be substantially longer than the Rh(1)–Cl(1) distance (2.4041(5) Å). The stereochemistry of **2b** is consistent with the known stereochemical preference for HCl addition to square-planar M^I centers,⁶⁰ and this precedent, coupled with the similarities in the NMR features, lead us to conclude that **2a** and **2c**, which were not crystallographically characterized, are isostructural with **2b**.

The addition of HCl to **1a–c** establishes the equilibrium shown in Scheme 6.2. The equilibrium constant for the reaction ($K_{\text{HCl}} = [\mathbf{2}]/[\mathbf{1}][\text{HCl}]$) was determined directly by the addition of known concentration of HCl to a 1,4-dioxane solution of **1a**. Integration of the ³¹P{¹H} NMR spectrum furnished the equilibrium concentrations of **1a** and **2a**. The equilibrium constants for the **1b/c** to **2b/c** conversions were too large to be easily determined by the direct addition of HCl to solutions of the starting complexes. Thus a thermodynamic cycle connecting HCl and the weaker acid, 2,6-lutidinium hydrochloride, was constructed. By using 2,6-lutidinium hydrochloride as the acid source in acetonitrile, an equilibrium between the Rh^I complex and Rh^{III} hydride was established. By coupling this measured equilibrium constant with the known



Scheme 6.3. Oxygen-reduction chemistry of **2a–c**.

pK_a 's of 2,6-lutidinium (14.13)⁶¹ and HCl (8.9)⁶² in acetonitrile,⁶³ the K_{HCl} values were determined and are tabulated in Scheme 6.2.

6.2.2 Oxygen-Reduction Chemistry of **2a–c**.

Hydride complexes **2a–c** react with O_2 , in the presence of additional HCl, as summarized in Scheme 6.3. In all cases, the final outcome of the reaction between the hydride complex and O_2 and HCl is the respective *trans*- $\text{Rh}^{\text{III}}\text{Cl}_3(\text{L})(\text{PET}_3)_2$, **3a–c**, which is produced cleanly. Products **3a–c** were prepared independently by PhICl_2 oxidation of Rh^{I} complexes **1a–c**, allowing the identities of the final products formed in the reactions of Scheme 2 to be ascertained unequivocally. The infrared- and NMR-spectral features of complex **3a**, formed exclusively when **1a** is treated with equimolar PhICl_2 , are consonant with the previously reported spectral data for this known compound;^{72,73} complexes **3b** and **3c** have not been reported. Oxidation of **1b**

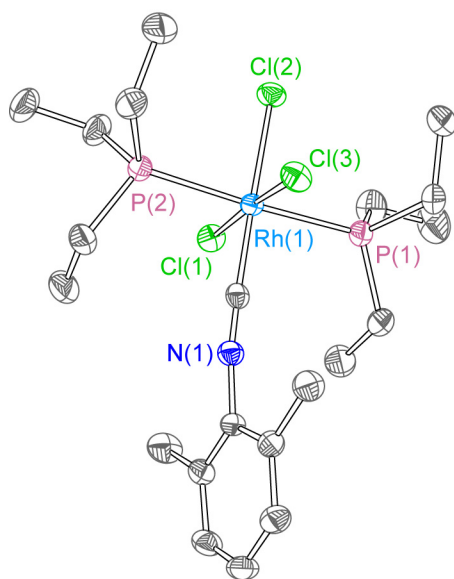


Figure 6.2. X-ray crystal structure of **3b**. Ellipsoids are shown at the 50% probability level, with hydrogen atoms are omitted for clarity.

with PhICl_2 initially forms a mixture of **3b** and a second isomer, *mer-cis*- $\text{Rh}^{\text{III}}\text{Cl}_3(\text{CNXy})(\text{PEt}_3)_2$, which converts to **3b** in ~ 48 h at room temperature. PhICl_2 oxidation of **2c** forms **3c** exclusively. **3b** and **3c** possess $^{31}\text{P}\{^1\text{H}\}$ spectral features similar to **3a**, and together with the X-ray crystal structure results of Figure 6.2, a *trans* arrangement of the PEt_3 ligands and corresponding meridional arrangement of Cl^- ligands in these products are established.

The reaction progression of hydride **2a** ($\text{L} = \text{CO}$) significantly deviates from that of **2b** and **2c**. Figure 6.3 shows the evolution of the $^{31}\text{P}\{^1\text{H}\}$ NMR spectra upon treatment of **2a** with HCl (2.1 M) and O_2 (ca. 0.2 atm) in 1,4-dioxane at room temperature. Over a long time course, the resonance attributed to **2a** (27.0 ppm, $^1J_{\text{Rh-P}} = 80$ Hz) gives rise exclusively to the resonance for **3a** (19.9 ppm, $^1J_{\text{Rh-P}} = 72$ Hz). Much like the dirhodium system,^{49,50} no intermediates are spectroscopically observed along the ORR conversion, suggesting that whatever intermediates are involved are short-lived and only present in very small quantities throughout the course of the reaction.

As shown in Figure 6.4a, the conversion of **2b** in the presence of HCl (77 mM) and O_2 (1 atm) in 1,4-dioxane to **3b** is also slow. However, in this case the growth of an intermediate species in the $^{31}\text{P}\{^1\text{H}\}$ NMR spectrum is clearly observed. Whereas a $^{31}\text{P}\{^1\text{H}\}$ NMR doublet of

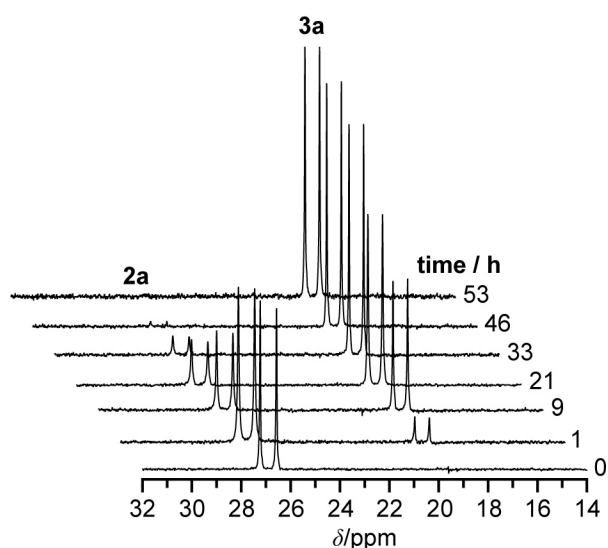


Figure 6.3. Temporal evolution of the $^{31}\text{P}\{^1\text{H}\}$ NMR spectra when **2a**, in the presence of 2.1 M HCl , is treated with ca. 0.2 atm of O_2 at room temperature. Spectra were collected at the time intervals depicted on the right of the plot. The resonances attributed to **2a** and **3a** are labeled.

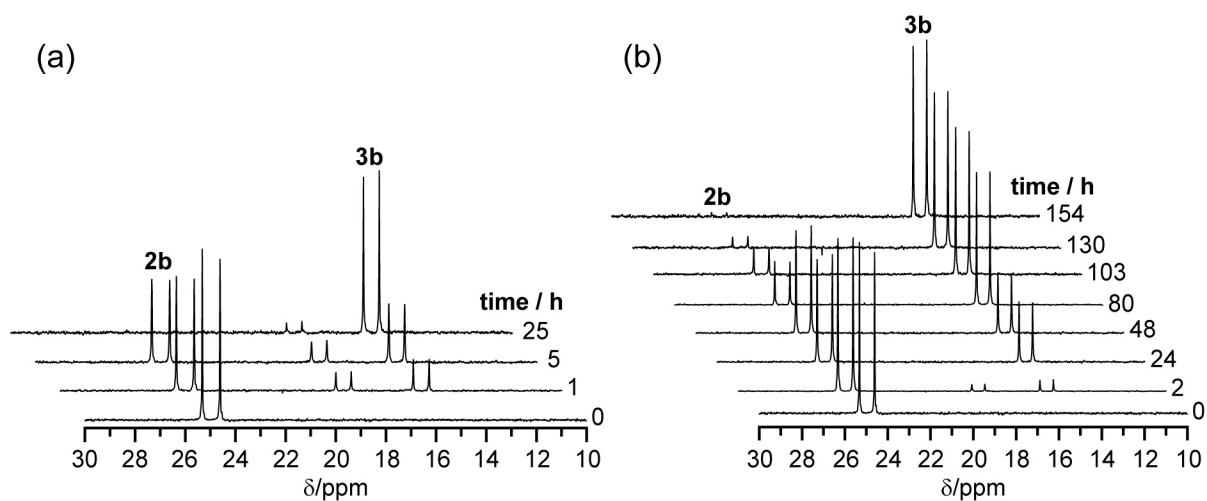


Figure 6.4. Time-resolved $^{31}\text{P}\{^1\text{H}\}$ NMR spectra when **2b**, in the presence of (a) 77 mM HCl or (b) 250 mM HCl, is treated with 1 atm of O_2 at room temperature. Spectra were collected at the time intervals depicted on the right of the plot. The resonances attributed to **2b** and **3b** are labeled.

2b (25.0 ppm, $^1J_{\text{Rh-P}} = 86$ Hz) is observed at early times, and that of **3b** (15.6 ppm, $^1J_{\text{Rh-P}} = 77$ Hz) is observed at late times, a unique species, with a chemical shift of 18.7 ppm and $^1J_{\text{Rh-P}} = 74$ Hz, is apparent at intermediate times. Under these conditions, the reaction requires in excess of 25 h to reach completion. When the concentration of HCl is augmented to 250 mM under otherwise identical conditions, the appearance of the intermediate species is noticeably suppressed, as shown in Figure 6.4b. At early time points a small amount of the intermediate is noted, but for all spectra at $t \geq 24$ h only **2b** and **3b** are present. It is also notable that, under these conditions with higher HCl, the reaction time to reach completion is substantially longer.

In a similar fashion, the conversion of **2c** (L = CNAd) to **3c** also involves an apparent intermediate species. Shown in Figure 6.5a, upon treating **2c** with additional HCl (77 mM) and O_2 (1 atm) the $^{31}\text{P}\{^1\text{H}\}$ NMR doublet of **2c** (24.2 ppm, $^1J_{\text{Rh-P}} = 87$ Hz) gives way to that of **3c** (14.5 ppm, $^1J_{\text{Rh-P}} = 78$ Hz), and a unique species, with a chemical shift of 17.4 ppm and $^1J_{\text{Rh-P}} = 75$ Hz, is apparent at intermediate times. Compared to **2b**, with **2c** increasing the concentration of HCl has less of an effect on the reaction progression, which is apparent from the data presented in Figure 6.5b. Qualitatively speaking, the intermediate builds in concentration to a comparable level with the higher acid concentration, although once again the timescale of the reaction is significantly longer. The precise kinetic origins of these qualitative observations will be of considerable interest in future studies of these and related complexes.

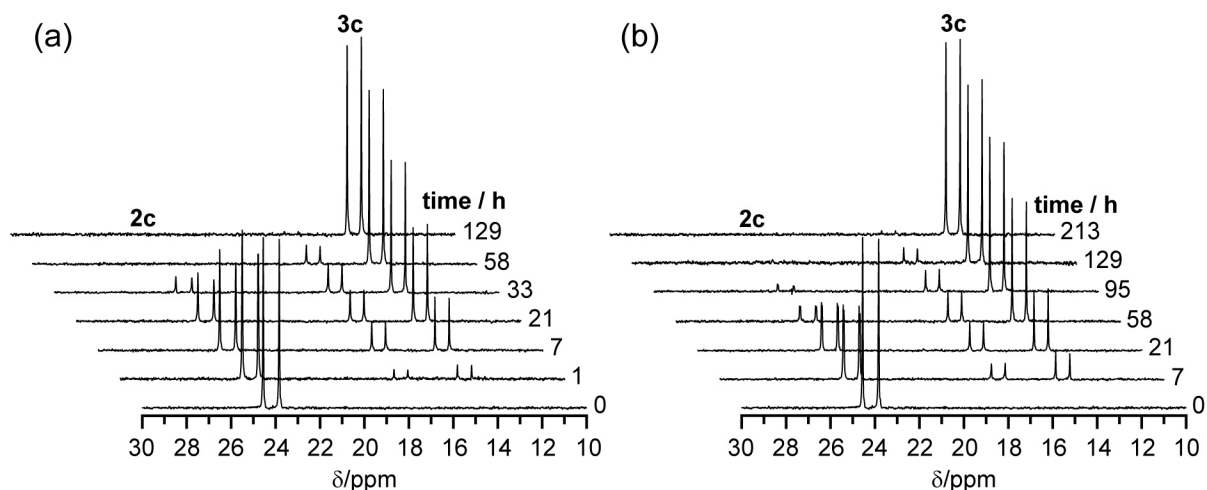
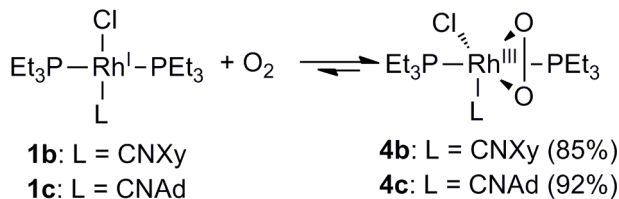


Figure 6.5. Time-resolved $^{31}\text{P}\{^1\text{H}\}$ NMR spectra when **2c**, in the presence of (a) 77 mM HCl or (b) 250 mM HCl, is treated with 1 atm of O_2 at room temperature. Spectra were collected at the time intervals depicted on the right of the plot. The resonances attributed to **2c** and **3c** are labeled.

Although this aforementioned intermediate forms in relatively small quantities during the O_2 -reduction reaction, making it difficult to positively identify under these conditions, it could be immediately ruled out that it is simply an isomer of $\text{Rh}^{\text{III}}\text{Cl}_3$ **3b/c**. The two other possible isomers of **3b** are formed at early time points when **1b** is oxidized with PhICl_2 . As expected, the $^{31}\text{P}\{^1\text{H}\}$ NMR spectrum of the *mer-cis* isomer contains two distinct doublet-of-doublet resonances, whereas the *fac* isomer gives rise to a doublet which is further downfield (31.1 ppm) and has a larger $^1J_{\text{Rh-P}}$ (102 Hz) than that of **3b/c**. As detailed below, an alternate reaction strategy furnishes this intermediate in much higher yields, ultimately allowing it to be identified as a Rh^{III} aqua complex.

6.2.3 Generation and Reactivity of Rh^{III} -peroxo Complexes

Addition of 1 atm of O_2 to a solution of **1a** produces only a small amount of a new product, **4a**, with mostly **1a** remaining. Product **4a**, which forms in < 5% yield under these conditions, shows a slightly downfield-shifted $^{31}\text{P}\{^1\text{H}\}$ resonance (30.0 ppm) with a smaller $^1J_{\text{Rh-P}}$ coupling constant (82 Hz) relative to that of **1a**. Over a period of 1 week, the compound decomposes and $\text{O}=\text{PEt}_3$ and an intractable mixture of metal-containing products are observed. The poor yield and stability of **4a** precluded its characterization and identification of its reactivity. In contrast, treatment of **1b/c** with O_2 at 1 atm leads to clean, quantitative formation of *trans*- $\text{Rh}^{\text{III}}\text{Cl}(\text{L})(\eta^2\text{-O}_2)(\text{PEt}_3)_2$ (**4b**: $\text{L} = \text{CNXy}$; **4c**: $\text{L} = \text{CNAd}$), illustrated in Scheme 6.4.



Scheme 6.4. Synthesis of Rh^{III}-peroxo complexes **4b/c**. Isolated yields are listed in parentheses.

Though these complexes suffer from limited solution stability, again decomposing to O=PEt₃ and a mixture of rhodium-containing products, the peroxo complexes can be isolated in pure form in the solid state and do persist long enough in solution to characterize their spectral properties and reactivity. In C₆D₆ solution, **4b/c** display characteristic ³¹P{¹H} NMR spectra, with doublets at 26.3 and 25.3 ppm for **4b** and **4c**, respectively. The ¹J_{Rh-P} values of 87 (**4b**) and 89 (**4c**) Hz are suggestive of Rh^{III} centers featuring a *trans* arrangement of the two PEt₃ ligands. Isolated solids of **4b/4c** give rise to nearly identical O–O bond stretching frequencies in their infrared spectra ($\bar{\nu}_{\text{O-O}} = 876 \text{ cm}^{-1}$ for **4b** and 877 cm^{-1} for **4c**); these values are suggestive of an O–O single bond.⁶⁴

The X-ray crystal structure of **4b**, shown in Figure 6.6, confirms that O₂ binds in a η²-peroxo motif. The geometry about the Rh^{III} center approximates trigonal-bipyramidal if the midpoint of the O–O vector is taken to occupy a coordination site. As established from the

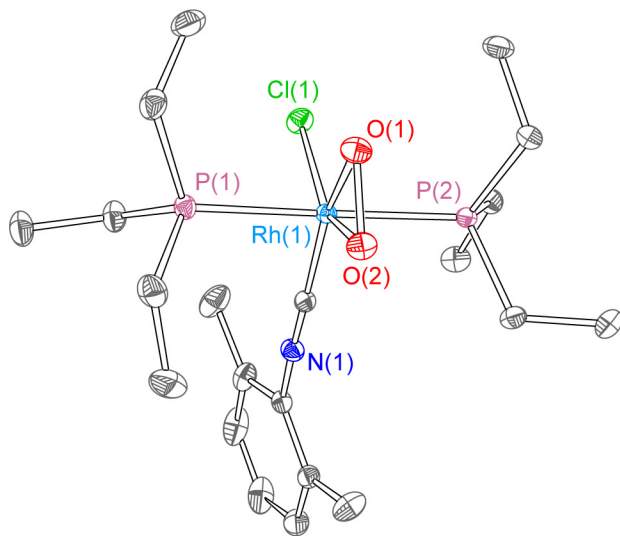
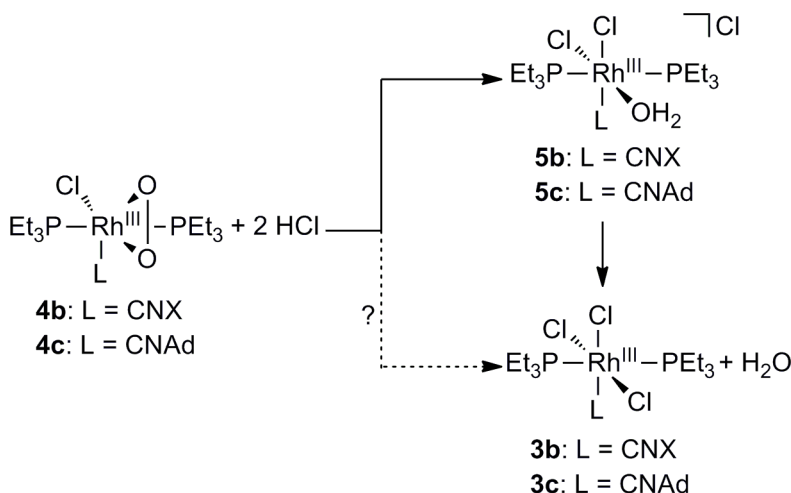


Figure 6.6. X-ray crystal structure of **4b**. Ellipsoids are shown at the 50% probability level with hydrogen atoms omitted for clarity.



Scheme 6.5. HCl reactivity of Rh^{III}-peroxo complexes **4b/c**.

³¹P{¹H} NMR spectrum the two PEt₃ ligands remain *trans* to one another, occupying the apical positions of the trigonal bipyramid. The O(1)–O(2) internuclear distance of 1.4413(12) Å is consistent with the formulation of an O₂²⁻ ligand with an O–O single bond.^{40,50,65,66} Although **4c** was not structurally characterized, its nearly identical spectral features to those of **4b** point to an analogous structure for **4c**.

With synthetic routes to **4b** and **4c** in hand, the reactivity of the compounds with HCl was interrogated, under conditions similar to those of the O₂-reduction experiments described above. This reactivity is summarized in Scheme 6.5. Whereas treatment of **4b** and **4c** with a single equivalent of HCl produces an intractable mixture of Rh^{III} products, use of three equivalents of HCl cleanly generates a mixture of two products. After 20 min, the major product (ca. 80%) is the same intermediate observed above in the reactions of O₂ with hydrides **2b/c**, with the balance accounted for by **3b/c**. The intermediate gradually converts to Rh^{III}Cl₃ products **3b/c** over time, in line with the observations in the previous section for the O₂-reduction experiments, where **3b/c** are formed as the exclusive products when the aqua intermediate disappears. Gas chromatographic analysis of the headspace gas, immediately following HCl addition, shows no evidence for gaseous products formed during this reaction, indicating that O₂ is not a reaction product. As such, the fate of the second oxygen atom in the peroxo remains unclear, but bimolecular reactions which could result in production of one-half of an equivalent of O₂ can be ruled out.

Having established a route to prepare the intermediate species in appreciable quantities by HCl addition to **4b/c**, interrogation of the compound with a variety of experimental methods leads to its unequivocal identification as the aqua complex, *cis-trans*-[Rh^{III}(OH₂)Cl₂(L)(PEt₃)₂]Cl (**5b**: L = CNXy; **5c**: L = CNAd). The IR spectrum of an isolated solid mixture of **5b/c** and **3b/c** shows only stretches attributed to the PEt₃ and isocyanide ligands. The region between 800 and 1000 cm⁻¹ is notably barren, suggesting the absence of an O–O bond in **5b/c** and discounting the formulation of these intermediates as hydroperoxo complexes. Furthermore, in the absence of HCl the ¹H spectra of **5b/c**, in addition to the expected resonances arising from PEt₃ and the respective isocyanide, show an additional singlet that integrates to two protons at 5.92 ppm (**5b**, CD₃CN) and 6.58 ppm (**5c**, C₆D₆). The positions of these new resonances, their slightly broadened lineshapes, and their rapid exchange with HCl on the NMR timescale suggest O–H protons. It has also been verified that **5c** cleanly converts to **3c** in C₆D₆ in the absence of HCl or O₂. Over a period of ca. 24 h, the NMR features of **5c** disappear, with concomitant growth of the peaks for **3c**, as well as a broad singlet at 0.60 ppm, which is attributed to free H₂O. The broadening of this water peak and the slight shift from the 0.40 ppm chemical shift of H₂O in C₆D₆⁶⁷ indicate a weak interaction of the liberated water with **3c**.

All spectroscopic results were confirmed with the solution of the single-crystal X-ray structure of **5c**. Figure 6.7 shows two views of the structure of **5c**. In Figure 6.7a, the cation *cis-trans*-[Rh^{III}(CNAd)(OH₂)Cl₂(PEt₃)₂]⁺ is depicted, which confirms the stereochemistry about the Rh^{III} center, where a *trans* arrangement of the two PEt₃ ligands and a *cis* arrangement of the two Cl⁻ ligands persists. In Figure 6.7b, the structure is extended to show the outer-sphere Cl⁻ counterion, as well as a neighboring molecule of **5c** that is related by a crystallographic inversion center. This view clearly shows a series of hydrogen-bonding interactions between the aqua protons and the outer-sphere Cl⁻ anions that stabilize the structure and give rise to a dimeric motif in the solid state. The hydrogen-bonding donor-acceptor distance between O(1) and Cl(1s) is 2.948(3) Å, whereas the distance is 3.056(3) Å between O(1) and the symmetry-generated equivalent of Cl(1s). This reveals a slight asymmetry in the two crystallographically independent hydrogen-bonding interactions.

In summary, treatment of **4b/c** with HCl results in rapid cleavage of the O–O bond and instantaneous generation of aqua intermediate **5b/c**, which liberates H₂O and forms **3b/c**

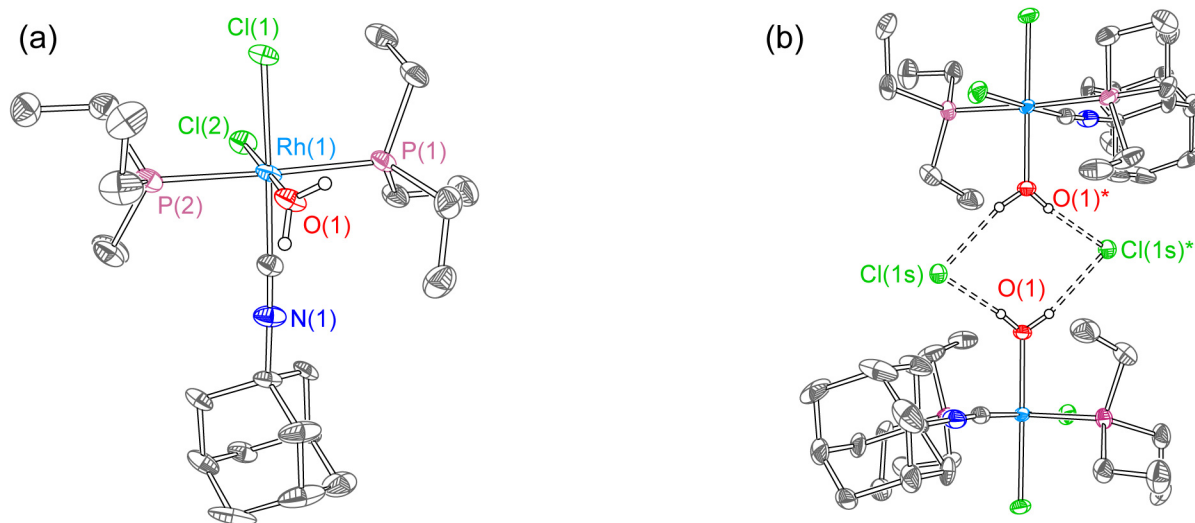


Figure 6.7. X-ray crystal structure **5c**, with ellipsoids shown at the 50% probability level. All carbon-bound hydrogen atoms and solvent molecules are omitted for clarity. In (a), the cation is shown, with the outer-sphere Cl^- omitted. In (b), the counterion is included, as well as a second molecule of **5c** generated by a crystallographic inversion center. Dashed lines indicate located hydrogen bonds, and atoms labeled with an asterisk (*) are symmetry equivalents of those with conventional labels.

irrespective of the presence of O_2 and HCl . It is not clear whether the conversion of peroxo complex **4b/c** to $\text{Rh}^{\text{III}}\text{Cl}_3$ complex **3b/c** necessarily proceeds through the aqua intermediate **5b/c**, or if the direct conversion is possible (dashed arrow in Scheme 4).

6.3 Discussion

Alteration of a single neutral donor ligand can have a profound effect on O_2 activation and reduction by late-metal molecular complexes. The dramatic effect of the ligand environment is manifested most profoundly in the equilibrium constant for HCl addition, K_{HCl} , an important parameter for O_2 activation, particularly when a HXRE mechanism is operative.^{44–46,50} The strongly π -acidic CO supporting ligand of **1a** renders the Rh^{I} center comparatively electron poor, and a K_{HCl} of 9.6 is observed. The small value of K_{HCl} precludes isolation of hydride complex **2a**, and in the absence of HCl , reversion to **1a** occurs with facility. Upon changing L to substituted isocyanides, HCl addition is strongly favored (see Scheme 6.2) and isolation of hydrides **2b/c** is readily achieved. Similar trends are observed for the addition of O_2 to **1a–c** to generate peroxo complexes **4a–c**. For **1a**, addition of 1 atm of O_2 generates only a small amount of the presumed peroxo complex **4a**, whereas quantitative formation of **4b/c** is observed under identical

conditions. The thermodynamic metrics for HCl addition, coupled with the qualitative observations on O₂ addition, readily demonstrate that the electronic environment of the rhodium center can be significantly altered by simple ligand substitution.

The O₂-reduction chemistry of *cis-trans*-Rh^{III}Cl₂H(L)(PEt₃)₂ (**2a–c**) is quite general. In all cases, treatment of the hydride with excess HCl and O₂ leads to smooth conversion to *trans*-Rh^{III}Cl₃(L)(PEt₃)₂ (**3a–c**) with concomitant formation of H₂O, monometallic analogs to previously reported bimetallic systems.⁴⁹ Though an intermediate is not observed for **2a** by traditional spectroscopic techniques, the aqua complex [Rh^{III}(OH₂)Cl₂(L)(PEt₃)₂]Cl (**5b/c**) appears during the course of the reaction of **2b/c** to **3b/c**. The identification of **5b/c** demonstrates that O₂ is being reduced to water in these systems, though it is unclear at this stage if there is a mechanistic significance of the bound aqua complex, which has not been detected for the ORR of bimetallic systems.

The reaction times for O₂ reduction by the monometallic systems described here are substantially longer than those required for bimetallic complexes. For hydride **2a** (L = CO), high concentrations of HCl are required to ensure **2a** as the majority species, whereas hydrides **2b/c** do react under identical conditions to those investigated for the dirhodium hydrides albeit over reaction times of ~ 4 to 5 days, as compared to a few hours for dirhodium complexes. These observations suggest a possible benefit of bimetallic cooperativity for the ORR promoted by late transition-metal systems, though more in-depth studies will be required to deconvolute effects associated with the disparate electronic parameters of the monometallic complexes described here compared to the bimetallic system initially studied. In particular, the dirhodium complexes were bridged by relatively electron-poor phosphite-based tfepma (CH₃[(P(OCH₂CF₃)₂)₂]) ligands, whereas the monometallic complexes here are ligated by electron-rich PEt₃ ligands.

As η²-peroxo species are keystones to the ORR, especially for reactions proceeding by a HXRE mechanism, peroxo complexes **4b/c** were independently prepared by pressurizing **1b/c** with 1 atm of O₂, and their reactivity was investigated with HCl under conditions analogous to those employed in O₂-reduction experiments. This study is especially valuable inasmuch as the dirhodium peroxo species are not synthetically accessible, and thus examination of peroxo reactivity has not been feasible. The peroxo complexes react rapidly with excess HCl, forming a

mixture of aqua complexes **5b/c** and $\text{Rh}^{\text{III}}\text{Cl}_3$ complexes **3b/c**, before final conversion to **3b/c**. Even at early time points, **3b/c** and **5b/c** are the only two species observed spectroscopically, indicating facile cleavage of the O–O bond under these conditions. It is reasonable to assume that a hydroperoxo intermediate forms initially upon reaction with HCl, given the reactivity of other late-metal peroxo systems.^{50,68–70} However, in the case of the rhodium complexes described here, such hydroperoxo complexes are apparently too unstable to observe, as even a single equivalent of HCl added to **4b/c** fails to produce any spectroscopic features that can be confidently assigned to a hydroperoxo complex. Notwithstanding, the reactivity of peroxo complexes **4b/c** with HCl, which generates water and trichloro complexes **3b/c** as the final outcome, bespeaks to the plausibility of an HXRE mechanism for ORR by hydride complexes **2b/c**. These results set the stage for a thorough and systematic mechanistic interrogation of O_2 activation and reduction by monometallic rhodium hydride complexes.

6.4 Conclusion

Monometallic Rh^{III} hydride complexes, in the presence of HCl, quantitatively reduce half of an equivalent of O_2 to water. The chemistry of independently prepared peroxo congeners points to HXRE as the mechanism of ORR. In this chapter, oxygen-reduction chemistry of rhodium hydride complexes was extended to a monometallic system. This new platform for oxygen-reduction reactivity provides several advantages for ongoing and future studies. These complexes facilitate direct comparisons to the previous bimetallic system, allowing the effects of bimetallic cooperativity to be assayed. Also, unlike the dirhodium complexes, the monorhodium complexes described here are synthetically tunable, and even by simple alteration of one supporting ligand it was shown that dramatic electronic effects are observed. In addition, some of the key reaction intermediates in O_2 -reduction chemistry, in particular the peroxo complexes (**4b/c**) and aqua complexes (**5b/c**), are accessible on a monometallic platform, permitting a detailed investigation of the structural and spectroscopic features and reactivity of these intermediate species. Forthcoming studies on oxygen reduction by rhodium hydride complexes can provide insight into the factors that govern the mechanistic preference for this reaction, be it HXRE, HAA, or some other as-yet uncharacterized sequence.

6.5 Experimental Details

6.5.1 General Considerations

All reactions involving air-sensitive materials were executed in a N₂-filled glovebox, on a Schlenk line or on a high-vacuum manifold using solvents previously dried by passage through an alumina column under Ar. HCl (4 M in dioxane, 1 M in Et₂O), anhydrous NaCl, concentrated H₂SO₄, anhydrous 1,4-dioxane, and 2,6-dimethylphenylisocyanide (CNXy) were obtained from Sigma-Aldrich, [Rh^I(CO)₂Cl]₂, [Rh^ICl(COD)]₂ (COD = 1,5-cyclooctadiene), and PEt₃ were purchased from Strem, and O₂ was purchased from Airgas. All commercially available starting materials were used as received. The complex *trans*-Rh^ICl(CO)(PEt₃)₂ (**1a**) was prepared by a modified procedure,⁵³ starting with [Rh^I(CO)₂Cl]₂ and using toluene as the solvent. The ligand 1-adamantylisocyanide (CNA_d) was prepared as described previously.⁷¹ Elemental analyses were performed by Midwest Microlab LLC.

6.5.2 Physical Methods

NMR spectra were recorded at the MIT Department of Chemistry Instrumentation Facility on a Varian Mercury-300 Spectrometer operating at 121.5 MHz for ³¹P acquisition, or a Varian Inova-500 NMR Spectrometer operating at 500 MHz for ¹H acquisition. ³¹P{¹H} NMR spectra were referenced to an external standard of 85% D₃PO₄ and ¹H spectra were referenced to the residual proteo solvent resonances. UV-vis spectra were recorded at 295 K in THF solutions in quartz cuvettes on a Varian Cary 5000 UV-vis-NIR spectrophotometer. Extinction coefficients were determined over a concentration range of ~ 10⁻⁶ to 10⁻⁴ M, for which all compounds obeyed Beer's Law. For hydride complexes **2b/c**, the UV-vis spectra were recorded in the presence of 52 mM HCl, whereas for **4b/4c**, the spectra were recorded with 1 atm of O₂ present, to prevent reversion to **1b/c**. Spectral data is summarized below. IR spectra were recorded on a PerkinElmer Spectrum 400 FT-IR/FT-FIR Spectrometer outfitted with a Pike Technologies GladiATR attenuated total reflectance accessory with a monolithic diamond crystal stage and pressure clamp. Samples were suspended in Nujol[®] for all IR measurements.

6.5.3 Preparation of *trans*-Rh^ICl(CNXy)(PEt₃)₂ (**1b**)

In a 20-mL scintillation vial, [Rh^I(COD)Cl]₂ (100 mg, 0.203 mmol, 1.00 eq) was suspended in 2 mL of THF. A solution of PEt₃ (120 μL, 0.811 mmol, 4.00 eq) dissolved in 2 mL

of THF was added, producing a light orange solution. Immediate addition of 2,6-dimethylphenylisocyanide (CNXy) (53 mg, 0.40 mmol, 2.0 eq) in 2 mL of THF caused the color to fade to bright yellow. The slightly cloudy mixture was stirred for 1 h at room temperature, and then filtered to remove a small amount of gray solid. The resulting yellow solution was concentrated in vacuo to give a sticky yellow solid, which was redissolved in 8 mL of hexane. The solvent was removed in vacuo, and the resulting microcrystalline yellow solid was dried in vacuo overnight to remove residual 1,5-cyclooctadiene. Yield: 200 mg (97.6%). ^1H NMR (500 MHz, C_6D_6) δ/ppm : 6.76–6.82 (m, 3H), 2.33 (s, 6H), 1.80 (m, 12H) 1.11 (quintet, 18H). $^{31}\text{P}\{^1\text{H}\}$ NMR (121.5 MHz, C_6D_6) δ/ppm : 23.6 (d, $^1J_{\text{Rh-P}} = 124$ Hz). UV-vis (THF): λ/nm ($\epsilon/(\text{M}^{-1} \text{cm}^{-1})$) 265 (24000), 302 (sh) (8100), 367 (sh) (2600). IR (Nujol): $\tilde{\nu}_{\text{C}\equiv\text{N}} = 2054 \text{ cm}^{-1}$. Anal. Calcd. for $\text{C}_{21}\text{H}_{39}\text{ClNP}_2\text{Rh}$: C, 49.86; H, 7.77; N, 2.77. Found: C, 49.59; H, 7.69; N, 2.64.

6.5.4 Preparation of *trans*- $\text{Rh}^{\text{I}}(\text{CNAd})\text{Cl}(\text{PEt}_3)_2$ (**1c**)

THF solutions (2-mL) of $[\text{Rh}^{\text{I}}(\text{COD})\text{Cl}]_2$ (100 mg, 0.203 mmol, 1.00 eq) and PEt_3 (120 μL , 0.811 mmol, 4.00 eq) were combined to afford a pale orange solution. 1-adamantylisocyanide (CNAd) (66 mg, 0.41 mmol, 2.0 eq) in 2 mL of THF was introduced, causing the color to fade to yellow. After stirring for 1 h at room temperature, the solution was concentrated in vacuo to leave a yellow residue, which was redissolved in 4 mL of pentane. The yellow solution was concentrated and dried in vacuo overnight, leaving the product as a bright yellow solid. Yield: 208 mg (95.8%). ^1H NMR (500 MHz, C_6D_6) δ/ppm : 1.88 (m, 12H), 1.80 (br, d, 6H), 1.73 (br, m, 3H), 1.33 (br, m, 6H), 1.20 (quintet, 18H). $^{31}\text{P}\{^1\text{H}\}$ NMR (121.5 MHz, C_6D_6) δ/ppm : 22.8 (d, $^1J_{\text{Rh-P}} = 127$ Hz). UV-vis (THF): λ/nm ($\epsilon/(\text{M}^{-1} \text{cm}^{-1})$) 282 (sh) (5700), 308 (9700), 369 (3900). IR (Nujol): $\tilde{\nu}_{\text{C}\equiv\text{N}} = 2068 \text{ cm}^{-1}$. Anal. Calcd. for $\text{C}_{23}\text{H}_{45}\text{ClNP}_2\text{Rh}$: C, 51.55; H, 8.46; N, 2.61. Found: C, 51.42; H, 8.15; N, 2.53.

6.5.5 Preparation and NMR Characterization of *cis-trans*- $\text{Rh}^{\text{III}}(\text{CO})\text{Cl}_2\text{H}(\text{PEt}_3)_2$ (**2a**)

A J. Young NMR tube was charged with **1a** (10 mg, 0.025 mmol, 1.0 eq) dissolved in 0.7 mL of THF- d_8 . The solution was freeze-pump-thaw degassed three times at $\sim 10^{-6}$ torr on a high-vacuum manifold. Anhydrous HCl, generated by dropping concentrated H_2SO_4 onto anhydrous NaCl (36 mg, 0.62 mmol, 25 eq), was vacuum-transferred to the solution of **1a**. While frozen, the

NMR tube was evacuated to $\sim 10^{-6}$ torr and then thawed to reveal a pale yellow solution. Under these conditions (where HCl transfer is not quantitative), **2a** and **1a** were observed to be present in a ca. 2:1 ratio. Removal of the volatiles resulted in complete reversion to **1a**, as judged by $^{31}\text{P}\{\text{H}\}$ NMR. ^1H NMR (500 MHz, THF- d_8) δ/ppm : 2.10 (m, 12H), 1.18 (quintet, 18H), -13.16 (dt, $^1J_{\text{Rh-H}} = 16.6$ Hz, $^2J_{\text{P-H}} = 10.4$ Hz, 1H). $^{31}\text{P}\{\text{H}\}$ NMR (121.5 MHz, THF- d_8) δ/ppm : 26.4 (d, $^1J_{\text{Rh-P}} = 81$ Hz).

6.5.6 Preparation of *cis-trans*- $\text{Rh}^{\text{III}}\text{Cl}_2(\text{CNXy})\text{H}(\text{PEt}_3)_2$ (**2b**)

A 25-mL Schlenk tube with a Teflon plug seal was charged with **1b** (100 mg, 0.198 mmol, 1.00 eq) dissolved in 3 mL of THF. The solution was freeze-pump-thaw degassed three times at $\sim 10^{-6}$ torr. Anhydrous HCl, generated by dropping concentrated H_2SO_4 onto anhydrous NaCl (58 mg, 0.99 mmol, 5.0 eq), was vacuum-transferred onto the still-frozen solution. The vessel was pumped down to $\sim 10^{-6}$ torr and then allowed to thaw slowly with stirring. Upon thawing, the now colorless solution was stirred for 10 min. The volatiles were removed in vacuo, and the resulting residue taken back into the glovebox, dissolved in 4 mL of THF and transferred to a scintillation vial. The solvent was removed in vacuo to yield a pale residue, which was suspended in 0.25 mL of toluene. Addition of 4 mL of hexane separated a white solid, which was decanted and dried in vacuo. Yield: 100 mg (93.4%). ^1H NMR (500 MHz, C_6D_6) δ/ppm : 6.74 (t, $^3J_{\text{H-H}} = 7.6$ Hz, 1H), 6.64 (d, $^3J_{\text{H-H}} = 7.6$ Hz, 2H), 2.29 (s, 6H), 2.08 (m, 6H), 1.90 (m, 6H), 1.05, (quintet, 18H), -14.48 (dt, $^1J_{\text{Rh-H}} = 18.1$ Hz, $^2J_{\text{P-H}} = 11.4$ Hz, 1H). $^{31}\text{P}\{\text{H}\}$ NMR (121.5 MHz, C_6D_6) δ/ppm : 24.7 (d, $^1J_{\text{Rh-P}} = 86$ Hz). UV-vis (THF): λ/nm ($\epsilon/(\text{M}^{-1} \text{cm}^{-1})$) 251 (27000). IR (Nujol): $\tilde{\nu}_{\text{C=N}} = 2147 \text{ cm}^{-1}$. Anal. Calcd. for $\text{C}_{21}\text{H}_{40}\text{Cl}_2\text{NP}_2\text{Rh}$: C, 46.51; H, 7.43; N, 2.58. Found: C, 46.29; H, 7.27; N, 2.41.

6.5.7 Preparation of *cis-trans*- $\text{Rh}^{\text{III}}(\text{CNAd})\text{Cl}_2\text{H}(\text{PEt}_3)_2$ (**2c**)

A 25-mL Schlenk flask was charged with **1c** (100 mg, 0.186 mmol, 1.00 eq) dissolved in 6 mL of Et_2O . After cooling to -78 °C in dry ice/acetone, a solution of HCl in Et_2O (1.03 M, 0.90 mL, 5.0 eq) was added via syringe. The reaction mixture was stirred for 10 min before removing the cold bath. A white precipitate that formed initially redissolved upon warming to room temperature, yielding a colorless solution that was stirred for 30 min. The

solution was concentrated in vacuo to give a white solid. In the glovebox, the solid was suspended in 8 mL of Et₂O and transferred to a scintillation vial. The solvent was removed in vacuo, and the solid redissolved in 0.5 mL of toluene. With stirring, 6 mL of hexane was added, freeing a colorless solid, which was decanted and dried in vacuo. Yield: 97 mg (91%). ¹H NMR (500 MHz, C₆D₆) δ/ppm: 2.14 (m, 6H), 1.98 (m, 6H), 1.65 (br, d, 6H), 1.61 (br, m, 3H), 1.17–1.27 (br, m, 6H), 1.15, (quintet, 18H), –15.09 (dt, ¹J_{Rh-H} = 17.9 Hz, ²J_{P-H} = 11.6 Hz, 1H). ³¹P{¹H} NMR (121.5 MHz, C₆D₆) δ/ppm: 24.1 (d, ¹J_{Rh-P} = 88 Hz). UV-vis (THF): λ/nm (ε/(M⁻¹ cm⁻¹)) 233 (sh) (14000), 277 (7200). IR (Nujol): ν_{C=N} = 2170 cm⁻¹. Anal. Calcd. for C₂₃H₄₆Cl₂NP₂Rh: C, 48.26; H, 8.10; N, 2.45. Found: C, 48.33; H, 7.81; N, 2.32.

6.5.8 Preparation of *trans*-Rh^{III}(CO)Cl₃(PEt₃)₂ (**3a**)

In a 20-mL scintillation vial, **1a** (50 mg, 0.12 mmol, 1.00 eq) was dissolved in 1 mL of CH₂Cl₂. Separately, PhICl₂ (28.5 mg, 0.104 mmol, 1.05 eq) was also dissolved in 1 mL of CH₂Cl₂. Both solutions were frozen in the coldwell of the glovebox. They were removed, and upon thawing the PhICl₂ was added dropwise to the stirred solution of **1a**, giving a bright yellow solution which was allowed to warm to room temperature and stirred for 30 min. At this time, 4 mL of hexane were added, and the solution was concentrated in vacuo to produce a sticky yellow solid. Washing the product with 2 mL of hexane at –20 °C gave a yellow solid, which was dried in vacuo. The spectral data reported here are a good match for those reported previously.^{72,73} Yield: 55 mg (93%). ¹H NMR (500 MHz, C₆D₆) δ/ppm: 2.02 (m, 12H), 0.98 (quintet, 18H). ³¹P{¹H} NMR (121.5 MHz, C₆D₆) δ/ppm: 19.3 (d, ¹J_{Rh-P} = 72 Hz). UV-vis (THF): λ/nm (ε/(M⁻¹ cm⁻¹)) 295 (20000), 371 (2000). IR (Nujol): ν_{C=O} = 2059 cm⁻¹. Anal. Calcd. for C₁₃H₃₀Cl₃OP₂Rh: C, 32.97; H, 6.38. Found: C, 32.48; H, 6.16.

6.5.9 Preparation of *trans*-Rh^{III}Cl₃(CNXy)(PEt₃)₂ (**3b**)

A sample of **1b** (50 mg, 0.099 mmol, 1.0 eq) was dissolved in 1 mL of toluene. In a separate vial, PhICl₂ (28.5 mg, 0.104 mmol, 1.05 eq) was also dissolved in 1 mL of toluene. Both solutions were frozen in the coldwell of the glovebox. They were removed, and upon thawing the PhICl₂ was added dropwise to the stirred solution of **1b** with a slight darkening in color observed. The solution was allowed to warm to room temperature and stirred for a total of 40 min. At this time, the solvent was removed in vacuo to leave a yellow-orange residue, which was

redissolved in 0.5 mL of CH₂Cl₂. With stirring, 3 mL of hexane was added, and the mixture was concentrated to ca. one-half its original volume, liberating a yellow-orange solid. The supernatant was decanted and the product dried in vacuo. The solid was redissolved in 2 mL of toluene, and after sitting for 4 d at room temperature complete conversion from a mixture of *trans*-Rh^{III}Cl₃(CNXy)(PEt₃)₂ and *mer-cis*-Rh^{III}Cl₃(CNXy)(PEt₃)₂ to the desired *trans* product was achieved. The toluene was removed in vacuo to reveal a yellow solid, which was dissolved in a mixture of 0.5 mL of CH₂Cl₂ and 4 mL of hexane. After concentrating in vacuo to < 2 mL, the supernatant was separated from the yellow-orange product, which was dried in vacuo. Yield: 46 mg (81%). ¹H NMR (500 MHz, C₆D₆) δ/ppm: 6.73 (t, ³J_{H-H} = 7.6 Hz, 1H), 6.63 (d, ³J_{H-H} = 7.6 Hz, 2H), 2.37 (s, 6H), 2.18 (m, 12H), 1.09 (quintet, 18H). ³¹P{¹H} NMR (121.5 MHz, C₆D₆) δ/ppm: 15.4 (d, ¹J_{Rh-P} = 77 Hz). UV-vis (THF): λ/nm (ε/(M⁻¹ cm⁻¹)) 254 (37000), 345 (2800), 398 (sh) (920). IR (Nujol): ν_{C≡N} = 2190 cm⁻¹. Anal. Calcd. for C₂₁H₃₉Cl₃NP₂Rh: C, 43.73; H, 6.82; N, 2.43. Found: C, 43.44; H, 6.50; N, 2.31.

6.5.10 Preparation of *trans*-Rh^{III}(CNAd)Cl₃(PEt₃)₂ (**3c**)

A 20-mL scintillation vial was charged with **1c** (50 mg, 0.093 mmol, 1.0 eq), and into a separate vial was weighed PhICl₂ (27 mg, 0.098 mmol, 1.05 eq). Both solids were dissolved in 1 mL of CH₂Cl₂ and frozen in the glovebox coldwell. They were removed, and upon thawing the PhICl₂ solution was added dropwise to the **1c** solution, yielding a bright yellow-orange solution which was warmed to room temperature and stirred for 30 min. The solution was diluted with 4 mL of hexane, and concentrated in vacuo to afford a yellow-orange residue. The residue was taken up in 0.25 mL of CH₂Cl₂, to which was added 4 mL of hexane to produce a cloudy mixture. Upon concentrating in vacuo to < 2 mL, a yellow-orange solid precipitated. The supernatant was decanted and the product dried in vacuo. Yield: 53 mg (93%). ¹H NMR (500 MHz, C₆D₆) δ/ppm: 2.25 (m, 12H), 1.72 (br, d, 6H), 1.61 (br, m, 3H), 1.13–1.25 (m, 24H). ³¹P{¹H} NMR (121.5 MHz, C₆D₆) δ/ppm: 14.4 (d, ¹J_{Rh-P} = 78 Hz). UV-vis (THF): λ/nm (ε/(M⁻¹ cm⁻¹)) 222 (25000), 262 (15000), 272 (sh) (14000), 341 (2100), 403 (560). IR (Nujol): ν_{C≡N} = 2194 cm⁻¹. Anal. Calcd. for C₂₃H₄₅Cl₃NP₂Rh: C, 45.52; H, 7.47; N, 2.31. Found: C, 45.26; H, 7.29; N, 2.37.

6.5.11 Preparation of *trans*-Rh^{III}Cl(CNXy)(η^2 -O₂)(PEt₃)₂ (**4b**)

A 10-mL Schlenk flask was charged with **1b** (50 mg, 0.099 mmol, 1.0 eq) dissolved in 4 mL of Et₂O. With vigorous stirring, the headspace was purged with O₂ for 1 min, and after removing the O₂ stream the solution was allowed to stir for an additional 5 min, leaving a dull yellow-brown solution. The solvent was removed in vacuo to give a brown solid, which was redissolved in Et₂O and transferred to a scintillation vial in the glovebox. The solvent was removed again in vacuo, and the resulting solid washed with 2 mL of hexane and dried in vacuo briefly (< 30 min). The NMR spectra show ca. 7% of **1b**, though the microanalytical data and IR spectrum suggest high purity for the isolated solid. Yield: 45 mg (85%). ¹H NMR (500 MHz, C₆D₆) δ /ppm: 6.73–6.79 (m, 1H), 6.66–6.69 (m, 2H), 2.35 (s, 6H), 1.90 (m, 6H), 1.72 (m, 6H), 1.09, (quintet, 18H). ³¹P{¹H} NMR (121.5 MHz, C₆D₆) δ /ppm: 26.3 (d, ¹J_{Rh-P} = 87 Hz). UV-vis (THF): λ /nm (ϵ /(M⁻¹ cm⁻¹)) 243 (40000). IR (Nujol): $\tilde{\nu}_{C\equiv N}$ = 2122 cm⁻¹, $\tilde{\nu}_{O-O}$ = 876 cm⁻¹. Anal. Calcd. for C₂₁H₃₉ClNO₂P₂Rh: C, 46.90; H, 7.31; N, 2.60. Found: C, 46.81; H, 7.24; N, 2.55.

6.5.12 Preparation of *trans*-Rh^{III}(CNAd)Cl(η^2 -O₂)(PEt₃)₂ (**4c**)

A solution of **1c** (50 mg, 0.093 mmol, 1.0 eq) in 4 mL of Et₂O was prepared in a 10-mL Schlenk flask. The headspace was flushed with O₂ for 1 min with vigorous stirring, and after removing the O₂ flow the stirring was continued for an additional 5 min. The resulting yellow-brown solution was concentrated in vacuo to give an olive-green solid. In the glovebox, the solid was dissolved in Et₂O and transferred to a scintillation vial. The volatiles were removed in vacuo, and the product washed with 2 mL of hexane before drying briefly in vacuo. Yield: 49 mg (92%). ¹H NMR (500 MHz, C₆D₆) δ /ppm: 1.93 (m, 6H), 1.82 (m, 6H), 1.76 (br, d, 6H), 1.64 (br, m, 3H), 1.15–1.28 (m, 24H). ³¹P{¹H} NMR (121.5 MHz, C₆D₆) δ /ppm: 25.3 (d, ¹J_{Rh-P} = 89 Hz). UV-vis (THF): λ /nm (ϵ /(M⁻¹ cm⁻¹)) 241 (23000). IR (Nujol): $\tilde{\nu}_{C\equiv N}$ = 2135 cm⁻¹, $\tilde{\nu}_{O-O}$ = 877 cm⁻¹. Anal. Calcd. for C₂₃H₄₅ClNO₂P₂Rh: C, 48.64; H, 7.99; N, 2.47. Found: C, 48.75; H, 7.75; N, 2.44.

6.5.13 O₂-Reduction Reactions of **2a–2c**.

All O₂-reduction reactions were executed and monitored in a screw-cap NMR tube with a PTFE septum seal. In all cases, the concentration of the hydride complex was 25 mM at the start

of the reaction. Hydride complex **2a** (L = CO) was generated in situ by dissolving a sample of **1a** (7.0 mg, 0.017 mmol, 1.0 eq) in 0.35 mL of 1,4-dioxane and adding 0.35 mL of a 4.13 M solution of HCl in dioxane. For **2b** (L = CNXy) and **2c** (L = CNAd), an appropriate amount of the hydride was dissolved in 1,4-dioxane, and the HCl/dioxane solution was added to produce a total volume of 0.7 mL with the desired concentration of HCl. Alternatively, the hydride complexes **2b** and **2c** could be generated in situ from **1b** and **1c** at no detriment to the observed reaction. After addition of the hydride complex and HCl, the headspace of the NMR tube was purged for ~ 1 min with O₂ at atmospheric pressure. The contents of the tube were shaken vigorously to ensure complete mixing, and periodically mixed throughout the course of the reactions, which were monitored by ³¹P{¹H} NMR spectroscopy.

6.5.14 Addition of HCl to **4b** to Generate **3b/5b**

Complex **1b** (9.0 mg, 0.018 mmol, 1.0 eq) was dissolved in 0.7 mL of THF-d₈ in a screw-cap, septum-sealed NMR tube. The headspace of the NMR tube was purged with O₂ (1 atm) and manually shaken to mix, generating a dull yellow solution of **4b**. A solution of HCl in dioxane (4.2 M, 13 μL, 0.054 mmol, 3.0 eq) was added via syringe, resulting in an immediate color change to bright yellow. The ³¹P{¹H} NMR spectra recorded immediately after showed a mixture of **5b** (80%), **3b** (17%), and ~ 3% of unidentified side products. The solution was transferred to a scintillation vial, concentrated in vacuo, and the resulting residue washed with hexane and dried in vacuo. Spectral data for **5b**: ¹H NMR (500 MHz, CD₃CN) δ/ppm: ~ 7.3 (m, 1H, overlapped with **3b**), 7.22 (m, 2H, overlapped with **3b**), 5.92 (br, s, 2H), 2.58 (s, 6H), 2.17 (m, 12H), 1.18 (quintet, 18H). ³¹P{¹H} NMR (121.5 MHz, CD₃CN) δ/ppm: 19.1 (d, ¹J_{Rh-P} = 74 Hz).

6.5.15 Addition of HCl to **4c** to Generate **3c/5c**

A solution of **1c** (9.0 mg, 0.017 mmol, 1.0 eq) in 0.7 mL of THF-d₈ was prepared in a screw-cap NMR tube with septum seal. The headspace was purged with 1 atm of O₂ for 1 min, and upon shaking the contents changed to a dull olive color, which was shown to be complex **4c**. Addition of an HCl/dioxane solution (4.2 M, 12 μL, 0.050 mmol, 2.9 eq) produced a bright yellow solution. At this stage, ³¹P{¹H} NMR indicates a mixture of **5b** (80%) and **3b** (20%). The solution was concentrated in vacuo, the product triturated with Et₂O/hexane, and the resulting

yellow solid dried in vacuo. Spectral data for **5c**: ^1H NMR (500 MHz, C_6D_6) δ/ppm : 6.58 (br, s, 2H), \sim 2.22–2.41 (m, 12H, overlapped with **3c**), 2.21 (br, s, 6H), 1.74 (br, s, 3H), 1.14–1.39 (m, 24H, overlap with **3c**). $^{31}\text{P}\{^1\text{H}\}$ NMR (121.5 MHz, C_6D_6) δ/ppm : 17.4 (d, $^1J_{\text{Rh-P}} = 76$ Hz).

6.5.16 X-Ray Crystallographic Details

Single crystals of **2b** were obtained by cooling a saturated toluene/hexane solution to -20 °C. **3b** and **5c** crystallized from saturated CH_2Cl_2 /hexane solutions at -20 °C, and crystals of **4b** formed by allowing O_2 to slowly diffuse into a hexane solution of **1b** at room temperature. Crystals of **3b**, **4b** and **5c** were mounted on a Bruker three-circle goniometer platform equipped with an APEX detector, whereas crystals of **2b** were mounted on a Bruker four-circle goniometer platform with an APEX 2 detector. A graphite monochromator was employed for wavelength selection of the Mo $K\alpha$ radiation ($\lambda = 0.71073$ Å). The data were processed and refined using the program SAINT supplied by Siemens Industrial Automation. Structures were solved by Patterson methods or direct methods in SHELXS and refined by standard difference Fourier techniques in the SHELXTL program suite (6.10 v., Sheldrick G. M., and Siemens Industrial Automation, 2000). Hydrogen atoms bonded to carbon were placed in calculated positions using the standard riding model and refined isotropically; all non-hydrogen atoms were refined anisotropically. In the structure of **2b**, the rhodium-bound hydrogen atom was tentatively located in the difference map and refined isotropically. The O–H hydrogen atoms in the structure of **5c** were also located in the difference map; they were restrained to a distance of 0.84 Å from the oxygen atom and refined isotropically. The structure of **3b** was refined as a racemic twin. In the structure of **5c**, the adamantyl group, one of the ethyl groups and a solvent dichloromethane molecule were all modeled as two-part positional disorders. The corresponding 1–2 and 1–3 distances of all disordered parts were restrained to be identical, and rigid bond restraints were used on all disordered atoms. Crystallographic details for **2b**, **3b**, **4b** and **5c** are summarized in Tables 6.1 and 6.2.

Table 6.1. Crystallographic summary for **2b** and **3b**.

| | 2b | 3b |
|--|--|--|
| Formula | C ₂₁ H ₄₀ Cl ₂ NP ₂ Rh | C ₂₁ H ₃₉ Cl ₃ NP ₂ Rh |
| fw, g/mol | 542.29 | 576.73 |
| Temperature/K | 100(2) | 200(2) |
| cryst. syst. | Monoclinic | Orthorhombic |
| space group | <i>Cc</i> | <i>Pna2</i> ₁ |
| color | Colorless | Yellow |
| <i>a</i> /Å | 11.4479(12) | 20.1861(8) |
| <i>b</i> /Å | 14.6692(15) | 10.3567(4) |
| <i>c</i> /Å | 15.4302(15) | 12.9174(5) |
| α /° | 90 | 90 |
| β /° | 93.787(2) | 90 |
| γ /° | 90 | 90 |
| <i>V</i> /Å ³ | 2585.6(5) | 2700.53(18) |
| ρ (calc.)/(g cm ⁻³) | 1.393 | 1.419 |
| <i>Z</i> | 4 | 4 |
| no. refl. | 25388 | 61558 |
| no. unique refl. | 6906 | 8130 |
| <i>R</i> _{int} | 0.0272 | 0.0353 |
| <i>R</i> ₁ ^a (all data) | 0.0229 | 0.0203 |
| <i>wR</i> ₂ ^b (all data) | 0.0465 | 0.0457 |
| <i>R</i> ₁ [(<i>I</i> > 2σ)] | 0.0205 | 0.0183 |
| <i>wR</i> ₂ [(<i>I</i> > 2σ)] | 0.0452 | 0.0442 |
| <i>GOF</i> ^c | 1.042 | 1.075 |
| <i>Flack param.</i> | -0.030(14) | 0.638(13) |

^a $R_1 = \frac{\sum ||F_o| - |F_c||}{\sum |F_o|}$. ^b $wR_2 = \frac{\sum (w(F_o^2 - F_c^2)^2)}{\sum (w(F_o^2)^2)}^{1/2}$. ^c $GOF = \frac{\sum (w(F_o^2 - F_c^2)^2)}{(n - p)}^{1/2}$ where *n* is the number of data and *p* is the number of parameters refined.

Table 6.2. Crystallographic summary for **4b** and **5c**.

| | 4b | 5c ·CH ₂ Cl ₂ |
|---|---|---|
| Formula | C ₂₁ H ₃₉ ClNO ₂ P ₂ Rh | C ₂₄ H ₄₇ Cl ₅ NOP ₂ Rh |
| fw, g/mol | 537.83 | 707.73 |
| Temperature/K | 100(2) | 100(2) |
| cryst. syst. | Monoclinic | Monoclinic |
| space group | <i>P</i> 2 ₁ / <i>n</i> | <i>P</i> 2 ₁ / <i>n</i> |
| color | Brown | Yellow |
| <i>a</i> /Å | 15.214(2) | 14.7676(19) |
| <i>b</i> /Å | 11.4156(18) | 11.0440(14) |
| <i>c</i> /Å | 15.778(3) | 19.617(2) |
| α /° | 90 | 90 |
| β /° | 113.796(2) | 90.952(2) |
| γ /° | 90 | 90 |
| <i>V</i> /Å ³ | 2507.3(7) | 3199.0(7) |
| ρ (calc.)/(g cm ⁻³) | 1.425 | 1.469 |
| <i>Z</i> | 4 | 4 |
| no. refl. | 57744 | 68331 |
| no. unique refl. | 7671 | 9363 |
| <i>R</i> _{int} | 0.0324 | 0.0722 |
| <i>R</i> ₁ ^{<i>a</i>} (all data) | 0.0246 | 0.0736 |
| <i>wR</i> ₂ ^{<i>b</i>} (all data) | 0.0508 | 0.1624 |
| <i>R</i> ₁ [(<i>I</i> > 2σ)] | 0.0195 | 0.0609 |
| <i>wR</i> ₂ [(<i>I</i> > 2σ)] | 0.0472 | 0.1564 |
| <i>GOF</i> ^{<i>c</i>} | 1.042 | 1.220 |

^{*a*} $R_1 = \frac{\sum ||F_o| - |F_c||}{\sum |F_o|}$. ^{*b*} $wR_2 = \frac{\sum (w(F_o^2 - F_c^2)^2)}{\sum (w(F_o^2)^2)}^{1/2}$. ^{*c*} $GOF = \frac{\sum (w(F_o^2 - F_c^2)^2)}{(n - p)^{1/2}}$ where *n* is the number of data and *p* is the number of parameters refined.

6.6 References

- (1) Barber, J. *Philos. Trans. R. Soc. A* **2007**, *365*, 1007–1023.
- (2) Barber, J. *Chem. Soc. Rev.* **2009**, *38*, 185–196.
- (3) Cook, T. R.; Dogutan, D. K.; Reece, S. Y.; Surendranath, Y.; Teets, T. S.; Nocera, D. G. *Chem. Rev.* **2010**, *110*, 6474–6502.
- (4) Lewis, N. S.; Nocera, D. G. *Proc. Natl. Acad. Sci. U.S.A* **2006**, *103*, 15729–15735.
- (5) Kaila, V. R. I.; Verkhovskiy, M. I.; Wikström, M. *Chem. Rev.* **2010**, *110*, 7062–7081.
- (6) Baik, M.-H.; Newcomb, M.; Friesner, R. A.; Lippard, S. J. *Chem. Rev.* **2003**, *103*, 2385–2420.
- (7) Himes, R. A.; Barnese, K.; Karlin, K. D. *Angew. Chem. Int. Ed.* **2010**, *49*, 6714–6716.
- (8) Collman, J. P.; Boulatov, R.; Sunderland, C. J.; Fu, L. *Chem. Rev.* **2004**, *104*, 561–588.
- (9) Rosenthal, J.; Nocera, D. G. *Acc. Chem. Res.* **2007**, *40*, 543–553.
- (10) Rosenthal, J. R.; Nocera, D. G. In *Progress in inorganic chemistry*; John Wiley and Sons: New York, 2007; pp. 483–544.
- (11) McGuire Jr., R.; Dogutan, D. K.; Teets, T. S.; Suntivich, J.; Shao-Horn, Y.; Nocera, D. G. *Chem. Sci.* **2010**, *1*, 411–414.
- (12) Dogutan, D. K.; Stoian, S. A.; McGuire, R.; Schwalbe, M.; Teets, T. S.; Nocera, D. G. *J. Am. Chem. Soc.* **2011**, *133*, 131–140.
- (13) Chang, C. J.; Deng, Y.; Nocera, D. G.; Shi, C.; Anson, F. C.; Chang, C. K. *Chem. Commun.* **2000**, 1355–1356.
- (14) Chang, C. J.; Loh, Z.-H.; Shi, C.; Anson, F. C.; Nocera, D. G. *J. Am. Chem. Soc.* **2004**, *126*, 10013–10020.
- (15) Collman, J. P.; Wagenknecht, P. S.; Hutchison, J. E. *Angew. Chem. Int. Ed. Eng.* **1994**, *33*, 1537–1554.
- (16) Collman, J. P.; Fu, L.; Hermann, P. C.; Zhang, X. *Science* **1997**, *275*, 949–951.
- (17) Halime, Z.; Kotani, H.; Li, Y.; Fukuzumi, S.; Karlin, K. D. *Proc. Natl. Acad. Sci. U.S.A.* **2011**, *108*, 13990–13994.
- (18) Stahl, S. S. *Angew. Chem. Int. Ed.* **2004**, *43*, 3400–3420.
- (19) Punniyamurthy, T.; Velusamy, S.; Iqbal, J. *Chem. Rev.* **2005**, *105*, 2329–2364.
- (20) Kunisu, T.; Oguma, T.; Katsuki, T. *J. Am. Chem. Soc.* **2011**, *133*, 12937–12939.
- (21) Frazier, C. P.; Engelking, J. R.; Read de Alaniz, J. *J. Am. Chem. Soc.* **2011**, *133*, 10430–10433.

- (22) Liu, L.; Yu, M.; Wayland, B. B.; Fu, X. *Chem. Commun.* **2010**, *46*, 6353–6355.
- (23) Li, H.; Wei, W.; Xu, Y.; Zhang, C.; Wan, X. *Chem. Commun.* **2011**, *47*, 1497–1499.
- (24) Fries, P.; Halter, D.; Kleinschek, A.; Hartung, J. *J. Am. Chem. Soc.* **2011**, *133*, 3906–3912.
- (25) Jiang, B.; Feng, Y.; Ison, E. A. *J. Am. Chem. Soc.* **2008**, *130*, 14462–14464.
- (26) Izawa, Y.; Pun, D.; Stahl, S. S. *Science* **2011**, *333*, 209–213.
- (27) Chuang, G. J.; Wang, W.; Lee, E.; Ritter, T. *J. Am. Chem. Soc.* **2011**, *133*, 1760–1762.
- (28) Zhang, J.; Khaskin, E.; Anderson, N. P.; Zavalij, P. Y.; Vedernikov, A. N. *Chem. Commun.* **2008**, 3625–3627.
- (29) Roberts, H. L.; Symes, W. R. *J. Chem. Soc. A* **1968**, 1450–1453.
- (30) Johnston, L. E.; Page, J. A. *Can. J. Chem.* **1969**, *47*, 4241–4246.
- (31) Gillard, R. D.; Heaton, B. T.; Vaughan, D. H. *J. Chem. Soc. A* **1970**, 3126–3130.
- (32) Endicott, J. F.; Wong, C.-L.; Inoue, T.; Natarajan, P. *Inorg. Chem.* **1979**, *18*, 450–454.
- (33) Atlay, M. T.; Preece, M.; Strukul, G.; James, B. R. *J. Chem. Soc., Chem. Commun.* **1982**, 406–407.
- (34) Atlay, M. T.; Preece, M.; Strukul, G.; James, B. R. *Can. J. Chem.* **1983**, *61*, 1332–1338.
- (35) Bakac, A. *J. Am. Chem. Soc.* **1997**, *119*, 10726–10731.
- (36) Thyagarajan, S.; Incarvito, C. D.; Rheingold, A. L.; Theopold, K. H. *Chem. Commun.* **2001**, 2198–2199.
- (37) Cui, W.; Wayland, B. B. *J. Am. Chem. Soc.* **2006**, *128*, 10350–10351.
- (38) Wick, D. D.; Goldberg, K. I. *J. Am. Chem. Soc.* **1999**, *121*, 11900–11901.
- (39) Konnick, M. M.; Gandhi, B. A.; Guzei, I. A.; Stahl, S. S. *Angew. Chem. Int. Ed.* **2006**, *45*, 2904–2907.
- (40) Denney, M. C.; Smythe, N. A.; Cetto, K. L.; Kemp, R. A.; Goldberg, K. I. *J. Am. Chem. Soc.* **2006**, *128*, 2508–2509.
- (41) Szajna-Fuller, E.; Bakac, A. *Inorg. Chem.* **2010**, *49*, 781–785.
- (42) Keith, J. M.; Nielsen, R. J.; Oxgaard, J.; Goddard, W. A. *J. Am. Chem. Soc.* **2005**, *127*, 13172–13179.
- (43) Keith, J. M.; Muller, R. P.; Kemp, R. A.; Goldberg, K. I.; Goddard, W. A.; Oxgaard, J. *Inorg. Chem.* **2006**, *45*, 9631–9633.
- (44) Popp, B. V.; Stahl, S. S. *J. Am. Chem. Soc.* **2007**, *129*, 4410–4422.
- (45) Konnick, M. M.; Stahl, S. S. *J. Am. Chem. Soc.* **2008**, *130*, 5753–5762.

- (46) Konnick, M. M.; Decharin, N.; Popp, B. V.; Stahl, S. S. *Chem. Sci.* **2011**, *2*, 326–330.
- (47) Decharin, N.; Stahl, S. S. *J. Am. Chem. Soc.* **2011**, *133*, 5732–5735.
- (48) Decharin, N.; Popp, B. V.; Stahl, S. S. *J. Am. Chem. Soc.* **2011**, *133*, 13268–13271.
- (49) Teets, T. S.; Cook, T. R.; McCarthy, B. D.; Nocera, D. G. *J. Am. Chem. Soc.* **2011**, *133*, 8114–8117.
- (50) Teets, T. S.; Nocera, D. G. *J. Am. Chem. Soc.* **2011**, *133*, 17796–17806.
- (51) Look, J. L.; Wick, D. D.; Mayer, J. M.; Goldberg, K. I. *Inorg. Chem.* **2009**, *48*, 1356–1369.
- (52) Gray, T. G.; Veige, A. S.; Nocera, D. G. *J. Am. Chem. Soc.* **2004**, *126*, 9760–9768.
- (53) Chatt, J.; Shaw, B. L. *J. Chem. Soc. A* **1966**, 1437–1442.
- (54) Jones, W. D.; Hessell, E. T. *Organometallics* **1990**, *9*, 718–727.
- (55) Vallarino, L. *J. Chem. Soc.* **1957**, 2287–2292.
- (56) Baker, R. T.; Calabrese, J. C.; Westcott, S. A.; Nguyen, P.; Marder, T. B. *J. Am. Chem. Soc.* **1993**, *115*, 4367–4368.
- (57) Carlton, L.; Mokoena, L. V.; Fernandes, M. A. *Inorg. Chem.* **2008**, *47*, 8696–8703.
- (58) Conkie, A.; Ebsworth, E. A. V.; Mayo, R. A.; Moreton, S. *J. Chem. Soc., Dalton Trans.* **1992**, 2951–2954.
- (59) Masters, C.; Shaw, B. L. *J. Chem. Soc. A* **1971**, 3679–3686.
- (60) Vaska, L. *J. Am. Chem. Soc.* **1966**, *88*, 5235–5327.
- (61) Kaljurand, I.; Kütt, A.; Sooväli, L.; Rodima, T.; Mäemets, V.; Leito, I.; Koppel, I. A. *J. Org. Chem.* **2005**, *70*, 1019–1028.
- (62) Izutsu, K. *Electrochemistry in nonaqueous solutions*; Wiley-VCH: Weinheim, Germany, 2002.
- (63) Wilson, A. D.; Miller, A. J. M.; DuBois, D. L.; Labinger, J. A.; Bercaw, J. E. *Inorg. Chem.* **2010**, *49*, 3918–3926.
- (64) Socrates, G. –O–O–Group. In *Infrared and Raman characteristic group frequencies: tables and charts*; J. Wiley: Chichester, 2001.
- (65) Lebel, H.; Ladjel, C.; Bélanger-Gariépy, F.; Schaper, F. *J. Organomet. Chem.* **2008**, *693*, 2645–2648.
- (66) Cramer, C. J.; Tolman, W. B.; Theopold, K. H.; Rheingold, A. L. *Proc. Natl. Acad. Sci. U.S.A.* **2003**, *100*, 3635–3640.
- (67) Fulmer, G. R.; Miller, A. J. M.; Sherden, N. H.; Gottlieb, H. E.; Nudelman, A.; Stoltz, B. M.; Bercaw, J. E.; Goldberg, K. I. *Organometallics* **2010**, *29*, 2176–2179.

- (68) Takahashi, Y.; Hashimoto, M.; Hikichi, S.; Akita, M.; Moro-oka, Y. *Angew. Chem. Int. Ed.* **1999**, *38*, 3074–3077.
- (69) Konnick, M. M.; Guzei, I. A.; Stahl, S. S. *J. Am. Chem. Soc.* **2004**, *126*, 10212–10213.
- (70) Ahijado, M.; Braun, T.; Noveski, D.; Kocher, N.; Neumann, B.; Stalke, D.; Stammeler, H.-G. *Angew. Chem. Int. Ed.* **2005**, *44*, 6947–6951.
- (71) Sasaki, T.; Nakanishi, A.; Ohno, M. *J. Org. Chem.* **1981**, *46*, 5445–5447.
- (72) Al-Jibori, S.; Crocker, C.; Shaw, B. L. *J. Chem. Soc., Dalton Trans.* **1981**, 319–321.
- (73) Intille, G. M. *Inorg. Chem.* **1972**, *11*, 695–702.

Acknowledgements

First off, before thanking individual people, I would like to thank the Hertz Foundation for fellowship support during all five years of graduate school.

The work contained in this thesis of course was not without the assistance and guidance of numerous individuals. In a slight departure from tradition, I won't be paying mention to each and every person I coexisted with in the Nocera Group. By my count, I have had ~ 75 co-workers during my time in the group, and with few exceptions I have had positive, stimulating interactions with all of them. I have learned a lot from my lab mates, and many of them I look forward to long-lasting friendships with, as bad as I am at such things. But the remainder of this Acknowledgements section will be dedicated to the subset of people who had the most profound impact on the scientific output that comprises this thesis.

I owe much gratitude to my thesis advisor, Dan Nocera. It's hard to explain to others what it is like to work for Dan, but despite his unconventional advising style I can say with certainty that I have learned a ton and grown immensely as a scientist during my time in his group. "Figure it out!" really is the best way to learn, and I will always appreciate the independence I was granted during my time here, and that I was given complete ownership of the projects such that no interesting result was ever brushed aside as a "side project" or "diversion." On the surface Dan and I are as incompatible as can be, but in all honesty I could not have picked a better group for myself.

There are a few other MIT faculty and staff I must thank. Professor Dick Schrock is acknowledged for serving as my thesis chair, and Kit Cummins for rounding out my committee. I also am indebted to Allison Kelsey, our administrative assistant, for all that she did (and still does) to make sure the wheels don't fall completely off of the Nocera Group Bus. Peter Müller is acknowledged for running a top-notch X-ray diffraction facility here and all that he has taught me about crystallography.

In the project area I worked on, typically referred to as the "HX Project" in Nocera Group circles, I have benefited from collaboration with several talented students and post-docs. Arthur Esswein, on his way out just as I was joining as an unofficial summer student, suggested I "look at some gold chemistry, there should be something interesting there," and this sage advice led to the work in Chapter 1. My more direct "mentor" was Tim Cook, who pioneered a lot of the X₂-elimination chemistry referenced in the intros of Chapters 1 and 2. Tim provided superb guidance, and we both managed to carve out some nice results without ever butting heads scientifically. I also had the privilege of mentoring two European Master's students in consecutive years, Markus Neumann and Noémie Elgrishi, who both did great work and were pleasures to oversee. And prior to his traitorous defection to Mircea's group (kidding), Brian McCarthy did some fine work in this area, including being the first to synthesize the two-electron mixed-valent dirhodium and diiridium complexes that became the cornerstones of Chapters 3–5. Danny Lutterman, a post-doc, became affiliated with the "HX Project" during his time here and performed some laser kinetic studies on X₂ photoelimination. And finally, I owe an acknowledgement to two recent additions to this subgroup, post-doc Dave Powers and new grad student Robert Halbach, who have already made substantial contributions in their short time in the group and I am confident will continue to do so.

There are a few other students and post-docs, not direct scientific collaborators, who were important figures nonetheless. Yogi Surendranath, one of my best friends from my time here and one of the most intellectually superb chemists I've ever met, was instrumental in shaping how I think about chemistry and work out ideas. In particular, he encouraged me to pursue the in-depth kinetic studies of the O₂-reduction chemistry, and thanks to his initial kick in the pants, the work contained in Chapter 4 was realized, and this became my favorite chapter in this thesis. And along with Tim, Yogi and I comprised the "Cornucopia," which to this day remains the absolute best Nocera Group subfaction to ever exist (sorry Synthesis Subgroup). There are also some graduate students and post-docs whom I must acknowledge for productive conversations. Post-doc Dino Villagrán was always a great source of guidance and condescension, "making me suggestions" which helped me learn what little computational chemistry I know. With post-docs Alex Radosevich and Mircea Dincă I had many a "philosophical" conversation about chemistry, and though not always uplifting, these talks were certainly thought-provoking and enjoyable. I must also thank Mircea for staying in touch as he's transitioned to his faculty position here, and for his willingness to write recommendations for post-docs and fellowships. Three current students in the group, classmate Matt Chambers, Kwabena Bediako, and Andrew Ullman, are my current most frequent partners for scientific conversation, and have helped me think deeply about things I would not normally consider. I should also thank Southernly hospitable Tim Kucharski for agreeing to proofread part of this thesis, among others who already are acknowledged for other contributions. And finally, I of course must thank Changhoon Lee, who in addition to being a "super best super friend" was a leader by example in how to properly look after lab space and equipment.

And outside of the MIT environs, there are a few acknowledgements which must be made. First, to my undergraduate advisor Thomas Gray, who got me started in inorganic chemistry and continued to be an invaluable advisor long after leaving his group. His continuing pointers on navigating the Nocera group, his thoughtful critique of my third-year orals proposal, and his ongoing guidance in career advancement are wholeheartedly appreciated. I also need to thank my family, parents Darcy and Kaye, twin Nick, brothers Joe and Jacob, and twin-in-law Julie, for staying in touch from afar, supporting my efforts, and giving me something to look forward to on those rare occasions when I took a break from MIT.

Biographical Note

The author was born on June 13, 1984 in Lorain, OH, as the first-born son of Darcy and Kaye Teets. At the age of four he moved to nearby Amherst, OH where he was raised along with his identical twin brother and two younger brothers. After a childhood fascination with the animal world, a particularly challenging and invigorating eighth grade biology course, led by Dean Runkle, and several enjoyable science courses at Amherst Steele High School, most notably Roy McCullough's calculus/physics sequence, cemented Tom's desire to further his study of science in his advanced education. In 2003 Tom graduated from Amherst Steele High School and enrolled as a chemistry major at Case Western Reserve University in Cleveland, OH. His introductory chemistry instructor, the late Dr. Ignacio Ocasio ("Doc Oc"), provided him with the initial impetus to pursue a career in chemical research. As an undergraduate at CWRU, Tom spent two and one-half years in the lab of Professor Thomas Gray, where he received his first exposure to inorganic chemistry. In the Gray lab Tom studied hexanuclear rhenium chalcogenide clusters, cadmium sequestration by synthetic phytochelatin peptides, and most significantly the synthesis and photophysical properties of transition-metal complexes of tetraarylazadipyrromethene ligands. He graduated *summa cum laude* from CWRU in 2007 with a Bachelor of Science in Chemistry and a minor in music. He immediately enrolled in the graduate program at MIT, where he pursued a PhD in inorganic chemistry in the laboratory of Professor Daniel G. Nocera with the support of a research fellowship from the Hertz Foundation. His thesis research involved the study of photochemical halogen elimination from late transition-metal complexes and oxygen-reduction chemistry of rhodium and iridium hydride complexes. After completion of the PhD degree, Tom will join the lab of Professor John Bercaw at the California Institute of Technology, to pursue postdoctoral studies in organometallic chemistry.

Curriculum Vitae

Thomas S. Teets

Department of Chemistry
Massachusetts Institute of Technology
77 Massachusetts Ave.
Room 18-172
Cambridge, MA 02139

Phone: (617) 258-7268
Email: tteets@gmail.com

Education

Massachusetts Institute of Technology

Ph.D. Inorganic Chemistry **2012**
Research with Professor Daniel G. Nocera
Hertz Foundation Graduate Fellow
Thesis Title: Halogen-Elimination Photochemistry and Oxygen-
Activation Chemistry of Late Transition-Metal Complexes
GPA: 5.0/5.0

Case Western Reserve University

B. S. Chemistry, *summa cum laude* **2007**
Research with Professor Thomas G. Gray
Thesis Title: Synthesis, Characterization and Photophysical Properties of
Transition-Metal Complexes of Tetraaryl-azadipyrromethenes
GPA: 4.0/4.0

Awards and Fellowships

ACS Division of Inorganic Chemistry Young Investigator Award **2012**
Hertz Foundation Graduate Fellowship **2007–2012**
IPMI Sabin Metals Corp. Graduate Student Award **2010**
Alpha Chi Sigma Scholar Award **2007**
Charles Mabery Undergraduate Thesis Prize, *CWRU* **2007**
Hypercube Scholar Award 2007, *CWRU* **2007**
Polymer Valley Undergraduate Research Award, *CWRU* **2006**
W. R. Veazey Prize, *CWRU* **2005**
Eli Lilly Award, *CWRU* **2005**
SOURCE Summer Research Fellow, *CWRU* **2005–2006**
Freshman Chemistry Achievement Award, *CWRU* **2004**
National Merit Scholar **2003–2007**
Trustee's Scholarship, *CWRU* **2003–2007**

Teaching Experience

Massachusetts Institute of Technology

Graduate Teaching Assistant

2007–2008

Courses Taught: General Chemistry, Laboratory Chemistry

Case Western Reserve University

Supplemental Instructor (SI)

2004–2007

Courses Taught: General Chemistry, General Chemistry for Engineers,
Introductory Organic Chemistry

Publications

21. Partyka, D. V.; **Teets, T. S.**; Zeller, M.; Updegraff, J. B. III, Hunter, A. D.; Gray, T. G. “Constrained Digold(I) Diaryls: Syntheses, Crystal Structures, and Photophysics”; *Chem. Eur. J.* **2012**, *18*, 2100–2112.
20. Pizano, A. A.; Lutterman, D. A.; Holder, P. G.; **Teets, T. S.**; Stubbe, J.; Nocera, D. G. “Photo-ribonucleotide reductase $\beta 2$ by selective cysteine labeling with a radical phototrigger”; *Proc. Natl. Acad. Sci. USA* **2012**, *109*, 39–43.
19. **Teets, T. S.**; Nocera, D. G. “Mechanistic Studies of O₂ Reduction Effected by Group 9 Bimetallic Hydride Complexes”; *J. Am. Chem. Soc.* **2011**, *133*, 17796–17806.
18. **Teets, T. S.**; Nocera, D. G. “Photocatalytic hydrogen production”; *Chem. Comm.* **2011**, *47*, 9268–9274.
17. **Teets, T. S.**; Cook, T. R.; McCarthy, B. D.; Nocera, D. G. “Redox Chemistry, Acid Reactivity, and Hydrogenation Reactions of Two-Electron Mixed Valence Diiridium and Dirhodium Complexes”; *Inorg. Chem.* **2011**, *50*, 5223–5233.
16. **Teets, T. S.**; Cook, T. R.; McCarthy, B. D.; Nocera, D. G. “Oxygen Reduction to Water Mediated by a Dirhodium Hydrido-Chloride Complex”; *J. Am. Chem. Soc.* **2011**, *133*, 8114–8117.
15. Schwalbe, M.; Dogutan, D. K.; Stoian, S. A.; **Teets, T. S.**; Nocera, D. G. “Xanthene-Modified and Hangman Iron Corroles”; *Inorg. Chem.* **2011**, *50*, 1368–1377.
14. **Teets, T. S.**; Neumann, M. P.; Nocera, D. G. “Heterobimetallic rhodium–gold halide and hydride complexes”; *Chem. Commun.* **2011**, *47*, 1485–1487.
13. Dogutan, D. K.; Stoian, S. A.; McGuire, R. Jr.; Schwalbe, M.; **Teets, T. S.**; Nocera, D. G. “Hangman Corroles: Efficient Synthesis and Oxygen Reaction Chemistry”; *J. Am. Chem. Soc.* **2011**, *133*, 131–140.
12. Cook, T. R.; Dogutan, D. K.; Reece, S. Y.; Surendranath, Y.; Teets, T. S.; Nocera, D. G. “Solar Energy Supply and Storage for the Legacy and Nonlegacy Worlds”; *Chem. Rev.* **2010**, *110*, 6474–6502.
11. **Teets, T. S.**; Cook, T. R.; Nocera, D. G. “The Diphosphine tfepma and its Diiridium Complex Ir₂^{0,II}(tfepma)₃Cl₂”; *Inorg. Synth.* **2010**, *35*, 164–168.
10. McGuire, R. Jr.; Dogutan, D. K.; **Teets, T. S.**; Suntivich, J.; Shao-Horn, Y.; Nocera, D. G. “Oxygen reduction reactivity of cobalt(II) hangman porphyrins”; *Chem. Sci.* **2010**, *1*, 411–414.

9. **Teets, T. S.**; Lutterman, D. A.; Nocera, D. G. “Halogen Photoreductive Elimination from Metal–Metal Bonded Iridium(II)–Gold(II) Heterobimetallic Complexes”; *Inorg. Chem.* **2010**, *49*, 3035–3043.
8. Dogutan, D. K.; Bediako, D. K.; **Teets, T. S.**; Schwalbe, M.; Nocera, D. G. “Efficient Synthesis of Hangman Porphyrins”; *Org. Lett.* **2010**, *12*, 1036–1039.
7. Partyka, D. V.; Gao, L.; **Teets, T. S.**; Updegraff, J. B. III; Deligonul, N.; Gray, T. G. “Copper-Catalyzed Huisgen [3 + 2] Cycloaddition of Gold(I) Alkynyls with Benzyl Azide. Syntheses, Structures, and Optical Properties”; *Organometallics* **2009**, *28*, 6171–6182.
6. Gao, L.; Peay, M. A.; Partyka, D. V.; Updegraff, J. B. III; **Teets, T. S.**; Esswein, A. J.; Zeller, M.; Hunter, A. D.; Gray, T. G. “Mono- and Di-Gold(I) Naphthalenes and Pyrenes: Syntheses, Crystal Structures, and Photophysics”; *Organometallics* **2009**, *28*, 5669–5681.
5. **Teets, T. S.**; Updegraff, J. B. III; Esswein, A. J.; Gray, T. G. “Three-Coordinate, Phosphine-Ligated Azadipyrrromethene Complexes of Univalent Group 11 Metals”; *Inorg. Chem.* **2009**, *48*, 8134–8144.
4. **Teets, T. S.**; Nocera, D. G. “Halogen Photoreductive Elimination from Gold(III) Centers”; *J. Am. Chem. Soc.* **2009**, *131*, 7411–7420.
3. Bachmann, J.; **Teets, T. S.**; Nocera, D. G. “Proton storage in the periphery of zirconium(IV) porphyrinogen”; *Dalton Trans.* **2008**, 4549–4551.
2. **Teets, T. S.**; Partyka, D. V.; Updegraff, J. B. III; Gray, T. G. “Homoleptic, Four-Coordinate Azadipyrrromethene Complexes of d¹⁰ Zinc and Mercury”; *Inorg. Chem.* **2008**, *47*, 2338–2346.
1. **Teets, T. S.**; Partyka, D. V.; Esswein, A. J.; Updegraff, J. B. III; Zeller, M.; Hunter, A. D.; Gray, T. G. “Luminescent Three-Coordinate Azadipyrrromethene Complexes of d¹⁰ Copper, Silver, and Gold”; *Inorg. Chem.* **2007**, *46*, 6218–6220.

Invited Seminars

3. Teets, T. S.; Nocera, D. G. “Mechanism of O₂ Reduction Reactions Mediated by Dirhodium and Diiridium Complexes”; Inorganic Reaction Mechanisms Gordon Research Conference, March 6–11 2011, Galveston, TX (selected for poster talk).
2. Teets, T. S. “A New Mechanism for Photocatalytic HCl Splitting Mediated by Dirhodium Complexes”; Inorganic Chemistry Gordon Research Seminar. June 19–20, 2010, University of New England, Biddeford, ME.
1. Teets, T. S. “Halogen Photoreductive Elimination from Late Transition Metal Complexes”; 22nd Boston Regional Inorganic Colloquium, June 12 2010, Brandeis University, Waltham, MA.